RICE UNIVERSITY

Direct Dark Matter Search with the XENON100 Experiment

by

Yuan Mei

A THESIS SUBMITTED
IN PARTIAL FULFILLMENT OF THE
REQUIREMENTS FOR THE DEGREE

Doctor of Philosophy

Approved, Thesis Committee:

Uwe Oberlack, Adjunct Associate Professor
Physics and Astronomy, Rice University
Professor, Physics,
Johannes Gutenberg Universität Mainz,
Germany

Jabus Roberts, Professor
Physics and Astronomy

Giovanni Fossati, Assistant Professor
Physics and Astronomy

Robert Raphael, Associate Professor
Bioengineering

Houston, Texas
May 2011

Abstract

Direct Dark Matter Search with the XENON100 Experiment

by

Yuan Mei

Dark matter, a non-luminous, non-baryonic matter, is thought to constitute 23 % of the matter-energy components in the universe today. Except for its gravitational effects, the existence of dark matter has never been confirmed by any other means and its nature remains unknown. If a hypothetical Weakly Interacting Massive Particle (WIMP) were in thermal equilibrium in the early universe, it could have a relic abundance close to that of dark matter today, which provides a promising particle candidate of dark matter. Minimal Super-Symmetric extensions to the standard model predicts a stable particle with mass in the range $10\,\mathrm{GeV/c^2}$ to $1000\,\mathrm{GeV/c^2}$, and spin-independent cross-section with ordinary matter nucleon $\sigma_\chi < 1 \times 10^{-43}\,\mathrm{cm^2}$.

The XENON100 experiment deploys a Dual Phase Liquid Xenon Time Projection Chamber (LXeTPC) of 62 kg liquid xenon as its sensitive volume, to detect scintillation (*S1*) and ionization (*S2*) signals from WIMP dark matter particles directly scattering off xenon nuclei. The detector is located underground at Laboratori Nazionali del Gran Sasso (LNGS) in central Italy. 1.4 km of rock (3.7 km water equivalent) reduces the cosmic muon background by a factor of 10^6. The event-by-event 3D positioning capability of TPC allows volume fiducialization. With the self-shielding power of liquid xenon, as well as a 99 kg liquid xenon active veto, the electromagnetic radiation background is greatly suppressed. By utilizing the difference of (*S2*/*S1*) between electronic recoil and nuclear recoil, the expected WIMP signature, a small nuclear recoil energy deposition, could be discriminated from electronic recoil background with high efficiency. XENON100 achieved the lowest background rate ($< 2.2 \times 10^{-2}$ events/kg/day/keV) in the dark matter search region ($< 40\,\mathrm{keV}$) among all direct dark matter detectors. With 11.2 days of data, XENON100 already sets the world's best spin-independent WIMP-nucleon cross-section limit of $2.7 \times 10^{-44}\,\mathrm{cm^2}$ at WIMP mass $50\,\mathrm{GeV/c^2}$. With 100.9 days of data, XENON100 excludes WIMP-nucleon cross-section above $7.0 \times 10^{-45}\,\mathrm{cm^2}$ for a WIMP mass of $50\,\mathrm{GeV/c^2}$ at 90 % confidence level.

This page intentionally left blank

Acknowledgments

I would like to thank my advisor Uwe Oberlack, for introducing me into the XENON experiment and low background rare event search field in general. The journey he guided me through from ground up, connecting every bits from hardware to software, and from experimental data to theoretical model, was better than I could ever imagined in scientific research. I also thank Elena Aprile from Columbia University, Laura Baudis from Universität Zürich, and other PIs in the XENON collaboration, for making the experiment possible.

Particularly I would like to thank people in the XENON collaboration I closely worked with, Marc Schumann, Peter Shagin, Guillaume Plante, Rafael Lang, Antonio Melgarejo, Karl Giboni, Kaixuan Ni, Kyungeun Lim, Alfredo Ferella, Alexander Kish and Teresa Marrodán, for wonderful discussions and debates over the years, and great advice I took from them which helped me in completing my thesis.

I also thank my thesis committee at Rice University, Jabus Roberts, Giovanni Fossati, and Robert Raphael, for their guidance at Rice and reading of this thesis.

I am especially grateful to my parents, who dedicated their unconditional support throughout my education, and allowed me to pursuit my interest into an area neither of them could understand. As the only child in the family, I am deeply sorry for not going back to China to visit them even once since I started graduate studies at Rice in early 2006.

Contents

List of Figures

List of Tables

Chapter 1

Introduction

Various astrophysical observations are confirming a consistent picture of our universe, a model known as the "standard model" of big bang cosmology: ΛCDM. In this model, our universe is made up of roughly 27 % of matter and the remaining 73 % of Dark Energy (WMAP Science Team [57]). While it is a true mystery that 73 % of the universe is 'required' to be filled with an unknown form of energy (Dark Energy) in order to explain the accelerated expansion, the matter component, which generates gravitational effects to glue stars, galaxies and the universe together, is not well understood either.

In the observable universe, ordinary matters—matter that we are made of: proton, neutron and electron; and other matter/anti-matter we have observed and are explained in the Standard Model of Particle Physics, account for only 4.6 % of the total mass-energy components. About 23 % of the universe is filled with an unknown form of matter: Dark Matter.

Dark Matter is a hypothetical matter that does not emit, absorb or scatter electromagnetic radiation (dark, or transparent), but has mass thus shows gravitational effects. The concept of Dark Matter is devised from the discrepancy between mass observed through its gravitational effects and mass contained in visible luminous matter. The term 'Dark Matter' was initially coined by Fritz Zwicky who found evidence for missing mass in spiral galaxies in the 1930s (Zwicky [62, 63]).

1.1 The Evidence and Theoretical Background of Dark Matter

Evidence for the existence of Dark Matter are mostly from the excess of gravitational effects not accounted for by the observed luminous (ordinary) matter. To call it 'excess', one assumes the gravitational laws in the framework of Newton and Einstein are correct. It has been challenged, with some success, that the gravitational laws are probably not the same as the distance gets very large or the gravity gets very small. On the other hand, if the current understanding of gravitational laws is indeed correct, then the extra amount of matter could be a form of ordinary matter, or a new (unknown) form of matter that interacts with electromagnetic radiation weakly. Currently it is widely acknowledged that a new form of matter, Weakly Interacting Massive Particle (WIMP) is the best candidate to explain the Dark Matter problem.

1.1.1 Observational Evidence

Various pieces of observational evidence suggest that Dark Matter exists at three drastically different size scales: in galaxies, in clusters of galaxies and in the whole universe. A few representative samples in each of their respective size scales are described in the following.

In Spiral Galaxies: Galactic Rotation Curve

In a galaxy at equilibrium, for a 'test particle' (i.e. a star or gas cloud) at distance r from the center, its rotation velocity is simply governed by the Kepler's law

$$v(r) = \sqrt{G\frac{M(r)}{r}}$$

where

$$M(r) = 4\pi \int_0^r \rho(r')r'^2 dr'$$

is the mass contained in r and $\rho(r)$ is the mass density profile (simplified: assuming isotropic mass distribution).

If there were no Dark Matter, and the majority of mass of a galaxy is contained in the visible disk, then at the outer edge of the galaxy, $M(r)$ would stay constant as r grows bigger since most of the mass is already contained. Under this assumption, $v(r)$ would fall as $\sqrt{1/r}$ at the outer edge of the galaxy.

The observation comes back with a big surprise (see Fig. 1.1). As presented by Begeman et al. [10], $v(r)$ at the outer edge of galaxies seem to be independent of r. Since $v(r)$ is not falling as the expected behavior $\sqrt{1/r}$, there must be additional mass within r that provides additional gravity to support the flat distribution of $v(r)$. And from the flat behavior of $v(r)$ it could be inferred that $M(r) \propto r$ which in turn requires $\rho(r) \propto 1/r^2$ for a spherical mass distribution.

Following the above argument, a Dark Matter 'halo' with mass density profile $\rho(r) \propto 1/r^2$ at the outer edge of the visible galaxy is proposed to exist.

Rubin et al. [46] investigated rotation curves at outer edge of many spiral galaxies and concluded that most of the galaxies contain a dark halo extending well beyond the visible galactic bulge.

In Clusters of Galaxies: Gravitational Lensing

When light passes by a massive object, the path of light is no longer straight but becomes bent by the gravitational field (Einstein [24]). When the massive object is compact (in the sense that the object is bound in a closed border, it doesn't mean the object is small), the gravitational field of the object bends light passing by the object. If observer, massive object and distant light source are roughly aligned, light is focused as if it passes through an optical lens (Fig. 1.2).

On an image of the target object distorted by a gravitational lens, the object could be seen as multiple distorted replica at different places. By analyzing the image, the mass distribution of the lens, usually clusters of galaxies, could be determined.

A survey with gravitational lensing on 22 galaxies by Gavazzi et al. [26] shows a consistent mass density profile of $\rho(r) \propto 1/r^2$ across galaxies.

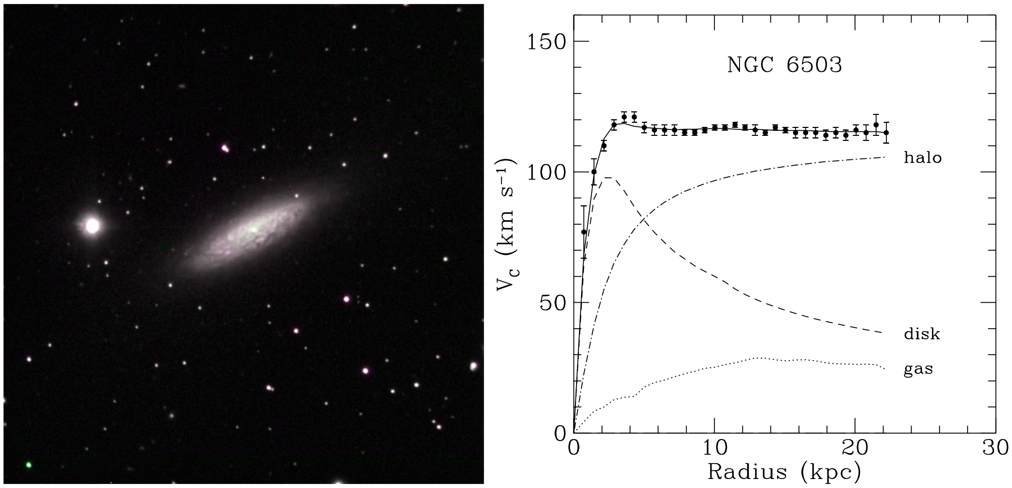

Figure 1.1: Galactic Rotation Curve. Left: visible light image of galaxy NGC6503 (image courtesy of NASA). Right: measured Rotation Curve of galaxy NGC6503 (Figure 1 in Begeman et al. [10]). See Begeman et al. [10] for rotation curves of several other galaxies which show similar flattening feature at large radii. The mass and rotation was also studied earlier by Burbidge et al. [14].

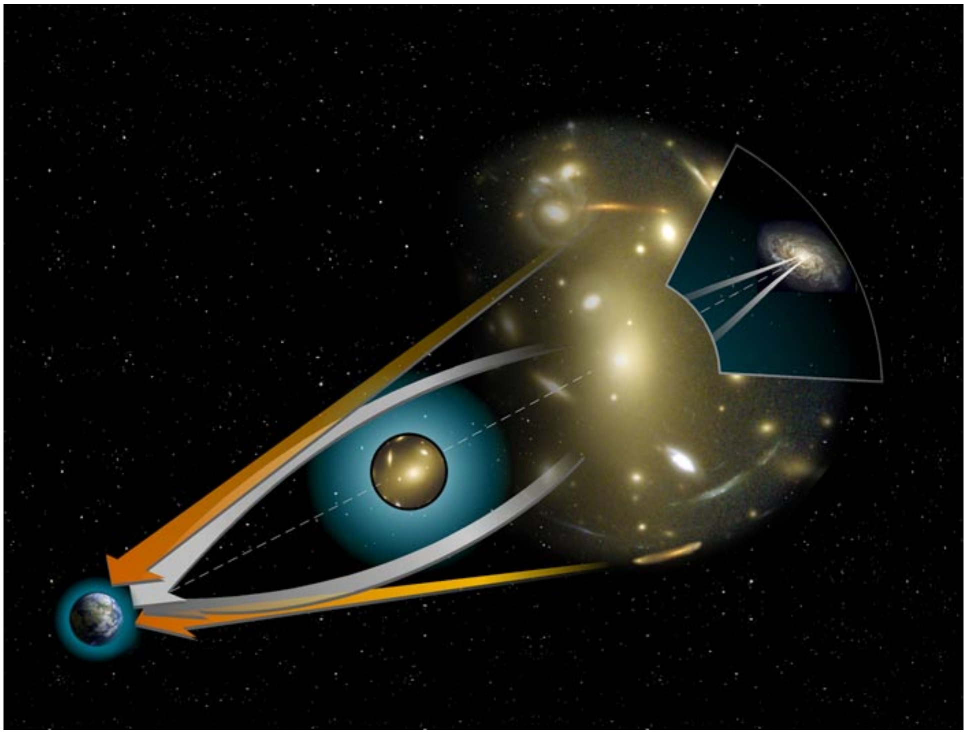

Figure 1.2: Gravitational Lensing. (image courtesy of NASA)

The advantage of gravitational lensing is that it can measure the mass distribution at much larger scale than a single galaxy. A strong evidence which is ruling out the alternative theories to the Dark Matter problem is supported by the gravitational lensing measurement of a cluster of galaxies (Fig. 1.4).

In the Whole Universe: Cosmic Microwave Background (CMB)

Cosmic Microwave Background (CMB) is the relic radiation of the big bang. It was discovered by radio-astronomers Arno Penzias and Robert Wilson in 1964. CMB is mostly a uniform black-body radiation throughout the universe with mean temperature $2.725 \pm 0.002\,\mathrm{K}$ (COBE/FIRAS [18]). CMB measurements with high precision (WMAP Science Team [57]) revealed small fluctuations in temperature that are spatially correlated. As shown in Fig. 1.3 (top), the CMB has anisotropy (fluctuations) below the mK level. A decomposition into spherical harmonics shows that the anisotropy is spatially correlated (Fig. 1.3 (bottom)). Expressed in multipole moment l, the first peak at $l \approx 200$ corresponds to the acoustic baryon-photon density oscillation scale in the early universe right before the decoupling of photons and baryons. It is the result of the competition between radiation pressure and gravitational contraction. The first peak tells the curvature of the universe. The ratio between first peak and second peak gives the baryon density. The third peak could be used to estimate the dark matter density.

The temperature fluctuations observed in CMB provides the information of densities of ordinary (baryonic) matter, dark matter, and the total energy density. The power spectrum of the CMB requires that about $23\,\%$ of the universe is filled with matter that does not interact with electromagnetic radiation.

1.1.2 Answers to the Problem without New Forms of Matter

All the evidence shows that the gravitational effect caused by luminous matter is not enough to account for the total amount of gravity observed. The evidence can be interpreted in two ways:

1. The current knowledge of gravitational laws and dynamics are correct; there are forms of matter that are non-luminous exist in the universe.

2. The forms of matter that exist in the universe are known ordinary matter, while the current knowledge of gravitational laws and dynamics are not correct at large scale. The modification to the gravitational laws and dynamics would explain the discrepancy between the observed luminous matter and the gravitational effects.

MACHO

Before the precision measurements of the CMB through WMAP, the mass deficit to account for the gravitational effect was thought to be constituted of Massive Astrophysical Compact Halo Objects (MACHOs) such as black holes, neutron stars, brown dwarfs, white dwarfs, very faint red dwarfs, unassociated planets, etc. MACHOs are objects of normal baryonic matter that hardly emit any radiation and drift through interstellar space. Combined with the fact that MACHOs are

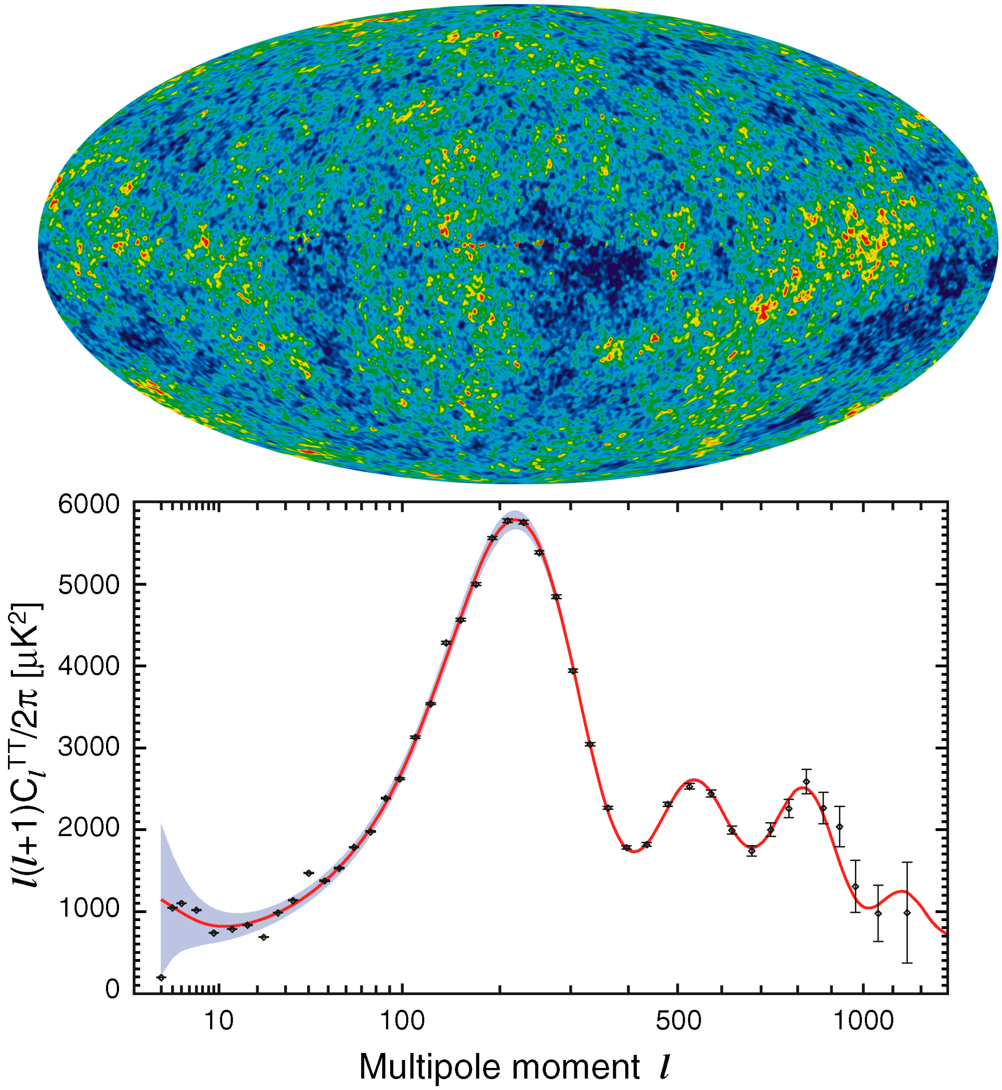

Figure 1.3: WMAP CMB Anisotropy. Top: temperature fluctuation in the cosmic microwave background from WMAP 7-year data. Colors from dark blue to red correspond to temperature range from $-200\,\mu K$ to $200\,\mu K$. Bottom: temperature and polarization power spectra derived from the WMAP 7-year data. Data are represented as points, curves correspond to the best-fit ΛCDM model, and shaded regions delineate cosmic variance about the model. (image courtesy of NASA/WMAP Science Team [57]).

massive, they appeared to be plausible candidates of the non-luminous mass in the universe. The major method to detect MACHOs is the gravitational microlensing (Alcock et al. [3]). Analogous to usual gravitational lensing which detects the bending of light by large scale structures of mass, microlensing detects the effect that when a MACHO passes in front or nearly in front of a star, light from the star is bent so that the star appears to be brighter.

Although MACHOs provide a favorable model of Dark Matter with special (but known) forms of ordinary matter, extensive astronomical surveys show that MACHOs can only make up to at most 20 % of Dark Matter component in the galaxy, while in most cases even less (Alcock et al. [3], Graff and Freese [27], Najita et al. [40], Tisserand et al. [54]). Therefore, while MACHOs do contribute to some of the Dark Matter components, it alone does not account for the majority of Dark Matter. It is constrained by the 4.6 % upper bound on baryonic matter.

MOND

MOdified Newtonian Dynamics (MOND) is an attempt to modify the gravitational law and dynamics at very large distance and very week gravitational field (Milgrom [39]), without the hypothetical dark matter component. The very basic version of MOND postulates that at very small acceleration, the gravitational law deviates from the Newtonian law and the orbiting velocity becomes $v = (GMa_0)^{1/4}$. a_0 is an acceleration constant introduced to be a measure when MOND starts to be effective.

Figure 1.4: Bullet Cluster. Pink: hot X-ray producing gas; orange and white: optical light from stars in the galaxies; blue: total mass concentration in the clusters. The Bullet Cluster is composed of two large clusters of galaxies colliding at high speeds. (image courtesy of NASA)

While MOND successfully explains the galactic rotation curve without Dark Matter, it is strongly challenged by the spatial separation of hot gas and mass observed in the Bullet Cluster shown in Fig. 1.4. Fig. 1.4 is a composite image of three different sources: orange and white shows the optical image of stars in the galaxies; pink shows the hot gas that produces X-ray; blue shows the total mass concentration inferred from gravitational lensing observations.

It is clearly visible that the hot X-ray emitting gas is separated from the mass distribution. This separation is produced by the high speed collision in which the gas component collided with each other but the stars and dark matter were intact. This phenomenon cannot be explained by an modified law of gravity centered on the hot gas, because a law of gravity should be independent of the type of matter but only be proportional to the mass. It provides direct evidence that a non-luminous matter, Dark Matter, is dominant in the Bullet Cluster.

1.1.3 Weakly Interacting Massive Particle (WIMP)

Despite the compelling evidence for the existence of Dark Matter, its nature remains unknown. Weakly Interacting Massive Particle (WIMP) is a favorable candidate for particle dark matter. WIMPs are thought to be massive particles of mass from tens to thousands of $\mathrm{GeV/c^2}$, traveling at non-relativistic velocity. WIMPs are weekly coupled to ordinary matter.

Supersymmetry (SUSY), a theory extending the standard model of particle physics, provides natural candidates for WIMP particles (Jungman et al. [32]). SUSY postulates every fermion has a supersymmetric boson partner while every boson has a supersymmetric fermion partner. The Lightest Supersymmetric Particles (LSP), which would be stable, serve as promising candidates for WIMP dark matter particles.

1.2 Principle of Direct WIMP Dark Matter Detection

Albeit weakly, WIMPs are expected to interact with ordinary matter providing detectable signatures through energy deposition. The major challenge of the detection is the control of background. The WIMP interaction is expected to be rare, while backgrounds from natural radioactivity and cosmic rays have many orders of magnitude higher interaction rate. Developing shielding and discrimination techniques is the key to a successful detection of WIMP signature. In the following, the expected WIMP signature in a dark matter detector is discussed.

1.2.1 The Standard Halo Model (SHM)

An isotropic distribution of Dark Matter in the Milky Way galaxy is consistent with the observed rotation curve, although a flattened rotating spherical distribution is also plausible and supported by simulations. In the following, we consider a spherical "halo", i.e., an isotropic distribution of mass, of which the density depends only on radius but not on angular positions. Dark Matter density is denoted by ρ_D. At the radial distance of our solar system in the galaxy, $\rho_\mathrm{D} \approx 0.3\,\mathrm{GeV/c^2/cm^3}$ (Bruch et al. [12]).

In the Dark Matter Halo, Dark Matter particles cannot be stationary but should have velocity in order to counteract the gravity to keep a stable galaxy in equilibrium. It is assumed that Dark Matter particles follow a simple Maxwellian velocity distribution

$$f(\mathbf{v}) \propto \left(\frac{-|\mathbf{v}|^2}{v_0^2} \right)$$

where $\mathbf{v}$ is defined in the galactic rest frame. More complicated astrophysics models are discussed in Savage et al. [48]. The velocity however has to be constrained below the galactic escape velocity v_{esc}. Beyond v_{esc}, the particle is no longer bound to the gravitational potential of the galaxy. At the earth position in the galaxy, $v_{\text{esc}} = 544\,\text{km/s}$ (Smith et al. [51]).

Although particles in the Halo follow a velocity distribution, the total sum of the velocity is zero. In the Standard Halo Model, the halo does not rotate in the galactic rest frame.

For Direct Dark Matter Search experiments performed on earth, the velocity (and its distribution) of interest is the observed Dark Matter velocity $\mathbf{v}_{\text{obs}}$ in the earth frame. Denoting the earth velocity in the galactic frame $\mathbf{v}_{\text{e}}(t)$, we can rewrite the Dark Matter velocity distribution observed in the earth frame as

$$f(\mathbf{v}_{\text{obs}}, t) \propto \left(\frac{-|\mathbf{v}_{\text{obs}} + \mathbf{v}_{\text{e}}(t)|^2}{v_0^2} \right) . \tag{1.1}$$

The time parameter t enters here because the earth velocity in the galactic frame $\mathbf{v}_{\text{e}}$ includes the velocity of earth orbiting the sun. Therefore a varying component in the measurable time scale of year has to be addressed with t.

The earth velocity in the galactic frame $\mathbf{v}_{\text{e}}$ has two components:

$$\mathbf{v}_{\text{e}}(t) = \mathbf{v}_{\odot} + \mathbf{v}_{\oplus}(t) .$$

$\mathbf{v}_{\odot}$ is the velocity of sun in the galactic frame. It can be further broken down into two terms: the local circular velocity $\mathbf{v}_{\text{circ}} = (0, 220, 0)\,\text{km/s}$ and the peculiar motion of the sun $\mathbf{v}_{\odot\text{pm}} = (10.0, 5.25, 7.17)\,\text{km/s}$ (Dehnen and Binney [20]). We simply use the combined velocity $\mathbf{v}_{\odot} = (10.0, 225.25, 7.17)\,\text{km/s}$.

The orbiting velocity of earth around the sun

$$\mathbf{v}_{\oplus}(t) = v_{\oplus}[\hat{\epsilon}_1 \cos\omega(t - t_1) + \hat{\epsilon}_2 \sin\omega(t - t_1)]$$

(see Savage et al. [48]) where

$$\hat{\epsilon}_1 = (0.9931, 0.1170, -0.01032)$$
$$\hat{\epsilon}_2 = (-0.0670, 0.4927, -0.8676)$$

are the directions of the Earth velocity in the galactic coordinates at the Spring equinox and Summer solstice. ω denotes the angular speed of earth rotation. $t_1 = 0.218$ is the fraction of the year before the Spring equinox (March 21). $v_{\oplus} \approx 29.8\,\text{km/s}$.

It is also shown in Drukier et al. [23] that in the flat part of the galactic rotation curve, the Dark Matter velocity dispersion $v_0 = v_{\text{circ}} \approx 220\,\text{km/s}$.

1.2.2 Scatter Rate and Spectra

XENON100 detector measures the recoil energy—the kinetic energy of the target after interaction E_r of each event, and the rate of events R. Therefore the physics outcome of the detector is the recoil energy spectrum dR/dE_r. The recoil energy spectrum can generally be expressed as

$$\frac{dR}{dE_\mathrm{r}} = R_0 S(E_\mathrm{r}) F^2(E_\mathrm{r}) I \tag{1.2}$$

(Lewin and Smith [35]), where R_0 represents the unmodified rate if earth were stationary in the Dark Matter Halo; $S(E_\mathrm{r})$ includes the effect of the velocity of earth traveling in the Dark Matter Halo as well as the instrumental effects such as energy threshold; $F(E_\mathrm{r})$ describes the form factor of target nuclei and I takes into account the spin interaction related factors. Each of the terms is discussed in the following except that we only consider spin-independent interactions in this thesis.

Velocity Dependence of Rate

For incoming particles of number density n and uniform velocity v, the scatter rate off a single target can be described as

$$R = \sigma n v$$

where σ is the interaction cross section. When the incoming particle velocity has a distribution $f(\mathbf{v})$ ($\mathbf{v}$ represents the 3-dimensional velocity vector), the scatter rate can be written in a differential form with respect to $d\mathbf{v}$:

$$dR = \sigma \cdot n v f(\mathbf{v}) d^3 v = \sigma \cdot v dn\,.$$

dn is regarded as the differential particle density

$$dn = \frac{n_0}{k} f(\mathbf{v})\, d^3 v$$

where $n_0 = \rho_\mathrm{D}/M_\mathrm{D}$ is the dark matter particle number density in the laboratory frame, and

$$k = \int_0^{2\pi} d\phi \int_{-1}^{1} d(\cos\theta) \int_0^{v_\mathrm{esc}} f(|\mathbf{v}|) v^2\, dv$$

is a normalization factor such that

$$\int_0^{v_\mathrm{esc}} dn \equiv n_0\,.$$

Assuming a Maxwellian dark matter velocity distribution $f(v = |\mathbf{v}|) \propto \exp(-v^2/v_0^2)$, when the escape velocity is allowed to be at infinity, the integral gives $k_0 = (\pi v_0^2)^{3/2}$. When the distribution is truncated at $v = |\mathbf{v}_\mathrm{obs} + \mathbf{v}_\mathrm{e}(t)| = v_\mathrm{esc}$, we have

$$k = k_0 \left[\mathrm{erf}\left(\frac{v_\mathrm{esc}}{v_0} \right) - \frac{2}{\sqrt{\pi}} \frac{v_\mathrm{esc}}{v_0} e^{-v_\mathrm{esc}^2/v_0^2} \right] \tag{1.3}$$

(Lewin and Smith [35]).

In the case $v_\mathrm{e} = 0$ and $v_\mathrm{esc} = \infty$, the total scatter rate

$$R_0 = \int_{v=0}^{\infty} dn = \int_{v=0}^{\infty} \sigma \cdot v dn = \frac{2}{\sqrt{\pi}} n_0 \sigma v_0 \, .$$

For other velocities, the total scatter rate is

$$\begin{aligned} R =& R_0 \frac{\sqrt{\pi}}{2} \frac{\int v f(\mathbf{v}) d^3 v}{v_0} \\ =& R_0 \frac{k_0}{k} \frac{1}{2\pi v_0^4} \int v f(\mathbf{v}) d^3 v \, . \end{aligned} \tag{1.4}$$

For detection on earth, what we are interested in is the observed WIMP velocity with respect to earth $\mathbf{v}_\mathrm{obs}$. Therefore we rewrite equation (1.4) with respect to $\mathbf{v}_\mathrm{obs}$

$$R(v_\mathrm{e}, v_\mathrm{esc}) = R_0 \frac{k_0}{k} \frac{1}{2\pi v_0^4} \int f(\mathbf{v}_\mathrm{obs} + \mathbf{v}_\mathrm{e}) d^3 v_\mathrm{obs} \, . \tag{1.5}$$

The integral with a few combination of parameters of equation (1.5) are

$$\frac{R(0, v_\mathrm{esc})}{R_0} = \frac{k_0}{k_1} \left[1 - \left(1 + \frac{v_\mathrm{esc}^2}{v_0^2} \right) e^{-v_\mathrm{esc}^2 / v_0^2} \right] \tag{1.6a}$$

$$\frac{R(v_\mathrm{e}, \infty)}{R_0} = \frac{1}{2} \left[\sqrt{\pi} \left(\frac{v_\mathrm{e}}{v_0} + \frac{1}{2} \frac{v_0}{v_\mathrm{e}} \right) \mathrm{erf} \left(\frac{v_\mathrm{e}}{v_0} \right) + e^{-v_\mathrm{e}^2 / v_0^2} \right] \tag{1.6b}$$

$$\frac{R(v_\mathrm{e}, v_\mathrm{esc})}{R_0} = \frac{k_0}{k_1} \left[\frac{R(v_\mathrm{e}, \infty)}{R_0} - \left(\frac{v_\mathrm{esc}^2}{v_0^2} + \frac{1}{3} \frac{v_\mathrm{e}^2}{v_0^2} + 1 \right) e^{-v_\mathrm{esc}^2 / v_0^2} \right] \tag{1.6c}$$

With incoming WIMP kinetic energy $E_\mathrm{k} = \frac{1}{2} M_\mathrm{D} v_\mathrm{obs}^2$, the recoil energy of the target nucleus is

$$E_\mathrm{r} = E_\mathrm{k} r (1 - \cos\theta)/2$$

where θ is the scattering angle defined in the center-of-mass frame and r is the kinematic factor

$$r = \frac{4 M_\mathrm{D} M_\mathrm{T}}{(M_\mathrm{D} + M_\mathrm{T})^2} \, . \tag{1.7}$$

Assume the scattering is isotropic therefore E_r is uniformly distributed in the range $0 \le E_\mathrm{r} \le E_\mathrm{k} r$, we have the differential rate

$$\frac{dR}{dE_\mathrm{r}} = \int_{E_\mathrm{min}}^{E_\mathrm{max}} \frac{1}{E_\mathrm{k} r} dR(E_\mathrm{k}) = \frac{1}{E_0 r} \int_{v_\mathrm{min}}^{v_\mathrm{max}} \frac{v_0^2}{v_\mathrm{obs}^2} dR(v_\mathrm{obs}) \tag{1.8}$$

where $E_\mathrm{min} = E_\mathrm{r}/r$ is the smallest particle kinetic energy that can give a recoil energy of E_r, $E_0 = \frac{1}{2} M_\mathrm{D} v_0^2$ and

$$v_\mathrm{min} = \sqrt{2 E_\mathrm{min} / M_\mathrm{D}} = v_0 \sqrt{E_\mathrm{r} / E_0 r}$$

is the WIMP velocity corresponding to E_min.

Writing equation (1.4) in the differential form and plugging it into equation (1.8), we have

$$\frac{dR}{dE_{\mathrm{r}}} = \frac{R_0}{E_0 r}\frac{k_0}{k}\frac{1}{2\pi v_0^4}\int_{v_{\min}}^{v_{\max}} \frac{1}{v} f(\mathbf{v}_{\mathrm{obs}} + \mathbf{v}_{\mathrm{e}}) d^3 v_{\mathrm{obs}} \,. \tag{1.9}$$

Performing the same type of integration as in equation (1.6) on equation (1.9), we get the form of dR/dE_{r}:

$$\frac{dR(0,\infty)}{dE_{\mathrm{r}}} = \frac{R_0}{E_0 r} e^{-E_{\mathrm{r}}/E_0 r} \tag{1.10a}$$

$$\frac{dR(0,v_{\mathrm{esc}})}{dE_{\mathrm{r}}} = \frac{k_0}{k_1}\frac{R_0}{E_0 r}\left(e^{-E_{\mathrm{r}}/E_0 r} - e^{-v_{\mathrm{esc}}^2/v_0^2}\right) = \frac{k_0}{k_1}\left[\frac{dR(0,\infty)}{dE_{\mathrm{r}}} - \frac{R_0}{E_0 r} e^{-v_{\mathrm{esc}}^2/v_0^2}\right] \tag{1.10b}$$

$$\frac{dR(v_{\mathrm{e}},\infty)}{dE_{\mathrm{r}}} = \frac{R_0}{E_0 r}\frac{\sqrt{\pi}}{4}\frac{v_0}{v_{\mathrm{e}}}\left[\mathrm{erf}\left(\frac{v_{\min}+v_{\mathrm{e}}}{v_0}\right) - \mathrm{erf}\left(\frac{v_{\min}-v_{\mathrm{e}}}{v_0}\right)\right] \tag{1.10c}$$

$$\frac{dR(v_{\mathrm{e}},v_{\mathrm{esc}})}{dE_{\mathrm{r}}} = \frac{k_0}{k_1}\left[\frac{dR(v_{\mathrm{e}},\infty)}{dE_{\mathrm{r}}} - \frac{R_0}{E_0 r} e^{-v_{\mathrm{esc}}^2/v_0^2}\right] \tag{1.10d}$$

For convenience, the target density is often absorbed into R_0 and a few "standard" numerical numbers could be plugged in to compute R_0 [events/kg/day] as

$$R_0 = \frac{361.1}{M_{\mathrm{D}} M_{\mathrm{T}}}\left(\frac{\sigma_0}{1\,\mathrm{pb} = 1\times 10^{-36}\,\mathrm{cm}^2}\right)\left(\frac{\rho_{\mathrm{D}}}{0.3\,\mathrm{GeV/c^2/cm^3}}\right)\left(\frac{v_0}{220\,\mathrm{km/s}}\right) \tag{1.11}$$

where M_{T} is the mass of the target nucleus in GeV/c^2 and approximately $M_{\mathrm{T}} = A_{\mathrm{T}} \cdot \mathrm{amu}$ where $1\,\mathrm{amu} \approx 0.931\,\mathrm{GeV/c^2}$.

Nuclear Form Factor

In scattering events, when the corresponding de Broglie wavelength h/q of momentum transfer $q = \sqrt{2M_{\mathrm{T}}E_{\mathrm{r}}}$ is comparable to the size of the target nucleus, an effect similar to waves scattering off a small object appears. The scattering amplitude drops as q gets higher. Nuclear from factor $F(q)$ is introduced to account for this effect and the cross-section becomes q dependent

$$\sigma(qr_n) = \sigma_0 F^2(qr_n)\,,$$

where r_n is the effective nuclear radius.

In the plane wave approximation, the Nuclear From Factor is the Fourier Transform of the density distribution of scattering centers in the nucleus $\rho(r)$ (considering an isotropic density):

$$\begin{aligned} F(q) &= \int\limits_{\mathrm{volume}} \rho(r) e^{\imath \mathbf{q}\cdot\mathbf{r}} d^3x \\ &= \frac{4\pi}{q}\int_0^\infty r\sin(qr)\rho(r)dr\,. \end{aligned} \tag{1.12}$$

Helm [29] suggested a density profile

$$\rho(r) = \int_{\text{volume}} \rho_0(\mathbf{r}')\rho_1(\mathbf{r}-\mathbf{r}')d^3x' \tag{1.13}$$

where

$$\rho_0(r) = \begin{cases} \frac{3}{4\pi r_n^3} & r < r_n \\ 0 & r > r_n \,, \end{cases} \tag{1.14a}$$

$$\rho_1(r) = \frac{1}{(2\pi s^2)^{\frac{3}{2}}} e^{-r^2/2s^2} \,. \tag{1.14b}$$

Essentially $\rho(r)$ in equation (1.13) describes a nuclear density profile with a core of constant density within r_n and a Gaussian falling density at the "skin" of the nucleus of thickness s. The advantage of Helm [29] nuclear density is that it yields an analytic form factor

$$F(qr_n) = 3\frac{j_1(qr_n)}{qr_n} e^{-(qs)^2/2} \tag{1.15}$$

where $j_1(x) = \frac{\sin x}{x^2} - \frac{\cos x}{x}$ is the first order Spherical Bessel Function. The parameters (r_n, s) for different target nuclei can be estimated as $s = 1\,\text{fm}$, $r_n = \sqrt{r_v^2 - 5s^2}$ and $r_v = 1.2A_{\text{T}}^{1/3}$ fm, suggested by Chang et al. [16].

The behavior of form factors $F^2(q)$ of a few target nuclei are shown in Fig. 1.5 as functions of recoil energy E_{r}.

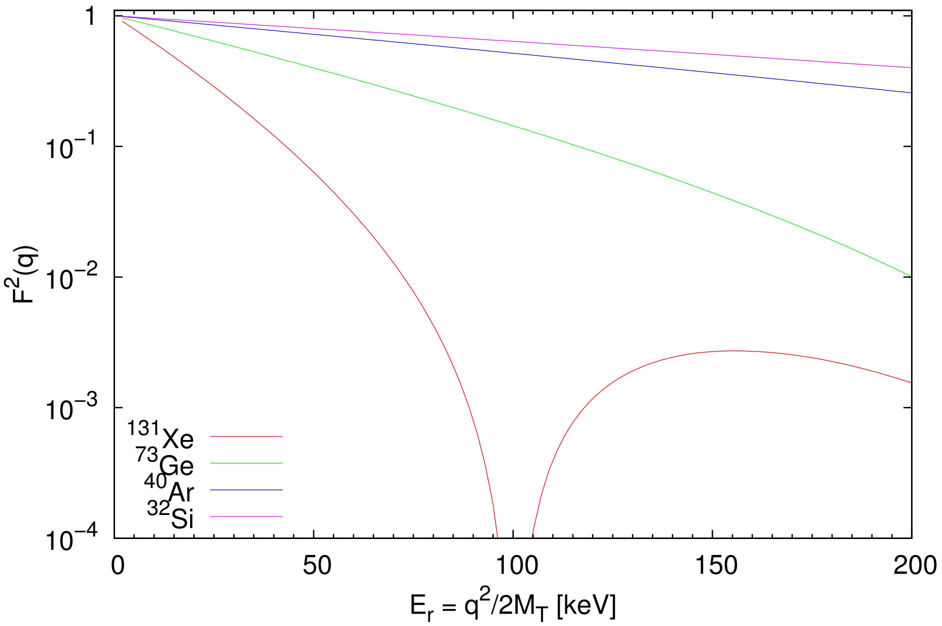

Figure 1.5: Nuclear Form Factor of a few common target nuclei used for WIMP Dark Matter search, plotted as function of recoil energy E_{r}

Comparison Between Different Targets

The scatter rate, as shown in equation (1.11), is expressed as events per unit time per unit target mass. This notation alone introduces bias when comparing experimental results using different target nuclei. The measurement outcome σ_0 should be expressed in a target independent way, for instance WIMP-single proton cross section. All the measurements should convert their results using different types of nuclei to the same WIMP-single proton cross section.

In order to do so, the first step is to multiply A_{T}^2 since in coherent scattering, the zero moment transfer scattering amplitude is proportional to the number of scattering centers squared. Secondly, a factor

$$\left(\frac{\mu_{\mathrm{T}}}{\mu_{\mathrm{p}}}\right)^2 = \left(\frac{M_{\mathrm{D}}M_{\mathrm{T}}}{M_{\mathrm{D}}+M_{\mathrm{T}}}\Bigg/\frac{M_{\mathrm{D}}M_{\mathrm{p}}}{M_{\mathrm{D}}+M_{\mathrm{p}}}\right)^2 \tag{1.16}$$

should be multiplied to account for the kinematic difference due to the mass difference of target nuclei. M_p is the mass of a single proton target and μ is generally regarded as the reduced mass of WIMP-target system.

To understand the factor $\mu_{\mathrm{T}}/\mu_{\mathrm{p}}$ in equation (1.16), one could imagine that the same WIMP particle (mass and incoming velocity) interacts with two different targets at rest of different mass but the same cross section. The target with less mass will get less momentum transfer, and the ratio of momentum transfer between heavy and light targets is preciously $\mu_{\mathrm{T}}/\mu_{\mathrm{p}}$. Therefore, the recoil energy spectra is precisely scaled by μ^2 since $E_{\mathrm{r}} = q^2/2M_{\mathrm{T}}$.

With all the above factors taken into account, the final recoil energy spectrum could be written as

$$\left.\frac{dR}{dE_{\mathrm{r}}}\right|_{\mathrm{obs}} = \frac{dR(v_{\mathrm{e}}, v_{\mathrm{esc}})}{dE_{\mathrm{r}}}\sigma_p\left(A_{\mathrm{T}}\frac{\mu_{\mathrm{T}}}{\mu_{\mathrm{p}}}\right)^2 F^2(E_{\mathrm{r}}) \tag{1.17}$$

where σ_p is the normalized WIMP-single proton cross section. Differential rate $\frac{dR}{dE_{\mathrm{r}}}$ of a few common targets is shown in Fig. 1.6. Differential rate of xenon target with a few different WIMP masses assuming the same cross section is shown in Fig. 1.7.

In light of equation (1.10a), it is shown in Lewin and Smith [35] that equations in (1.10) can all be approximated by a simple exponential power spectra with the coefficient $R_0/E_0 r$ in front. From equation (1.11) we know that $R_0 \propto 1/M_{\mathrm{D}}M_{\mathrm{T}}$; combined with $1/r = [(M_{\mathrm{D}}+M_{\mathrm{T}})/(M_{\mathrm{D}}M_{\mathrm{T}})]^2$, from equation (1.17) we arrive at

$$\left.\frac{dR}{dE_{\mathrm{r}}}\right|_{\mathrm{obs}} \propto \frac{1}{\mu_{\mathrm{p}}^2}A_{\mathrm{T}}^2\sigma_{\mathrm{p}}F^2(E_{\mathrm{r}})\,.$$

The observed differential rate in terms of [events/day/kg/keV] is independent of target nuclear mass but only dependent on the number of scattering centers A_{T} in the target nucleus.

Detector Effects

Dark Matter Detectors are set out to measure the WIMP-nuclear recoil energy spectrum dR/dE_{r} in order to measure the WIMP-nucleon interaction cross section σ. Due to instrumental limitations, the measured recoil energy spectrum $\left.\frac{dR}{dE_{\mathrm{r}}}\right|_{\mathrm{obs}}$ is distorted from the true spectrum. Two key instrumentation factors contribute to the distortion:

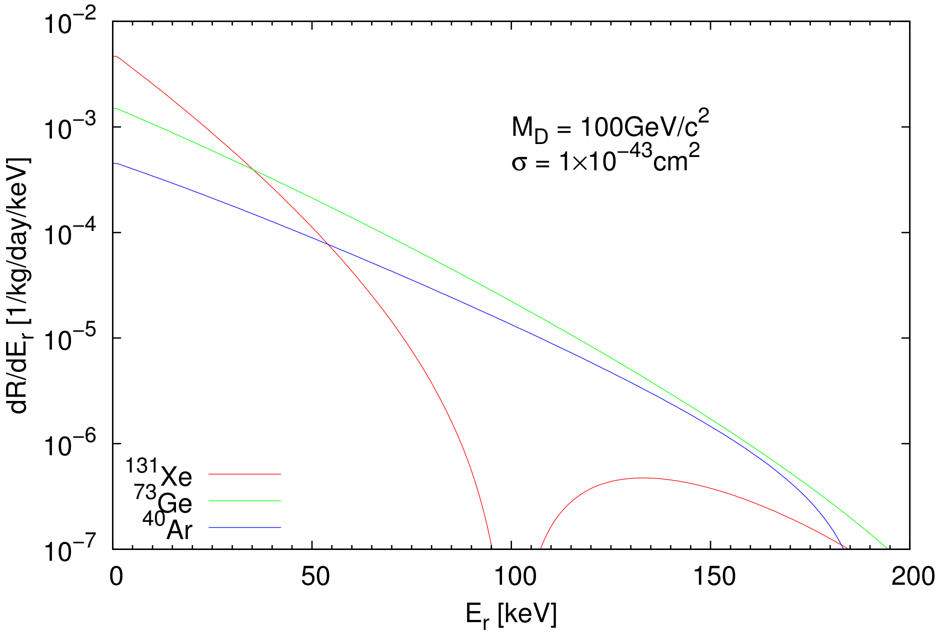

Figure 1.6: Differential recoil energy spectra of a few common targets. $\sigma = 1 \times 10^{-43}\,\mathrm{cm}^2$ and WIMP mass $M_{\mathrm{D}} = 100\,\mathrm{GeV/c}^2$.

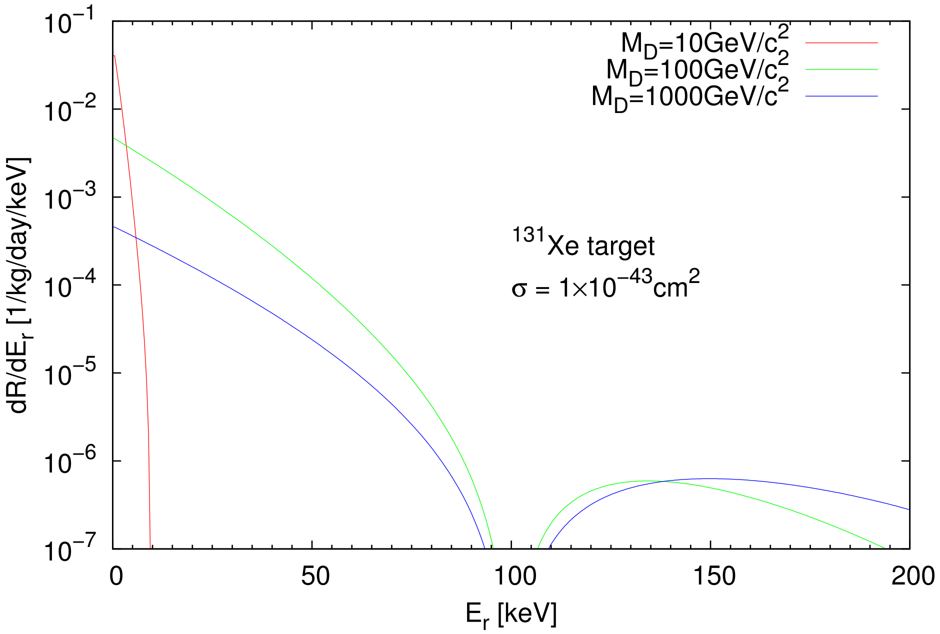

Figure 1.7: Differential recoil energy spectra of xenon target. $\sigma = 1 \times 10^{-43}\,\mathrm{cm}^2$ and three different WIMP masses.

1. Detection Efficiency and Energy Threshold: Not all events happen in the appropriate energy range are registered in the detector as potential WIMP events. Several reasons contribute to the loss of detection efficiency: the trigger setup is not 100% efficient in capturing all the events, especially at low energies; the data processing procedure is not 100% efficient to capture legitimate events; the analysis procedure is not 100% efficient to pick WIMP events out of the background event; etc. Particularly, below certain very low energy E_{th}, the signal drops below the noise level therefore the efficiency drops to zero. E_{th} is referred to as the energy threshold.

2. Energy Resolution: In the real detector, the recoil energy E_{r} of each event is not precisely measured but has a finite resolution. Particularly in experiments like XENON100 which uses number of photons collected for energy determination, at low recoil energy, when each keV corresponds to only a few photons (or photo-electrons), the energy resolution is dominated by the Poisson counting statistics which has very large uncertainty. While the large energy uncertainty distorts the measured spectrum, it helps at the energy threshold that it allows events with very low recoil energy to fluctuate in produced number of photons into higher number that is beyond the energy threshold so that low energy events could still be detected. It especially helps the detection of low mass WIMP particles.

An example showing both of the above two effects is in Fig. 1.8. The continuous differential rate spectrum is first broken down into discrete photon counting bins. Photon counting spectrum is then convoluted with detection efficiency curve yielding the finally observed spectrum in the detector. The conversion between photo-electron and recoil energy is described in Chapter 3.

Detection Limits

So far most of experiments have not claimed any discovery of WIMP dark matter. Instead, experimental results are usually given as a 90 % upper limit of cross-section as a function of WIMP mass (Fig. 1.9). It states that at 90 % confidence level, WIMP-nucleon cross section is excluded to be above the curve.

The procedure to compute such curve is the following: First, a WIMP search window is defined with an recoil energy range $[E_l, E_h]$, and the 90 % upper limit of WIMP events n_{90} considering truly observed events and background event estimation is computed. Second, for a given WIMP mass M_D, the recoil spectrum could be computed and detector effects are convolved. Third, by integrating from E_l to E_h, the expected number of events is obtained, which remains as a function of σ: $n(\sigma)$. By solving the equation $n(\sigma) = n_{90}$, the 90 % upper limit of cross section of WIMP mass M_D is obtained. Repeating the same procedure for every WIMP mass, the limits curve is established.

Summary

In summary, for direct WIMP detection, targets of heavy nuclei are favored. Heavier nuclei have greater atomic number A_{T}, and the scatter rate at E_{r} close to zero is proportional to A_{T}^2 hence the increase in A_{T} drastically increases the detection sensitivity. However, as A_{T} gets bigger, the size of the nucleus r_n gets larger therefore the form factor $F(E_{\mathrm{r}})$ falls faster, as shown in Fig. 1.6. To

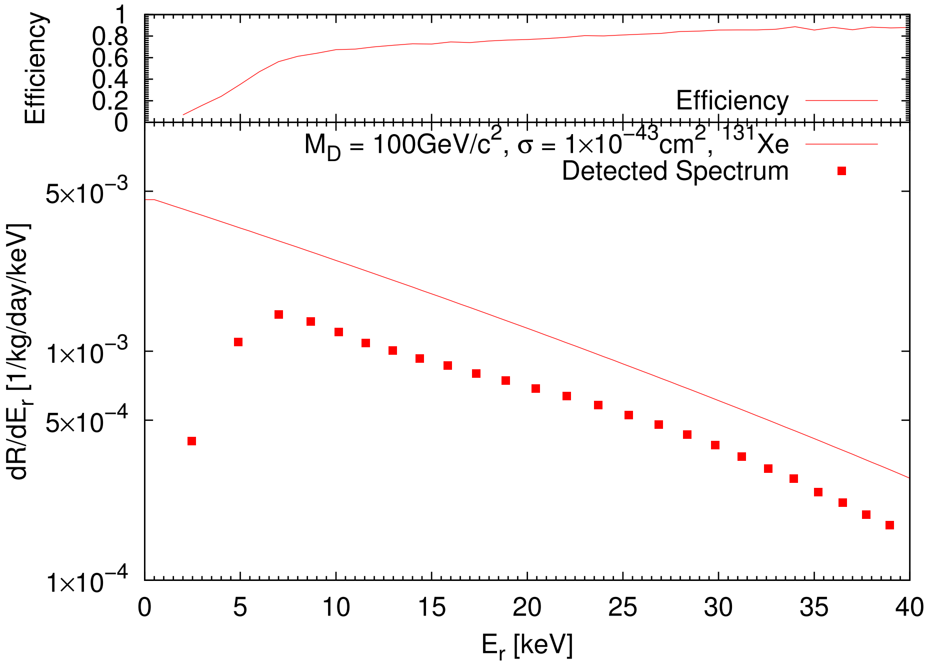

Figure 1.8: Differential recoil energy spectra with detector effects. The Poisson fluctuation in photon counting is taken into account. The detection efficiency and threshold effect are folded in as well.

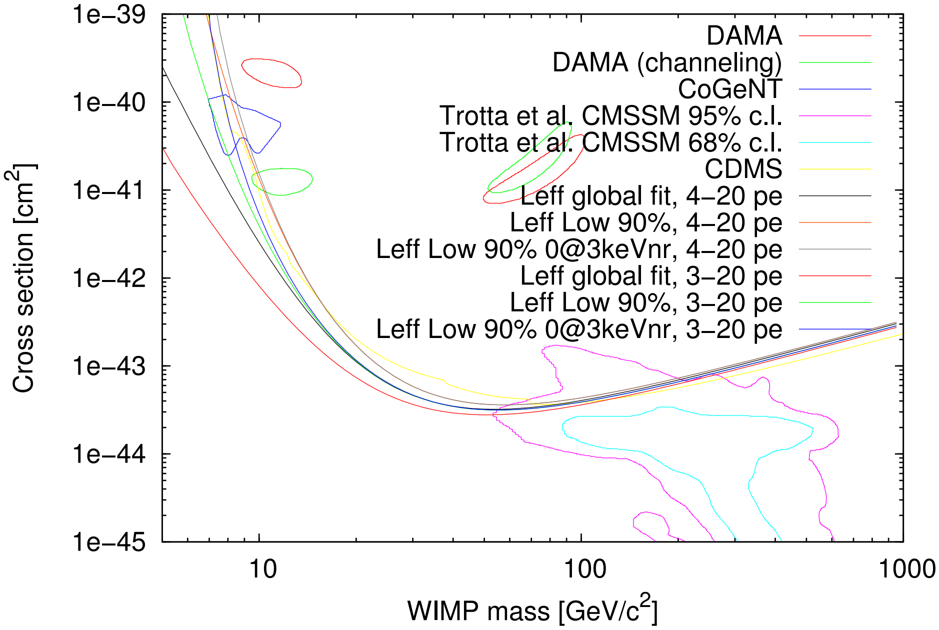

Figure 1.9: Dark matter exclusion limits. Energy range at lower end (energy threshold) affects the detection sensitivity significantly, especially for low mass WIMPs.

fully utilize the benefit of heavy nuclei, a detector shall be designed to have energy threshold as low as possible in order to capture the drastically increased rate at low E_{r}.

1.2.3 The Impact of Earth Velocity: Summer and Winter

The observed WIMP velocity on earth is

$$\mathbf{v}_{\mathrm{obs}}(t) = \mathbf{v}_{\odot} + v_{\oplus}[\hat{\epsilon}_1 \cos\omega(t - t_1) + \hat{\epsilon}_2 \sin\omega(t - t_1)] \tag{1.18}$$

where

$$\begin{aligned} \hat{\epsilon}_1 &= (0.9931, 0.1170, -0.01032) \\ \hat{\epsilon}_2 &= (-0.0670, 0.4927, -0.8676) \end{aligned} \tag{1.19}$$

are the directions of the Earth velocity in the galactic coordinates at the Spring equinox and Summer solstice. $t_1 = 0.218$ is the fraction of the year before the Spring equinox (March 21).

For a given WIMP mass m_χ, density ρ_χ, target medium and cross-section with target σ, the recoil energy spectrum is affected by the WIMP velocity in the detector rest frame $\mathbf{v}_{\mathrm{obs}}$ (mean value). A Gaussian velocity distribution of WIMPs with a fixed dispersion is assumed and is independent of $\mathbf{v}_{\mathrm{obs}}$. There are two important aspects of the effect of $\mathbf{v}_{\mathrm{obs}}$ as it varies year-wise due to the earth orbiting around the sun.

First, the WIMP flux measured on the earth Φ $[1/\mathrm{L}^2/\mathrm{T}]$ is proportional to the mean WIMP velocity or equivalently the earth velocity in the dark matter halo rest frame $\mathbf{v}_{\mathrm{obs}}$. Therefore the total rate $\int_0^\infty \frac{dR}{dE} dE$, or in other words the total area under the recoil energy spectrum is proportional to v_{obs}. Since $v_{\mathrm{obs}}(\text{winter}) < v_{\mathrm{obs}}(\text{summer})$, the total area under the spectrum in winter (Fig. 1.11, red curve) is less than that in summer (Fig. 1.11, blue curve).

Second, as recoil energy E_r approaches zero, WIMPs with higher velocity thus higher kinetic energy give lower differential rate. Therefore

$$\left.\frac{dR}{dE}\right|_{E_r=0}(\text{winter}) > \left.\frac{dR}{dE}\right|_{E_r=0}(\text{summer})$$

In observing both of the above two points, the differential rate in winter $\frac{dR}{dE}(\text{winter})$ at $E_r = 0$ is higher than that in summer, but the total area under the spectrum for winter is less than that in summer, then there must be a crossing point for the two spectra lines (Fig. 1.11). The slight change in spectra, as well as the crossing point, also reveal themselves in the detection limit shown in Fig. 1.10 (top).

Summary

Dark Matter is the most plausible explanation of missing gravity problem in astrophysics. According to observations, dark matter exists universally from galactic scale up to the whole universe. Super symmetric extension to the Standard Model of particle physics suggests WIMP to be a particle candidate of Dark Matter. WIMPs are expected to interact with nucleon of normal matter and

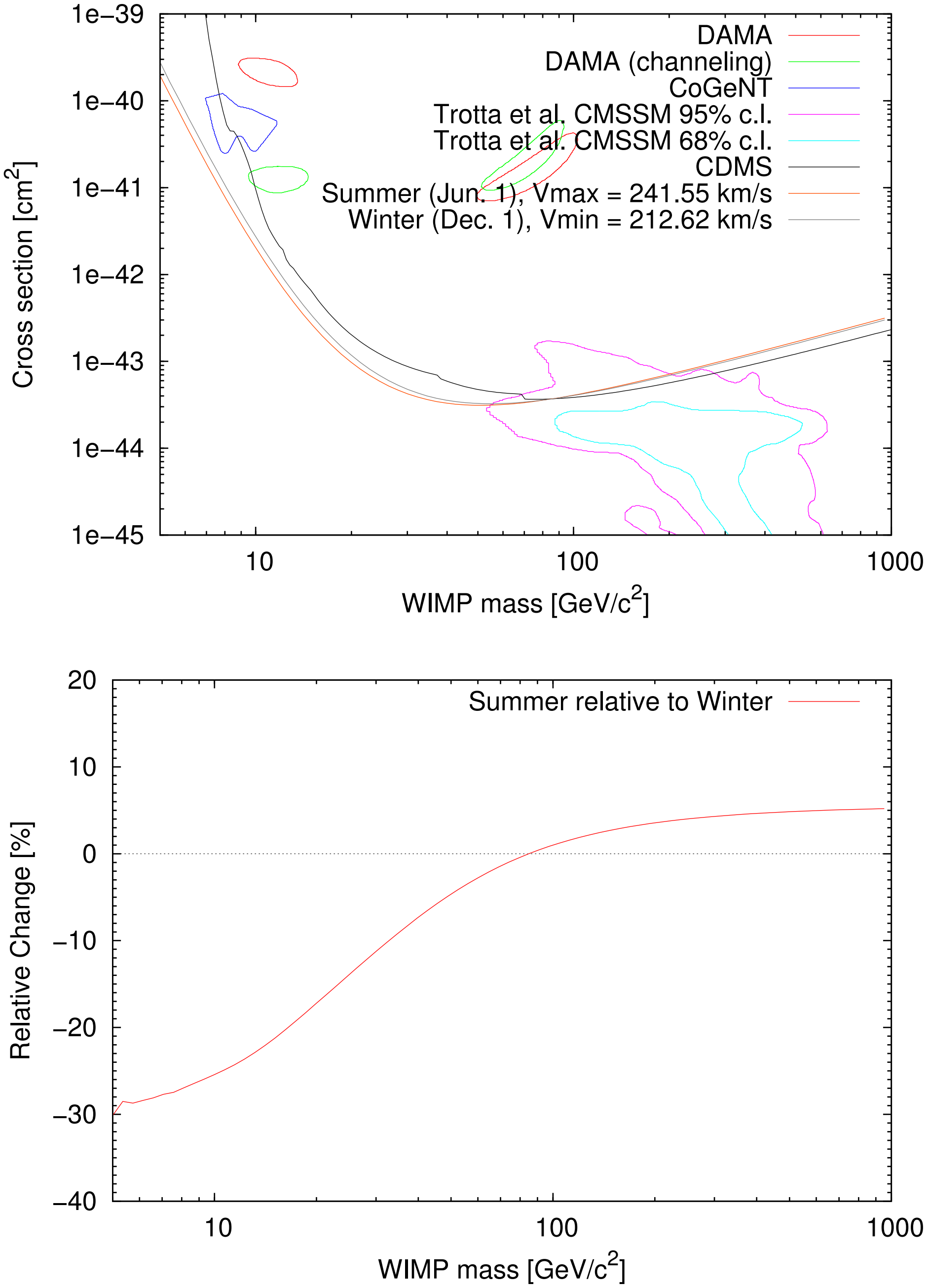

Figure 1.10: Limits difference between Summer and Winter

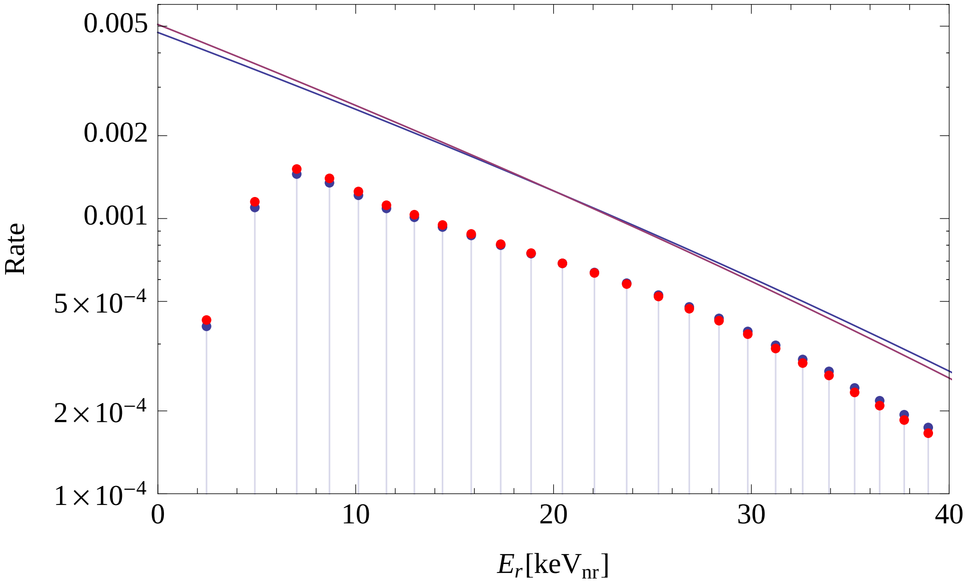

Figure 1.11: Spectra for 100 GeV WIMP with $\sigma = 1 \times 10^{-43}\,\mathrm{cm}^2$

deposit detectable amount of energy. Earth is expected to be sailing in the Dark Matter halo of Milky Way galaxy. Earthborn detectors should observe exponential energy spectra due to WIMP interaction with detector medium.

This page intentionally left blank

Chapter 2

The XENON100 Detector

XENON100 is a Dual Phase Time Projection Chamber (TPC) filled with about 161 kg of Liquid Xenon as the working medium. The target volume, a cylinder about 30 cm in height and 30 cm in diameter, placed in the center of the detector and surrounded by PTFE panels, electric grids and PMTs, constitutes about 62 kg of liquid xenon and is sensitive to both scintillation and ionization from particle interactions. The chamber utilizes both light and charge produced at a particle interaction to acquire energy deposition and particle type information. Also, from charge drifting under electric field in the sensitive volume, as well as electron proportional scintillation in the gas phase (*S2*), 3D positions of interaction vertices are reconstructed. Thanks to the high electron density hence high stopping power of liquid xenon, with 3D position information, xenon volume fiducialization is realized. It significantly reduces electromagnetic radiation background from external sources. In addition, the yield difference between charge and scintillation provides the discrimination between electronic recoil and nuclear recoil. Combining the background reduction power and particle type discrimination capabilities, XENON100 is currently the most sensitive experiment in direct WIMP dark matter search. In this chapter, the working principle and detector details of XENON100 are discussed.

2.1 Principle of the Liquid Xenon Time Projection Chamber (LXeTPC)

When particles interact with xenon, the energy deposition results in both excitation (Xe^{*}) and ionization (Xe^{+}) of xenon atoms. Excited Xe^{*} atoms combine with ground state Xe atoms to form excimers

$$\mathrm{Xe}^{*} + \mathrm{Xe} \longrightarrow \mathrm{Xe}_2^{*}\,. \tag{2.1}$$

Ionized Xe^{+} atoms combine with ground state Xe atoms to form ionized dimers

$$\mathrm{Xe}^{+} + \mathrm{Xe} \longrightarrow \mathrm{Xe}_2^{+}\,. \tag{2.2}$$

The combination processes happen in the time scale of pico-second (Martin [37]).

Subsequently, the excimer decays to the ground state

$$\mathrm{Xe}_2^* \longrightarrow 2\,\mathrm{Xe} + h\nu \tag{2.3}$$

emitting VUV light of wavelength 178 nm (Jortner et al. [31]). The ionized Xe_2^+ dimers recombine with free electrons produced in the early ionization process and reduce to excimers (Xe_2^*)

$$\mathrm{Xe}_2^+ + \mathrm{e}^- \longrightarrow \mathrm{Xe}_2^* + \mathrm{heat}\,. \tag{2.4}$$

The excimers then again decay as in equation (2.3) and produce additional photons. In the presence of an external electric field, part of free electrons e^- produced in the ionization process are extracted hence the recombination process (2.4) is suppressed and the amount of scintillation photons emitted is reduced. The reduction of scintillation under external electric field is referred to as the Electric Field Quenching. Since there is no atomic energy gap matching with the 178 nm scintillation energy of about 7 eV in the xenon atom, xenon scintillation light does not get absorbed by liquid xenon itself. Xenon scintillation light travels far in the liquid. It allows liquid xenon detectors to be built at large scale without significantly losing scintillation light, which is essential for achieving low energy threshold that leads to high dark matter detection sensitivity.

The ionization charge, on the other hand, is extracted by an external electric field applied through out the liquid xenon volume. A usual Dual Phase LXeTPC is setup as shown in Fig. 2.1. The TPC is enclosed by optically reflective side walls, cathode mesh on the bottom, and anode mesh on the top a few mm above the liquid-gas interface. The cathode is connected to a negative high voltage of −16 kV while the anode is maintained at a positive high voltage of +4.5 kV. Close to the anode and liquid-gas interface, there are two more meshes. The lower (gate) mesh, which is just below the liquid-gas interface, is fixed on ground potential to separate the electric fields in the bulk of liquid xenon and in the vicinity of liquid-gas interface. The top mesh, also on ground potential, is placed a few mm above the anode to close off the electric field. Two PMT arrays are placed on top and bottom collecting scintillation photons.

When a particle comes in and interacts with liquid xenon, it produces both scintillation light (*S1*) and ionization electrons. Primary scintillation light is immediately collected by PMTs producing *S1* pulse on the signal waveform. The ionization electrons, at the same time, are pulled out of the interaction site by the electric field created between cathode and lower (gate) mesh of 0.53 kV/cm. Under the electric field, electrons drift upwards at velocity $v_\mathrm{d} \approx 1.74\,\mathrm{mm/\mu s}$. When electrons reach the liquid-gas interface, a stronger electric field, maintained between the lower (gate) mesh and anode, extracts electrons from the liquid into the gas phase. As soon as electrons get into the gas phase, they start to excite gaseous xenon atoms to produce proportional scintillation light, which is seen by PMTs producing *S2* pulse on the waveform. The time difference between *S1* and *S2* pulses determines electron drift time *dt*. Since the electric field in the liquid is largely uniform, the electron drift velocity v_d is constant. The z position of an interaction is computed using *dt* and v_d. Because electrons drift upwards, the position of *S2* is right above the site of interaction. *S2* is close to the top PMT array so that it creates a localized pattern on the top array. This *S2* pattern is used to reconstruct the (x, y) position of the interaction. Combined, the 3D position of interaction

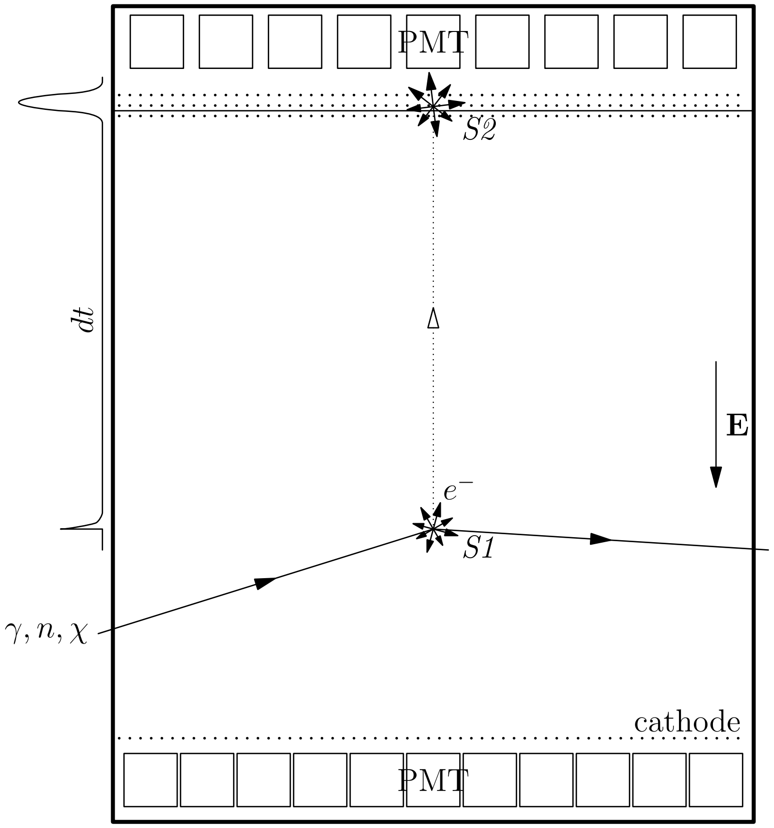

Figure 2.1: Principle of Dual Phase LXeTPC. Cathode mesh is on negative high voltage. Near the top liquid-gas interface, there are three meshes: lower (gate) mesh is just below the liquid-gas interface and is on ground potential; anode is just above the liquid-gas interface and is on positive high voltage; top mesh is a few mm above the anode mesh and is on ground potential. The electric field created between cathode and lower (gate) mesh drives ionization electron to drift upwards in liquid xenon. The enhanced electric field between lower (gate) mesh and anode extracts electrons from liquid into gas phase, and excite gaseous xenon to produce proportional scintillation signal (*S2*). PMT arrays are covering top and bottom area collecting both *S1* and *S2* light. The corresponding signal waveform to is illustrated on the left side.

is recovered from electron drift time and *S2* PMT pattern. The sizes of *S1* and *S2*, eventually converted to the number of scintillation photons and ionization electrons, respectively, provide both energy deposition and particle type information.

2.2 Detector Structure

The main structure of XENON100 is a cylindrical Dual Phase LXeTPC of approximately 30 cm in diameter and 30 cm in height, with two PMT arrays covering top and bottom. The structure is enclosed in a vacuum insulated stainless steel cryostat filled with about 161 kg of liquid xenon, as shown in Fig. 2.2. The sensitive volume is enclosed by 24 interlocking PTFE panels forming an approximate cylindrical wall, as well as a cathode mesh on the bottom and an anode mesh together with a gate mesh and a top mesh on top of the PTFE wall. The total sensitive volume contains about 62 kg of liquid xenon. PTFE was chosen to construct the wall because it has very high reflectivity for xenon scintillation light of wavelength 178 nm. It is also a good insulator for high voltage, and its dielectric constant is similar to that of liquid xenon. On top of the sensitive volume, there is a "diving bell" structure enclosing the top PMT array. A positive pressure inside of the diving bell with respect to outside of the bell is maintained by a gaseous recirculation pump so that xenon gas is filling inside of the bell and the liquid-gas interface is kept at the desired level in between the gate mesh and the anode. The space outside of the bell and the sensitive volume is filled with 99 kg of liquid xenon serving as shield. 64 PMTs are observing light produced in the shield, making the shield an active veto.

The cryostat of XENON100 is installed inside of a passive shield box constructed, from inside to outside, of 5 cm of OFHC copper, 20 cm of polyethylene, 20 cm of lead, and 20 cm of water or polyethylene on top and on 3 sides of the shield. The whole shield box is sitting on 10 cm of polyethylene. Two vacuum insulated tubes are extended from top of the cryostat to outside of the shield where there is no water or polyethylene, allowing cable connections to be made outside of the shield. Also, a third vacuum insulated tube is connecting the side of cryostat to the cooling tower outside of the shield. The whole idea of the construction is to make radioactive parts, connectors, cooling tower, etc., to be far away from the detector and outside of the passive shield. In normal operations, the passive shield is completely closed. A small diameter copper tube is placed penetrating the passive shield and circling the detector. Calibration sources can be introduced into the passive shield through the copper tube. Fig. 2.3 shows a 3D rendering of detector and a photo of the detector in the partially open passive shield.

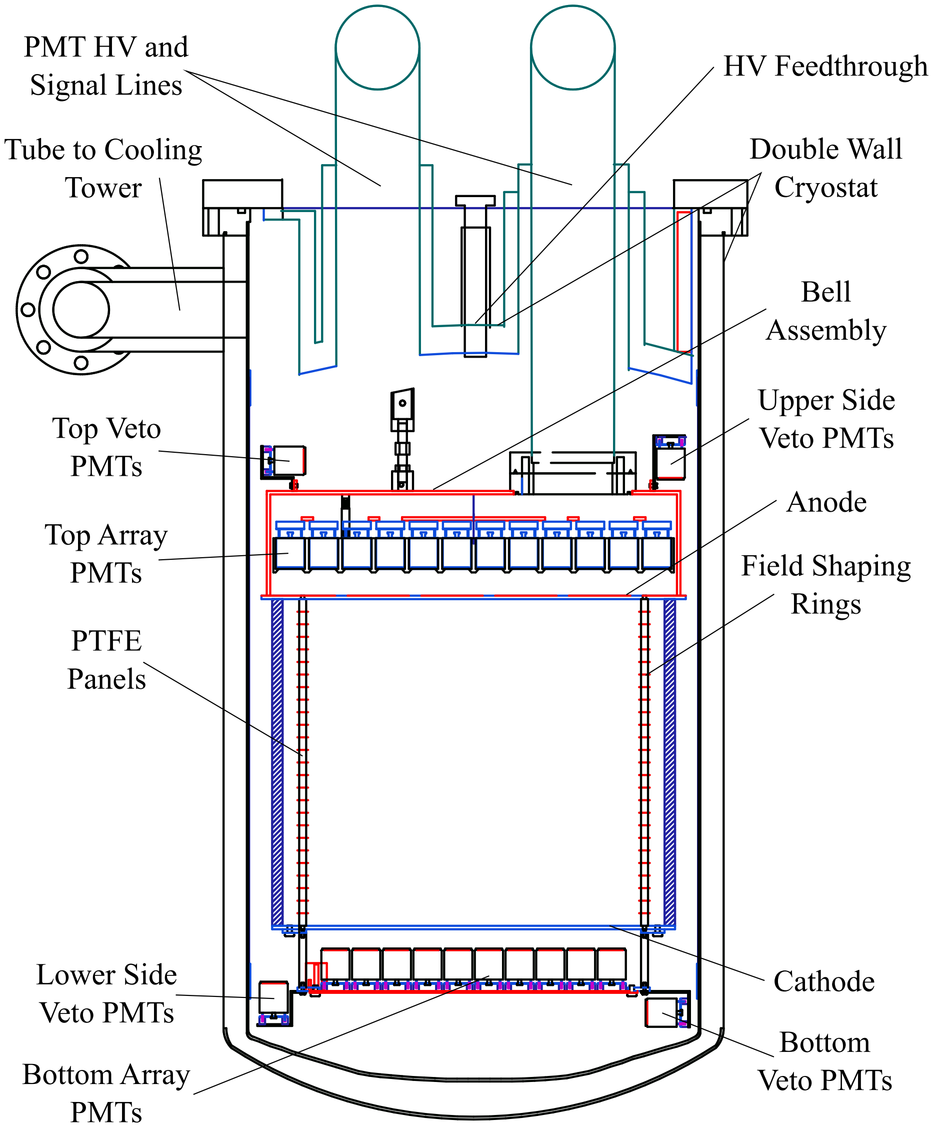

Figure 2.2: XENON100 Detector Structure

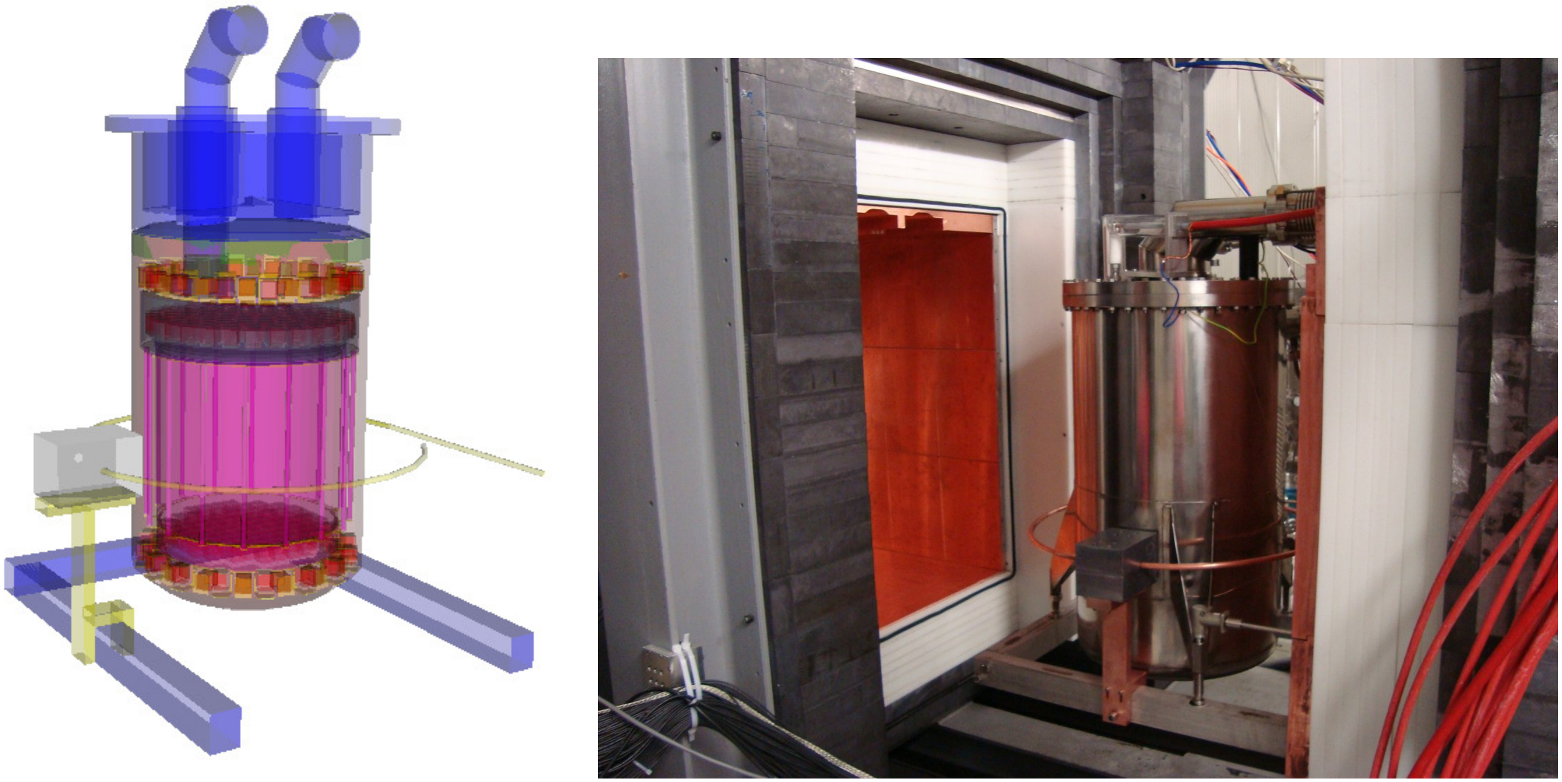

Figure 2.3: XENON100 Detector Structure and Passive Shield. A copper tube circling the detector is used to introduce calibration sources inside the passive shield and around the detector. The copper tube goes through a lead brick at one point. The ^{241}AmBe neutron source was placed at this point inside of the lead brick so that gamma radiation is suppressed.

XENON100 is housed underground at Laboratori Nazionali del Gran Sasso (LNGS) in central Italy. The mountain above the experimental site serves as cosmic ray shield. The depth of 3700 m water equivalent reduces the muon flux by a factor of 10^6 compared to that at the surface. During normal operation, the passive shield is completely closed and the shield cavity is constantly being purged to flush radon out. Radon is a contaminating radioactive source common in underground cavities. Its activity is controlled to be $< 0.5\,\mathrm{Bq/m^3}$ by constant nitrogen purging.

2.3 Electric Field Cage

In order for the LXeTPC to function properly, a few key factors regarding the electric field have to be maintained:

1. In the bulk of liquid xenon that is above the cathode and below the gate mesh, a uniform electric field with $\mathbf{E}$ pointing downwards is desired. The electric field strength $|\mathbf{E}|$ is desired to be at $\sim 1\,\mathrm{kV/cm}$. In order to achieve this, a cylindrical electric field cage is constructed with two meshes covering the opposing sides and 24 interlocking PTFE panels forming the side wall. The gate mesh on the top is kept at ground potential while the cathode mesh on the bottom is connected to a high voltage power supply in order to be powered at negative voltage. $-16\,\mathrm{kV}$ was applied on cathode for XENON100 at normal operation. On the side PTFE wall, there are 40 pairs of equally spaced copper wires forming concentric rings covering the whole vertical length of the PTFE wall. These wires not only divide the length between gate and cathode meshes equally but also maintain equal and uniform electric potential difference from one ring to the immediate next, implemented by a chain of resistors connecting the cathode and the gate mesh. With such electric field cage structure, a uniform electric field inside of the cage is expected.

2. On top of the gate mesh, there are two more meshes: anode mesh and top mesh. The space between them is 5 mm. The liquid-gas interface is placed above the gate mesh and below the anode mesh. 4.5 kV is applied on the anode while both the gate and top meshes are kept at ground potential. In this configuration, a much higher electric field is achieved around the liquid-gas interface allowing electrons to be fully extracted from the liquid into gas phase, and scintillate again in the gaseous xenon. The top mesh is necessary to close off the electric field lines from the anode.

3. Below the cathode mesh and above the bottom PMT array, there is another mesh—screen mesh kept at ground potential. The purpose of the screen mesh is to close off the high electric field from the cathode. It is suspected that PMTs do not function properly under high electric field therefore the screen mesh connected to a electric potential that is close to the PMT photo-cathode potential, in this case close to ground potential, is needed to provide a healthy working condition for the bottom PMTs.

An electric field cage structure together with meshes are built based on the above considerations. The simulated electric potential distribution in the detector is shown in Fig. 2.4.

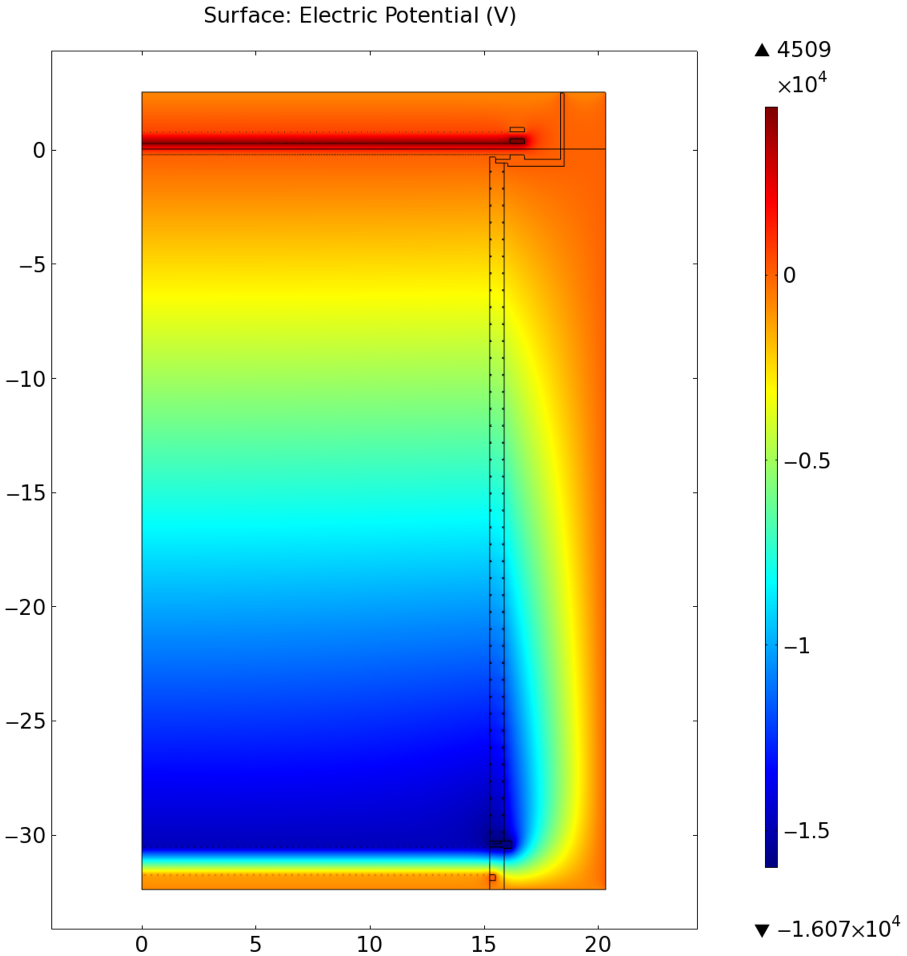

Figure 2.4: Electric Field Structure in the TPC. Color shows electric potential in V.

Meshes are important to maintain the desired electric field in relevant regions in the detector. The denser the mesh wires, the better the electric field. However, denser mesh wires reduce optical transparency which impairs both *S1* and *S2* light collection. Therefore, a compromise has to be made between electric field effect and mesh transparency. The mesh transparency is modeled such that any photon hits mesh wire is completely lost. Under this assumption, optical transparency of meshes of various pitch and wire sizes are computed and gathered in Fig. 2.5. Mesh transparency is plotted as a function of incident angle θ while the dependence of ϕ is already averaged. Also the solid angle averaged overall transparency is computed. The procedure for the transparency computation can be found in Appendix A. Meshes with $> 90\,\%$ transparency at normal incident ($\theta = 0$) are used in XENON100. The electric field aspect of meshes is discussed in Chapter 4.

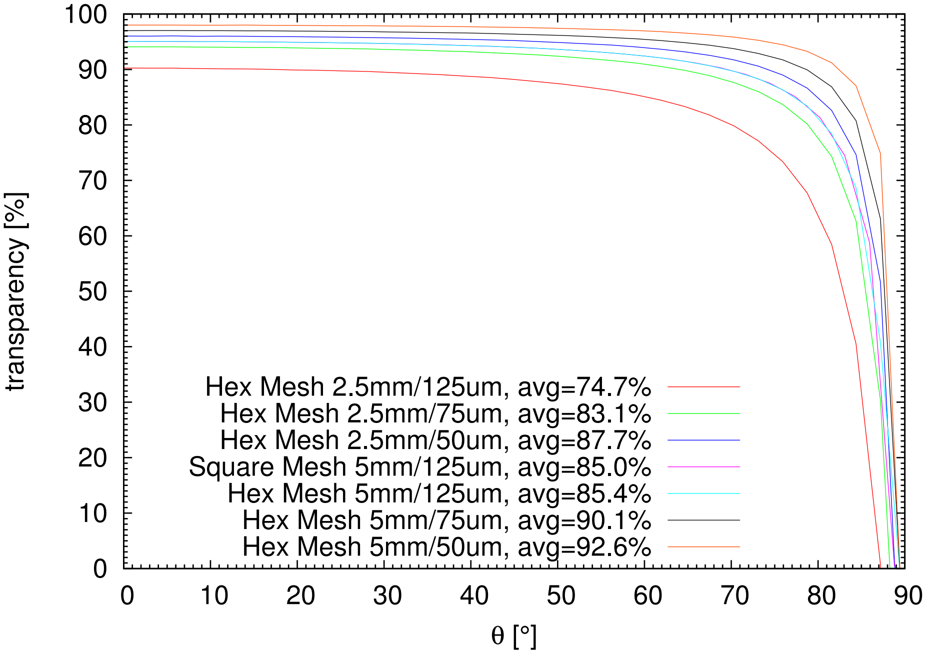

Figure 2.5: Mesh Transparency as a function of incident angle θ. ϕ dependency has been averaged. "`avg`" in figure legend shows the total solid angle averaged mesh transparency. "a/b" means pitch size a and wire width b. Meshes in XENON100 as of `run_10` are hexagonal meshes of pitch/wire sizes: top: 5 mm/125 µm, anode: 2.5 mm/125 µm, gate: 2.5 mm/125 µm, cathode: 5 mm/75 µm, screen: 5 mm/50 µm.

2.4 Material Screening

When constructing the XENON100 detector, materials used went through a careful selection procedure. Radioactive contamination in materials, including the passive shield materials, is measured using a high purity germanium counter. The background contribution from material radioactivity is summarized in Tab. 2.1. A Monte Carlo model is built based on the material screening results to estimate the electromagnetic background expectation in the detector. The simulated background spectrum is directly compared with the measured background, and the result is shown in Fig. 2.6.

Component	Amount	Total radioactive contamination in materials [mBq/amount]				
		^{238}U	^{232}Th	^{60}Co	^{40}K	other nuclides
Cryostat and 'diving bell' (^{316}Ti SS)	73.6 kg	< 130	< 140	400 ± 40	< 660	
Support bars (^{316}Ti SS)	49.7 kg	< 65	140 ± 30	700 ± 20	< 350	
Detector PTFE	11.86 kg	< 0.7	< 1.2	< 0.4	< 8.9	
Detector copper	3.9 kg	< 0.86	< 0.62	0.78 ± 0.31	< 5.2	
PMTs	242 pcs	36 ± 5	41 ± 10	150 ± 20	2700 ± 500	^{137}Cs: < 190
PMT bases	242 pcs	39 ± 5	17 ± 5	<2.42	<39	
TPC resistor chain	1.47 g	1.1 ± 0.2	0.57 ± 0.12	< 0.12	7.8 ± 1.2	
Bottom electrodes (^{316}Ti SS)	225 g	0.81 ± 0.06	0.39 ± 0.04	1.6 ± 1.0	< 1.1	
Top electrodes (^{316}Ti SS)	236 g	< 0.64	< 0.35	3.1 ± 0.2	< 2.8	
PMT cables	1.8 kg	< 2.9	6.7 ± 3.2	< 1.2	63 ± 23	^{108m}Ag: 9.0 ± 1.6
Copper shield	2.1 t	170 ± 50	25 ± 11	82 ± 12	6.7 ± 2.1	
Polyethylene shield	1.6 t	370 ± 80	< 150	-	1100 ± 600	
Lead shield (inner layer)	6.6 t	< 4400	< 3600	< 730	< 9600	^{210}Pb: $(1.7\pm0.4)\times10^{8}$
Lead shield (outer layer)	27.2 t	< 25000	< 19600	< 3300	380 ± 80	^{210}Pb: $(1.4\pm0.2)\times10^{10}$

Table 2.1: Adopted from [58]. Materials used to construct the XENON100 detector and shield, and their radioactive contamination from measurements at underground facilities at LNGS. The cryostat vessels with the top flange and pipes, and the 'diving bell' system are made from the ^{316}Ti SS and shown as one unit. The resistive voltage divider network for the TPC drift field is simplified in the model with a thin tube. The PMT bases made from *Cirlex* have been screened fully assembled, with the resistors and capacitors.

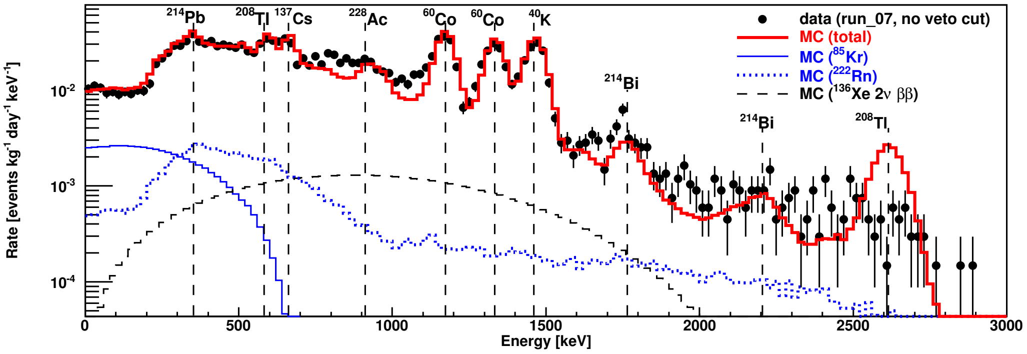

Figure 2.6: Electromagnetic background: comparison of Monte Carlo and data. The simulated electromagnetic background based on material counting results is in good agreement with the measured background. Figure adopted from [58].

Since Liquid Xenon has very good stopping power on electromagnetic radiation, and detector materials are all located at the surfaces of the detection volume, the contribution from detector materials is reduced by fiducialization. Additional reduction is achieved through the liquid xenon veto. However, another electromagnetic background source, ^{85}Kr, which is well mixed with liquid xenon itself thus cannot be removed by fiducialization, constitutes a big portion of the background. In order to reduce the ^{85}Kr content, xenon was passed through a distillation tower utilizing the boiling point difference between krypton and xenon to remove krypton, prior to dark matter data taking. A few hundred ppt of Kr (all isotopes combined) concentration was achieved.

2.5 Trigger and Data Acquisition

There are in total 242 PMT channels in XENON100 detector. Every channel is digitized at 100 MS/s using ADCs with 14 bit resolution and 40 MHz input bandwidth. During normal data taking, each event has about 40 000 samples or 400 µs in length. If all waveforms were digitized, each event would occupy 18.5 MiB resulting in extensive DAQ dead time since the DAQ machine can only sustain up to 100 MiB/s data transfer and recording rate. To reduce the data rate, a Zero Length Encoding (ZLE) algorithm is implemented on the ADC hardware. It works in a way that only when a sample is above a set threshold from the baseline, the sample, as well as certain number of adjacent samples before and after, are digitized and stored. Samples below the threshold are ignored while the timing of individual signals is preserved. In XENON100 the ZLE threshold is set to be 0.8 mV or roughly 0.3 p.e. of a typical single photo-electron peak. The windows before and after the sample are both 50 samples.

The event trigger is generated from the summed signal from part of inner PMTs. By running the summed signal through a spectroscopic amplifier, the signal shape information is extracted to be employed in the trigger decision. *S2* is selected to be the major triggering pulse. An *S2* trigger of threshold 300 p.e. is achieved for dark matter data taking.

2.6 Primary Scintillation Light (*S1*)

In time domain, xenon scintillation light has a characteristic time span of tens of nano-seconds. There are three time constants involved. At zero electric field, the electron recombination process (2.4) dominates the scintillation light pulse behavior and has a time constant of 45 ns (Doke and Masudab [21], Hitachi and Takahashi [30]). When an external electric field is applied and recombination is suppressed, the excimer decay becomes dominant. The excimer Xe_2^* could initially be excited at two different molecular states in terms of spin-orbit coupling: singlet $({}^1\Sigma_u^+)$ state and triplet $({}^3\Sigma_u^+)$ state. For electronic recoil, singlet $({}^1\Sigma_u^+)$ states decay with time constant $\tau_S \approx 2.2\,\mathrm{ns}$ and the triplet $({}^3\Sigma_u^+)$ states decay with time constant $\tau_T \approx 27\,\mathrm{ns}$ (Kubota et al. [34]). The two decay constants reveal themselves on the scintillation light pulse as an initial fast decay followed by a longer tail. Due to this reason the two decay constants are usually referred to as fast component and slow component.

2.6.1 *S1* Waveform

The Xenon excimer Xe_2^* is the source of primary scintillation light *S1*. Xe_2^* decay constitutes two possible channels: from singlet state with decay time $\tau_S \approx 2.2\,\mathrm{ns}$ (fast component) and from triplet state with $\tau_T \approx 27\,\mathrm{ns}$ (slow component) (see Kubota et al. [34], measured in electronic recoil). It can also be found in literature, measurements using alpha particles showing that $\tau_S \approx 4\,\mathrm{ns}$ and $\tau_T \approx 22\,\mathrm{ns}$ (Doke and Masudab [21]). Alpha particles deposit energy in xenon largely through nuclear recoil. There are hardly any physical reasons why molecular state decay time should depend on recoil type, however, to serve the purpose of dark matter search, which is nuclear recoil, we use the values measured from using alpha particles. The relative contribution of the two decay channels are different from nuclear recoil and electronic recoil. The intensity ratio $I_S/I_T \equiv A_S\tau_S/A_T\tau_T$ is a measure of the relative contribution of the two components. For electronic recoil $I_S/I_T \approx 0.05$ thus $A_S/A_T \approx 0.275$; for nuclear recoil $I_S/I_T \approx 0.43$ thus $A_S/A_T \approx 2.365$ (Doke and Masudab [21]).

Combining the two decay processes, *S1* pulse shape could be described as the sum of two exponential functions with time constants τ_S and τ_T

$$S1(t) = A_S \cdot e^{-t/\tau_S} + A_T \cdot e^{-t/\tau_T}\,. \tag{2.5}$$

The behavior of function (2.5) is shown in Fig. 2.7. Xenon primary scintillation light pulse has very short width in time. It reaches 90 % of the total amount of light in less than 50 ns. Due to the large difference of intensity ratio between nuclear recoil and electronic recoil, the nuclear recoil pulse emits light faster than that of electronic recoil pulse. This presents an opportunity to utilize the pulse shape information to distinguish electronic recoil and nuclear recoil events. However, to achieve such discrimination power, fine sampling of light pulse is required. With the data acquisition system in XENON100 running at 100 MS/s, pulses are sampled by 10 ns bins. An *S1* pulse is only a few bins wide. There is practically no discrimination power using pulse shape information at all.

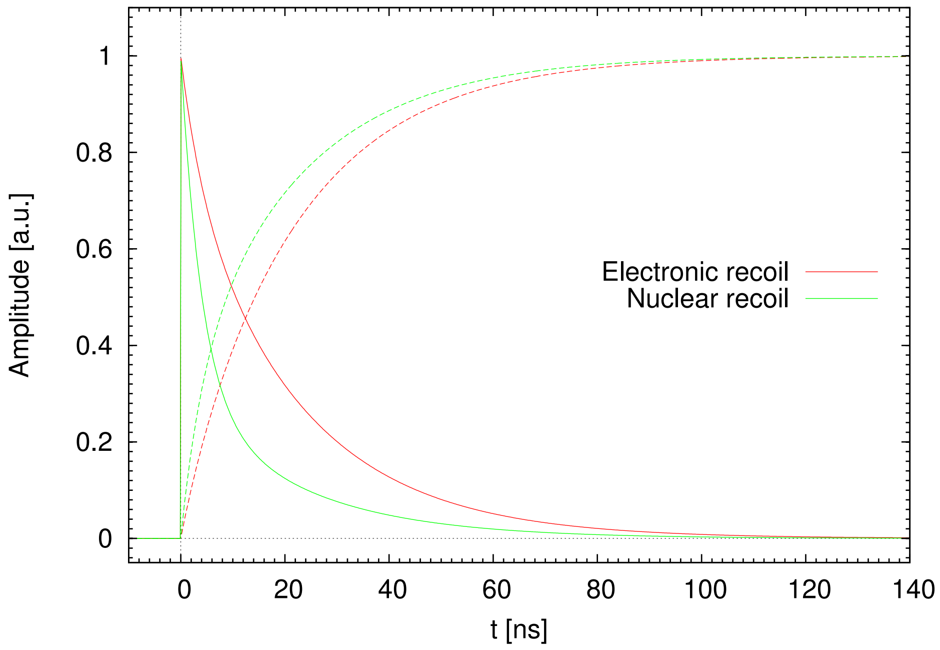

Figure 2.7: *S1* Pulse Shape. Fast component $\tau_S \approx 4\,\mathrm{ns}$ and slow component $\tau_T \approx 22\,\mathrm{ns}$. For electronic recoil, $A_S/A_T \approx 0.275$; for nuclear recoil $A_S/A_T \approx 2.365$. Pulses are normalized to have $S1(t=0)=1$. Dashed curves are integral from $t=0$, normalized to reach 1 at $t=\infty$.

2.6.2 *S1* Coincidence

XENON100 PMTs (Hamamatsu R8520) has a dark count rate of about 50 Hz at −100 °C. In the largest electron drift time window of about 180 µs, 1 ∼ 2 PMT dark counts are expected. To select true *S1* peaks from real particle interactions and distinguish them from dark counts and other “noise” peaks, more than one PMTs detect photo-electrons within a narrow time window is required. This requirement is referred to as the *S1* coincidence.

There are two aspects regarding *S1* coincidence: spatial distribution of photons and time window. *S1* photons are emitted from a single point in space at the interaction cite. More than half of the emitted photons are lost while only a small percentage of photons arrive at PMTs therefore are detected. At low energy, when the total amount of *S1* photons is small, the chance that several PMTs see at least one photo-electron becomes smaller. Requiring an *S1* coincidence results in rejecting legitimate physical events which do not distribute photons to a number of PMTs such that the coincidence requirement is fulfilled. To study this efficiency loss, a Monte Carlo simulation is performed taking into account *S1* light collection loss, PMT *QE*, single photo-electron signal fluctuation, and multinomial statistics. In the simulation, however, there is no temporal information included. It effectively assumes an infinite time window for photons to arrive. Such spatial *S1* coincidence probability is shown in Fig. 2.8.

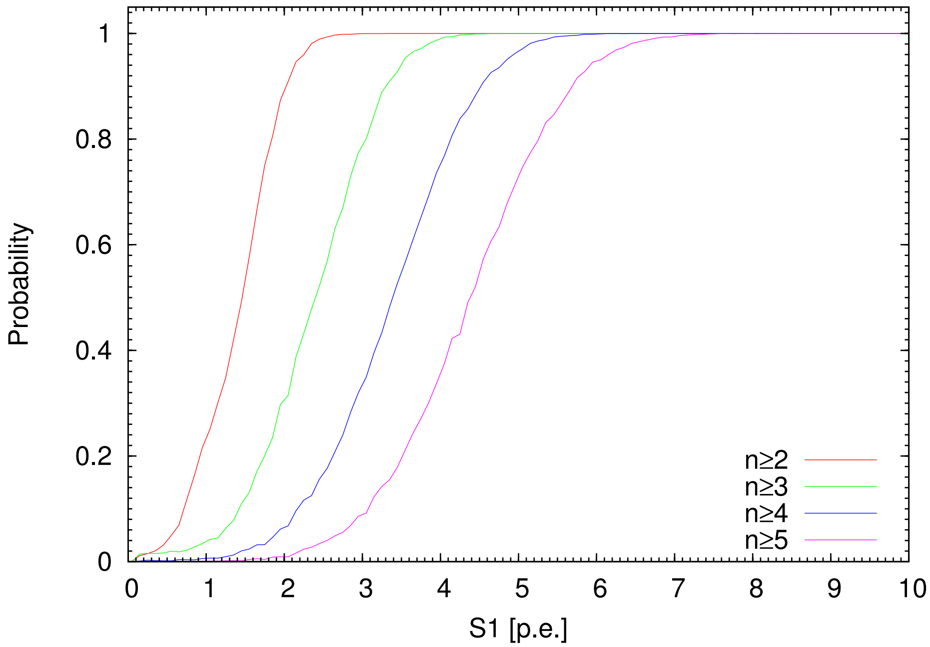

Figure 2.8: *S1* Coincidence Probability (Spatial) as a Function of total *S1* photo-electrons.

In time domain, due to finite width of *S1* pulses as shown in Fig. 2.7, at low photon counts, photons might not arrive at PMTs at the same time. When a small time window is required to achieve *S1* coincidence, there are chances that good physical events with photons arrive at time differences greater than the time windows resulting in event rejection and efficiency loss. On the other hand, the coincidence time window size should be minimized to reject accidental coincidences from dark counts. A Monte Carlo simulation using the time characteristics of *S1* pulse from nuclear recoil is performed to simulate the time window effect on coincidence probability. A few different time windows are simulated and the results are in Fig. 2.9. In the simulation, the signal threshold is set to 0.35 p.e., i.e. only when a PMT sees greater than 0.35 p.e. will it be considered in the coincidence calculation.

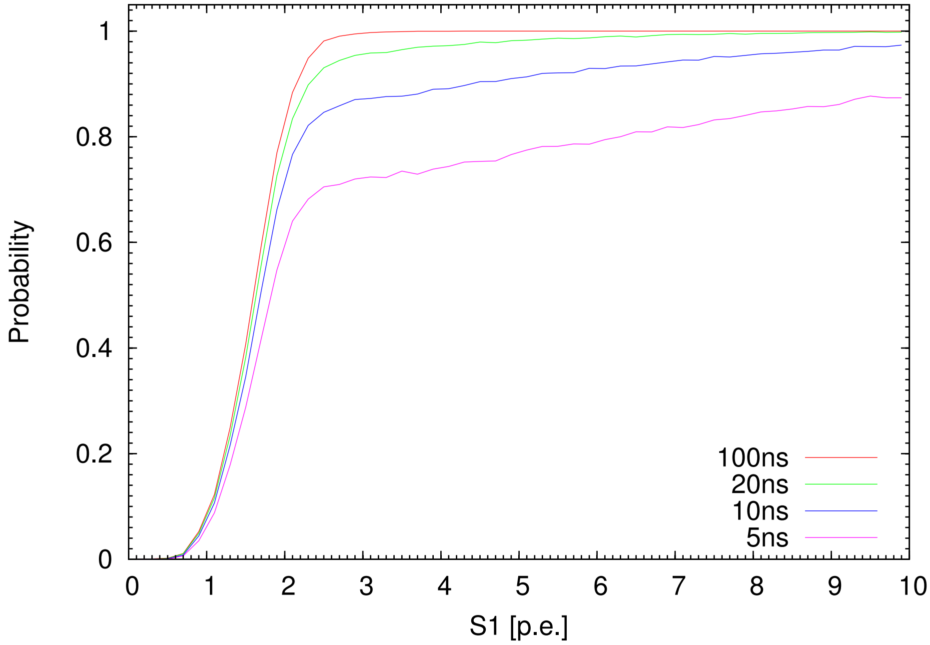

Figure 2.9: *S1* Coincidence Probability (Temporal) as a Function of total *S1* photo-electrons. 2-fold coincidence is required.

Combining both spatial and temporal information, in the final XENON100 analysis, we require at least two PMTs to see photo-electrons within a 20 ns time window for an *S1* peak to be selected. At the lower energy threshold 4 p.e., this two-fold coincidence requirement has almost 100 % acceptance.

2.6.3 *S1* Light Collection

Due to the arrangements of reflective PTFE wall, xenon liquid-gas interface, and PMT arrays, *S1* light emitted at different locations in the TPC has different probabilities to be detected by the PMTs. The total *S1* collection in the TPC is not uniform but has spatial dependence. In principle this dependence can be characterized by light collection simulation. However, many material optical properties are unknown therefore the simulation is not reliable. Instead, since the 3D position of each interaction is known, if the energy deposition of interaction is also known, the spatial dependence of light collection can be directly obtained from data. As shown in Fig. 2.10, the 40 keV line is used to probe the *S1* light collection. Total amount of light collected by all the PMTs is shown as a function of r and z, assuming a cylindrical symmetry. The light collection efficiency is better in the lower central region close to the bottom array, and decreases as the position becomes close to the top or to the edge.

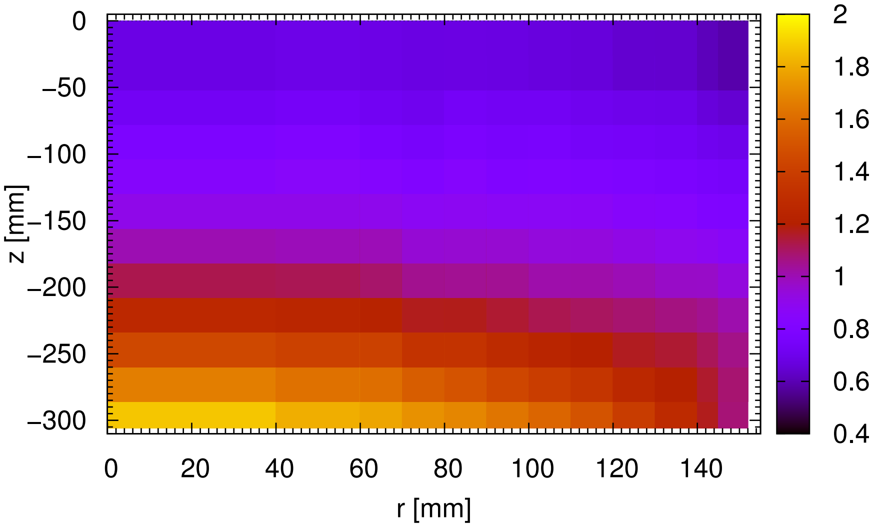

Figure 2.10: Spatial Dependence of Light Yield. Calibrated with 40 keV gamma produced from inelastic neutron scattering ($^{129}\mathrm{Xe}(n, n'\gamma)\,^{129}\mathrm{Xe}$) data. Color shows the ratio of spatial dependent light yield $\mathcal{L}_{\mathrm{y}}(r, z)$ over the TPC mean value of 2.9 p.e./keV.

2.7 Electron Proportional Scintillation Light (*S2*)

When ionization charge (free electrons) drift upwards and pass through the lower (gate) mesh, a ten times higher electric field extracts electrons out of the liquid phase in to gas phase. When the electric field in the gas phase is higher than a certain threshold, electrons could gain enough of kinetic energy between two consecutive collisions with Xe atoms such that the collected kinetic energy is over the xenon scintillation threshold. Under this condition, electrons start to cause xenon atoms to produce scintillation light. This phenomenon is known as electroluminescence or proportional scintillation (Favata et al. [25]). The amount of light produced per electron drift length, dL/ds, is proportional to the electric field E above a threshold and below the electron multiplication threshold. Since XENON100 utilizes this proportional regime to determine the amount of ionization charge from scintillation light, it is referred to as proportional scintillation as well. Of course the gaseous xenon density plays an important role here since the electron mean free path counter acts the external electric field for an electron to gain enough kinetic energy between collisions. Therefore, the light yield depends on the reduced electric field (E/n) where n is the number density of gas atoms.

The amount of scintillation could be computed using equation (2.6)

$$\begin{aligned} \frac{1}{n}\frac{dL}{ds} &= a\left[\frac{E}{n} - \left(\frac{E}{n}\right)_{\text{ex}}\right] \\ \left(\frac{E}{n}\right)_{\text{ex}} &= 2.87\,\text{Td}\,. \end{aligned} \tag{2.6}$$

$(E/n)_{\text{ex}}$ is the reduced electric field threshold above which electrons start to excite xenon. $1\,\text{Td} = 1 \times 10^{-17}\,\text{Vcm}^2$, is a unit commonly used for reduced electric field (E/n). $a = 0.1389$ photon/electron/V is considered as electric field scintillation yield (Favata et al. [25]). The total amount of scintillation light each electron produces is the integral

$$L = \int \frac{dL}{ds}\,ds = a[U_{\text{anode}} - U_{\text{liquid-gas interface}}] - an\left(\frac{E}{n}\right)_{\text{ex}} l\,. \tag{2.7}$$

l is the total length of electron path from liquid-gas interface to the anode.

XENON100 operates at about 2.3 bar vapor pressure. The corresponding gaseous xenon number density $n = 9.6 \times 10^{19}\,\text{cm}^{-3}$. The anode voltage is usually set to 4.5 kV. Electrons travel from the liquid-gas interface to the anode for about 2.5 mm. With these parameters, by integrating equation (2.6), we could estimate that one electron roughly produces 500 *S2* scintillation photons.

To go beyond simple estimation, and to study energy resolution of *S2*, as well as the shape and time behavior of *S2* pulses, details of electric field around anode have to be acquired. In addition, the electron cloud size and shape contribute to the *S2* pulse shape as well. Details are discussed in the following.

2.7.1 Electron Lifetime

As ionization electrons drift in liquid xenon, electro-negative impurities, oxygen, water, etc., bind with part of electrons so that those electrons do not reach the liquid-gas interface. The loss of electrons causes *S2* signal reduction. Besides diffusion of air though the detector vessel O-ring into the detector, the major source of electro-negative impurities is outgassing from inner surfaces of detector material. In order to reduce and control the electro-negative impurity level, xenon in the detector is being constantly recirculated in gaseous form through a heated Zr alloy getter. O_2 and other electro-negative impurities reacts with Zr and diffuses into the bulk of Zr alloy cartridge and are removed from xenon. After getter the impurity content is below 1 ppb.

It took several months of continuous recirculation of xenon gas through Zr alloy getter to reach a low enough electro-negative impurity level such that electrons have a lifetime of a few hundred µs. The loss of electrons as they drift follow a simple exponential function. As shown in Fig. 2.11, the electron lifetime is well determined by fitting an exponential to *S2* versus drift time dt. As the experiment is ongoing and data is being taken, the electron lifetime is improving continuously. For *S2*s at different z in datasets taken at different times to be directly comparable, *S2*s have to be corrected regarding their respective electron lifetime. Electron lifetime is being monitored at regular interval using ^{137}Cs calibration data, and the result of the data taken have *S2*s divided by $\exp(-dt/\tau)$ where τ is the estimated (interpolated) electron lifetime at the time when the data is taken.

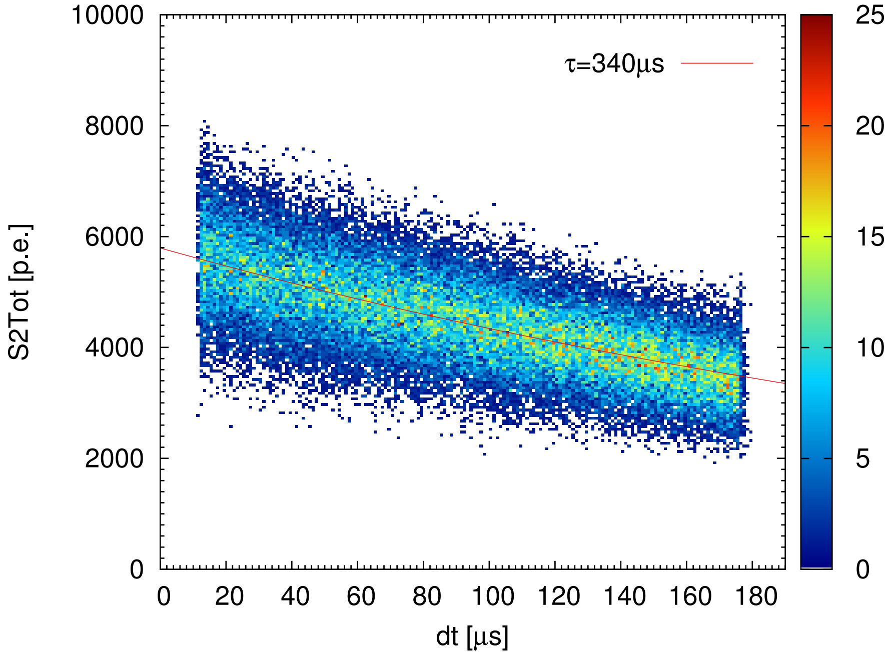

Figure 2.11: *S2* Electron Loss vs. Drift Time. 164 keV full energy peak from neutron activated xenon data is selected. Liquid xenon is in a relative clean state in terms of electronegative impurities. Fitting a simple exponential function reveals the electron lifetime to be about 340 μs.

Interestingly, unlike in liquid xenon, electrons drift freely and are not lost in gaseous O_2 and Xe mixture. The drastic affinity difference between electron and O_2 in liquid or gaseous xenon can be explained by energy transfer at the event of electron attachment. When electrons attach with O_2, energy, usually in the form of heat, has to be dissipated into the environment for the attachment to be stable. In liquid xenon, since xenon atoms are densely distributed around O_2 impurities, the energy transfer can be easily achieved through atomic collision. In gaseous O_2 and Xe mixture, however, the atom density is much lower so that the energy at electron-O_2 attachment cannot be dissipated easily. It results in an unstable attachment and the O_2^- releases the electron immediately. Therefore electrons are not lost while drifting in gaseous xenon with the presence of O_2.

2.7.2 Anode Structure and Electric Field

As the first approximation, the space between lower (gate) mesh and anode could be considered as half filled parallel-plate capacitor. The lower (gate) mesh and the anode are the two electrodes of distance $d = 5\,\mathrm{mm}$ apart. Liquid xenon is filling the space in between and leaving gas gap d_g. In this simplified model, the electric field in the gas gap where *S2* is produced, could be computed using equation (2.8):

$$\begin{aligned} E_\mathrm{g} \cdot d_\mathrm{g} + E_\mathrm{g} \frac{\epsilon_\mathrm{g}}{\epsilon_\mathrm{l}} (d - d_\mathrm{g}) &= U \\ E_\mathrm{g} \left[\frac{d_\mathrm{g}}{d} + \frac{\epsilon_\mathrm{g}}{\epsilon_\mathrm{l}} \left(1 - \frac{d_\mathrm{g}}{d} \right) \right] &= \frac{U}{d} \,. \end{aligned} \tag{2.8}$$

The parameters are defined in the following:

E_g	Electric field in gas gap	
d_g	Distance between liquid-gas interface to anode	
d	Distance between anode and lower mesh	5 mm
U	Voltage applied on anode	$2 \sim 5\,\mathrm{kV}$
$\frac{\epsilon_\mathrm{g}}{\epsilon_\mathrm{l}}$	Ratio of electrostatic constant between gaseous and liquid xenon	1/1.96

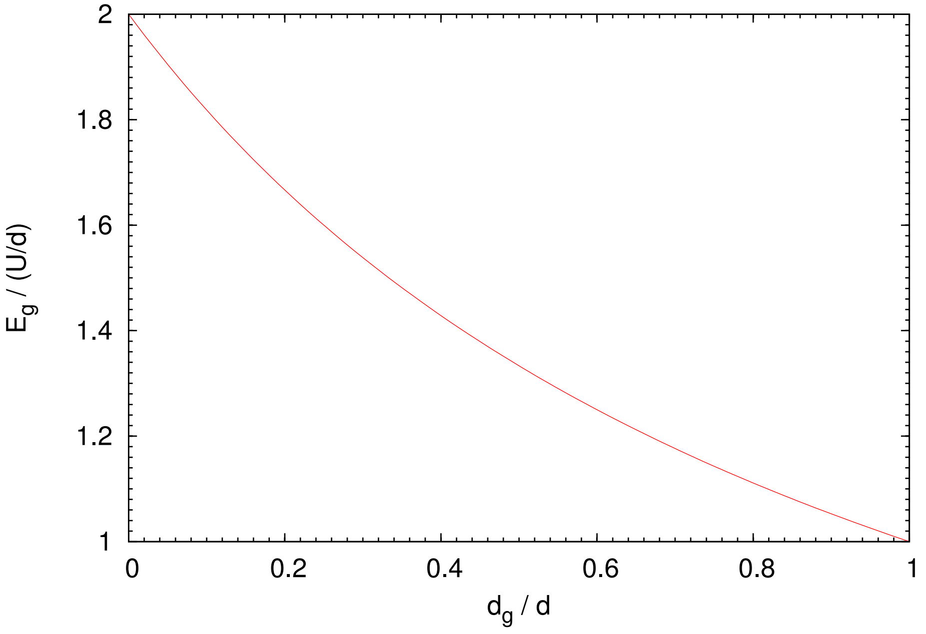

Figure 2.12: Electric Field in the *S2* Generating Gas Gap. $d = 5\,\mathrm{mm}$ is the distance between lower (gate) mesh and anode.

The behavior of electric field E_g as a function of gas gap d_g and anode high voltage U is plotted in Fig. 2.12. In the detector, E_g is controlled by both high voltage on the anode and the liquid interface height. Depending on high voltage applied on anode, the electric field in the gas phase E_g could vary from 5 kV/cm to 15 kV/cm.

Since meshes are not plates, detailed 3D simulation is required to study the electric field that drives electrons. The top three mesh stack is an assembly of three equally spaced hexagonal meshes. The three meshes are of the same 125 µm wire size but different pitches. The lower (gate) mesh and the anode have pitch size 2.5 mm while the top mesh has pitch size 5 mm. Pitch size is defined as the incircle diameter of the hexagonal unit cell. The three meshes are aligned such that combined they have 2D translational symmetry with hexagonal unit cell of 5 mm pitch. A picture of the meshes and the unit cell configuration is shown in Fig. 2.13.

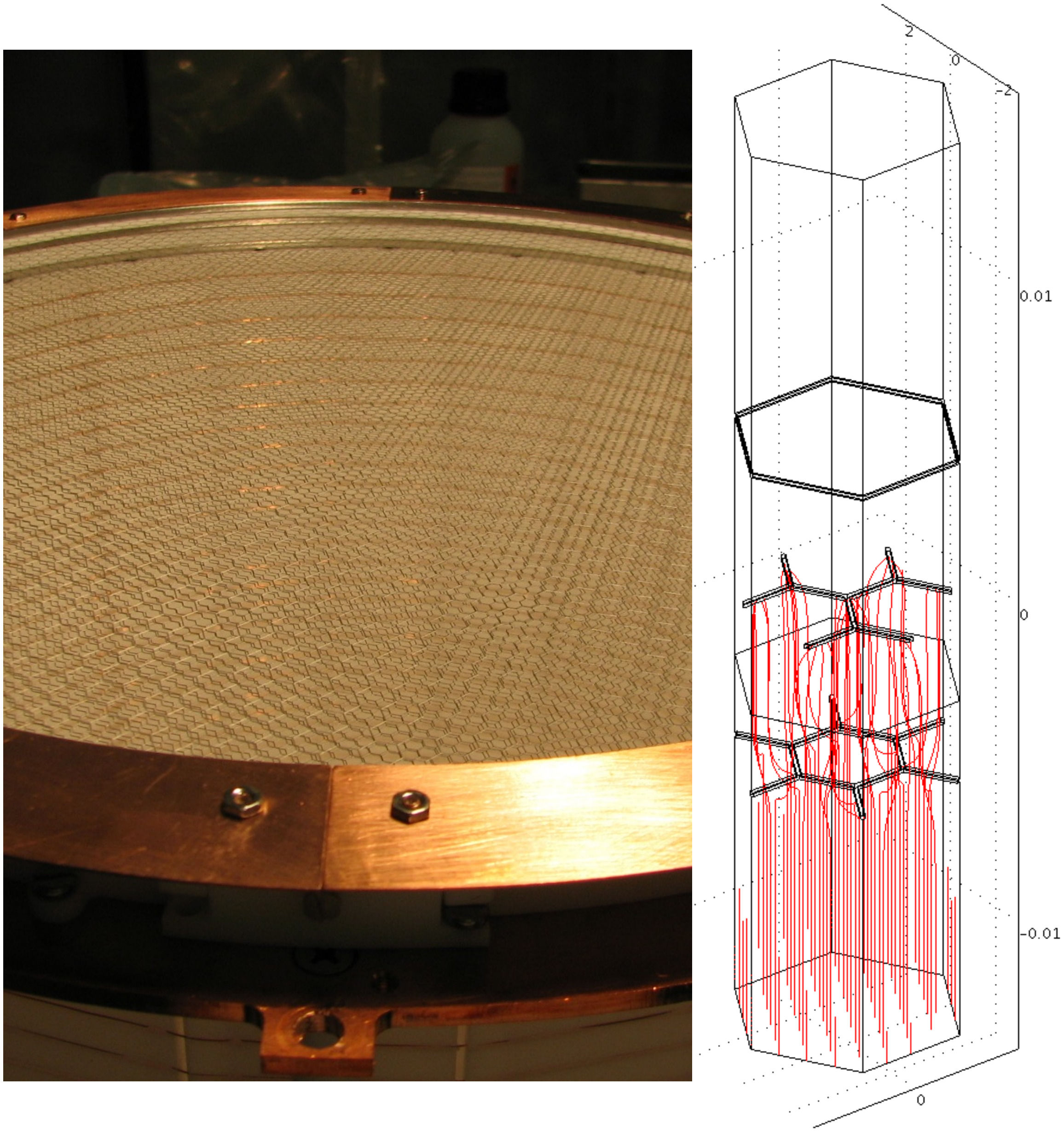

Figure 2.13: Top Three-Mesh Structure and Electric Field Simulation. Left: Photograph of top three-mesh assembled on the TPC wall. Right: electric field simulation setup of a hexagonal unit cell in the three-mesh stack. Lower (gate) mesh and anode meshes are of 2.5 mm pitch and the top mesh is of 5 mm pitch. They all have 125 µm wire diameter. Red lines are simulated electric field lines.

With the symmetry, only one unit cell has to be simulated in 3D and periodical boundary conditions are set to connect the three pairs of facing sides of the hexagonal extrusion. The top side is set to be on −800 V to mimic the top PMT photo-cathode potential. The bottom side is set to have 530 V/cm electric field pointing downwards to confirm with the electric field strength in the bulk part of TPC. The liquid-gas interface is fixed at exactly half-way between the lower (gate) mesh and the anode. Anode is set to 4.5 kV and both upper and lower meshes are set to ground potential.

The simulation is carried out using COMSOL Multiphysics® Finite Element Analysis software. The resulting electric field lines are shown as red curves in Fig. 2.13 (right). Following an electric field line starting from about 2 cm below the lower (gate) mesh, as the field line grows upwards and approaches the lower mesh, the field lines are focused to stay away from the lower mesh wires through the open hole. Eventually the field lines cross the liquid/gas boundary into the gas phase and end at anode wires.

The special alignment of the top three mesh is designed to minimize the deviation of electric field line length from liquid-gas interface to anode, depending on where the field line starts in (x, y). In the gas phase, electrons drift following electric field lines, hence electric field lines are electron trajectories. As shown in equation (2.7), the total amount of light an electron produces is a function of potential difference and total drift length. The relative change in L directly contribute to *S2* energy resolution. The relative change in potential difference $U_{\text{anode}} - U_{\text{liquid-gas interface}}$ is very small as a function of (x, y), however, the total drift length l could change substantially as (x, y) vary if meshes are not properly aligned. The alignment shown in Fig. 2.13 (right) ensures the relative change in l has σ less than 3 %.

2.7.3 *S2* Waveform and Simulation

To understand the shape and time behavior of the *S2* pulse, three factors have to be taken into consideration: electric field, electron drift velocity, and initial electron cloud size and shape.

Based on Santos et al. [47], electron drift velocities in liquid and gaseous xenon, v_{g} and v_{l}, could be approximated by

$$v_{\text{g}} = \frac{0.58}{4.0}\frac{E}{760 \times 4.0} \tag{2.9a}$$

$$v_{\text{l}} = \frac{0.1 \times 0.32545 \times E^{0.44926}}{1.0 + 0.12521 \times E^{0.43508}} \,. \tag{2.9b}$$

They are of units cm/µs. E denotes electric field strength and is of units V/cm. Plugging $ds = v(E) \cdot dt$ into equation (2.6), one gets a time dependent differential equation of dL/dt depending on electric field $E(x, y, z)$ only. It contains enough of information to establish a function characterizing, for a single electron, the amount of light produced as a function of time $L(t)$.

To establish function $L(t)$, one takes an electric field line starting from about 2 cm below the lower mesh. Following the electric field line, the drift velocity is computed using the electric field strength on the line, and dt step is established from ds. dL is then integrated along dt. When the electric field line is still in the liquid phase, the addition to dL is always zero. As soon as the electric field line enters the gas phase, the addition to dL follows equation (2.6). As the electric field line hits the anode, the integration ends. It is important to start integration from below the lower mesh rather than from the liquid-gas interface due to the focusing effect. Although the liquid phase part doesn't produce any light, it affects the timing when electrons reach the liquid-gas interface. Since electrons come from the bulk of the TPC, it is important to account for the drift path distortion, thus the timing difference, induced by the lower mesh.

As discussed previously, $L(t)$ for a single electron is actually a function of parameters (x_0, y_0, z_0) denoting where the electron starts: $L(t; x_0, y_0, z_0)$. The ionization electron cloud usually has a spatial distribution and extends to µm or mm level. To simulate an *S2* pulse, the spatial distribution of electron has to be convolved with L.

In the simulation, the electron cloud is assumed to have 3D isotropic Gaussian density profile characterized by σ. When electron cloud size σ is small, the whole electron cloud acts like a single particle following electric field lines. The Gaussian shape of electron cloud doesn't play an important role here since the electron cloud is still very much point like. As seen in Fig. 2.13, from different starting point (x_0, y_0), electrons follow quite different paths to reach anode. It is expected that following different paths the time behavior of proportional scintillation, $L(t)$, shows different features. Fig. 2.14 shows the simulated $L(t)$ behavior of small electron clouds ($\sigma = 0.08\,\text{mm}$) starting at a few (x_0, y_0) positions.

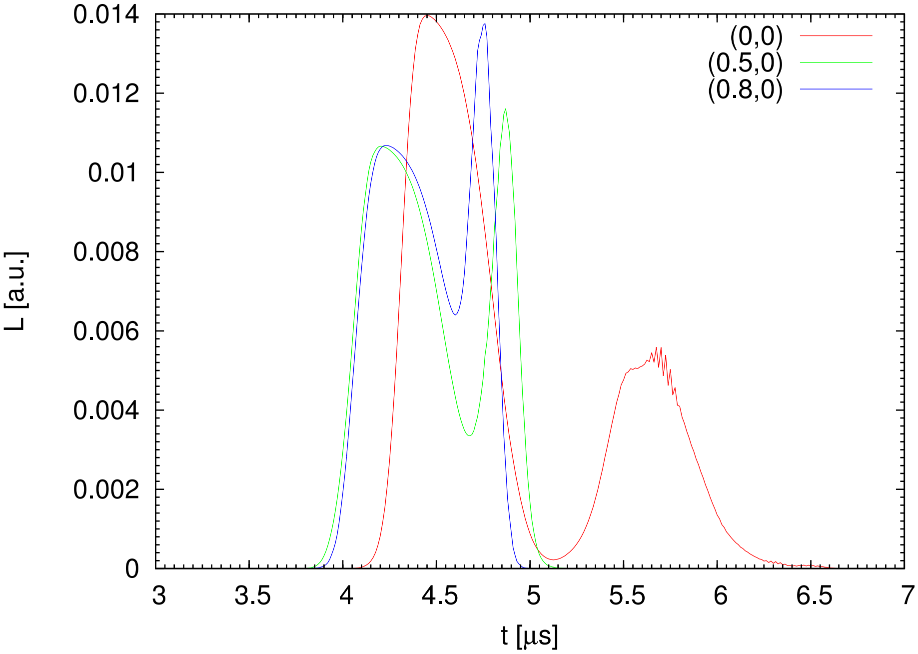

Figure 2.14: Simulated *S2* Pulse Shape: Small Electron Cloud. Electron close has Gaussian $\sigma = 0.08\,\text{mm}$. Three starting points along x-axis are shown. Figure legend shows starting point coordinates (x_0, y_0) in units mm. Axis definition is shown in Fig. 2.13. Note that the time resolution in simulation is much finer than the experimental sampling (10 ns). Vertical axis is defined such that the integral of each curve equals 1.

In general $L(t)$ for a small electron cloud has double-peak structure. The first peak appears when electrons just left liquid and entered gaseous xenon phase. The second peak appears when electrons are about to arrive at the anode wire. Both of the two regions have relative higher electric field thus producing more light in a unit time. In between the two regions, electrons pass through a spacial area with relatively lower electric field. Depending on the starting point of electron cloud, electrons experience different paths and different electric field strength at different time, therefore the shape and relative height of the two peaks vary.

As the electron cloud size gets larger, the convolution of the electron density distribution and $L(t; x_0, y_0, z_0)$ starts to dominate. There are two aspects of the convolution. Firstly, the spread of electron cloud in x-y causes $L(t)$ curves corresponding to different (x_0, y_0) positions to be summed together. Secondly, the electron cloud spread in z causes $L(t)$ curves with different shift in time to be summed together, since electrons leave the liquid at different times. The net effect of the two is the double-peak structure starts to blur as the electron cloud size becomes larger. When the electron cloud size becomes sufficiently large, the *S2* peak becomes very close to Gaussian without any specific features due to mesh and electric field structures. Fig. 2.15 shows simulated *S2* pulses of a medium size ($\sigma = 0.1\,\mathrm{mm}$) and a large size ($\sigma = 0.5\,\mathrm{mm}$) electron cloud. Note that for the medium size electron cloud, the *S2* pulse shape still changes as the position of electron cloud center (x_0, y_0) changes, while for the large size electron cloud, the *S2* pulse shape is almost independent of electron cloud center position.

In liquid xenon, electrons have a diffusion constant $D \approx 50 \sim 80\,\mathrm{cm}^2/\mathrm{s}$ (Doke [22]). A point like electron cloud could become a cloud with $\sigma \approx 1.5\,\mathrm{mm}$ after 180 µs of drifting. 180 µs is roughly the maximum drift time with drift velocity in the bulk being 1.74 mm/µs. To compare the *S2* pulse shape in real data with the simulation, it is convenient to select on drift time in order to select electron cloud size. Fig. 2.16 shows two *S2* waveform samples from 662 keV gamma (^{137}Cs) data which have very short drift time thus small electron cloud size. Double peak structures are clearly visible. Compare to the simulation shown in Fig. 2.15 (top), qualitatively the simulated *S2* pulse shape matches with the real data pretty well. For events with long drift time, as shown in Fig. 2.17, the double peak structure is no longer visible, as expected from simulation.

In summary, the detailed structure of the top three-mesh stack, hence the specific electric field structure in the *S2* generating region, does result in a two-peak structure in the *S2* peak. It is predicted by electric field simulation and convolution with electron cloud of 3D Gaussian density profile, and is verified with real *S2* shape in data. However, due to electron diffusion in liquid xenon, for most dark matter relevant events, namely events in the fiducial volume ($dt > 10\,\mu\mathrm{s}$), we could simply expect *S2* pulses to have Gaussian shape. The Gaussian shape could be slightly skewed, but the double-peak structure is certainly non-visible.

2.7.4 Effects on *S2* from Electron Cloud and Diffusion

XENON100 detector has a charge sensitive volume of about 30 cm in height, which allows electrons to drift up to 180 µs. Measurement of *S2* pulse width with such a long drift time provides a good opportunity to study electron diffusion in liquid xenon.

For electrons drifting in gas under the influence of and external electric field, it is known that the drifting along the direction of electric field, which is the same as the direction of drift velocity, has a different diffusion constant than that in the direction perpendicular to the electric field (Parker Jr. and Lowke [42], Skullerud [50]). It is also demonstrated recently that the electron diffusion is

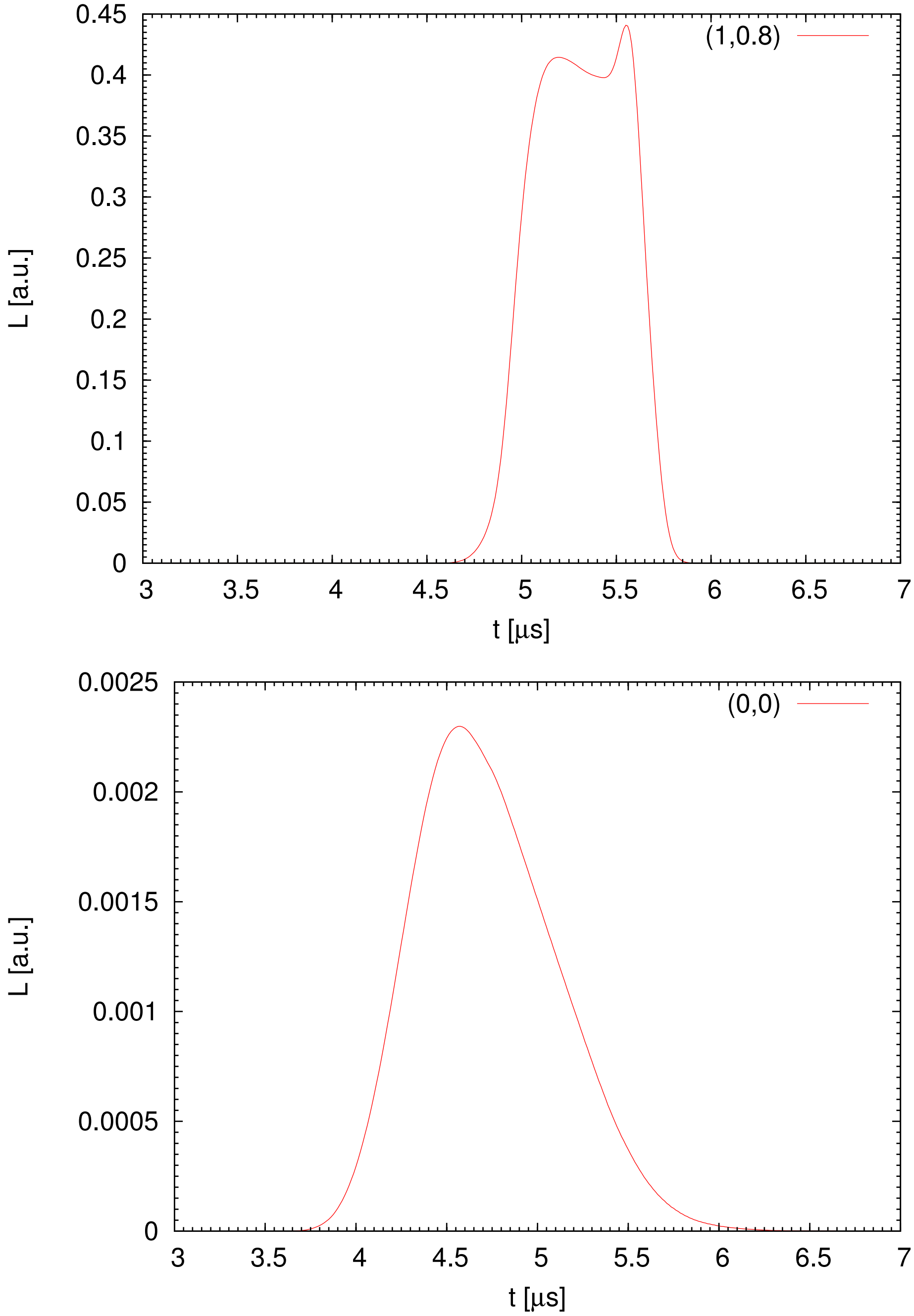

Figure 2.15: Simulated *S2* Pulse Shape: Large Electron Cloud. Top: electron cloud has Gaussian $\sigma = 0.1\,\mathrm{mm}$. Bottom: electron close has Gaussian $\sigma = 0.5\,\mathrm{mm}$.

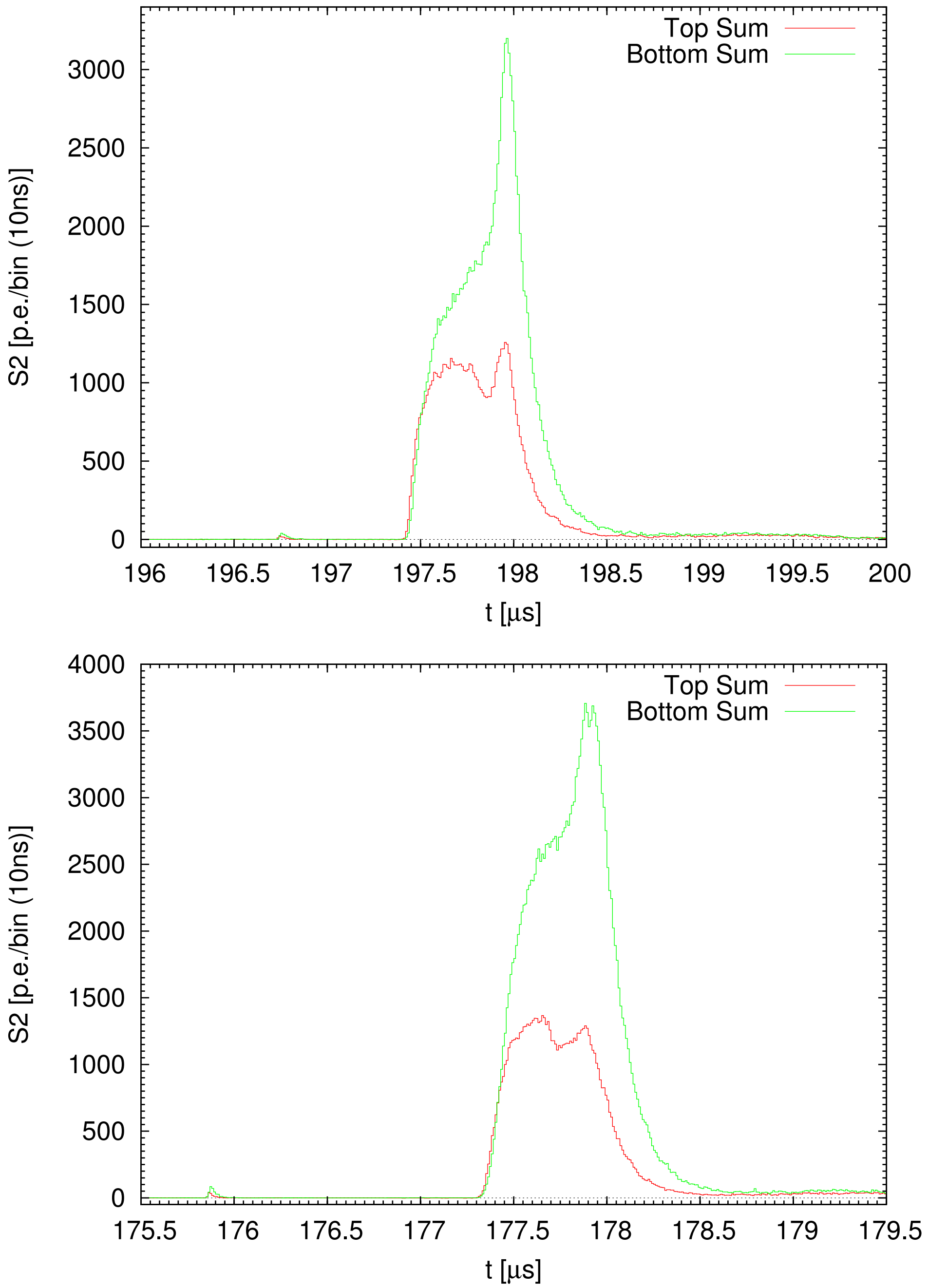

Figure 2.16: *S2* of XENON100 Event: Short Drift Time. *S1*s are visible in the same window. Top waveform has $dt = 0.6\,\mu\text{s}$ and bottom waveform has $dt = 1.5\,\mu\text{s}$

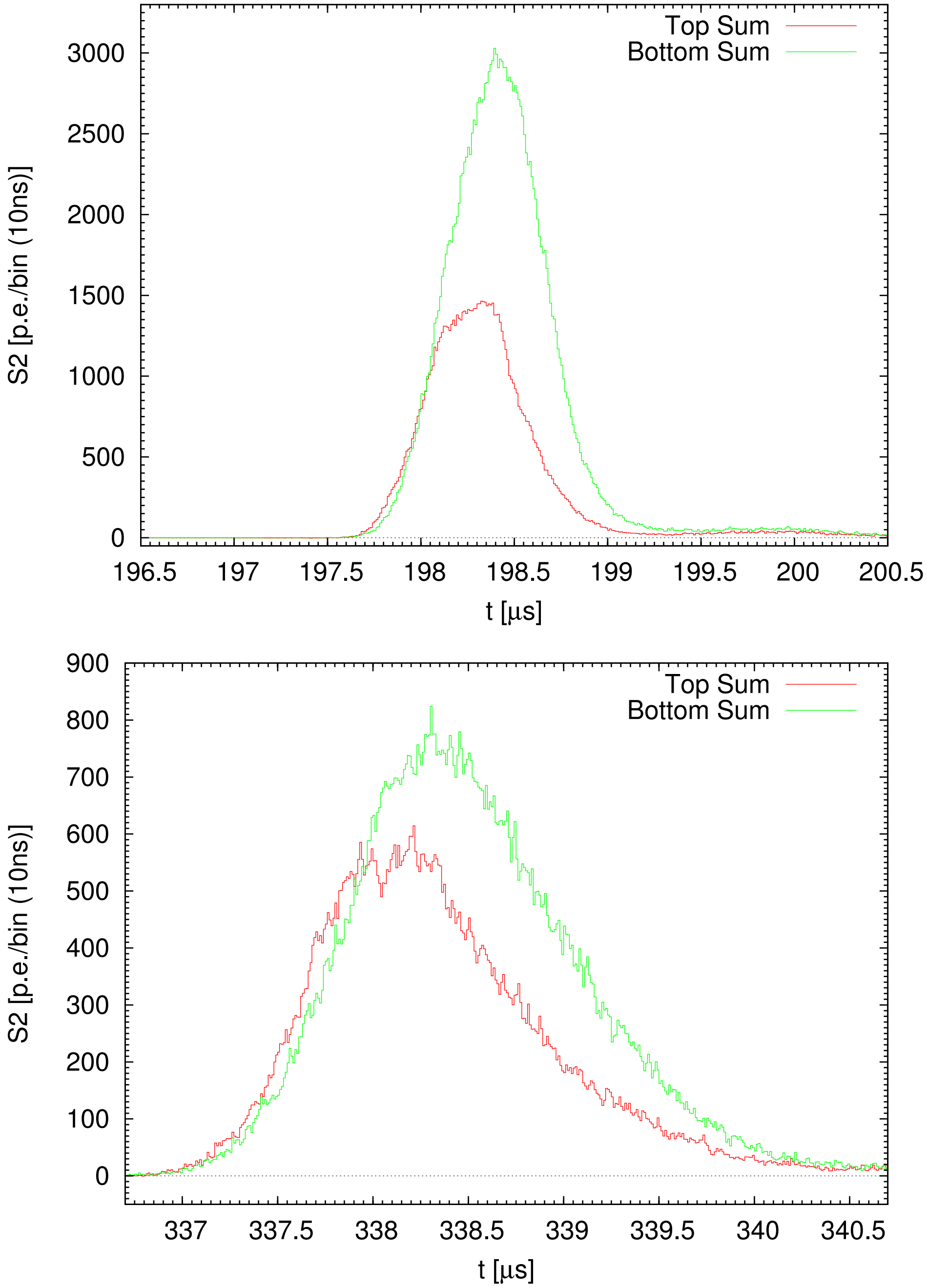

Figure 2.17: *S2* of XENON100 Event: Long Drift Time. Top: $dt = 20\,\mu\text{s}$. Bottom: $dt = 160\,\mu\text{s}$.

indeed anisotropic in liquid xenon under external electric field (Sorensen [52]). Sorensen [52] also estimated that the ratio between longitudinal and transverse diffusion constants, $D_\mathrm{L}/D_\mathrm{T}$, is of the order 0.15 under an external electric field of about 700 V/cm. The small ratio of $D_\mathrm{L}/D_\mathrm{T}$ means that after certain time of drifting, the electron cloud becomes much compressed in z while extended in x-y.

As discussed in the *S2* waveform simulation, electron cloud spread in both x-y and z contribute to the *S2* pulse shape. For the spread in x-y, although electrons starting from different (x, y) coordinates result in different *S2* pulse shape, except for a small fraction of outliers, the majority of *S2* pulses have similar duration in time for about 1 µs, as shown in Fig. 2.14. It means electron diffusion in transverse direction, thus the spread in x-y, wouldn't give significant contribution to the overall *S2* pulse width. It also implies that the *S2* pulse width is mainly due to the spread in z, or equivalently the diffusion in longitudinal direction. Considering the much compressed shape of electron in z due to the small ratio $D_\mathrm{L}/D_\mathrm{T}$, it is seemingly counter-intuitive that the large spread in x-y results in little effect on the *S2* pulse width, while the relatively much smaller spread in z dominates the *S2* pulse width. However, electric field and *S2* waveform simulation confirms that the time difference for electrons traveling from the liquid-gas interface to the anode, starting at different (x, y) coordinates, is small. This observation also justifies the use of an isotropic Gaussian electron distribution in the simulation to model the electron cloud that is known to be anisotropic in reality. Because after a certain drift time, when the electron cloud becomes reasonably large, the transverse spread is irrelevant to the corresponding *S2* pulse width that is modeled by Gaussian.

Since the observed *S2* width is only dependent on the electron cloud width in z, the diffusion model becomes one dimensional and the electron cloud size in terms of Gaussian *sigma* in z direction, as a function of drift time t, can be written as

$$\sigma_z = \sqrt{2D_\mathrm{L}t} \quad \text{Units: [L]}\,. \tag{2.10}$$

D_L is the diffusion constant concerning only the longitudinal direction of the electric field, which is in z. Since the width of the *S2* pulse is measured in time, it is convenient to convert spatial spread in z, σ_z, to time spread by dividing the drift velocity v_d. Also, because even the smallest electron cloud—single electron, has a fixed non-zero width, it is useful to assume an offset in *S2* width, σ_0, at zero drift time. With all the models assumed to be Gaussian, the variances, σ^2's, can be summed up directly, yielding equation (2.11).

$$\begin{aligned} \sigma_{S2}^2 &= \left(\frac{\sigma_z}{v_\mathrm{d}}\right)^2 + \sigma_0^2 \\ \sigma_{S2} &= \sqrt{\frac{2D_\mathrm{L}t}{v_\mathrm{d}^2} + \sigma_0^2} \quad \text{Units: [T]} \end{aligned} \tag{2.11}$$

The equation shows that *S2* pulse width has a square-root dependence on drift time. By fitting equation (2.11) to the real XENON100 data in σ_{S2}^2 versus dt space, D_L and σ_0 are determined, as shown in Fig. 2.18.

Note that for *S2* pulses in data, the pulse width is first measured as the full width at 10 %

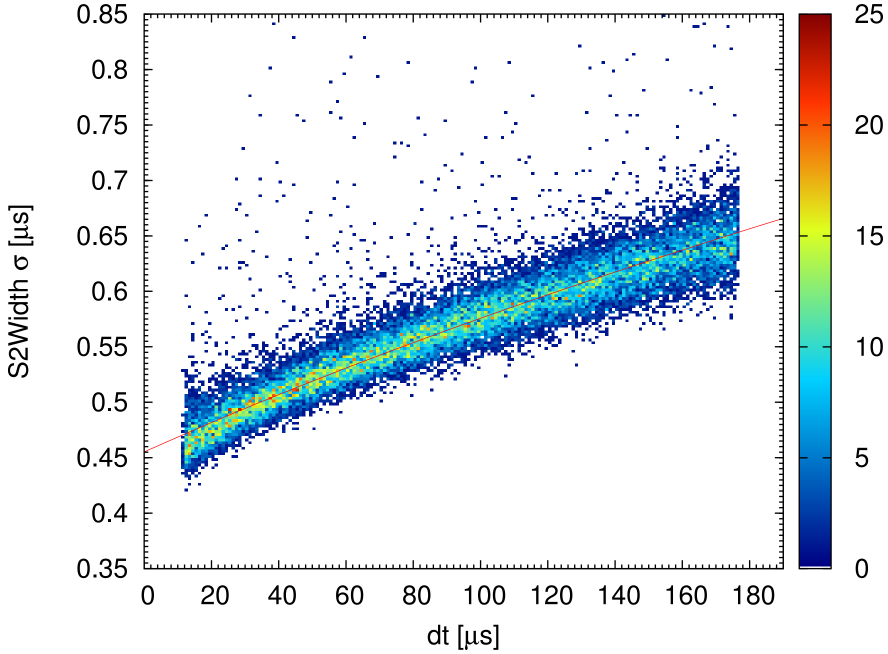

Figure 2.18: *S2* Pulse Width vs. Drift Time. Pulse width (σ) is inferred from full width at 10 % pulse height divided by 4.292. Fit shows diffusion constant $D_\mathrm{L} = 18.8\,\mathrm{cm}^2/\mathrm{s}$, $\sigma_0 = 0.455\,\mu\mathrm{s}$ (equivalently about 1 mm). 164 keV full energy peak from neutron activated xenon data.

of maximum pulse height, then divided by a factor 4.292 to infer the corresponding Gaussian σ. Although the commonly used Full Width Half Maximum (FWHM) values are also computed, due to the fluctuations in *S2* waveform, FWHM is proven to be less reliable than the full width at 10 % of maximum height. A clear improvement, which requires significant amount of computing power, is to fit each individual *S2* pulse with Gaussian to obtain the width more properly. The observed value of D_{L} in this study is consistent with the findings in Sorensen [52].

Summary

XENON100 is constructed using carefully screened materials regarding their radioactivity. The dual-phase LXeTPC allows 3D positioning of interaction and both scintillation and ionization measurements. Both *S1* light response and *S2* behavior are well understood. Continuous recirculation of gaseous xenon through a hot getter removes electro-negative impurities and extends electron lifetime while drifting. Distillation removes ^{85}Kr which reduces the electromagnetic radiation background in the bulk xenon. With both electromagnetic radiation background reduction and background discrimination capabilities, the XENON100 detector shows great potential in WIMP dark matter search.

Chapter 3

Detector Calibration and Background Discrimination

It is difficult, and largely inaccurate, from either first principle or empirical calculation/Monte Carlo simulation, to estimate the detector response. A more practical way is to use various sources to probe the detector response. The detector response in terms of *S1* and *S2* has been described in Chapter 2. For dark matter search, the more important aspect is to calibrate the energy scale and discrimination parameter for electronic and nuclear recoil signals.

3.1 Position Dependent *S1* and *S2* Corrections

S1 and *S2* are both spatial position dependent. The dependence in *S1* is due to the light collection variation as shown in Fig. 2.10. The dependence in *S2* comes from both electron loss (Fig. 2.11) and light collection. Since the whole sensitive volume is expected to have equal probability to detector dark matter, it is desirable to have measurable parameters with uniform responses across the whole sensitive volume. Therefore, corrected *S1* and *S2*, c*S1* and c*S2*, are created for each event. c*S1* is achieved by dividing measured *S1* over the light yield at the position of interaction relative to the volume mean. c*S2* is achieved first by dividing the exponential due to the electron lifetime, then corrected for the *S2* light collection.

For a specific energy line observed in liquid xenon, it is known that scintillation and ionization are anti-correlated (Conti et al. [19]). It means for the specific energy line, when *S2* is plotted against *S1*, a 2D Gaussian shape with main axis not parallel to either x or y axis should appear. The 2D Gaussian represents the intrinsic property of liquid xenon responding to energy deposition. In addition, particles hit liquid xenon at various different location, and the detector response of *S1* and *S2* are position dependent. If the raw *S1* and *S2* are used regardless of the position of interaction, additional detector specific fluctuation would be added to the intrinsic fluctuation resulting in non-Gaussian correlation. As shown in Fig. 3.1, for 164 keV and 236 keV lines, when raw *S1* and *S2* are used, the correlation is extensively elongated. After *S1* and *S2* are corrected for position dependence, the correlation becomes 2D Gaussian. Therefore *S1* and *S2* corrections eliminates distortions from detector response and improves the resolution in both *S1* and *S2*. And the corrections are only achievable thanks to the 3D positioning capability of the LXeTPC.

Note that the corrections are done on top array and bottom array total for both *S1* and *S2*, but not for each individual PMT.

In the following studies, all the quantities regarding energy and discrimination are computed from c*S1* and c*S2*.

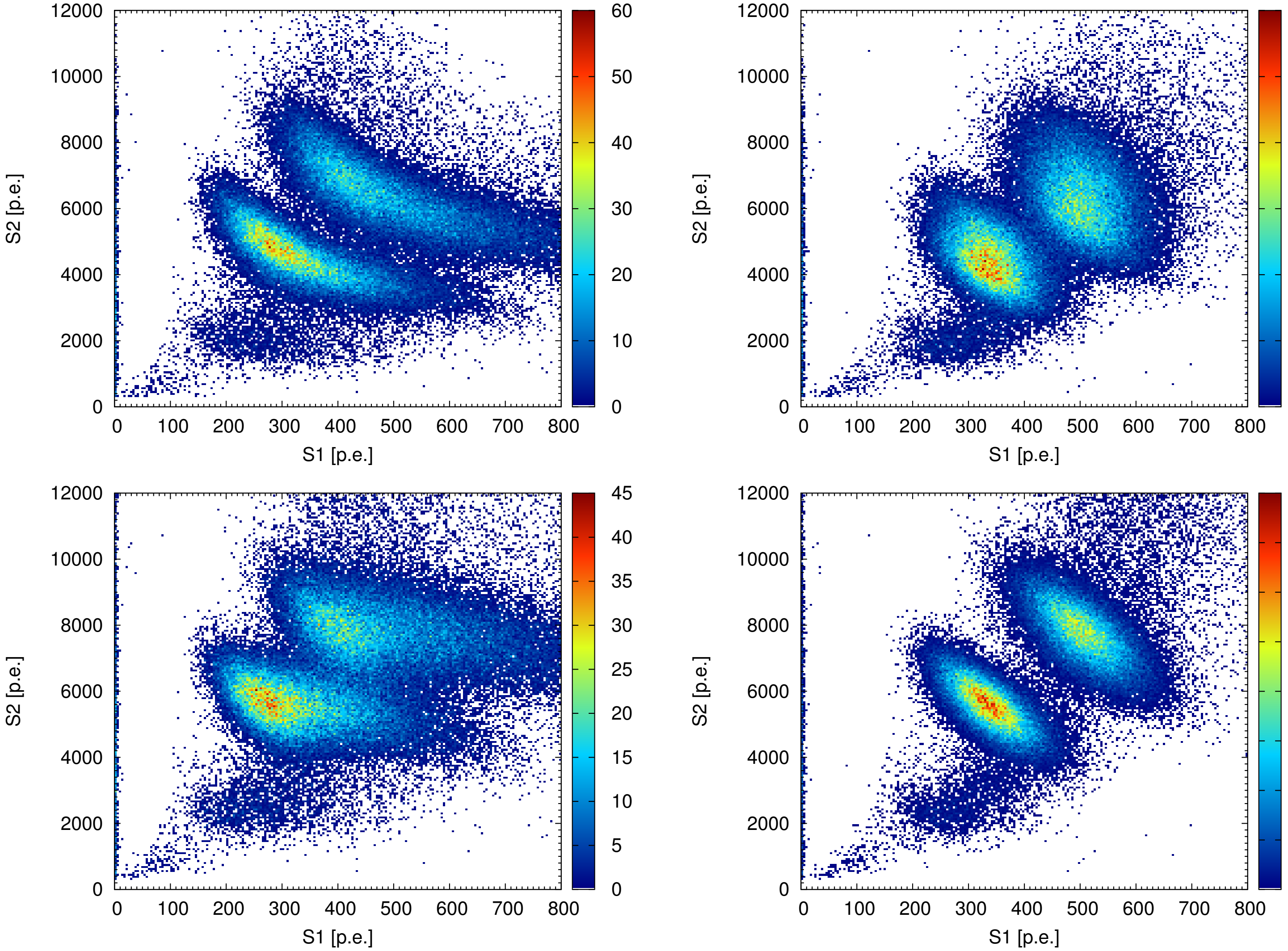

Figure 3.1: Position Dependent *S1* and *S2* Corrections. 164 keV and 236 keV lines. Top left: no correction. Top right: *S1* corrected only. Bottom Left: *S2* corrected only. Bottom right: both *S1* and *S2* corrected.

3.2 Energy Scale

When a particle interacts with xenon, the energy deposition is converted to measurable quantities in terms of primary scintillation light *S1*, and ionization charge which is converted into *S2* light through gaseous xenon proportional scintillation. The particle energy deposition can be determined from the amount of *S1* and *S2* produced, i.e., an energy scale function $E_{\mathrm{r}}(S1, S2)$ could be determined. It is known that for the same amount of energy deposition, nuclear recoil and electronic recoil interactions produce different amounts of *S1* and *S2*, therefore two different energy scale functions, E_{nr} and E_{er}, have to be established separately.

Due to historical reasons, the energy scale is determined solely on the primary scintillation light *S1*. One of the reasons is many xenon based detectors do not detect the ionization charge at all. Another reason, more relevant to dark matter detection, is that only light yield of nuclear recoil has been measured down to very low nuclear recoil energy, while charge yield remains largely unknown in the low energy region (Aprile et al. [5], Sorensen and Dahl [53]). Building energy scales on *S1* only results in highly non-linear energy scale functions.

The inverse of the energy scale function $E_{\mathrm{r}}(S1)$ is usually expressed as light yield $\mathcal{L}_{\mathrm{y}}(E_{\mathrm{r}})$ in units p.e./keV. From an experimental point of view, it is very convenient to use light yield as a measure of detector response to energy deposition. For instance, if on average all the PMTs detect 300 p.e. for the 122 keV gamma full absorption peak, the light yield $\mathcal{L}_{\mathrm{y}}(122\,\mathrm{keV}) = 300/122 \approx 2.5\,\mathrm{p.e./keV}$. Absolute values of $\mathcal{L}_{\mathrm{y}}$ and E_{r} do not reflect the intrinsic scintillation yield of liquid xenon, but convolves geometrical configurations in the detector affecting light collection and PMT's sensitivity for turning photons into photo-electrons. Therefore $\mathcal{L}_{\mathrm{y}}$ and E_{r} are detector specific and have to be calibrated for each specific detector.

As shown in Fig. 3.2, the electronic light yield in XENON100 detector is calibrated at several energies using gamma sources both outside and inside of the detector. The 662 keV line is from a ^{137}Cs source placed outside of the detector. The 40 keV and 80 keV lines are from inelastic neutron scattering $^{129}\mathrm{Xe}(n, n'\gamma)\,^{129}\mathrm{Xe}$ and $^{131}\mathrm{Xe}(n, n'\gamma)\,^{131}\mathrm{Xe}$ produced inside the detector during an AmBe neutron calibration. 164 keV and 236 keV lines are from decays of neutron activated xenon metastable states in the detector after an AmBe neutron calibration. They have half-life of about 8.8 and 11.9 days, respectively. It is clear that the light yield is highly non-linear as a function of electronic recoil energy deposition. As energy deposition get higher, the amount of light produced per keV becomes lower. The unusually high light yield of 236 keV is a good demonstration of the non-linearity. The 236 keV line is actually a two-step de-excitation: a 196 keV gamma followed immediate by a 40 keV gamma. Therefore the apparent light yield at 236 keV is the sum of light yields at 196 keV and 40 keV, which is higher than the true light yield at 236 keV. When fitting the light yield as a function of energy, the point at 236 keV is excluded.

Although the nuclear recoil energy scale $E_{\mathrm{nr}}(S1)$ is the most relevant for dark matter, it is difficult to calibrate the $E_{\mathrm{nr}}(S1)$ function directly. The major difficulty lies in the determination of true nuclear recoil energy deposition of particles interacting with xenon nuclei, such as neutron. The neutron energy deposition has to be measured independent of the xenon response. It is unrealistic to have neutron source with near monochromatic energy close to the dark matter detector. Instead, we break down the calibration procedure for $E_{\mathrm{nr}}(S1)$ into two steps. First, we determine the

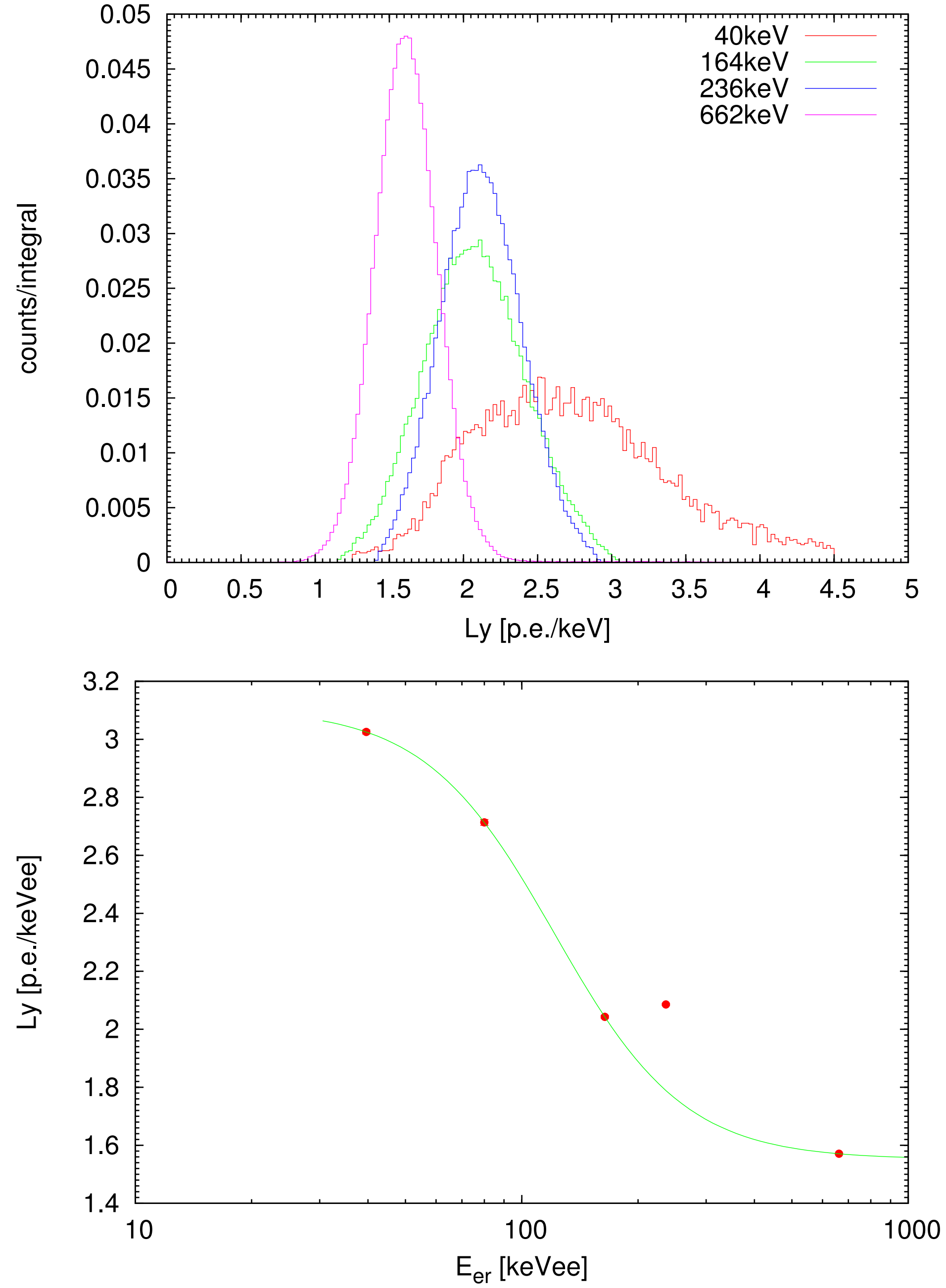

Figure 3.2: Electronic Recoil Light Yield. Top: *S1* spectra of full absorption peaks from 40 keV (^{129}Xe$(n, n'\gamma)\,^{129}$Xe), 164 keV ($^{131\mathrm{m}}$Xe), 236 keV ($^{129\mathrm{m}}$Xe) and 662 keV (^{137}Cs) sources. Bottom: electronic recoil light yield as a function of gamma energy. 236 keV line has an unusually high light yield because it from a two-step de-excitation: a 196 keV gamma followed immediate by a 40 keV gamma.

electronic recoil energy scale $E_{\mathrm{er}}(\mathit{S1})$ function on the gamma full absorption energy spectrum of several calibration sources emitting gamma-ray of fixed energies, and obtain the light yield of the detector at 122 keV. Second, we rely on neutron scattering experiments performed on small detectors, to determine the nuclear recoil light yield relative to the light yield of a 122 keV gamma ray. With the small detector, the true nuclear recoil energy deposition could be determined by measuring the scattering angle of the neutron (Aprile et al. [6]). The relative nuclear recoil light yield with respect to the light yield of 122 keV gamma ray is referred to as $\mathcal{L}_{\mathrm{eff}}$. The separately determined electronic recoil light yields at 122 keV of larger detector and small detector serve as the anchor point, allowing the measurements of nuclear recoil light yield on the small detector to be used in the large detector. The choice of 122 keV gamma as anchor point is largely due to historical reasons. The ^{57}Co source emitting a 122 keV gamma was frequently used to calibrate small xenon detectors. However, 122 keV gamma doesn't travel far in liquid xenon. It makes direct calibration of light yield at 122 keV unpractical in large liquid xenon detectors. Therefore, large detectors like XENON100 are calibrated with other gamma sources, and the light yield is interpolated from light yield measurements at other energy lines. As in Fig. 3.2, the interpolation shows XENON100 has a light yield of 2.20 ± 0.09 p.e./keV at 122 keV.

$\mathcal{L}_{\mathrm{eff}}$ is always smaller than one, which indicates a quenching of nuclear recoil (Lindhard and Scharff [36]). With the independently measured $\mathcal{L}_{\mathrm{eff}}$, to convert *S1* to nuclear recoil energy E_{nr}, one more factor has to be taken into account: electric field quenching. As external electric field pulls ionization electrons away hence suppresses the recombination process (2.4), the amount of light produced is decreased. The electric field quenching factors are different for electronic recoil (S_{er}) and nuclear recoil (S_{nr}), and are measured in other experiments (Aprile and Doke [4] and references therein).

Combining all the factors together, the nuclear recoil energy could be expressed as

$$E_{\mathrm{nr}} = \frac{\mathit{S1}}{\mathcal{L}_{\mathrm{y}}} \cdot \frac{1}{\mathcal{L}_{\mathrm{eff}}} \cdot \frac{S_{\mathrm{er}}}{S_{\mathrm{nr}}} \tag{3.1}$$

where $\mathcal{L}_{\mathrm{eff}}$ is the nuclear recoil scintillation efficiency (nuclear recoil light yield relative to electronic recoil light yield of 122 keV gamma-ray) at zero electric field, S_{er} and S_{nr} are electric field scintillation quenching factors for electronic recoil and nuclear recoil, respectively. S_{er} and S_{nr} are measured, under XENON100 operation condition with electric field of 530 V/cm, to be 0.58 and 0.95 (Aprile et al. [5]).

$\mathcal{L}_{\mathrm{eff}}$ has been measured independently in many detectors by many groups (Akimov et al. [2], Aprile et al. [8], Arneodo et al. [9], Bernabei et al. [11], Chepel et al. [17]). Although the measurement accuracy and understanding of systematic uncertainties have been improving over the years, there is no global agreement on the value of $\mathcal{L}_{\mathrm{eff}}$, especially at low energy. Columbia group (Plante et al. [43]) made the most recent measurement, both narrowing down the uncertainty and reaching the lowest energy (3 keV) ever measured. Nevertheless, to make the best estimate of $\mathcal{L}_{\mathrm{eff}}$ for XENON100 results, we took all the available direct measurement of $\mathcal{L}_{\mathrm{eff}}$ and perform a fit assuming $\mathcal{L}_{\mathrm{eff}}$ can be described by a Gaussian at each E_{nr} value. The measurement points and fits are shown in Fig. 3.3.

The fit only allows us to go down in E_{nr} to 3 keV. Below 3 keV, since no direct measurements

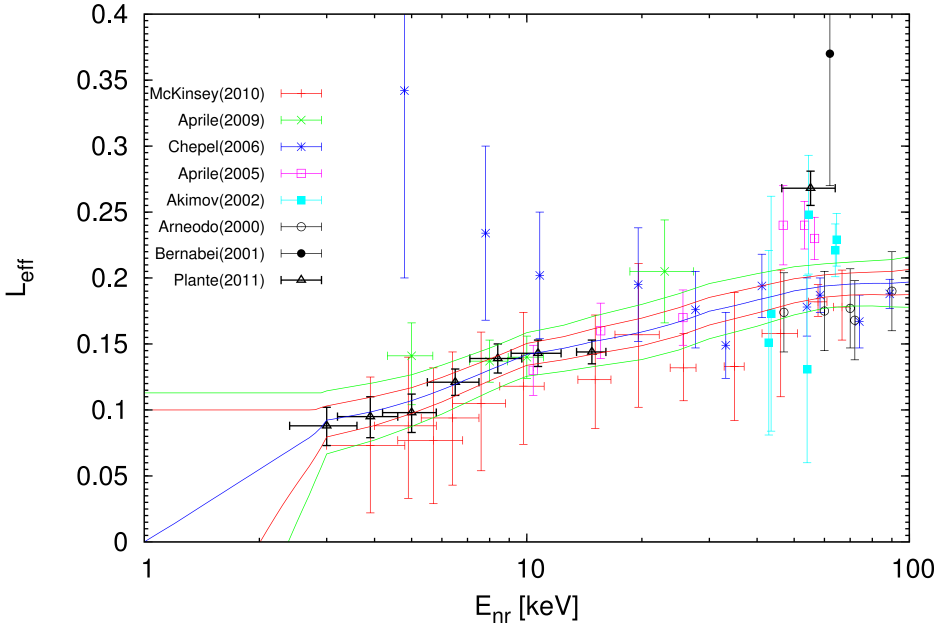

Figure 3.3: $\mathcal{L}_{\mathrm{eff}}$ Measurements and Global Fits. The best fit is shown as the blue curve. 1σ and 2σ contours are shown as red and green curves, respectively. Extrapolations below 3 keV are made. New measurements made by Columbia group (Plante et al. [43]) are shown as black triangle.

exist, extrapolation is unavoidable to make estimations of $\mathcal{L}_{\rm eff}$. A conservative choice, extrapolating $\mathcal{L}_{\rm eff}$ logarithmically to 0 at 1 keV, was chosen for the computation of final results.

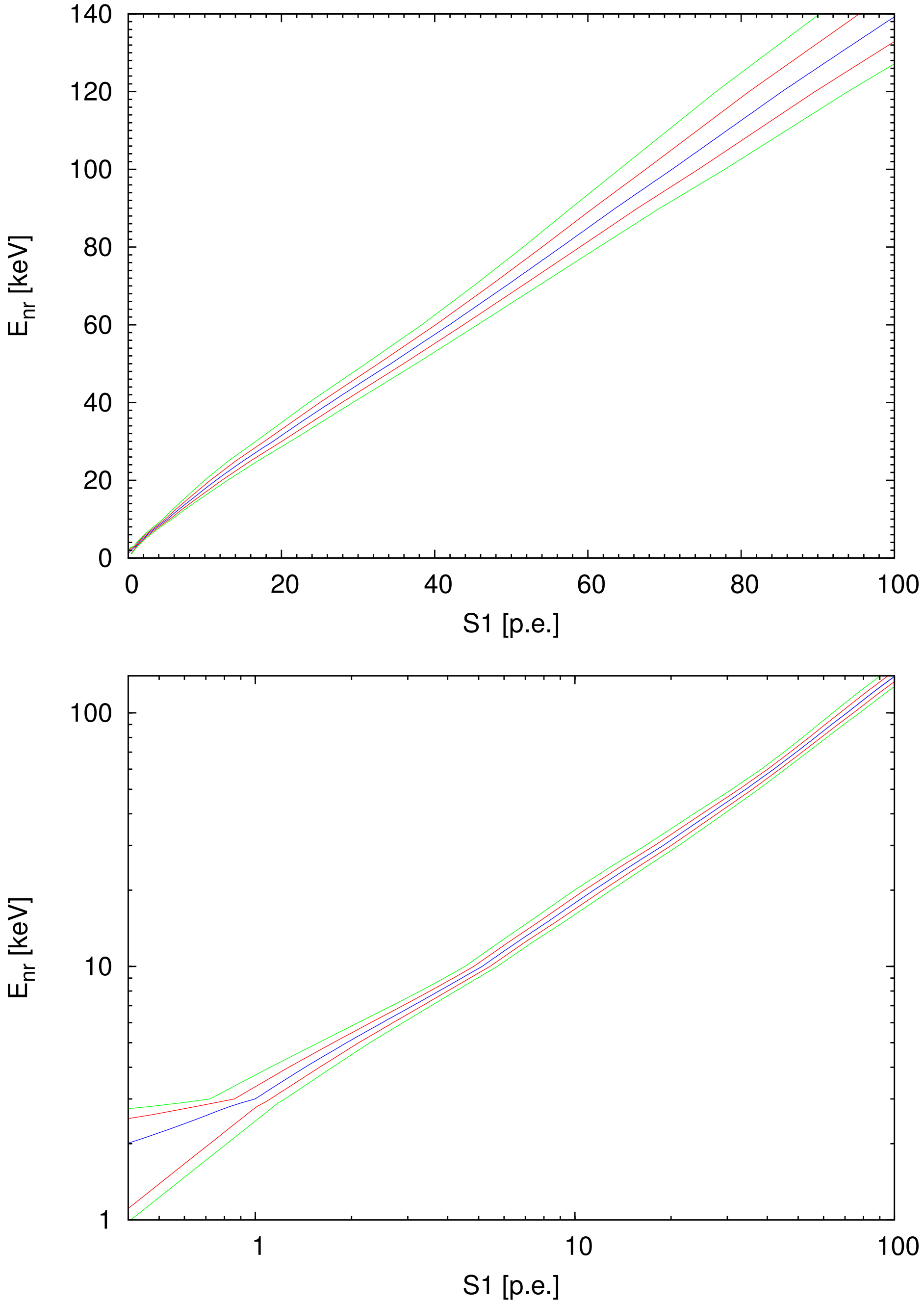

Figure 3.4: Conversion from *S1* to $E_{\rm nr}$. Top: linear scale. Bottom: log-log scale. Lines correspond to global fit, 1σ and 2σ contours in Fig. 3.3.

With $\mathcal{L}_{\rm eff}$ determined, using equation (3.1), the conversion function from *S1* to $E_{\rm nr}$ is constructed. The conversion function corresponding to the global fit is shown in Fig. 3.4. The conversion function is largely linear. Lower $\mathcal{L}_{\text{eff}}$ would result in the same *S1* value corresponding to a higher nuclear recoil energy.

3.3 Discrimination

XENON100 has the capability of discriminating electronic recoil from nuclear recoil, utilizing the ionization and scintillation yield difference between the two types of interactions. Traditionally, while *S1* is used for energy scale determination, $\log(S2/S1)$ is used as the discrimination parameter. To characterize the behavior of discrimination parameter, the detector has to be calibrated with electronic recoil particles and nuclear recoil particles separately. The challenge, however, is to probe the discrimination at very low energies.

3.3.1 Electronic Recoil Calibration

^{60}Co source is placed at a few places around the detector. 1.17 MeV and 1.33 MeV gammas are emitted from ^{60}Co source. However, the full energy peaks of $\sim$ MeV gammas are not of interest for dark matter search, rather the forward Compton scatters depositing small amount of energies in liquid xenon are the events probing the parameter space. In fact, the DAQ is most of the time set such that the high energy depositions are automatically rejected and not recorded.

The low energy single scatter event distribution is shown in Fig. 3.5. Since ^{60}Co source is placed outside of the detector, most of interactions happen at the edge of the detector, and the inner volume is poorly probed. To gain enough of statistics in the center of the detector, a large amount of data was acquired.

The electronic recoil band—discrimination parameter versus energy parameter *S1*, is shown in Fig. 3.6. Most of electronic recoil events reside above the nuclear recoil band median, which indicates a good separation between electronic recoil and nuclear recoil using the discrimination parameter.

Another use of ^{60}Co data is to estimate the anomalous leakage background in the dark matter search region. Gammas scatter once in the charge sensitive volume and one or more times in the charge insensitive region. It provides a good sample of anomalous events. It is also verified that the distribution of anomalous events sampled by ^{60}Co is very close to that in the background data. Details are discussed in Chapter 5 and Chapter 6.

3.3.2 Nuclear Recoil Calibration

The nuclear recoil band is calibrated using a ^{241}AmBe source placed at one point in a lead brick shield to reduce the gamma output, as shown in Fig. 2.3. Ideally neutron calibration should be done as ^{60}Co in that the source should be placed around the detector to probe the sensitive volume evenly. However, due to the high probability for neutron to activate surrounding materials, the allowed exposure time of neutron source was very limited. The outcome of neutron calibration with source placed at only one point, as shown in Fig. 3.7, is good enough in covering the whole sensitive volume.

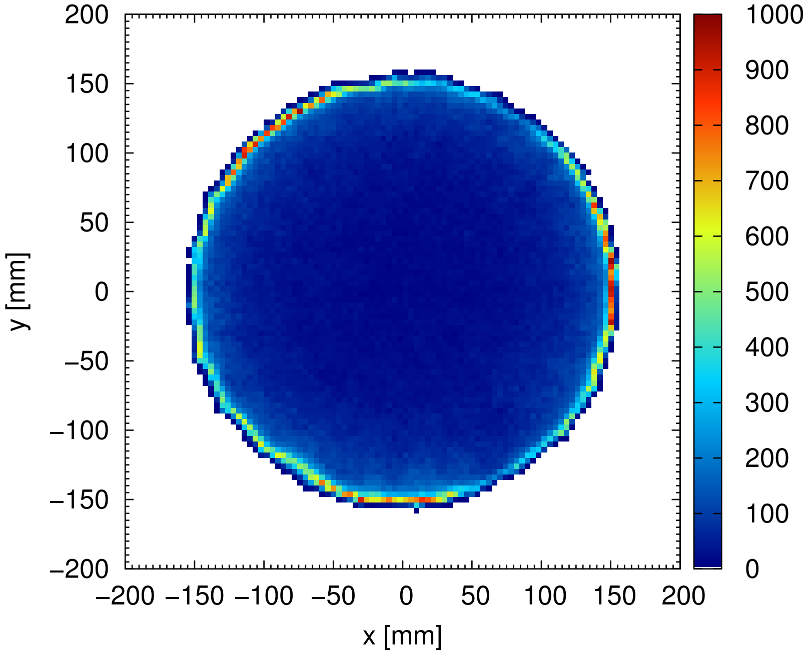

Figure 3.5: Electronic Recoil Events from ^{60}Co Data.

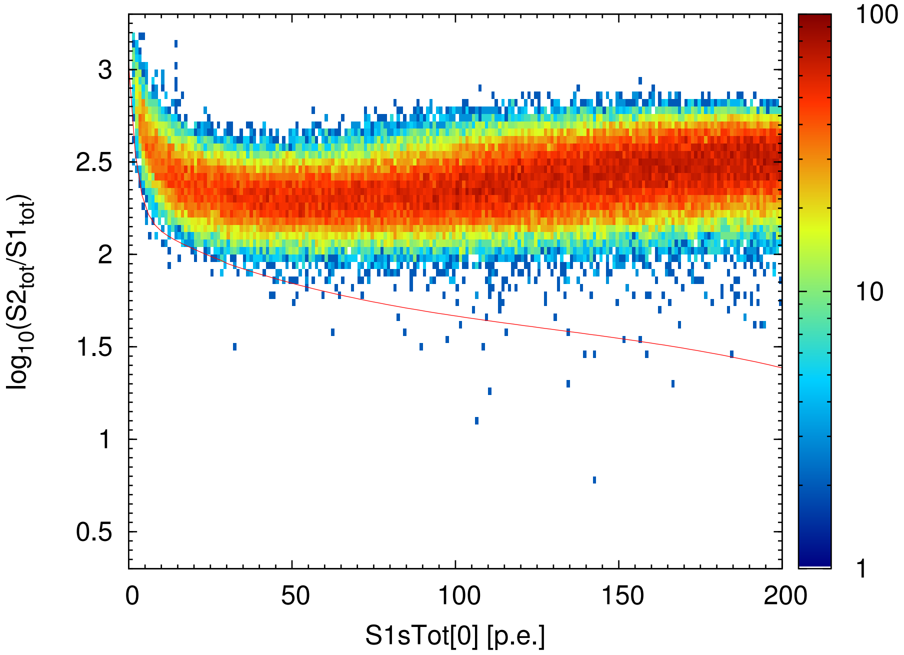

Figure 3.6: Electronic Recoil Band from ^{60}Co Data. Red curve shows the median of nuclear recoil band.

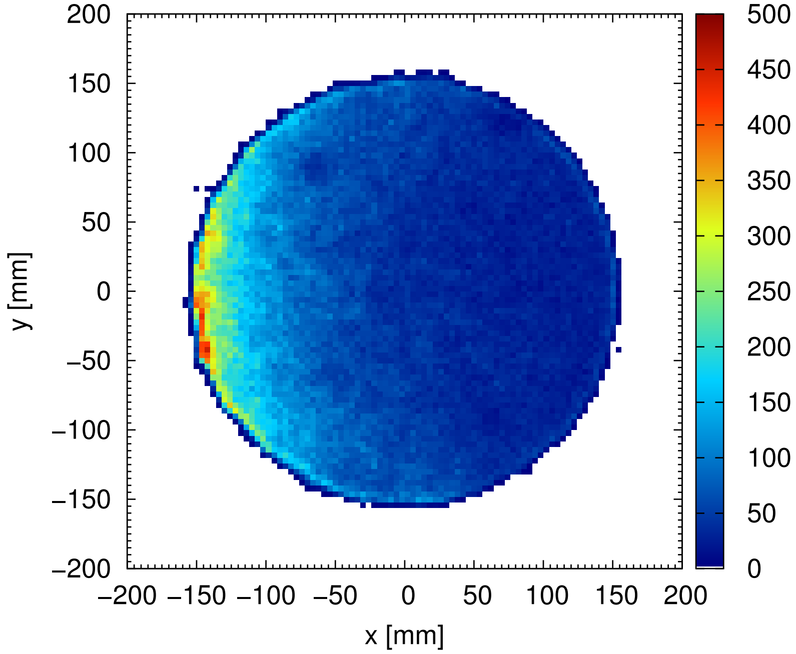

Figure 3.7: Nuclear Recoil Event Distribution from ^{241}AmBe Data.

The nuclear recoil band, as shown in Fig. 3.8, has a feature that, in addition to the main band, there are islands at higher $\log(S2/S1)$ values. Those islands are the results from fast neutron activation of xenon (Ni et al. [41]). Specifically the two islands shown in Fig. 3.8 correspond to 40 keV and 80 keV inelastic nuclear excitation lines. These two lines are well above the WIMP search region therefore are not of any concern to WIMP signal expectation. However, these lines provide additional calibration opportunities for light and charge yield in liquid xenon since they have specific line energies and their energies are close to WIMP search energies.

There is no detailed theory that can describe the nuclear recoil and electronic recoil band shape at the moment. Therefore we have to take the nuclear recoil and electronic recoil data as is, and rely on data to determine the discrimination power between electronic recoil and nuclear recoil interactions. More importantly, we use neutron calibration data as WIMP signal expectation.

Summary

The detector response to energy deposition is calibrated using various sources. Light ($S1$) and charge ($S2$) responses are corrected for their spatial dependence so that the whole detector responds uniformly regardless of the position of interaction. The energy scale is determined using $S1$ only and relies on external measurements of $\mathcal{L}_{\text{eff}}$. Gamma from ^{60}Co and neutron from ^{241}AmBe are used to calibrate electronic recoil and nuclear recoil responses, respectively. Discrimination is established from such calibrations.

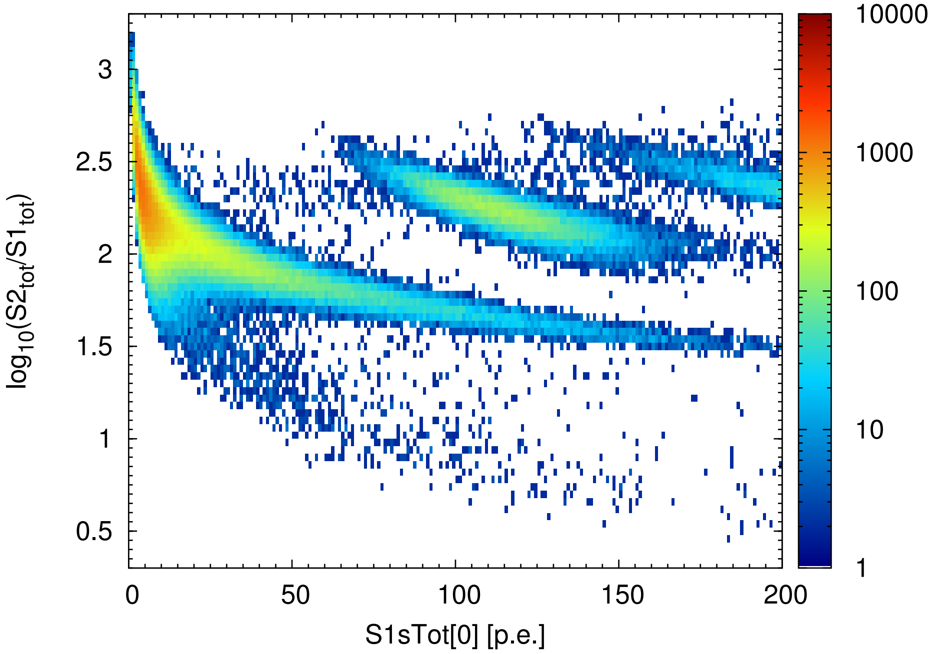

Figure 3.8: Nuclear Recoil Band from ^{241}AmBe Data.

Chapter 4

Position Reconstruction and Correction

A great advantage of the dual-phase LXeTPC is that the information of 3D position of interaction could be recovered from the PMT hit pattern and the electron drift time to a precision of mm. Because of the excellent stopping power of liquid xenon for electromagnetic (EM) radiation, EM background cannot penetrate deep into the center of the xenon volume. In order to take advantage of the xenon stopping power to realize a low electromagnetic radiation background environment in the central part of the sensitive xenon volume, good 3D position information of each interaction is required. Also, good 3D position information is needed for the precise determination of target volume and mass for Dark Matter detection.

When a particle interaction happens at position (x, y, z) in the detector, scintillation light *S1* and charge (free electrons) are produced simultaneously at the same position (x, y, z). The 3D interaction position (x, y, z) is to be reconstructed from spatial and temporal information of each event recorded in the data.

If the electric field inside of the TPC were uniform, electrons would drift straight up so that *S2* would have exactly the same (x, y) position as the primary interaction *S1*. *S2* happens right above the liquid gas interface and is close to the top PMT array thus has a localized PMT pattern on the top array. The localized PMT pattern allows good position determination. Under these conditions, the position reconstruction procedure can be broken down into two steps. First, the (x, y) position is reconstructed from the *S2* PMT pattern on the top array; second, the z position is reconstructed from the drift time—the time difference between *S1* and *S2* assuming a constant drift velocity.

In reality, the electric field in the TPC is skewed so that the corresponding *S1* and *S2* do not share the same (x, y) position. Due to the cylindrical symmetry, the lateral shift in r between *S1* and *S2* is dependent on drift time (or z) and radius r. Electric field simulations are performed to map the relationship between the lateral shift of *S1* and *S2*, and the (r, z) coordinates. To obtain the true 3D position of interaction, an additional step is required using the simulated electric field to correct the lateral shift between *S1* and *S2*.

4.1 X-Y Position Reconstruction of *S2* Using Least Squares

(x, y) positions are reconstructed from *S2* PMT pattern on the top array. Three algorithms, Neural Network (NN), Support Vector Machine (SVM), and Least Squares (χ^2), have been independently developed for the XENON100 experiment.

Although they differ in details, the basic working principle for all the three algorithms is the same: compare the signal pattern to the *S2* light collection simulation and find the simulated pattern from coordinates (x, y) that fits best with the signal pattern, then (x, y) is the reconstructed position.

The *S2* light collection is simulated with positions either randomly distributed, or on a regular grid, in the x-y plane placed half way between the liquid-gas interface and the anode. Because of the discrete nature of x-y sampling in light collection simulation, an interpolation scheme is needed to achieve position reconstruction resolution better than the x-y sampling. Neural Network and Support Vector Machine methods use the randomly distributed simulation and employs machine learning techniques to train a set of coefficients that maps an input signal to an output (x, y) position according to certain internal model. In this process the interpolation in x-y is achieved implicitly. For Least Squares method, an explicit interpolation scheme is used on regular grid.

Every *S2* signal shows a PMT pattern on the top array. We denote the number of photons collected on PMTi as $N_{\mathrm{ph},i}$ and the pattern on the top array as $\{N_{\mathrm{ph},i} | i = 1 \ldots 98\}$. From the *S2* light collection simulation, the PMT pattern or detector response is obtained and denoted as $\{\nu_{\mathrm{ph},i}(x, y) | i = 1 \ldots 98\}$. The simulation establishes the relation from (x, y) to $\{\nu_{\mathrm{ph},i} | i = 1 \ldots 98\}$ and allows a backward mapping from pattern to the position. A measure T indicating the difference between the signal pattern $\{N_{\mathrm{ph},i} | i = 1 \ldots 98\}$ and the simulated detector response at position $\{\nu_{\mathrm{ph},i}(x, y) | i = 1 \ldots 98\}$ is to be established. When the measure T is minimized, the position (x, y) is determined. In Neural Network and Support Vector Machine methods, the measure T is complicated and implicit. In Least Squares method, T is a modified version of the sum of square differences between $N_{\mathrm{ph},i}$ and $\nu_{\mathrm{ph},i}(x, y)$ which, when minimized, gives a proper statistical measure χ^2. This is the main advantage of the Least Square method.

In the following, the Least Square method is described.

4.1.1 Simulation of *S2* Light Collection

A Monte Carlo simulation based on GEANT4 with a realistic geometry and light propagation model is performed on the XENON100 geometry with liquid-gas interface exactly half way between the lower mesh and the anode. Meshes are modeled as attenuation discs. Photon starting points are set to be half way between the liquid-gas interface and the anode. The x-y plane is scanned on a 2.5 mm spacing square grid up to the inner bell wall. On each grid point exactly 70 000 photons are emitted with directions random-uniformly distributed in solid angle. Since the top PMT array collects only about 16 % of the total number of photons started, large amounts of starting photons are needed to minimize the statistical fluctuations in the simulated detector response. While fine scanning of the x-y plane is desired to achieve good position reconstruction resolution and to minimize the impact of interpolation, the total number of grid points is limited by the computation time of simulations.

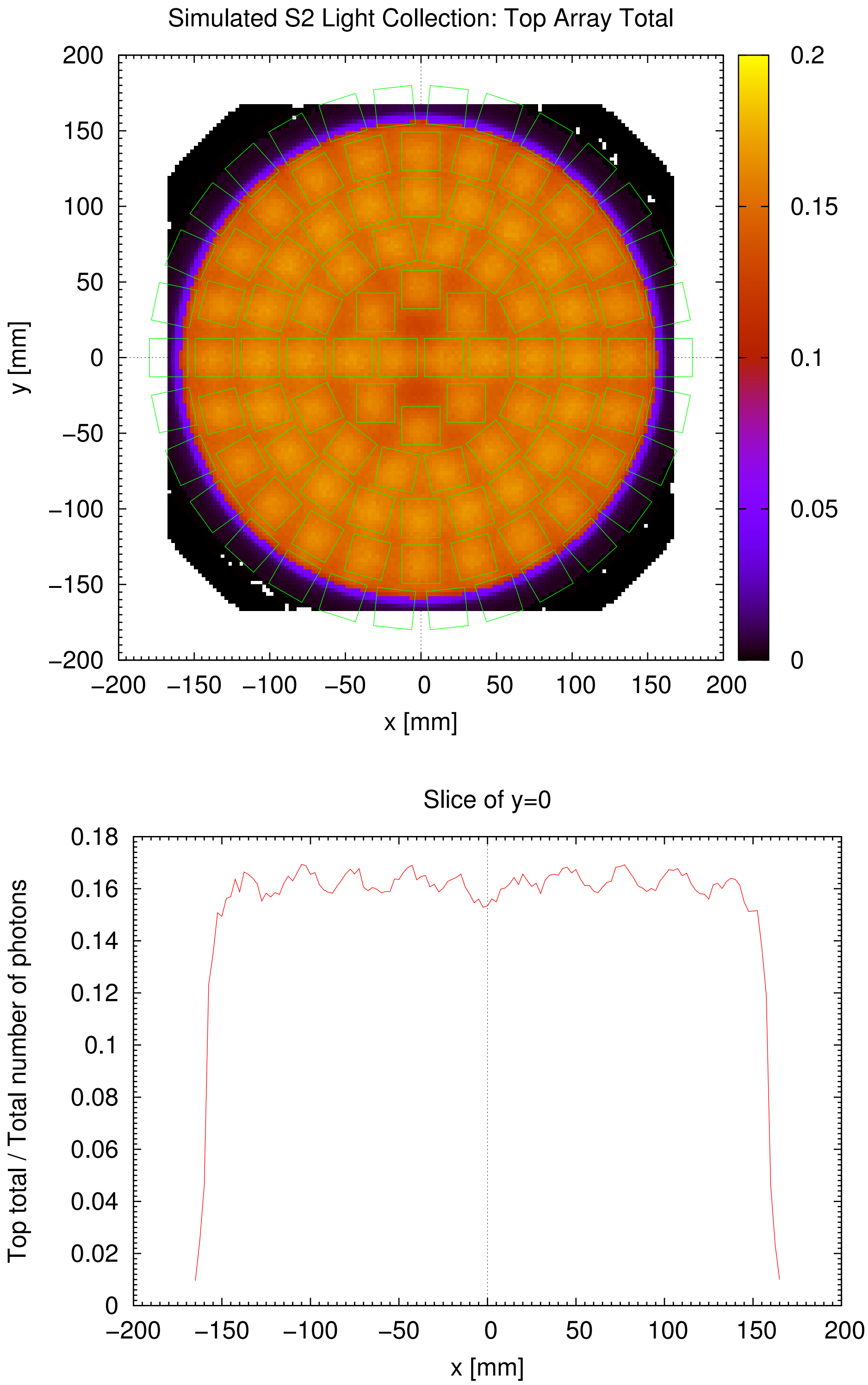

Figure 4.1: Simulated *S2* Light Collection Map: Top Total. Color scale in top plot and y axis in bottom plot show the fraction of photons collected by the top array over the total number of photons started. Green boxes represent the PMT windows.

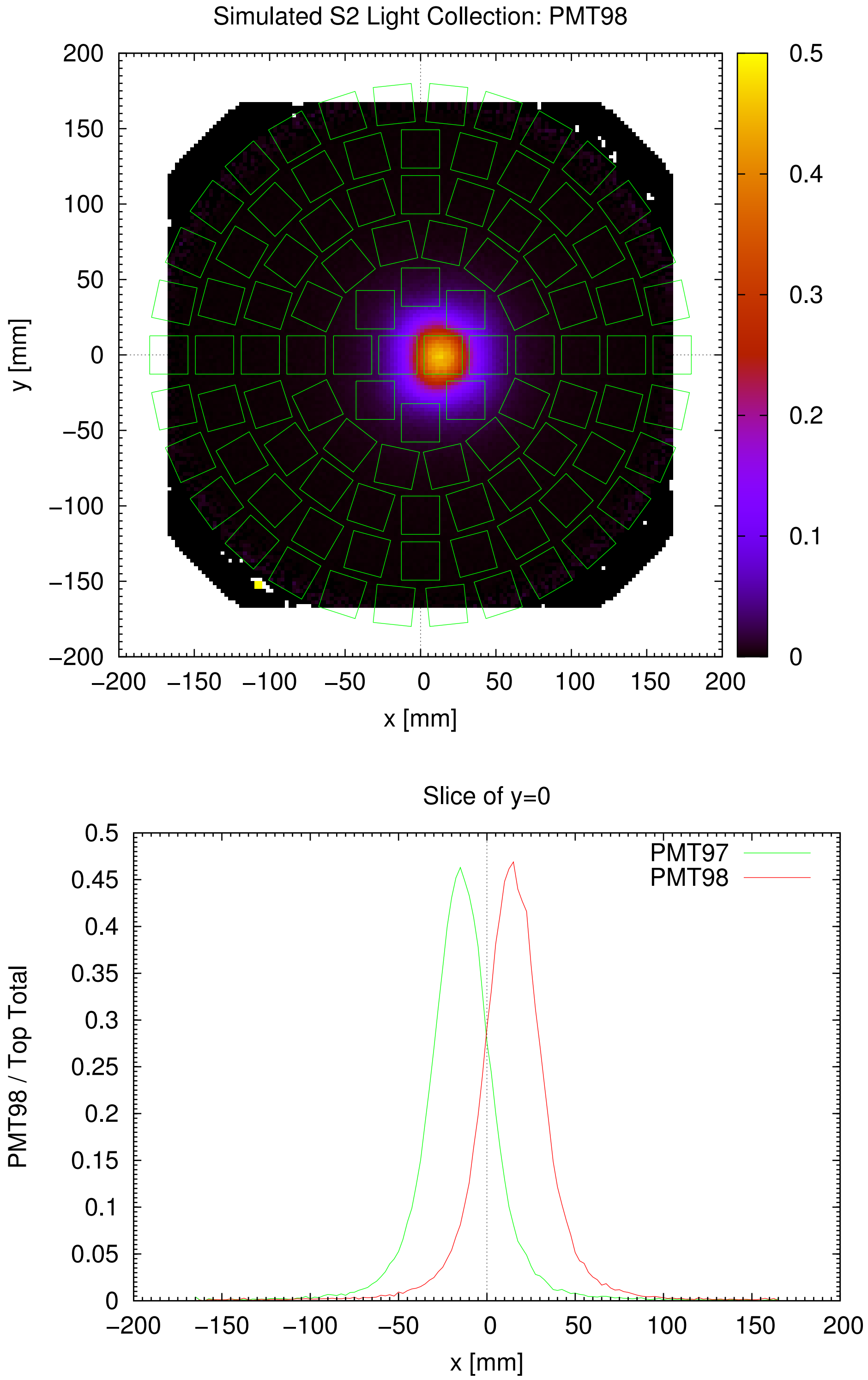

Figure 4.2: Simulated *S2* Light Collection Map: PMT98. Color scale in top plot and y axis in bottom plot show the fraction of photons collected by PMT98 out of the top array total. Green boxes represent the PMT windows. The collection on the adjacent PMT97 is overlaid for comparison.

The simulation results are shown in Fig. 4.1 and Fig. 4.2. In Fig. 4.1, the fraction of photons collected by the top array out of the total number of photons started is shown as a function of (x, y). In Fig. 4.2, the fraction of photons collected by a PMT located close to the center, PMT98, out of the top array total, is plotted as a function of (x, y). Overall, *S2* light collection in terms of top array total is largely uniform across the x-y plane, with slight fluctuation from right under a PMT to in between PMTs. However, the amount of photons in top array total is largely concentrated on one or two PMTs that are close to the light source. For instance, in Fig 4.2, if the light source is right under PMT98 ($x = 15\,\text{mm}, y = 0$), nearly half of the light in the top array is concentrated on PMT98. The reason for this effect is that the *S2* light source—the gap between liquid-gas interface and the anode, is placed close to the top array. The localization of PMT pattern can also be viewed from a representative event in Fig. 4.3. Only a small number of PMTs close to the position of *S2* are illuminated.

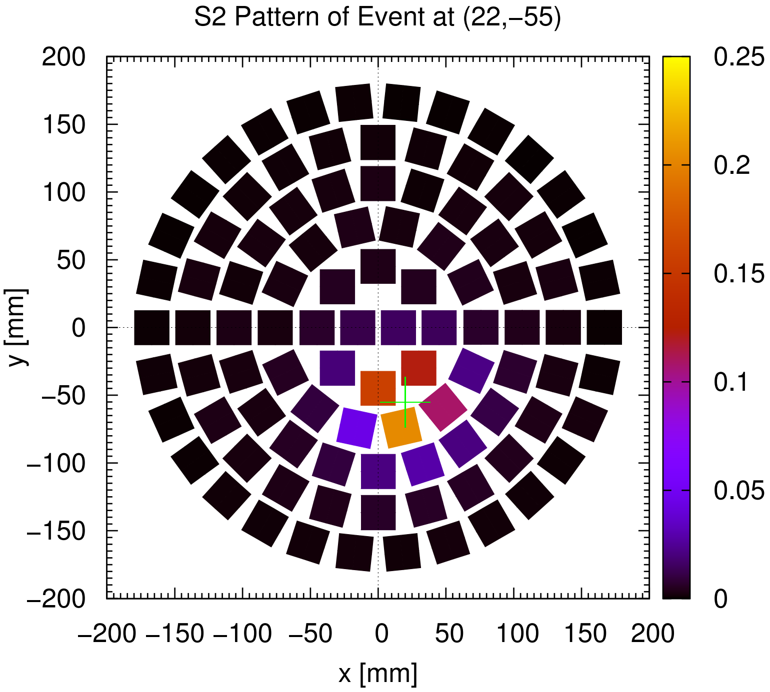

Figure 4.3: A Representative *S2* Pattern (Simulated). Color scale shows the fraction of photons arrive at each PMT out of the top array total. Green cross marker indicates the position of the *S2*.

A localized PMT pattern is needed to achieve a good position resolution, however, the concentrated light collected on a single PMT would amplify the difference, i.e. Quantum Efficiency, between PMTs resulting in poor *S2* energy resolution. Also the uncertainty in *S2* x-y position reconstruction is dependent on PMT array arrangement and light source placement. The exact placement of the *S2* generating area relative to the top array has to be optimized.

4.1.2 Position Reconstruction Procedure

Modified Formula for Least-Squares at Low Counts

For simulated *S2* light response $\{\nu_{\mathrm{ph},i}(x,y)|i=1\ldots 98\}$, the normalized probability for PMT$_i$ to receive photon out of the top array total can be written as

$$p_i(x,y)=\frac{\nu_{\mathrm{ph},i}(x,y)}{\sum_{i'=1}^{98}\nu_{\mathrm{ph},i'}(x,y)}\,. \tag{4.1}$$

For a given real event, the directly measured quantity on each PMT is the number of photo-electrons $\{N_{\mathrm{pe},i}|i=1\ldots 98\}$. Then the number of photons arrived at each PMT is estimated as

$$n_i=\frac{N_{\mathrm{pe},i}}{QE_i} \tag{4.2}$$

where QE_i is the Quantum Efficiency of PMT$_i$. For normalization, the top array total is computed as $N_{\mathrm{ph}}^{\mathrm{top}}=\sum_{i'=1}^{98}n_i$. The test statistic can be written as

$$T(x,y)=\sum_{i=1}^{98}\frac{\Big[n_i+\min(n_i,1)-N_{\mathrm{ph}}^{\mathrm{top}}p_i(x,y)\Big]^2}{\sigma_i^2} \tag{4.3}$$

where

$$\sigma_i^2=n_i^2\left[\left(\frac{\sigma_{QE,i}^2}{QE_i^2}\right)^2+\left(\frac{\sigma_{gain,i}}{gain_i}\right)^2\right]+N_{\mathrm{ph}}^{\mathrm{top}}p_i(x,y)+1.0 \tag{4.4}$$

is the deviation of n_i combining uncertainties from Quantum Efficiency, PMT amplification (gain) and Poison fluctuation. Equations (4.3) and (4.4) is the modified version of Neyman's or Pearson's χ^2 statistic according to Mighell [38]. The advantage of the modified test statistic is that it recovers the true mean when the distribution is close to the Poisson distribution. The use of the modified χ^2 statistic is vital in reconstructing XENON100 *S2* because most of PMTs are having low counts therefore the distribution cannot be approximated by Gaussian but has to be modeled by Poisson statistics.

The uncertainty of PMT gain is estimated from PMT calibration using LED pulses. *QE* values and the uncertainty of *QE* was initially estimated from the correlation between measured *QE* and Skb values provided by PMT manufacturer Hamamatsu [28]. Surprisingly the inclusion of *QE* and *QE* uncertainty resulted in unusually high χ^2 values while setting all the PMTs to the same *QE* value with zero uncertainty yielded reasonable χ^2. It is suspected that the *QE* and Skb relation was not well established from the data provided by the manufacturer and it is more preferable to assume a uniform *QE* for all the PMTs in the top array without uncertainty.

When PMT$_i$ is broken, the corresponding n_i and $\nu_{\mathrm{ph},i}$ are both set to zero and $N_{\mathrm{ph}}^{\mathrm{top}}$ is recomputed to ensure proper normalization. Since this step is done on event by event basis, the Least Squares algorithm can handle PMT addition or breakage without any modification to the code or configuration. The same procedure is also applied to handle PMT saturation. Under normal XENON100 operation conditions, individual PMT response starts to behave non-linearly above about 6000 photo-electrons, where the output of PMT becomes lower than that is expected by linearly extrapolating from low photo-electron counts. This behavior is referred to as PMT saturation. If saturated PMTs were treated as normal PMTs in the position reconstruction procedure, the reconstructed positions would be systematic biased to move away from saturated PMTs. Since there is no prior knowledge of the PMT behavior at the non-linear regime, saturated PMTs are treated as dead PMTs and removed from reconstruction on an event to event basis.

Interpolation Between Simulated Grid Points

For a given event with *S2* pattern $\{N_{\mathrm{pe},i} | i = 1 \ldots 98\}$, the test statistic $T(x, y)$ can be directly computed on simulated grid points. In between simulated grid points, bi-cubic interpolation (Press et al. [45]) is performed to enforce a smooth 2D function $T(x, y)$ at any size scale. Across the whole x-y plane, $T(x, y)$ is referred to as the χ^2 landscape. An example of the χ^2 landscape is shown in Fig. 4.4. $T(x, y)$ includes contributions from all of the alive PMTs in the top array including a large fraction of PMTs receiving very low or zero counts. Thanks to the modified test statistic, the χ^2 landscape shows only one global minimum, which is desirable.

Least Squares Minimization

After the computational procedure of the test statistic $T(x, y)$ is determined, the remaining task is to efficiently search for the global minimum on the χ^2 landscape. The Conjugate gradient method (Press et al. [44]) is employed to minimize the function $T(x, y)$ on the x-y plane. The algorithm starts from the PMT photon counts weighted mean (x, y) which places the starting point already close to the true *S2* position, and searches downhill on the χ^2 landscape towards the minimum. The position where $T(x, y)$ reaches the global minimum is the reconstructed position.

Despite the fact that the $T(x, y)$ has only one global minimum (Fig. 4.4), due to the roughness of the χ^2 landscape at small scales, there are many local minima. Conjugated gradient method is a gradient based search algorithm which can be trapped in a local minimum and fails to find the global minimum. Tests show that less than 1 % of the time the algorithm fail to reach the global minimum. However, the position of a local minimum has higher χ^2 value than that of the global minimum, therefore, the bad reconstruction can be identified. Additionally, χ^2 provides a quality measure of the fit for determining the (x, y) position of *S2*. It potentially provides a way to identify anomalous events with abnormal *S2* pattern.

Fig. 4.5 shows the detailed shape of χ^2 landscape close to the minimum. The 68.3 % and 95.45 % confidence level contours are small compared to the simulated grid size 2.5 mm. It indicates that the interpolation dominates the uncertainty expressed as σ of the reconstruction.

4.1.3 Position Reconstruction Performance

The performance of Least Squares position reconstruction algorithm in terms of position uncertainty and χ^2 behavior are tested on both Monte Carlo generated samples and real data with externally measured *S2* positions.

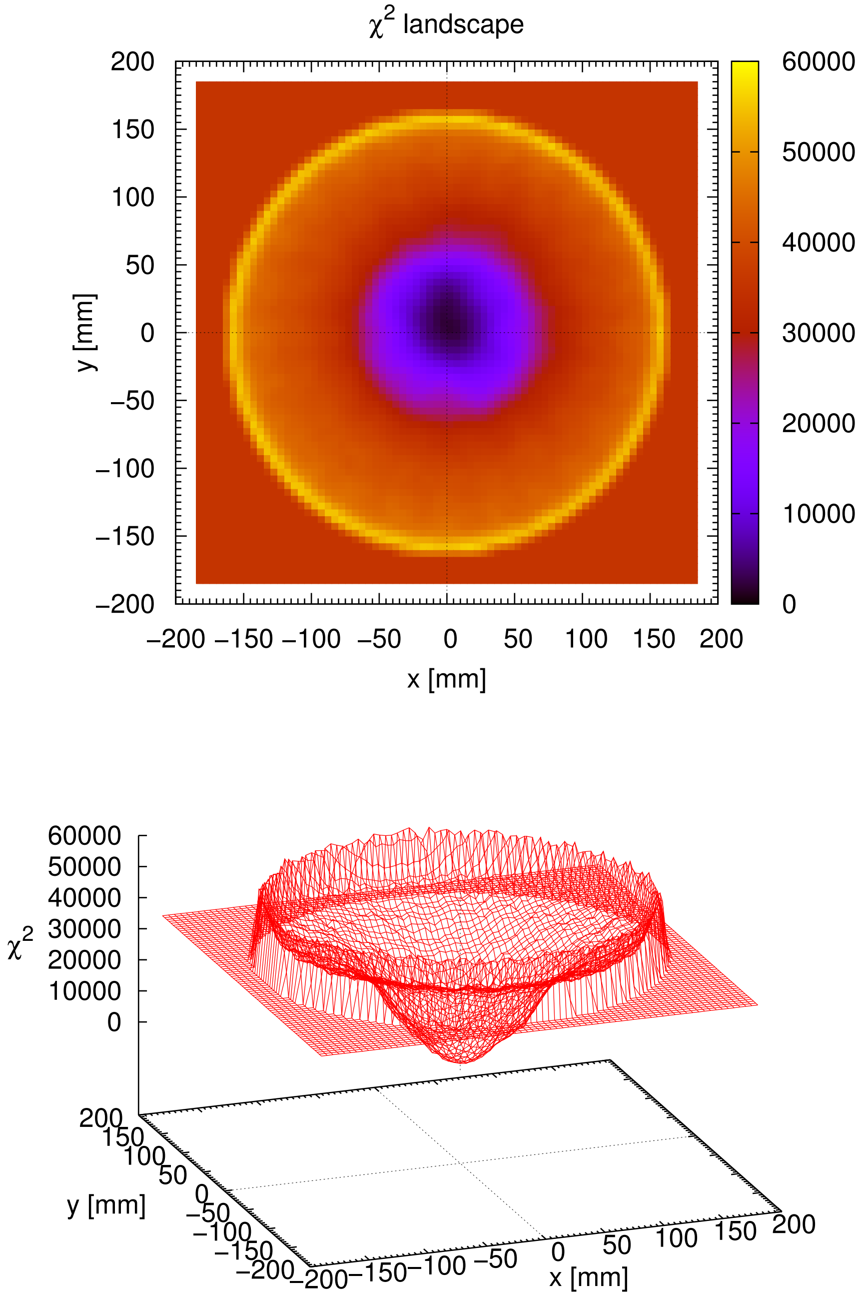

Figure 4.4: χ^2 Landscape. The event from real data is located close to the origin where χ^2 is close to the minimum.

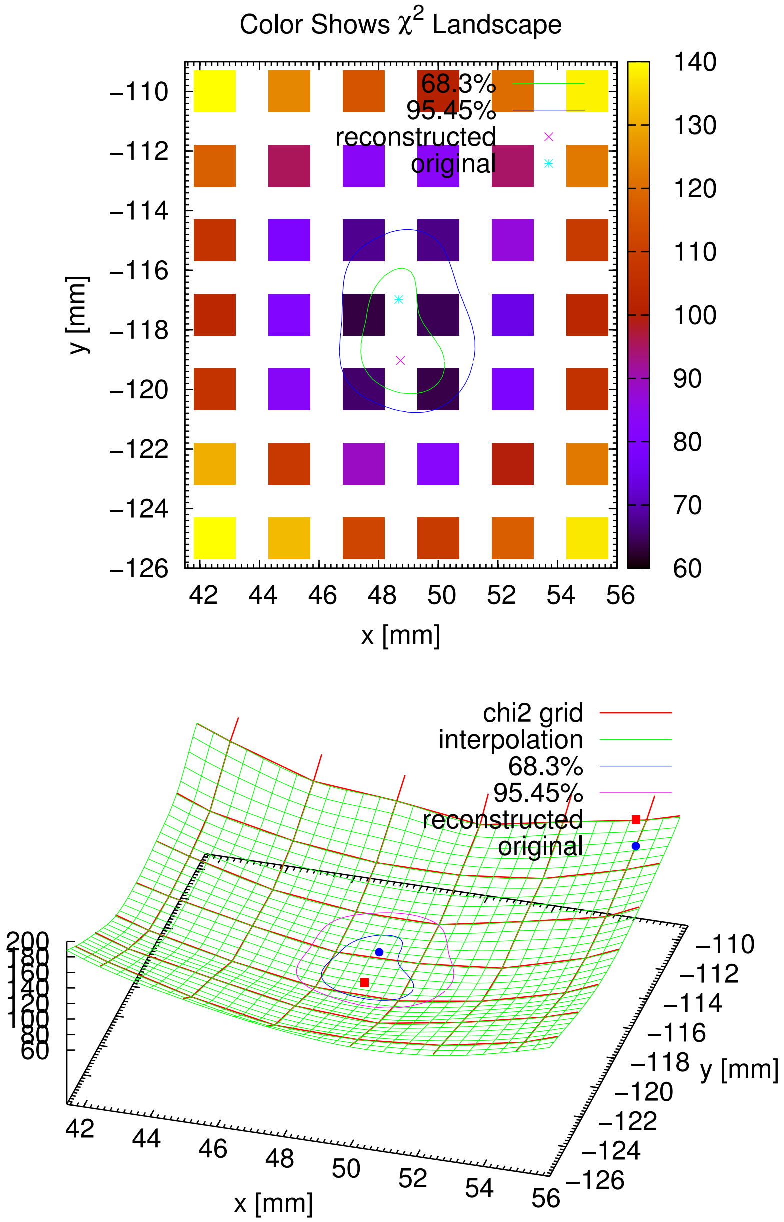

Figure 4.5: χ^2 and Confidence Contour. Top: color block shows χ^2 value at simulated grid points. Bottom: red line shows simulated grid and green line shows the interpolation. From the minimum, χ^2 increases by 2.3 gives the 68.3 % contour; increases by 6.18 gives the 95.45 % contour.

On Monte Carlo Generated Samples

Monte Carlo simulation is performed to generate a test dataset. Events are random-uniformly distributed in the x-y plane. In each event, 3000 photons are generated, out of which about 480 photons on average reach the top array. The number 3000 is chosen such that it is close to number of photons generated at the real low energy threshold. Since the position reconstruction algorithm produces less fluctuation as the total number of photons increases, using the low-photon-simulation tests the worst behavior of the algorithm. In the real XENON100 detector, PMT9,12,39,58 are dead. In the simulation, the corresponding PMTs are also set to dead in order to test the performance of the algorithm with dead channels. Since it is the simulation and the true position is known, the reconstruction error can be directly computed by measuring the distance between the reconstructed position and the true position. Some samples are shown in Fig. 4.6.

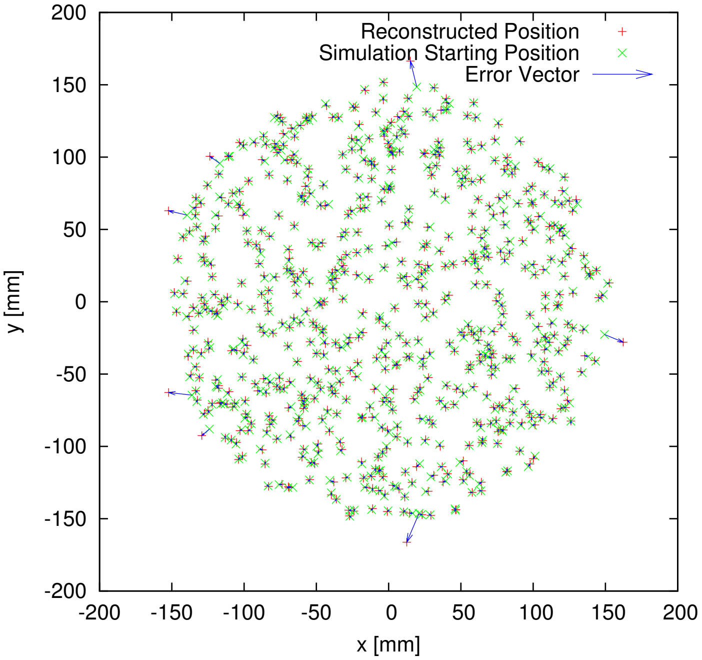

Figure 4.6: Random starting point and reconstruction error. Green marker shows the true position and red marker shows the reconstructed position. Blue arrow points from green marker to the corresponding red marker showing the size and direction of reconstruction error.

As shown in Fig. 4.7, the position reconstruction error overall peaks at about 1.5 mm and extends to about 7 mm in the tail of the distribution. The reconstruction error is also uniform across the x-y plane. At dead PMTs, the reconstruction error increases in areas surrounding the dead PMT windows.

Fig. 4.8 shows that the reconstruction error slightly increases at high r where reconstructed positions are systematically shifted inwards resulting in higher event density inside of the edge of the sensitive volume. This systematic behavior is due to insufficient sampling of detector response at the edge. Close to the edge, the detector response changes drastically with r. A grid of 2.5 mm

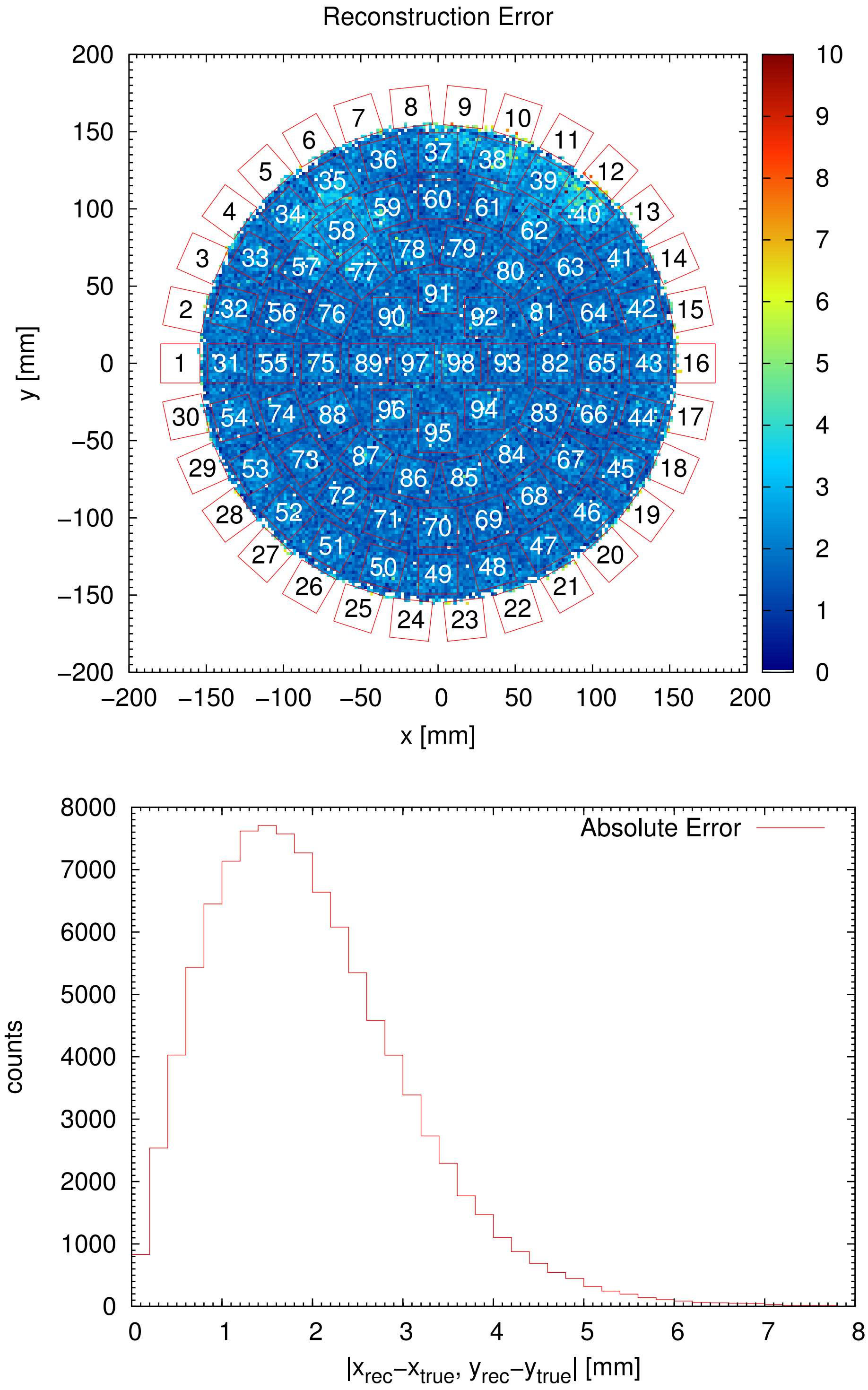

Figure 4.7: Position Reconstruction Error on Monte Carlo Generated Samples. Color scale in the top plot shows the absolute error in mm. The bottom plot shows the absolute reconstruction error of all events random-uniformly distributed in the detector. PMT9,12,39,58 are dead in the real detector and are simulated as dead as well.

could account for the detector response in the bulk well but fails to capture the steep change at the edge. The algorithm relies on the interpolation between grid points across the edge which pushes the χ^2 minimum towards the center of the detector, hence the bias. This effect vanishes at 5 mm away from the edge and does not contribute to the main physics analysis which uses a tighter r selection.

There are 98 PMTs in the top array, of which 4 are dead. Combining with the fact that the model is normalized to the top total of the signal and there are two fitting parameters (x, y), the Number of Degrees of Freedom (NDF) should be $98 - 4 - 2 - 1 = 91$. However, as shown in Fig. 4.9 (top), the χ^2 is better represented by a χ^2 p.d.f with NDF= 79. The loss of NDF is due to the localization of top PMT pattern. In the test statistic $T(x, y)$, PMTs with both signal and model of absolute zero counts doesn't contribute to the χ^2 at all. It also explains the behavior that χ^2 drops as r gets higher to the edge of the detector. At high r, smaller number of PMTs are involved than that at the center of the detector, therefore, the effective NDF decreases, as shown in Fig. 4.9 (bottom).

From the performance test on Monte Carlo generated samples, the Least Squares position reconstruction algorithm shows reasonable resolution of a mean error of 2 mm with photon counts close to that of the lower energy threshold. The algorithm successfully reconstructs events with broken PMTs at the cost of only slightly higher reconstruction error. The algorithm also produces the χ^2 measure of goodness-of-fit with a well understood behavior.

On Collimated 122 keV gamma-ray Data

Since the algorithm compares the signal to the simulated model, using simulated random-uniformly distributed events to test the algorithm only serves as the self-consistency check. The simulation model could differ from the real detector response. To quantify the systematic error of the algorithm, real data with known *S2* positions is needed. Data with a ^{57}Co source placed at the end of a collimator was taken during the time when no liquid xenon was covering the top of the Bell. The 122 keV gamma-ray exiting the collimator is traveling downwards and arrives directly at the top layer of the liquid xenon just below the anode. The collimator was placed along a diameter at 6 different locations. The exact locations are measured and the placement uncertainty of the collimated beam spot at the xenon liquid-gas interface is about 3 mm. Fig. 4.10 shows the collimator construction and the 6 spots where data were taken. As can be seen in the photo, the space on top of the detector is quite limited so that measurements were only made at a handful of positions.

The peak in each of the 6 data sets corresponding to the 122 keV gamma-ray is selected and fitted with a Gaussian to determine its mean location and spread in both radius and angle θ. Fig. 4.11 (top) shows an example. The spread (σ) of each peak is at the level of 2 mm and as shown in Fig. 4.11 (bottom) the reconstructed radius and the preset radius of the collimator agree well. Also, it is verified in Fig. 4.12 that all the 6 points agree to have the same angle so that they are reconstructed to be on the same line in the x-y plane.

The result of the collimator test verifies that the position reconstruction algorithm works well on real data and the systematic uncertainty is below $2 \sim 3$ mm.

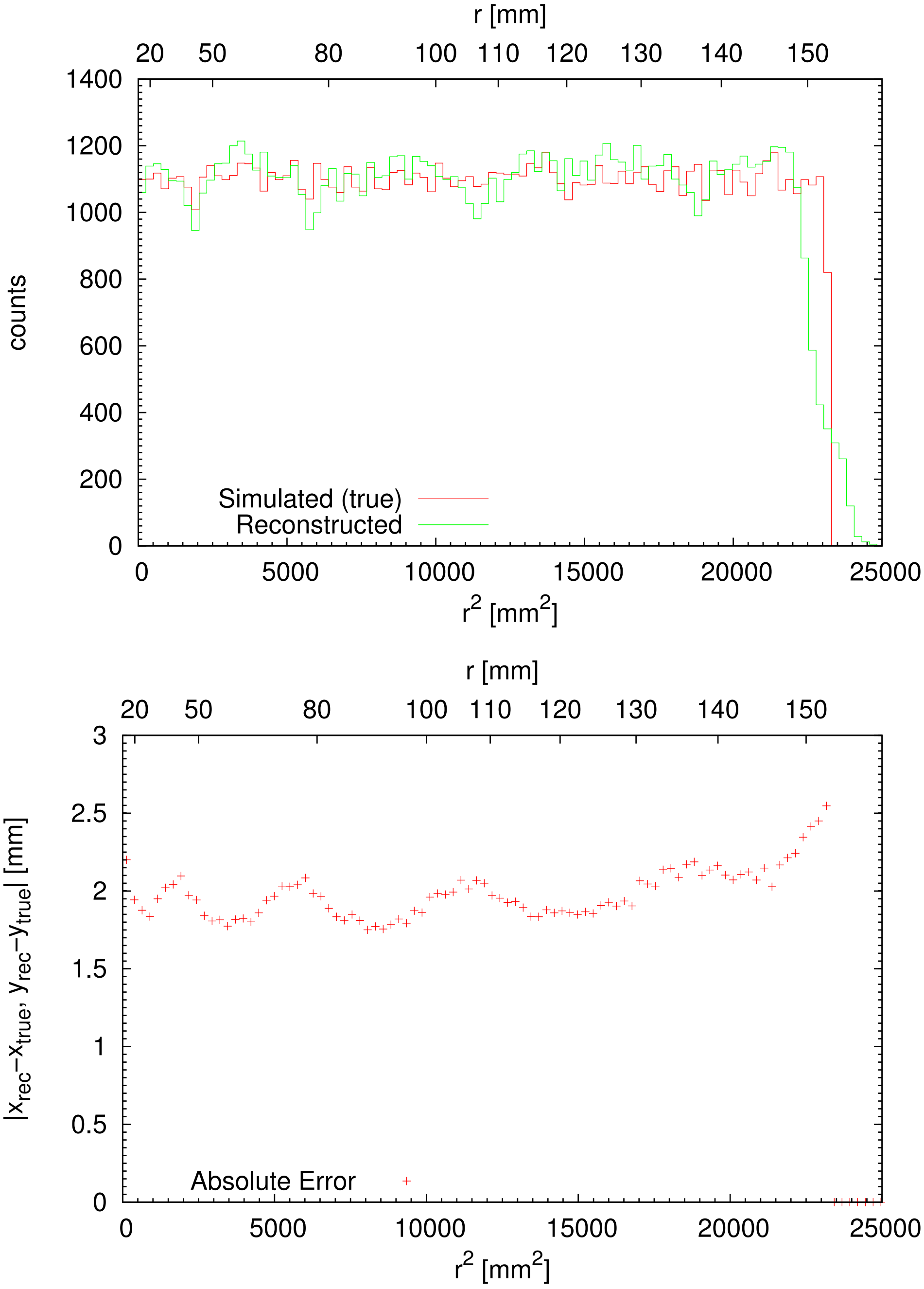

Figure 4.8: Position Reconstruction on MC: Radial Distribution and Error. Top: r^2 spectrum of true and reconstructed positions. Bottom: absolute error in position reconstruction as a function of r. Plots are binned in r^2 to achieve a constant number of events in each bin.

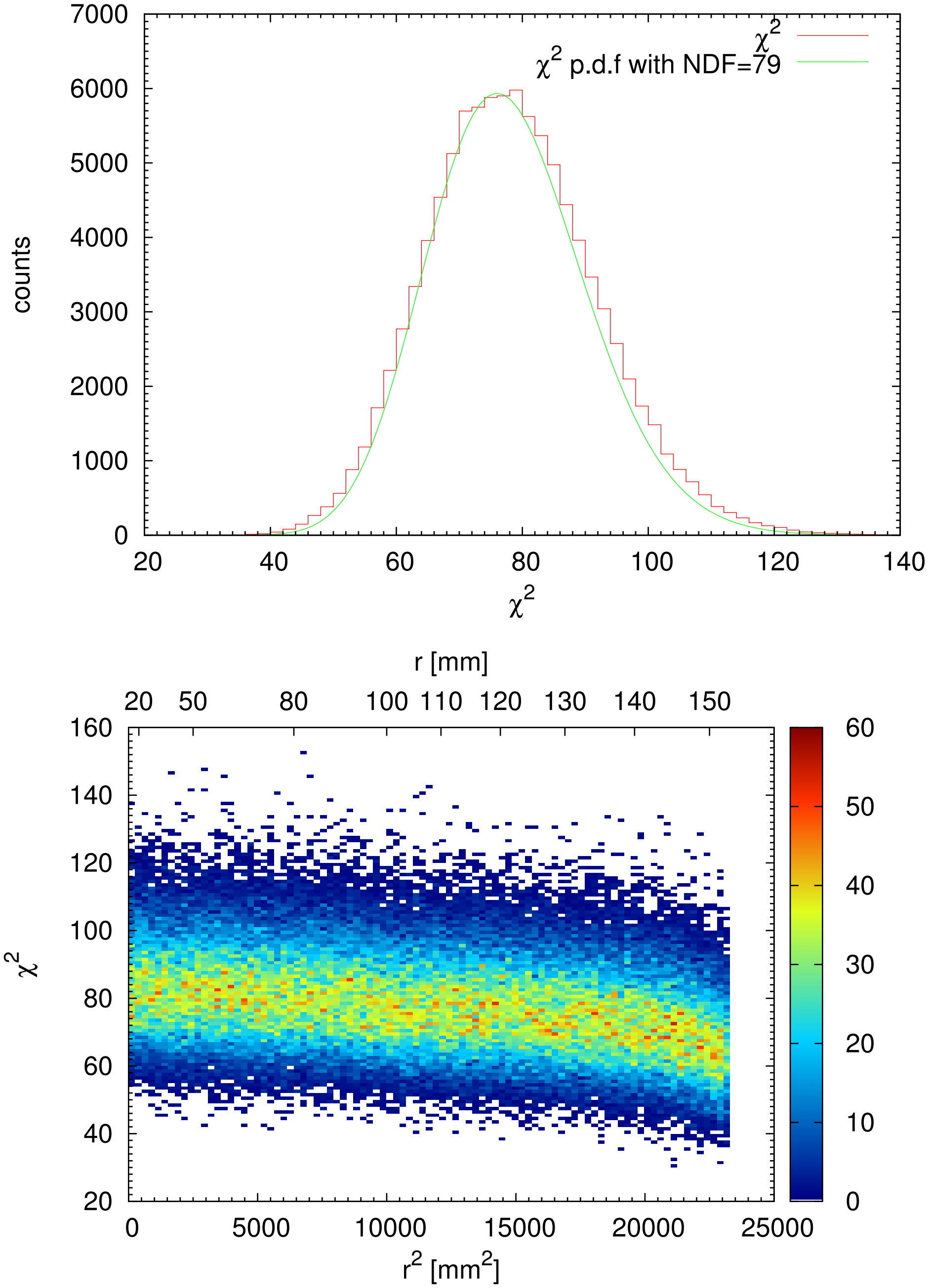

Figure 4.9: Position Reconstruction on MC: χ^2. Top: χ^2 distribution of all events random-uniformly distributed in the detector. Bottom: χ^2 distribution as a function of radius.

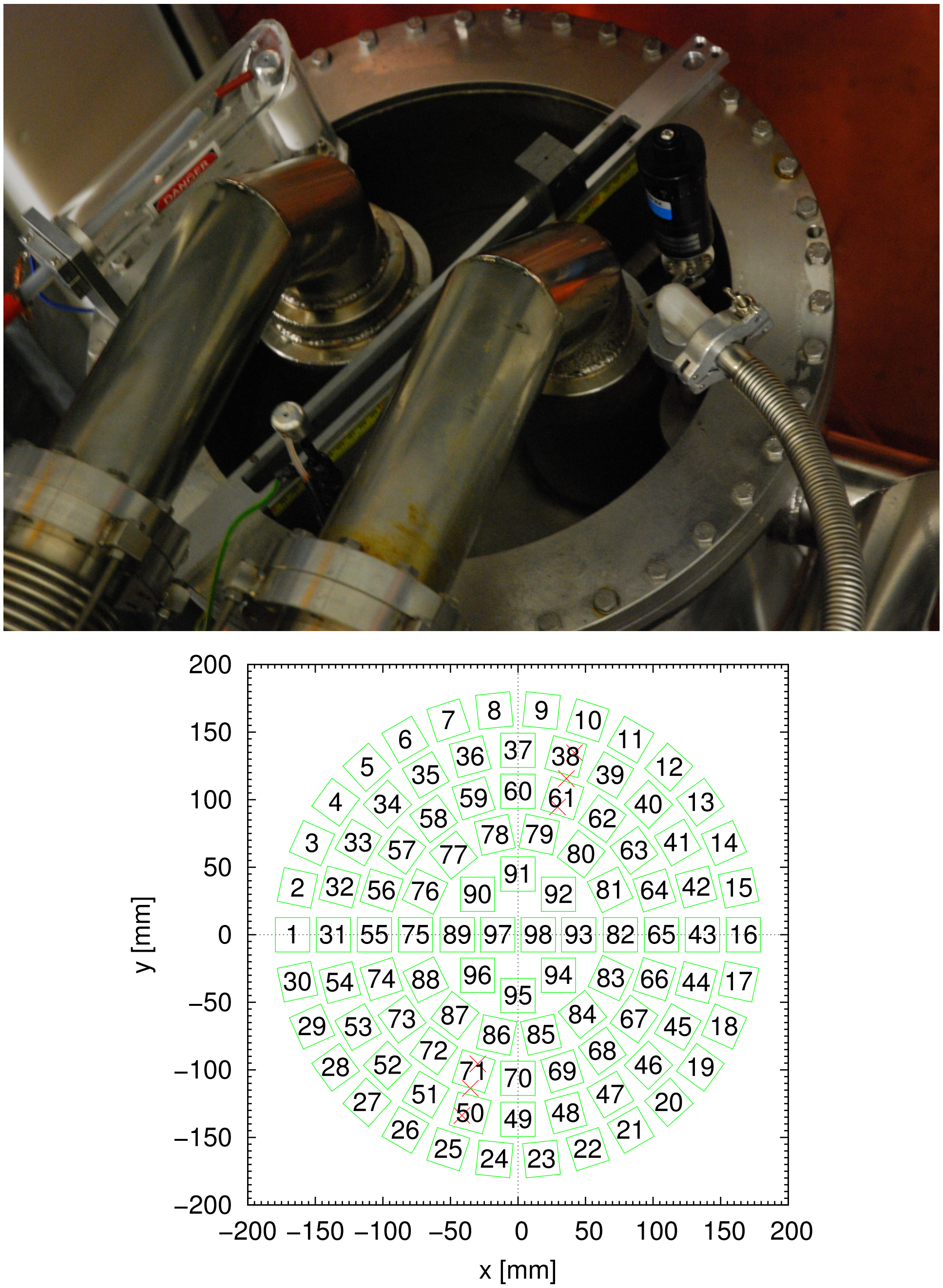

Figure 4.10: Position Reconstruction on Collimated Data: The Collimator. The collimator is made of a long lead brick with a through-hole of small diameter along the long axis. The long axis is aligned vertically that is perpendicular to the xenon liquid-gas interface. The collimator is allowed to slide along a rail to be placed at different radii. The source is placed at the top end of the through-hole. The bottom plot shows the placement of beam spots (red cross) hence the *S2* positions.

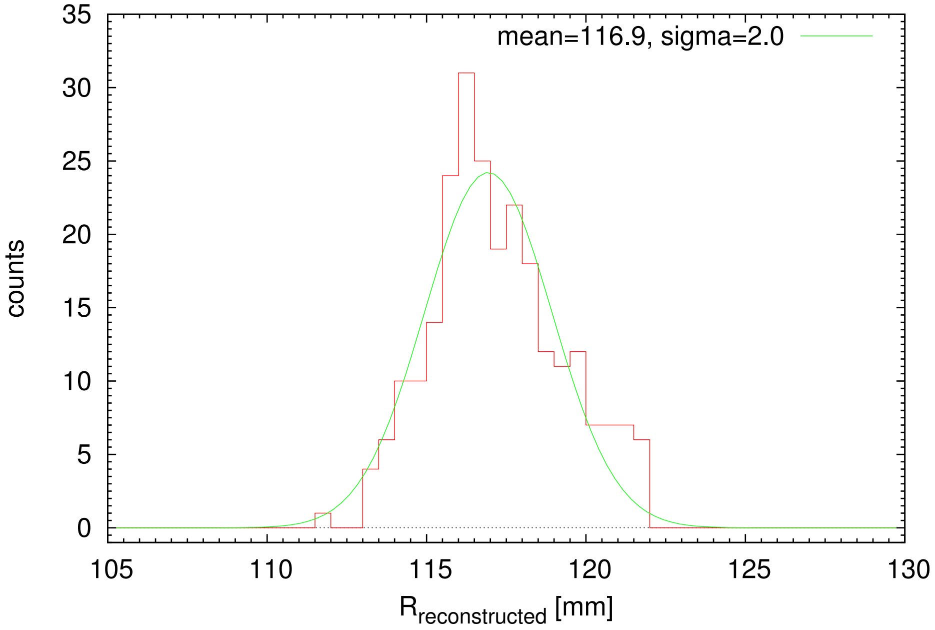

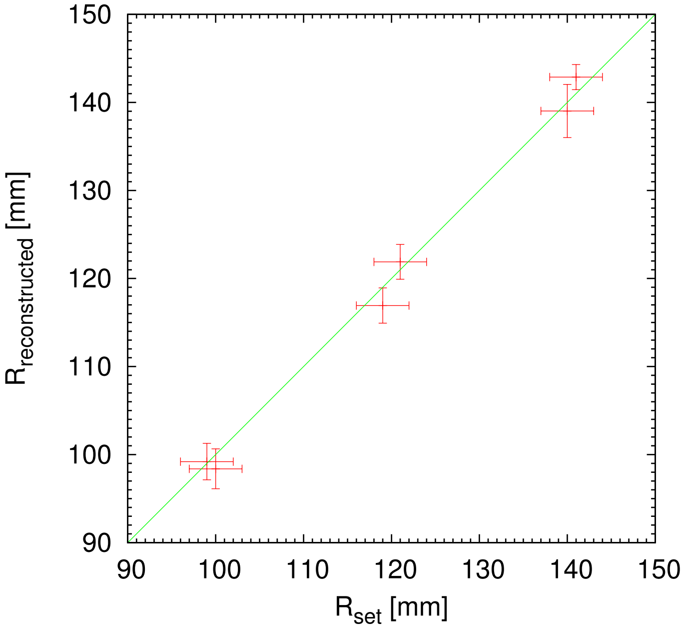

Figure 4.11: Position Reconstruction on Collimated Data: Radius. Top: radial distribution of one gamma-ray spot and the Gaussian fit. Bottom: the correlation between reconstructed and preset radial positions.

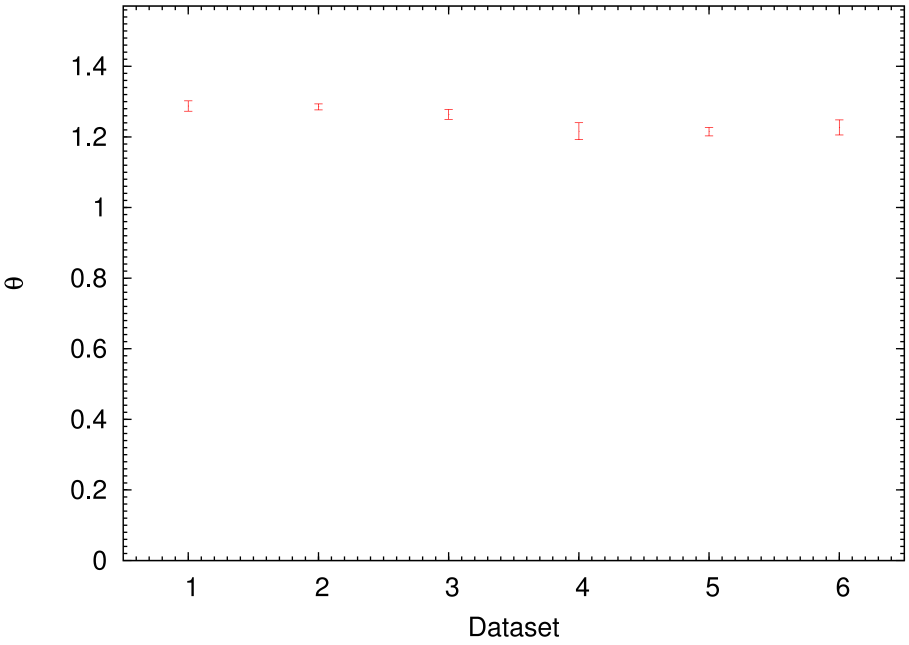

Figure 4.12: Position Reconstruction on Collimated Data: Angle. The definition of angle is $\tan\theta = y/x$. Since the 6 points are set to be on the same line, all of them are expected to have the same θ.

4.1.4 The Effect of Simulated Grid Size

5 mm simulated grid points are proven to be too coarse, especially at the edge of the TPC, to capture the proper response of PMTs on *S2* signal. A portion of events that are close to the edge of the TPC are reconstructed nonphysically outside of the TPC. 2.5 mm simulated grid points significantly improved the situation compare to the 5 mm grid points.

Since the light collection simulation of *S2* is expensive in time, one alternative way of achieving a finer grid is to interpolate the PMT response in between simulated points, knowing that the PMT response should be smooth and slow-varying in short distance (< 2.5 mm). Following this line, a 0.5 mm grid was generated by bi-linearly interpolating a 2.5 mm simulated grid. When tested on MC datasets, there is no obvious difference of using 0.5 mm or 2.5 mm grid. It indicates that the χ^2 landscape is smooth on MC datasets thus the interpolation on PMT response or on χ^2 yield similar results. While tested on real data, using 0.5 mm and 2.5 mm grid both show clustering tendency on simulated grid lines but at different scale (0.5 mm and 2.5 mm respectively). It indicates that the χ^2 landscape is rough and oscillatory on real data therefore the interpolation on χ^2 yields local minima that are close to the grid points, hence the clustering effect.

4.2 Optimization of Geometry for X-Y Position Resolution

This section describes a simple 2-dimensional model of a point light source placed at distance h away from three 1D "PMTs". The multinomial nature of photon counting statistics is incorporated to account for the fluctuation of number of photons detected on each PMT . A semi-analytical least squares algorithm is used to reconstruct the lateral position of the point source in this very ideal case. The dependence of reconstruction uncertainty on the relative position between the light source and the PMTs is presented.

The main goal of this study is to reveal the theoretical limit of accuracy in position reconstruction for a given PMT—light source arrangement. The setup is motivated by the following constraints:

1. The model should be perfectly known: a 2D model with three 1D "PMTs" is constructed and the model is analytical and relatively simple.

2. No interpolation should be used on either PMT response or χ^2: the analytical model doesn't need interpolation, and the χ^2 is analytical as well and its minimization with only one parameter is relatively easy.

3. Photon counting statistics should be taken into account: multinomial distribution is implemented instead of running a photon tracing simulation.

4.2.1 Setup

To minimize the number of free parameters, but not to lose the generality, three 1D "PMTs" of the same size (length) l are placed symmetrically on the x-axis. They are from $-a-l \leq x \leq -a$, $-l/2 \leq x \leq l/2$ and $a \leq x \leq a+l$. A point light source is placed at distance h above the three PMTs. The point source is allowed to move horizontally while h is fixed (Fig. 4.13). Its horizontal position x is to be reconstructed from the number of photons collected on the three PMTs.

Assuming photons come out of the point source uniformly in solid angle, the fraction of photons arriving at each PMT is proportional to the angles $\theta_{0,1,2}$:

$$\begin{aligned}
\theta_0(x) &= \arctan\left(\frac{x+\frac{l}{2}}{h}\right) - \arctan\left(\frac{x-\frac{l}{2}}{h}\right)\\
\theta_1(x) &= \arctan\left(\frac{a+l-x}{h}\right) - \arctan\left(\frac{a-x}{h}\right)\\
\theta_2(x) &= \arctan\left(\frac{a+l+x}{h}\right) - \arctan\left(\frac{a+x}{h}\right) .
\end{aligned} \tag{4.5}$$

The mean fraction of photons arriving at each PMT out of the total number of photons emitted from the point source is

$$\mu_{0,1,2}(x) = \frac{\theta_{0,1,2}(x)}{2\pi} . \tag{4.6}$$

A sample of μ's is shown in Fig. 4.14.

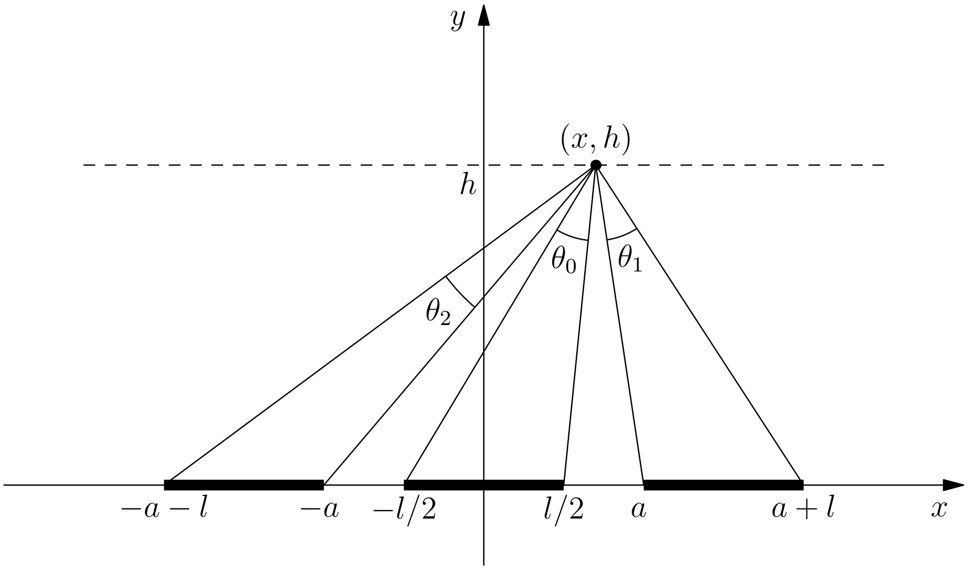

Figure 4.13: 1D Position Reconstruction Model Setup. Three 1D "PMTs" of equal size (length) l are placed symmetrically on the x-axis. A point source located at coordinate (x, h) is allowed to move horizontally along the dashed line. The distance h is fixed in advance. The position of the point source x is to be reconstructed.

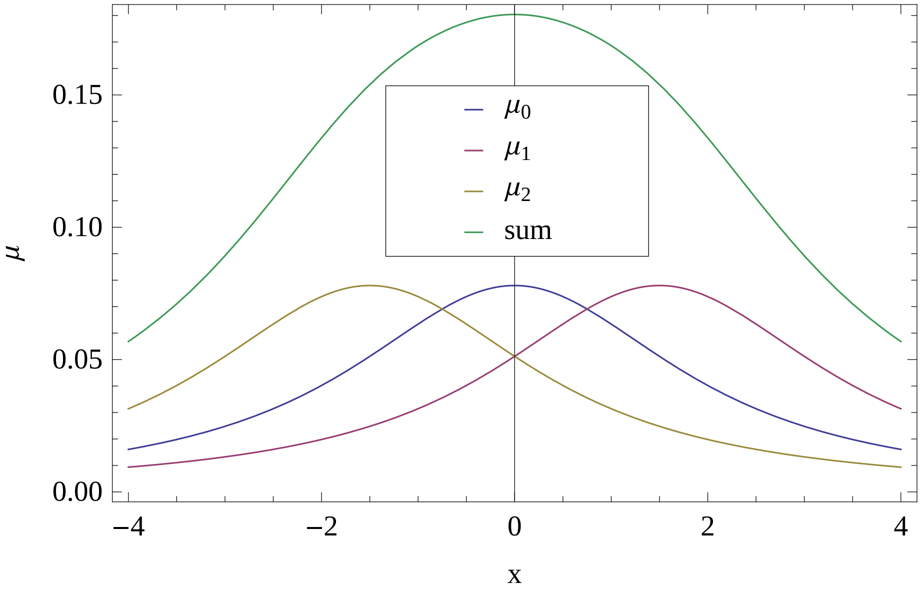

Figure 4.14: Light Distribution in 1D Model. $\mu_{0,1,2}$ and the sum of the three as a function of x. Here $a = 1, l = 1, h = 2$.

4.2.2 Number of Photons on PMTs

For each event, n photons are emitted from the point source uniformly in solid angle into space. $n_{0,1,2}$ photons arrive at each PMT respectively. The probability density of $n_{0,1,2}$ out of n photons arrive at each respective PMT is

$$f(n_0, n_1, n_2; n) = \frac{n!}{n_0! n_1! n_2! (n - n_0 - n_1 - n_2)!} \mu_0^{n_0} \mu_1^{n_1} \mu_2^{n_2} (1 - \mu_0 - \mu_1 - \mu_2)^{n - n_0 - n_1 - n_2} \, . \tag{4.7}$$

A tuple of random integer numbers $n_{0,1,2}$ is drawn from such distribution to simulate one event.

4.2.3 Least Squares Reconstruction

If the total number of photons emitted from the source is n, and the number of photons detected at each PMT is $n_{0,1,2}$, the Pearson's χ^2 test statistic could be written as

$$\chi^2(x) = \sum_{i=0}^{2} \frac{(n_i - n\mu_i(x))^2}{n\mu_i(x)} \, . \tag{4.8}$$

$\chi^2(x)$ is minimized in Mathematica® in a semi-analytical fashion to eliminate the discretization error introduced by normal numerical minimization algorithms. Moreover, there is no interpolation performed here since the "model" is analytical.

4.2.4 Results

For simplicity, the parameters are set to be $a = 1, l = 1$ and $n = 1000$. At each (x, h) starting point, 1000 events are examined. The mean and standard deviation of reconstructed x are recorded.

As shown in Fig. 4.15, for most of the x-h space with the exception of the lower left and lower right corners, the overall reconstruction error in terms of $|\text{mean}(x_{\text{rec}}) - x_{\text{true}}|$ is small and acceptable.

The main focus of this study is the standard deviation x_{sd} of reconstruction shown in Fig. 4.15C. A few observations can be made. First, the lowest x_{sd} is achieved in between PMTs and close to PMTs ($0.5 < x < 1$). It is the closer the better. Second, in the area where the point source is in front of PMTs ($-0.5 < x < 0.5 \cup 1 < x < 2$), x_{sd} gets a lot worse. In those areas x_{sd} is the lowest at $h \approx 0.4$, and x_{sd} is close to the theoretical reconstruction accuracy limit which is not 0.

Conclusion

Compare to the real situation of position reconstruction in XENON100, the setup in this study is far more "ideal" in the sense as follows: first, there are no PMT gain and QE variations or uncertainties in this study; second, one additional piece of information, the total number of photons emitted from the source, is given in the χ^2, while this information is unknown in XENON100; third, the model in this study is 2D and analytical (perfectly known), while in XENON100 we know there is discrepancy between the 3D Monte Carlo (MC) simulation model and the real situation, and even the MC on MC study is not perfect since the simulation in MC couldn't incorporate infinitely high number of started photons and the model requires interpolation. Therefore, in this "ideal" case

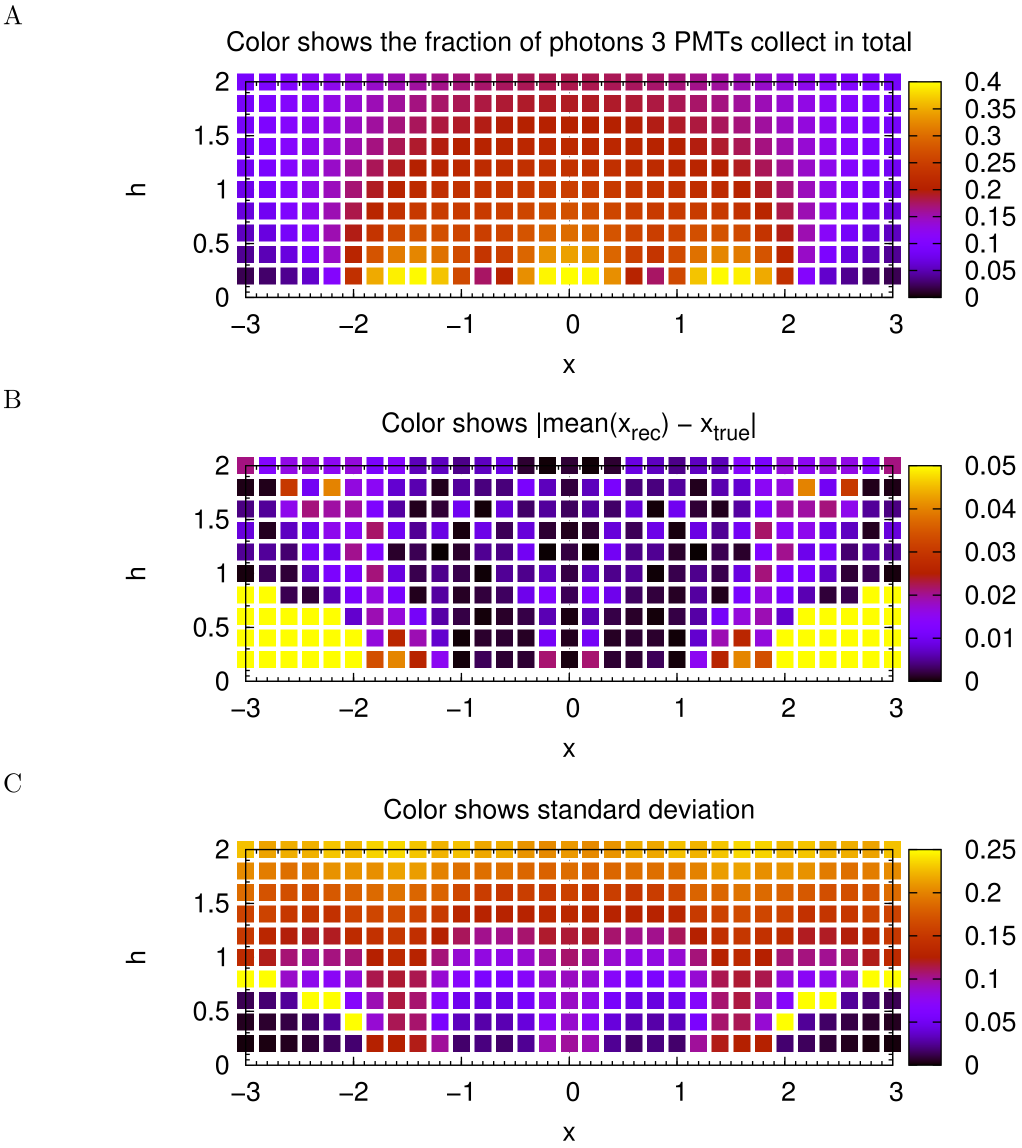

Figure 4.15: Reconstruction and standard deviation. The $x < 0$ side is a simple mirror of the $x \geq 0$ side. The lower left and lower right corners below the yellow points are the areas where the position reconstruction fail to converge. PMTs are located at $y = 0$ and $-2 \leq x \leq -1, -0.5 \leq x \leq 0.5, 1 \leq x \leq 2$.

study, the $x_{\rm sd}$ value obtained should be a good estimation to the theoretical reconstruction accuracy limit.

In the real detector, the light source (between liquid-gas interface and anode) is always placed at a fixed distance h away from PMTs, and is allowed to move in lateral direction x. To achieve the overall best reconstruction accuracy, the h value that minimizes $x_{\rm sd}$ when in front of PMTs should be used. When $a = 1$ and $l = 1$, this h value is about 0.4. I expect this value to be dependent on a and l and there could be a unique combination of a and l that minimizes the absolute value of $x_{\rm sd}$.

To guide the next generation detector design, this study should be carried out in 2D with simulations incorporating real detector geometry. The distance between the *S2* generating region and the PMT array should be optimized to achieve desired position resolution and *S2* photon collection uniformity.

4.3 Determination of True 3D Position

After the (x, y) position of *S2* is reconstructed, the 3D position of interaction could be completed by computing the z position from drift time dt as $z = v_{\rm d} \cdot dt$ where dt is determined as the time difference between *S1* pulse and the corresponding *S2* pulse and $v_{\rm d}$ is the electron drift velocity which is an assumed constant. This standard procedure assumes a uniform electric field in the detector such that electrons drift straight up with trajectories parallel to the main axis of the cylindrical sensitive volume. However, XENON100 shows substantial deviations from electric field uniformity, as discovered from data.

Fig. 4.16 shows event distribution in the r-dt space. dt is defined as $t_{S1} - t_{S2}$ so that dt is negative and has the same growth direction as z. Events are expected to occupy all the space in the area above the cathode and below the liquid-gas interface: $-180\,\mu\text{s} < dt < 0$, and within the PTFE wall of the TPC: $r < 153\,\text{mm}$. In the figure, there is no event occupying the area in the right bottom corner. The right-most event edge is not a vertical straight line in alignment with the TPC wall as expected, but a curved line on which points are being pushed inwards as the drift time gets longer. Another distinct feature on the figure is the “dip” at $r \approx 110\,\text{mm}$ and $dt < -180\,\mu\text{s}$. Events happening in this “dip” must have undergone longer drift time than the maximum that is allowed along vertical lines between the cathode and the liquid-gas interface.

From the observations in data, it is hypothesized that electric field lines in the TPC are not straight and vertical but significantly skewed. Due to the fact that events at the TPC wall are reconstructed towards lower r as drift time gets longer, the electric field line must be skewed in the same way: as z get higher, r gets lower, since electrons drift following the electric field lines precisely. The reason for the non-uniformity and the exact electric field distribution in the TPC shall be revealed from the electric field simulation. A correction scheme is constructed based on the simulated field lines to map from the raw (r, dt) to the true (r, z) position of the interaction.

4.3.1 2D Simulation of Electric Field in the TPC

The electric field inside of the detector cryostat is simulated using Finite Element Analysis (FEA) method with COMSOL Multiphysics® software. Due to the large dynamic range in dimensions

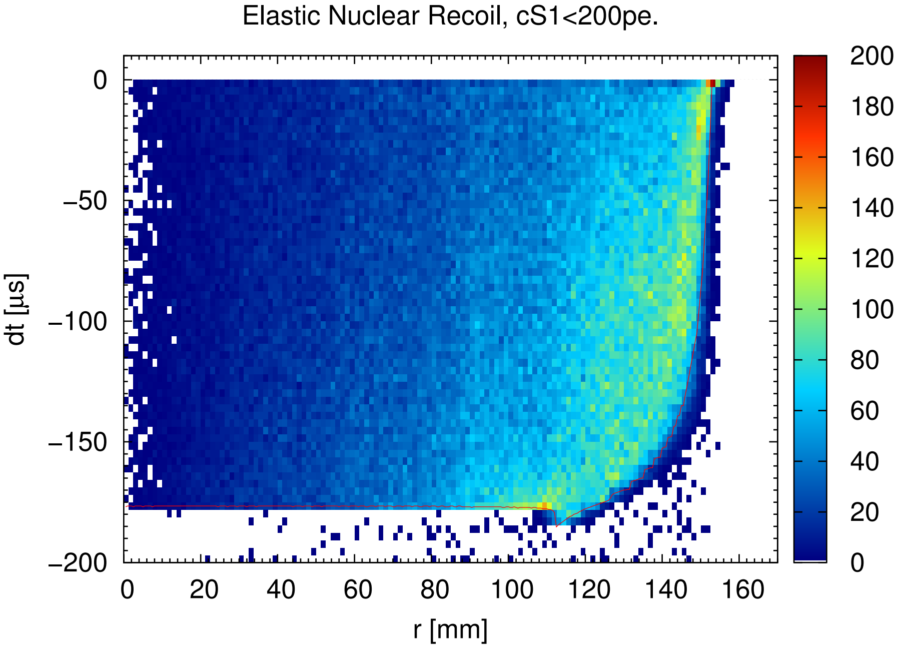

Figure 4.16: Outer Event Edge. Color shows event distribution in r and dt of neutron calibration data with inelastic scattering events removed. Red line shows the simulated outer event edge that best fits the data. The cathode is at $dt \approx -180\,\mu\text{s}$ and the wall of TPC is at $r \approx 153\,\text{mm}$.

spanned in the detector, from wire sizes of $50 - -125\,\mu\text{m}$ to the cryostat at the scale of 1 m, with FEA, only two-dimensional simulation, instead of a full three-dimensional simulation, is manageable for the whole detector with a state-of-the-art computer workstation to achieve an electric field resolution at mm level.

The XENON100 detector is largely of cylindrical symmetry. The relevant exceptions are the arrangement of PMTs, the PTFE wall of panels, and the hexagonal meshes. To set up the geometry in a 2D simulation consisting of coordinates radius r and height z, cylindrical symmetry is assumed and approximations are made. The segmented (panel) PTFE TPC wall is approximated by a continuous cylindrical tube; the PMT arrays are approximated by two planes of metal at $-800\,\text{V}$ mimicking the photo-cathodes.

During the design phase, all the meshes were simulated as solid lines in the 2D r-z space which represents solid plates in 3D geometry. This approximation left out an important difference between mesh and solid plate. Meshes are hollow which allow electric field to “leak” through, while solid plates completely shield off the electric field.

Meshes with large hole and small wire size were chosen to maximize the optical transparency for better *S1* light collection efficiency and lower energy threshold. Only after non-uniform event distribution as shown in Fig. 4.16 was discovered, the inappropriate approximation of meshes was realized.

To simulate the effect of meshes but staying in 2D cylindrical symmetry, a line of equally spaced circles are constructed to represent a mesh. This construction corresponds in 3D to a mesh made of concentric wires equally spaced in radius. In the simulation, the wire diameter is set to be the same as the real mesh in the detector, while the spacing between the wires is left as a parameter with the scaling constrain. The scaling constraint is: if a real mesh A has pitch size half of that of another real mesh B, the spacing used for simulating A is set to 1/4 of that for simulating B. In XENON100, the anode and gate meshes have pitch size 2.5 mm and the top, cathode and screen meshes have pitch size 5 mm.

The simulation is carried out at several different mesh spacing parameter values. For a specific mesh spacing, the outer most event edge is computed from simulated electric field lines in the sensitive volume. For an interaction happening at the outer edge of the detector, the generated electrons would follow electric field lines to the liquid-gas interface, therefore the r coordinate at the liquid-gas interface of an electric field line would be the reconstructed position from *S2*, and the integral of the length of electric field line would correspond to $v_\text{d} \cdot dt$. With the above procedure, the outer event edge is computed for each mesh spacing parameter. The outer event edge is then compared with observed data as shown in Fig. 4.16. The best fitting outer event edge determines the mesh spacing parameter.

In summary, this simulation uses concentric wires to approximate the 2D hexagonal meshes because only concentric wires could be implemented in 2D cylindrical symmetry. Since there is no direct correspondence of the concentric wire spacing to the hexagonal wire pitch size, the concentric wire spacing is left as a free parameter in the simulation. The free parameter is determined by fitting the simulated outer event edge to measured data.

With the best fitting spacing parameter of 2.7 mm, the simulation shows the electric field in

Fig. 4.17. The electric field strength (norm) gets slightly lower when the position gets closer to the cathode. However, since the electron drift velocity is varying slowly at this electric field strength, it is still safe to assume a constant drift velocity $v_\mathrm{d} = 1.74\,\mathrm{mm/\mu s}$.

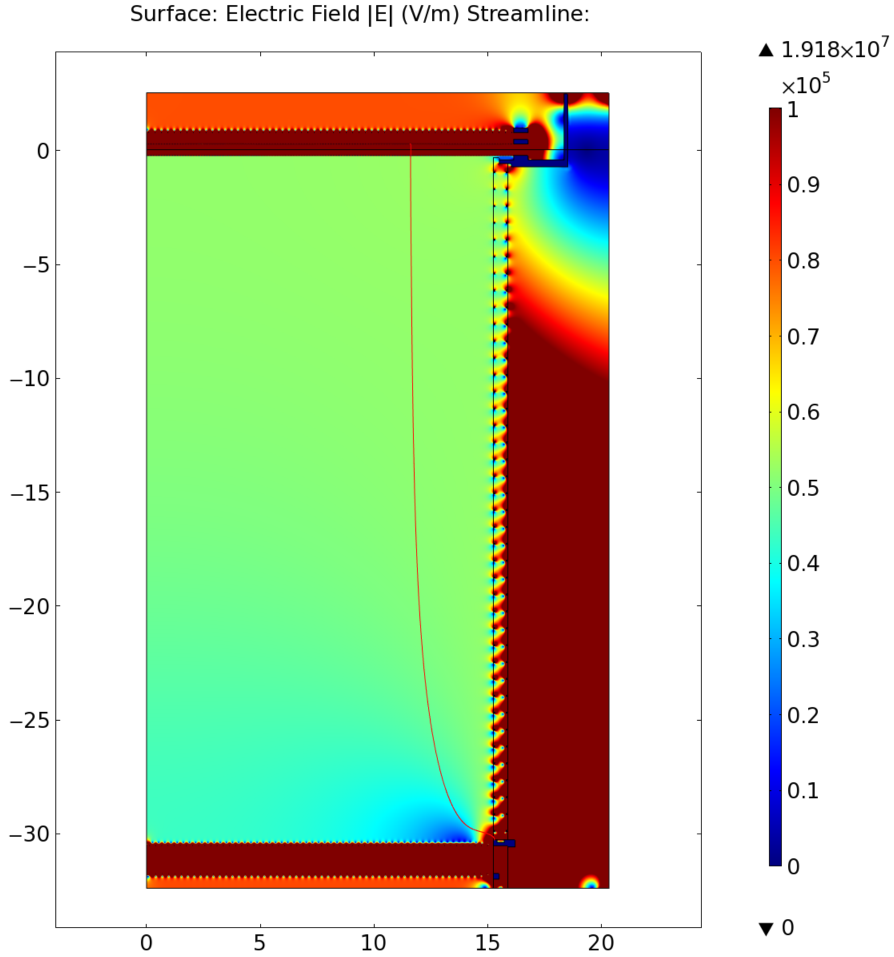

Figure 4.17: Electric Field in the TPC. r and z in cm. Color shows the electric field strength. Dark red indicates $|E| > 1\,\mathrm{kV/cm}$. Red curve shows the electric line or electron drift path starting from the outer bottom corner of the sensitive volume.

The detailed electric field lines in the sensitive volume are shown in Fig. 4.18. Field lines starting at the outer bottom corner have noticeably longer length than those of other field lines. They are responsible for producing the “dip” with dt longer than the maximally allowed drift time between cathode and liquid-gas interface seen in Fig. 4.16. Since the electric field lines are skewed in r-z space, there is no shift in the direction perpendicular to the radial direction (azimuthally independent). The correction only has to be carried out in each of the r-z planes.

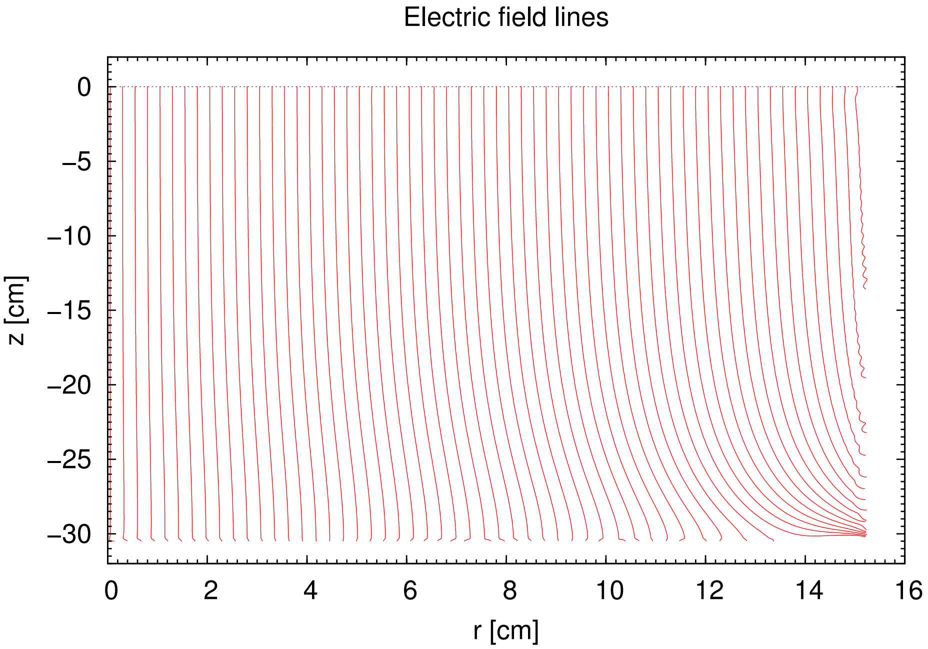

Figure 4.18: Electric Field Lines in the Sensitive Volume. The PTFE TPC wall is at $r \approx 153\,\mathrm{mm}$ and the cathode is at $z \approx -308\,\mathrm{mm}$.

4.3.2 The Correction Procedure

To recover the true position of interaction (r, z) from uncorrected coordinates $(r', v_\mathrm{d}dt)$, a function

$$f : (r', v_\mathrm{d}dt) \to (r, z) \tag{4.9}$$

mapping from uncorrected coordinate space to the true (r, z) space has to be constructed. To construct the function numerically, the function is effectively separated into two parts:

$$f_r : (r', v_\mathrm{d}dt) \to r \tag{4.10a}$$

$$f_z : (r', v_\mathrm{d}dt) \to z \tag{4.10b}$$

If the uncorrected $(r', v_\mathrm{d}dt)$ space is discretized on a regular grid, the functions (4.10a) and (4.10b) can be stored in two two-dimensional arrays. The arrays are initialized with the simulated electric field lines following this procedure: Pick an electric field line and follow its path from $z = 0$ (also $v_\mathrm{d}dt = 0$) downwards in reverse-drift-time. Its starting radial position is the uncorrected r' hence the row of the array. Use a variable z' to track the integral of path length starting from $v_\mathrm{d}dt = 0$; when z' hits a discretization point, record true z and r in the columns of the respective arrays. Move to next electric field line and repeat the procedure.

After the mapping arrays are initialized, the correction function is straightforward to construct. In between discretized grid points, r and z are computed from two separate bi-linear interpolations using 4 surrounding points in $(r', v_\mathrm{d}dt)$.

One special case needs to be handled differently. As seen in Fig. 4.16, after fitting the outermost event edge to the data, there are still events outside of the event edge and there is no simulation corresponding to those events. It is understandable that due to the uncertainties in *S2* position reconstruction and dt measurement, events happening at the edge of the PTFE wall are reconstructed to spread around the edge. So events have a chance to be reconstructed outside of the TPC. In order to correct the position of those events in a meaningful way, a special procedure is designed for events outside of the simulated event edge. For one such event at uncorrected position $\mathbf{A'}$, first a point on the simulated outer event edge closest to $\mathbf{A'}$, point $\mathbf{B'}$, is found. Second, since $\mathbf{B'}$ is a simulated point, its corresponding corrected position $\mathbf{B}$ is known. Then the corrected position $\mathbf{A} = (\mathbf{A'} - \mathbf{B'}) + \mathbf{B}$. Effectively this procedure parallel translates the vector $\mathbf{A'} - \mathbf{B'}$ to the new location according to the correction of $\mathbf{B'}$.

The amount and direction of correction is shown in Fig. 4.19. The correction is mostly in the radial direction, while only events in the "dip" have significant correction in both r and z. The amount of correction is increasing towards the outer bottom edge, where the maximum amount of correction can reach up to 4 cm.

4.3.3 Validation

The accuracy of the r-z correction has significant impact on the target (fiducial) volume determination and the background comparison to the Monte Carlo results. Its performance has to be validated.

So far the only indication that the correction is working well is that the simulated outer event edge matches the observed one, and after correction the outer event edge becomes straight. To go beyond this limited indication, a uniformly distributed source in the sensitive volume is required. Neutron activated xenon metastable states $^{129\text{m}}$Xe and $^{131\text{m}}$Xe serve the purpose well.

$^{129\text{m}}$Xe and $^{131\text{m}}$Xe are (activated) metastable xenon nuclei produced from fast neutron activation (Ni et al. [41]). They remain in the background data after the neutron calibration run for several weeks. $^{129\text{m}}$Xe emits 236 keV and $^{131\text{m}}$Xe emits 164 keV gamma-rays. They serve as point light sources in the detector. Since activated xenon atoms are chemically identical to the rest of the "normal" xenon, they mix and distribute within the xenon volume very well. More over, $^{129\text{m}}$Xe and $^{131\text{m}}$Xe have half-lives of 8.9 days and 11.8 days respectively, which allow them to distribute evenly in the xenon volume before decaying away. One caveat is that 236 keV and 164 keV energy deposits produce large *S2*s that saturate the top PMTs and systematically bias x-y position reconstructions. In order to avoid the top PMT saturation problem, the anode voltage was lowered to 2.2 kV right after neutron calibration run to reduce the *S2* size in the following background data.

The activated xenon data with 2.2 kV anode voltage was taken towards the end of February 2011, right after a neutron calibration run with the ^{241}AmBe neutron source. Without specifically selecting on event energy, the event distribution before and after r-z correction are shown in Fig. 4.20. The areas in the top and high radius have high event density because of background. In the bulk where background is minimal, it is expected that in the uncorrected r-z space, the event density gets higher in the more distorted area, i.e. close to the cathode; while in the corrected r-z space the event density becomes uniform everywhere.

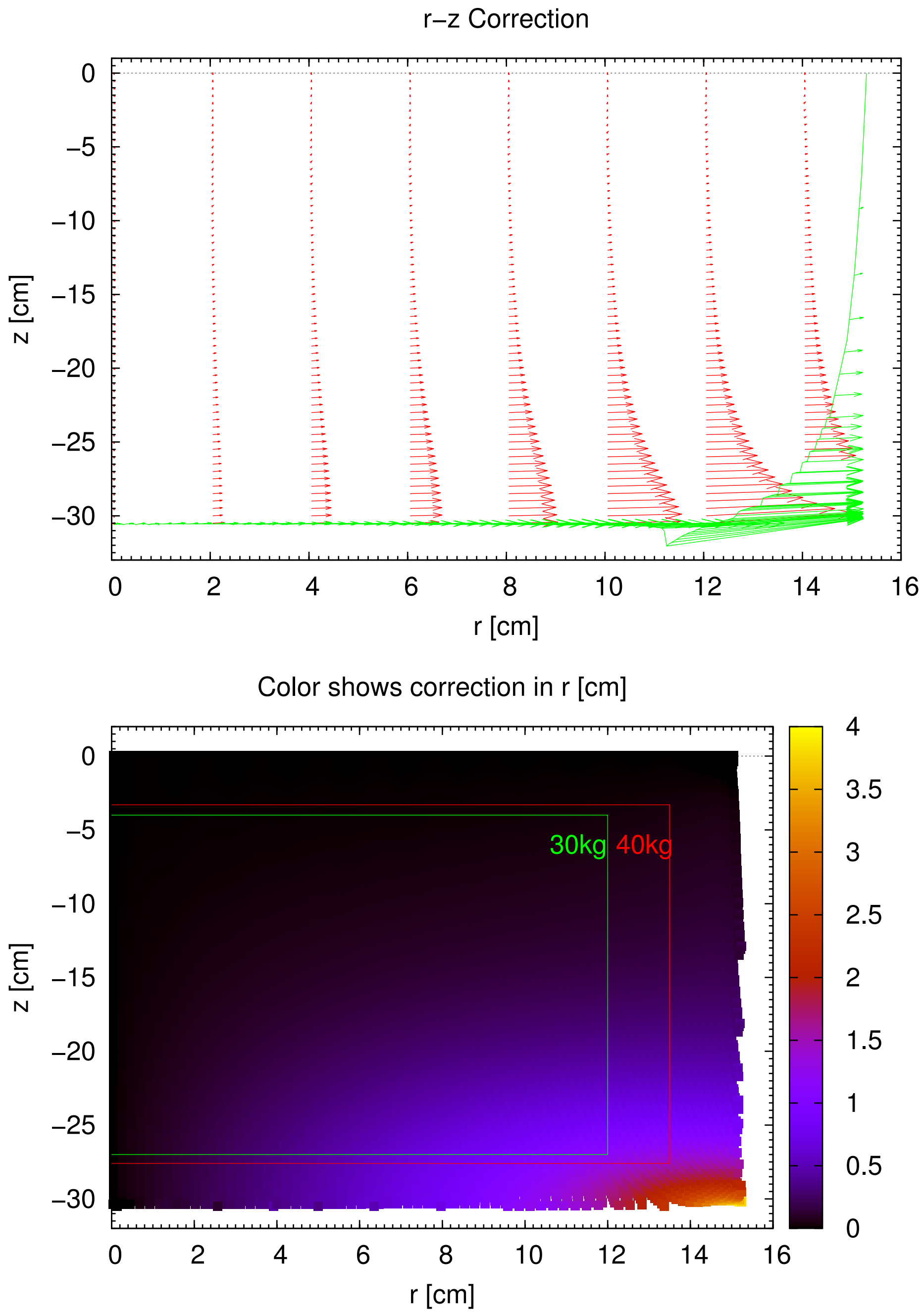

Figure 4.19: Direction and Amount of Correction. Top: each vector shows the direction and size of the correction. The tail of each vector is at the uncorrected coordinate $(r', v_\mathrm{d} dt)$ and the head of the vector is at the corrected coordinate (r, z). The green line and vectors show the events and corrections at the outermost edge. Bottom: the color at (r, z) shows the amount of displacement (correction) in r in order for events to be corrected to the position (r, z).

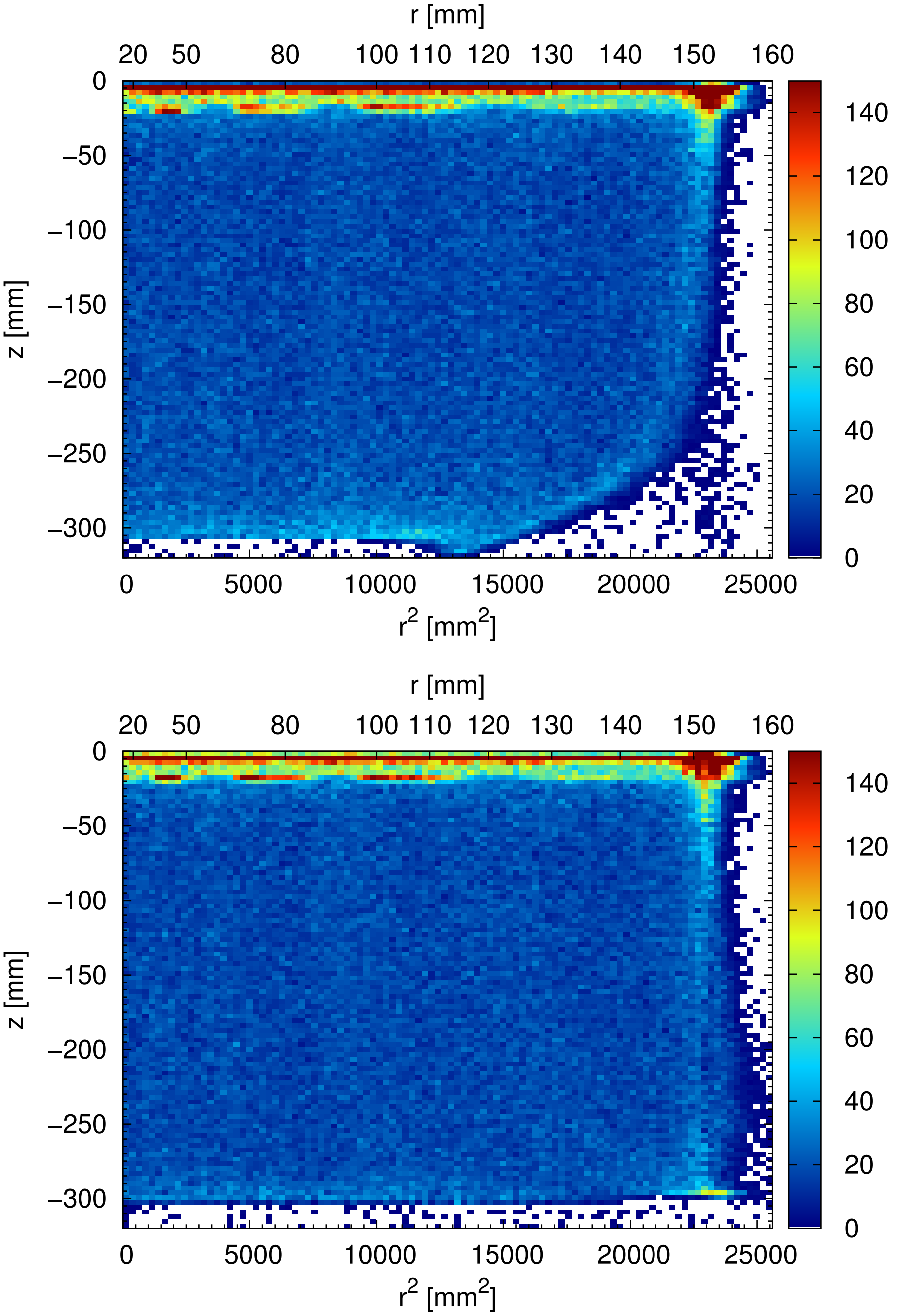

Figure 4.20: $^{129\mathrm{m}}$Xe and $^{131\mathrm{m}}$Xe: Before and After r-z Correction. All events including background are included. Color scale shows number of events in each bin. Events are plotted in r^2-z space so that each bin represents the same volume regardless of the position in r.

One problem for this study is the background events which are not activated xenon lines. To best estimate the number of 164 keV and 236 keV events while subtracting the contribution from background events, selections are made on the energy scale. As shown in Fig. 4.21 (top), when plotted in position dependent light/charge yield corrected space c*S2* versus c*S1*, 164 keV and 236 keV lines appear to distribute in two ellipsoids with long axis not in alignment with either c*S2* or c*S1*. To minimize the width of the spectra lines, the two ellipsoids are projected to the direction that is perpendicular to the long axis of the ellipsoids. The projection is referred to as the Combined Energy Scale (CES). In this particular case, CES is defined as $cS2/12\,000 + cS1/800$. In the CES spectrum, 164 keV and 236 keV peaks together with the background are fitted as the sum of three Gaussian function, that is one Gaussian for each of the two peaks and the third Gaussian for the underlying background. Afterwards, the number of events in each peak is computed from the respective fitted Gaussian function. In this way the background is subtracted. One example of the CES spectrum and the fit is shown in Fig. 4.21 (bottom).

Since the target (fiducial) volume would be defined up to $r = 145$ mm, we would like to test if in the corrected r-z space, within the area of $r < 145$ mm, the 164 keV and 236 keV event density is uniform. To do so, events in $r < 145$ mm are selected and binned in z slices. In each z slice, the CES spectrum is fit and event density is determined and normalized to events/cm^3. As shown in Fig. 4.22 (top), the event density integrating from $r = 0$ to $r = 145$ mm is uniform from $z = 0$ down to the next-to-last bin at $z = -295$ mm. The binning is not uniform but kept large (30 mm) from $z = 0$ down to $z = -270$ mm, and becomes small (5 mm) from $z = -270$ mm to $z = -300$ mm. The idea was to test the area where the larger amount of correction takes place with better resolution, within the limit of statistics. The points are in agreement with a horizontal line with $1 \sim 2\,\%$ deviation. The significant drop of density in the lowest z bin could be due to the large uncertainty of correction of events at the edge, i.e. those in the "dip".

To translate the deviation in density to the deviation in radius, a simple argument in terms of area can be made: consider the selection of area from r_0 to r in corrected radius, where r could be shifted by Δr from the true radius. Denoting the true density as ρ_0 and the density with biased radius as ρ, we have

$$\frac{(r + \Delta r)^2 - r_0^2}{r^2 - r_0^2} = \frac{\rho}{\rho_0}\,. \tag{4.11}$$

In Fig. 4.22 (top), we have $r_0 = 0$ and $r = 145$ mm, it is straight forward to compute that 1.2 % drop of density corresponds to $\Delta r \approx 0.9$ mm.

The above argument tests the overall density integrating from $r = 0$. To probe the area of the largest correction, another selection setting $r_0^2 = 145^2/2\,\mathrm{mm}^2$ is chosen and the result is plotted in Fig. 4.22 (bottom). To infer the bias in r using equation (4.11), we assume the bias in r_0 is already negligible. Fig. 4.22 (bottom) show the two spectral lines combined, the density is consistent with a horizontal line with 2 % deviation, which corresponds to $\Delta r \approx 0.7$ mm.

In conclusion, using evenly distributed events producing 164 keV and 236 keV gamma lines, it is confirmed that the corrected radius has an uncertainty less than 1 mm at $r = 145$ mm in the region $-295\,\mathrm{mm} < z < 0$. Therefore the position correction has negligible impact on the rest of data analysis.

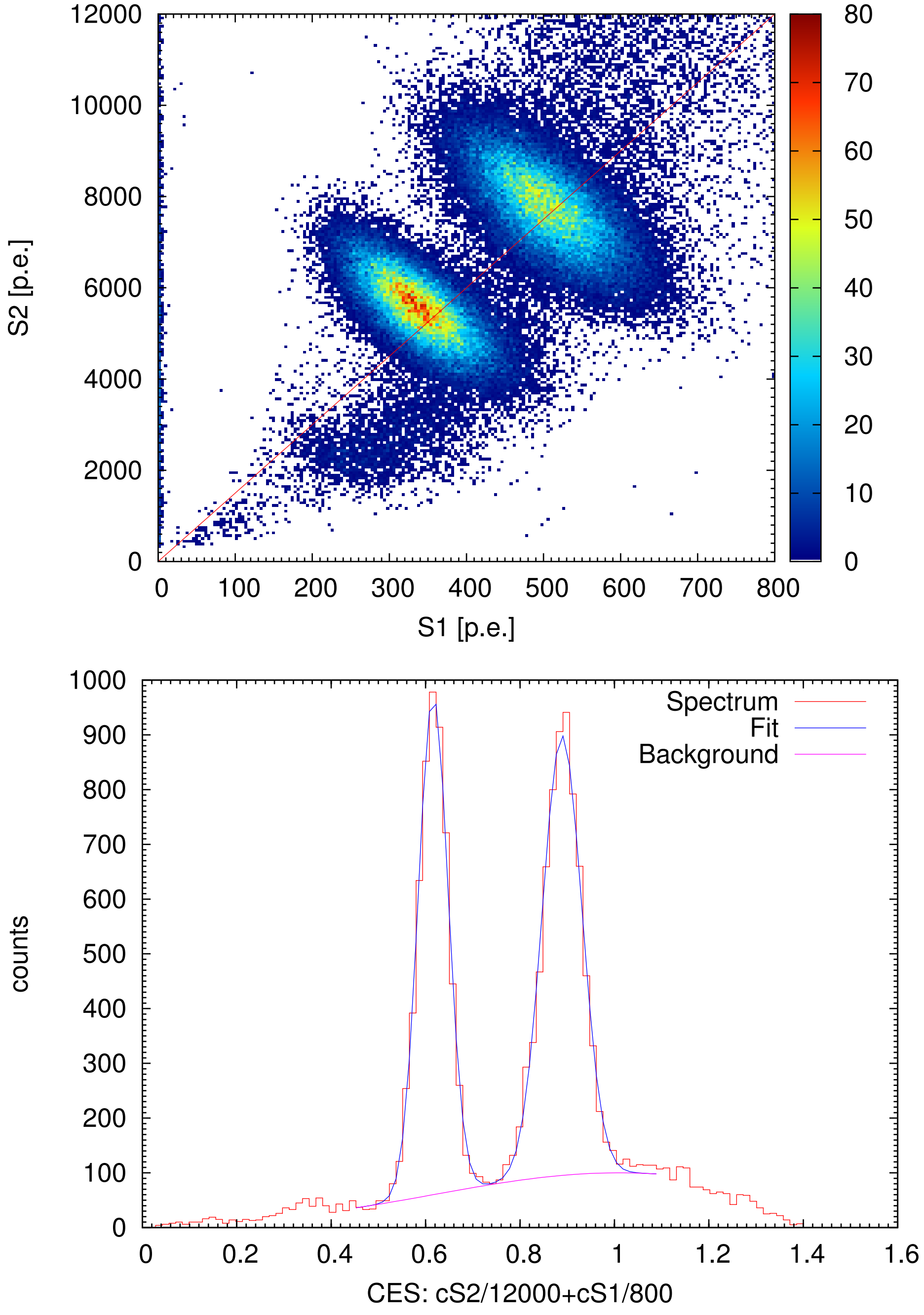

Figure 4.21: $^{129\mathrm{m}}$Xe and $^{131\mathrm{m}}$Xe: Energy Spectra. Top: Corrected *S2* versus corrected *S1* of events within the 50 kg cylindrical fiducial volume. Bottom: Combined energy scale (CES) spectrum and fit. CES is defined as $cS2/12\,000 + cS1/800$, which corresponds to the diagonal line in the top figure.

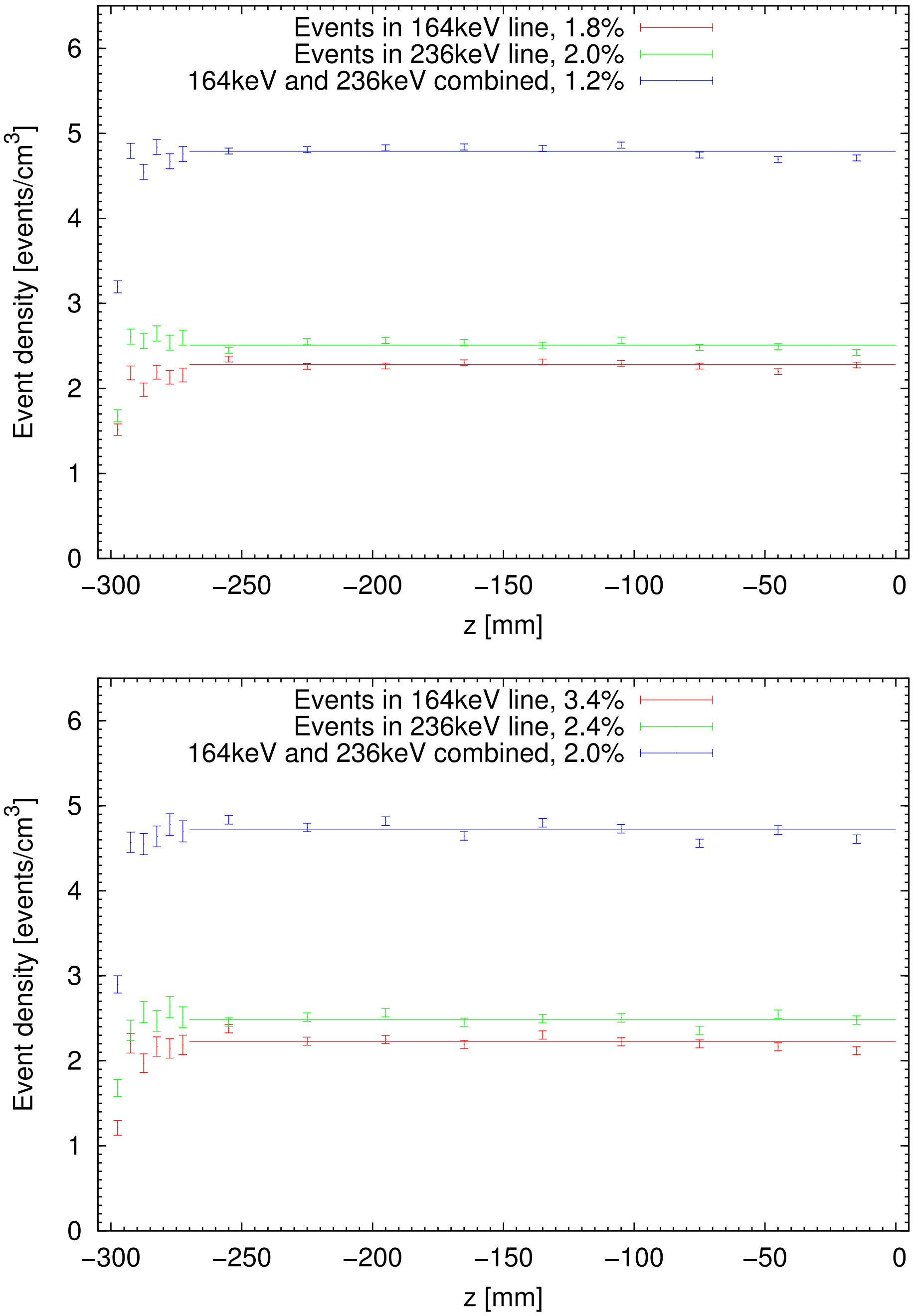

Figure 4.22: $^{129\mathrm{m}}$Xe and $^{131\mathrm{m}}$Xe: Event Density. Top: event density integrating from $r = 0$ to $r = 145\,\mathrm{mm}$. Bottom: event density integrating from $r^2 = (145^2/2)\,\mathrm{mm}^2$ to $r = 145\,\mathrm{mm}$. In $-300\,\mathrm{mm} \le z < -270\,\mathrm{mm}$, each z slice is 5 mm wide. In $-270\,\mathrm{mm} \le z < 0\,\mathrm{mm}$, each z slice is 30 mm wide. Error bar on each point shows the statistical error only. The percentage shown in the legend is the relative deviation of points from the mean shown as the horizontal line.

4.3.4 Future Improvement on Electric Field Simulation

The simulation used to reproduce the outer event edge is done in 2D with cylindrical symmetry and contains a number of assumptions. The biggest weakness is that the mesh spacing is left as a free parameter so that only by comparing to the real data the parameter could be determined. To reveal the exact nature and detail of electric field lines penetrating through the mesh wholes, a full scale 3D simulation is required. Boundary Element Method (BEM) which only discretizes the boundaries in the geometry, instead of the volume as in FEM, poses a viable option to perform a full scale 3D simulation of the XENON100 detector within the limit of computing resources. BEM requires far less storage than that of FEM, however, BEM is only applicable to problems for which Green's functions can be calculated, while FEM could be applied to a lot wider range of problems solving differential equations. At the time of this thesis is written, no commercial BEM software is available to the author's knowledge and freely available packages have difficulties to build and handle complicated geometries. Nevertheless, a full scale 3D simulation incorporating all the details is vital for the design of next generation larger detectors to achieve desired electric field uniformity in the TPC. The XENON collaboration has started to work with tools developed for the KATRIN experiment to study its applicability to problems in liquid xenon TPCs.

Summary

We acquire the first stage of (x', y') position from PMT pattern on the top array, and the drift time which is directly converted to z' from the time difference between *S1* and *S2* pulses in waveform. Afterwards, the true 3D position of interaction (x, y, z) is obtained from first stage coordinates (x', y', z') by correcting the electric field line distortion. From the test using real data, we conclude that the 3D position reconstruction is accurate to the level of 3 mm in the target volume for Dark Matter search.

Chapter 5

PMT Pattern Likelihood Method for Anomalous Event Identification

Background discrimination in the XENON100 Dark Matter experiment relies on the identification of events with a single interaction in a selected fiducial volume. The yield difference in primary scintillation light (*S1*) and ionization charge (*S2*) distinguishes nuclear recoils from electronic interactions. Anomalous events with apparent single *S1* and single *S2*, but which are truly multiple scatter events, constitute a substantial fraction of background in the Dark Matter region of interest. Such events have additional scattering sites, yielding *S1* PMT patterns different from those of true single scatters. We have developed a method to discriminate against these anomalous events, using the Log Likelihood Ratio of measured PMT patterns over expected single scatter patterns obtained from calibration data. Since the method directly compares the information from background data with calibration data, it is robust against systematic uncertainties in, e.g., PMT quantum efficiencies, position reconstruction, or light collection efficiency.

The dominant type of event that constitute an anomalous event population is known as the gamma-X event. Gamma-X events are due to one or two gamma-rays with one interaction in the charge sensitive volume and at least one interaction in the charge insensitive volume. The interactions in the charge insensitive volume do not produce *S2*, but add additional *S1* light to the *S1* in the charge sensitive volume. Therefore their *S2*/*S1* ratio is reduced and the events can look similar to a nuclear recoil event. From the *S2* and *S1*–*S2* time difference, the 3D position of interaction is reconstructed, however, the *S1* from the interaction in the charge insensitive volume has a different 3D position. *S1*s from charge sensitive and charge insensitive regions are not distinguishable in time, but they sum up to give a PMT pattern that is different from the normal PMT pattern corresponding to the reconstructed position. One example of a gamma-X event is shown in Fig. 5.1. This event has a typical single scatter event signature in the waveform: single *S1* and single *S2*. Also, it has a good single *S2* PMT pattern. When z is determined from drift time and (x, y) is determined from *S2*, the event is reconstructed in 3D at the red point, which is close to the bottom but above the cathode. If the *S1* light comes only from the light source at the red point, then only PMT161 and the surrounding PMTs will receive photons. However, in this event, PMT113, which is far away from the reconstructed event position, receives a significantly high number of photons. The high concentration of light on PMT113 indicates that there is a second interaction very close to that PMT. The second interaction right above PMT113 is below the cathode therefore does not produce *S2* at all. This is a typical example of a gamma-X event with one interaction in the sensitive volume and one interaction below the cathode.

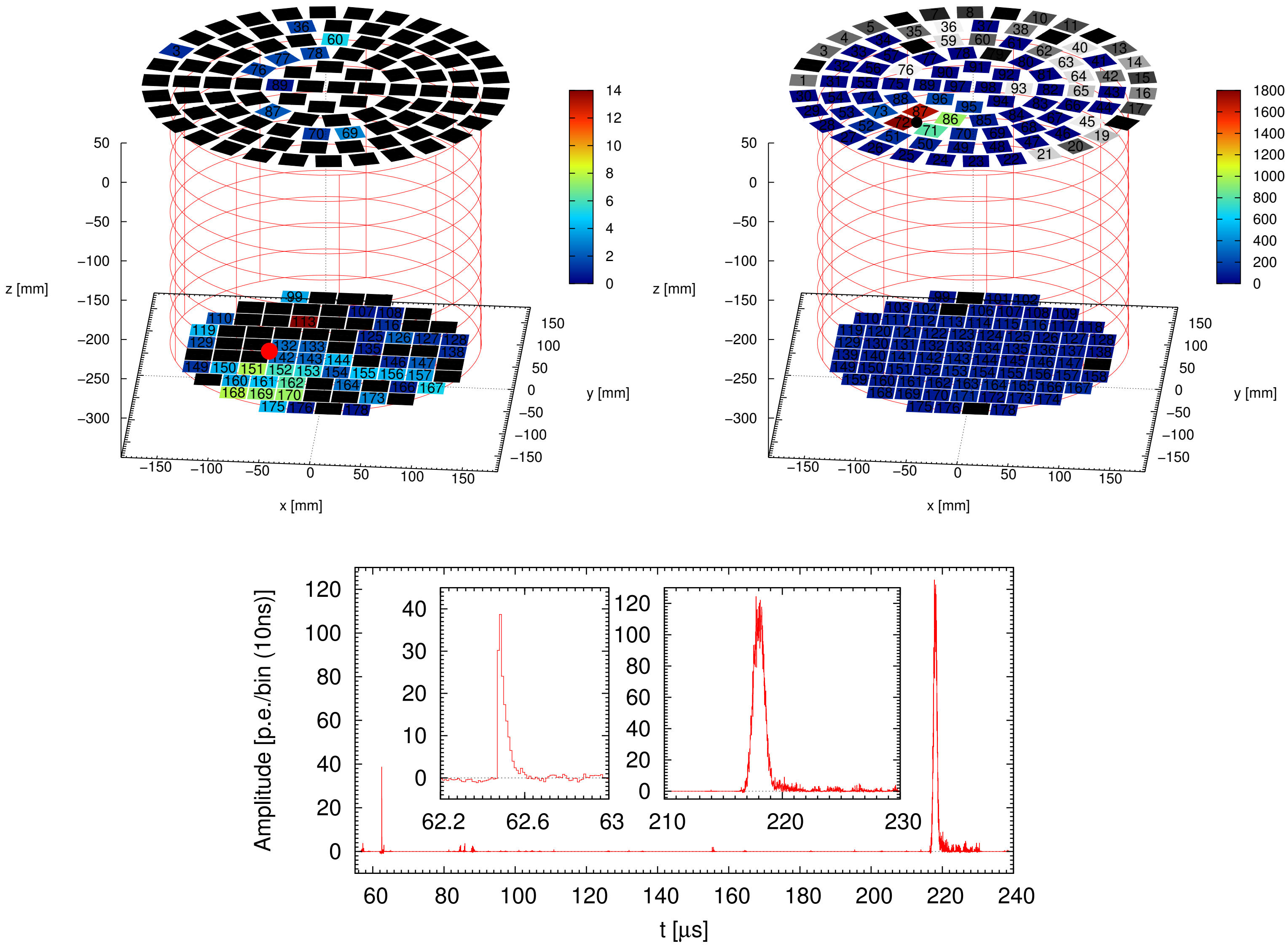

Figure 5.1: Example of an Anomalous Event. `EventId: xe100_100211_1149_143804`. Top left: PMT pattern of *S1* signal. Top right: PMT pattern of *S2* signal. Bottom: trace of the summed waveforms with zoom-ins of *S1* and *S2*. This event has a good scattering site (red filled circle) in the charge sensitive volume and an additional scattering site right above PMT113. Color scale shows number of photo-electrons [p.e.].

Because of the additional *S1* light, the nuclear/electronic recoil discrimination parameter log(*S2*/*S1*) becomes lower for gamma-X events, making them look like nuclear recoils. This is the type of false nuclear recoil events we would like to reject. The *S1* PMT Pattern Likelihood method catches the discrepancy between the observed *S1* pattern and the expected pattern. Therefore, the method not only catches the gamma-X type of events, but also catches other types of events with unexpected *S1* patterns. For instance, it catches events with *S1* and *S2* not corresponding to the same interaction, which would have passed all other event selection criteria. Another possibility is a multiple scatter with multiple scattering sites in the charge sensitive region at the same z but different (x, y), so that it has only one *S2* peak.

The PMT Pattern Likelihood parameter is developed by computing the Poisson Likelihood of the *S1* PMT Pattern of an event under examination on the "standard" *S1* PMT Pattern of single scatter events happening at the same (x, y, z) position. The "standard" *S1* PMT Pattern is determined using the full absorption peak of low anode voltage (2.2 kV) ^{137}Cs calibration data. Low anode voltage is required to avoid the *S2* saturation problem in order to ensure consistent behavior of X-Y position reconstruction algorithms for both calibration data with high *S2* and events under examination with low *S2*. The full absorption peak in ^{137}Cs is required to have a clean single scatter sample and to have the highest possible *S1* in order to minimize the photon counting fluctuations in the "standard" *S1* PMT pattern. The whole 3D sensitive volume is coarsely binned to get a sufficient number of events in each spatial bin such that the mean values of the *S1* PMT patterns have statistical fluctuations below 10 %. The PMT Pattern Likelihood parameter is the sum of three parts: the likelihood of the top PMT array only; the likelihood of bottom PMT array only; and the likelihood of the top total/bottom total ratio. When computing the likelihood for the top PMT array, the response is normalized to the top *S1* total. The same applies to the bottom array.

5.1 *S1* PMT Pattern from Calibration Data

Since the essence of this method is to compare the *S1* PMT pattern of an event under examination to the "model"—the expected single scatter *S1* PMT pattern happening at the same 3D position, acquiring an accurate and reliable *S1* PMT pattern map as a function of 3D position of interaction is of vital importance to the performance of this method. In principle the *S1* PMT patterns could be generated from Monte Carlo light collection simulations, however, they have too many uncertainties and approximations which make the simulated *S1* PMT pattern unreliable. For instance in the simulation, the model for light reflection on the inner PTFE wall is unknown, the photon transport through the meshes is approximated, and the exact PMT quantum efficiencies are unknown.

As shown in Chapter 4, in real data, the position of interaction in 3D could be well reconstructed for each event, and the *S1* PMT pattern is readily available for each event. It is certainly feasible to obtain the *S1* PMT pattern map from the real calibration data of single scatters directly. The advantage of doing so, unlike acquiring the map from the simulation, is that all the light loss/transmission in the detector, and the PMT quantum efficiencies, are already folded into the map in the units of photo-electrons. The event under examination will also have its *S1* PMT pattern in terms of photo-electrons thus can be directly compared to the model.

The caveat is that high amount of statistics, not only in terms of number of events, but also the number of *S1* photons in each event, is required. Furthermore, we need to minimize anomalous events in the sample. This is accomplished by selections on the photo-peak, as described below. To achieve high amount of *S1* photons in each event, the use of a high energy gamma source is desired. However, a high energy gamma source also produces a high amount of electrons causing the *S2* saturation problem. While *S2* is not used in this method, *S2* saturation biases the (x, y) position reconstruction therefore skews the map which requires accurate 3D positioning. To balance both requirements, 662 keV gamma from ^{137}Cs source is chosen, and the data is taken with low anode voltage (2.2 kV) to avoid the *S2* saturation problem. The source is placed outside of the detector at a few places surrounding the cryostat to maximize the coverage of 3D position sampling in the detector by the gamma-ray.

In the data analysis, events in the 662 keV full absorption peak are selected (in *S2* vs. *S1* space) to produce the *S1* PMT pattern map. The reason is that we want to build a map of *S1* PMT patterns of true single scatters. 662 keV gamma does Compton multiple scattering in the detector. Selecting the full absorption peak guarantees the event has one single scatter site (or multiple scatter sites very close to each other, which serves the same purpose as well).

To produce the *S1* PMT pattern map, the sensitive volume is coarsely divided into 3D spatial bins. The sensitive volume is first divided into 2 cm z slices. Each z slice is then divided into 2D bins resembling the arrangement of the top PMT array, as shown in Fig. 5.2. For a specific spatial bin, the mean value of photo-electrons collected by each PMT is computed.

Eventually, the *S1* PMT pattern map is a 4-dimensional function defined as

$$M(x, y, z, i) \tag{5.1}$$

where (x, y, z) locates the position of interaction and i is the index of PMT number.

Since M is a high dimensional function, one could only fix some of the parameters and plot it as a function of the rest of variables. Fig. 5.2 (top) is one way of plotting it (fixing z and i), while Fig. 5.3 shows the PMT pattern of a spatial bin close to the center of the TPC (fixing (x, y, z)). While light collection from each individual event is fluctuating, after averaging over a substantial number of events, the PMT pattern becomes smooth, as expected. It is shown in Fig. 5.3 (bottom) that the statistical uncertainty on each PMT in the *S1* PMT pattern is reasonably small.

5.2 PMT Pattern Likelihood

When an event interacts at position (x, y, z) in the sensitive volume, it is assigned to the spatial bin as described in Section 5.1 first, then the model *S1* PMT pattern is retrieved from function (5.1)

$$\nu_i = M(x, y, z, i)\,. \tag{5.2}$$

$\{\nu_i | i = 1 \dots N_{\mathrm{PMT}}\}$ represents the model or expected mean value of *S1* PMT pattern with position of interaction at (x, y, z), while $\{n_i | i = 1 \dots N_{\mathrm{PMT}}\}$ denotes the *S1* PMT pattern of the event under examination.

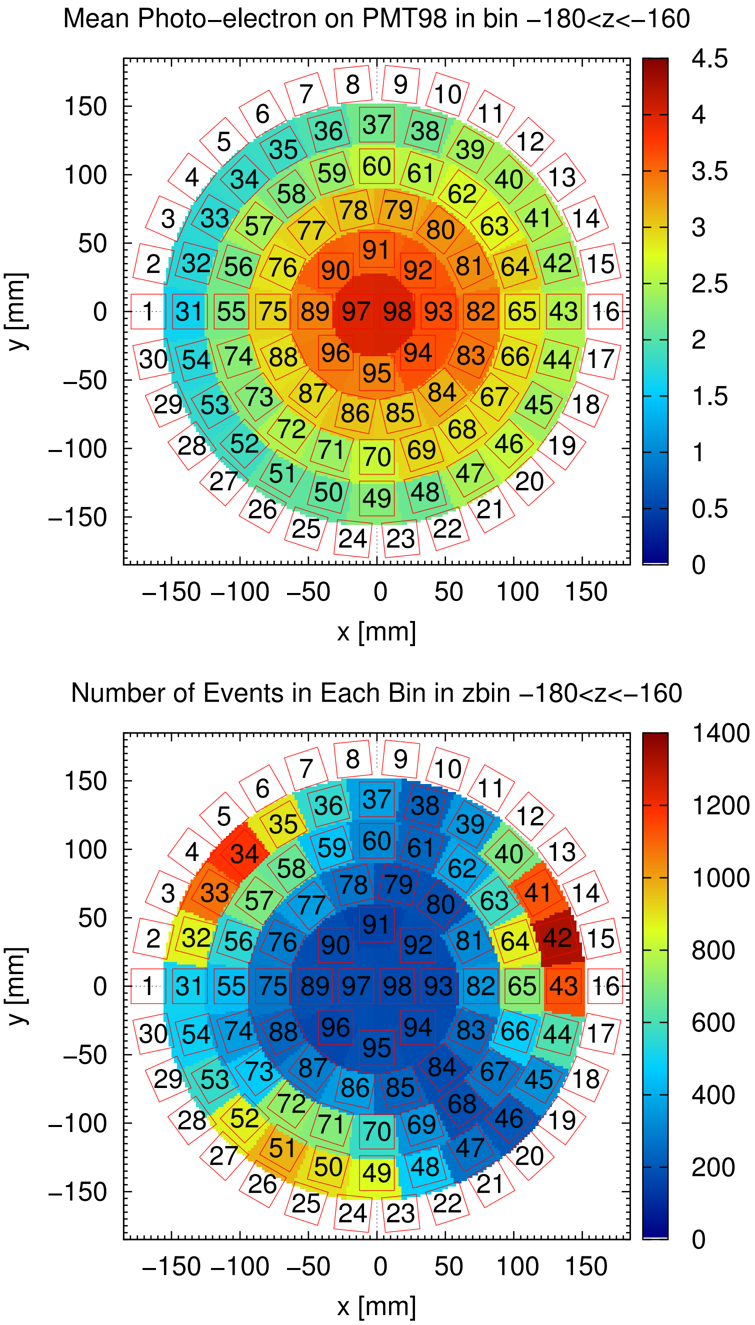

Figure 5.2: Binning, Counts and Light Collection. Top: In z bin $-180\,\text{mm} < z < -160\,\text{mm}$, mean number of photo-electrons collected by PMT98 as a function of (x, y). The binning in (x, y) resembling the top PMT array arrangement is also visible. Bottom: number of events in each bin. Statistics is sufficient to obtain good mean value of light collection throughout the (x, y) range.

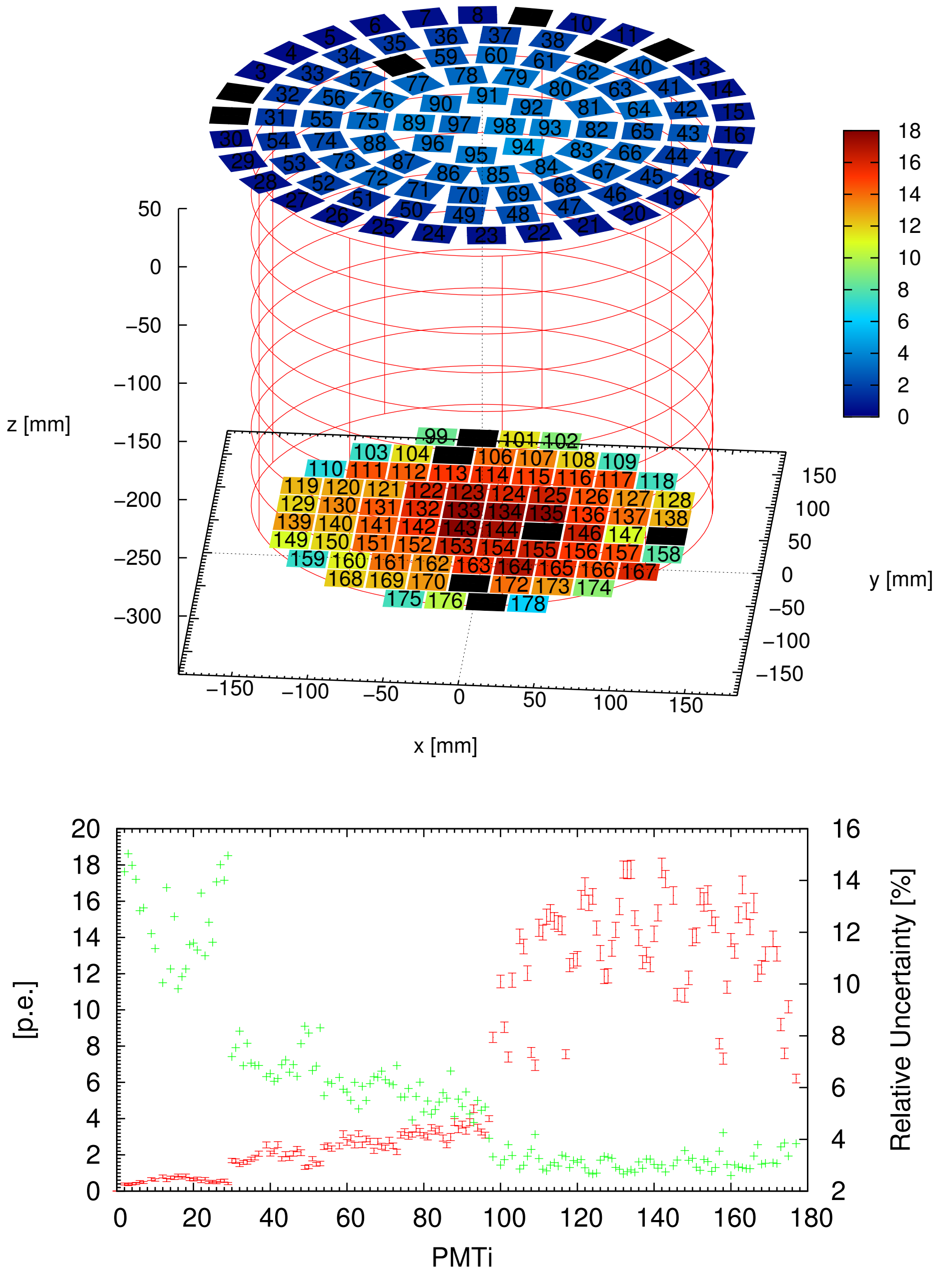

Figure 5.3: Mean PMT Pattern of a Spatial Bin. z bin $-180\,\mathrm{mm} < z < -160\,\mathrm{mm}$, (x, y) bin directly under PMT98. Top: Color shows mean number of photo-electrons collected at each PMT; black color indicates dead or completely non-illuminated PMTs. Bottom: Number of photo-electrons collected on each PMT and uncertainty due to counting statistics (red error bars). Green points (corresponding to right side y axis) shows relative uncertainty.

For the most relevant energy range, each of the PMTs in the TPC (PMT1 to PMT178) gets only a small number of photo-electrons ranging from a few to tens at most. It is reasonable to assume the number of photo-electrons on each PMT follows a Poisson distribution of p.d.f.

$$p_i = \frac{\nu_i^{n_i}}{n_i!} e^{-\nu_i} \tag{5.3}$$

where i is the PMT index. Then the Likelihood Function, the product of all the Poisson probabilities, is written as

$$L(n|\nu) = \prod p_i = e^{-\nu_{\text{tot}}} \prod \frac{\nu_i^{n_i}}{n_i!} \,. \tag{5.4}$$

The Likelihood Ratio, comparing the likelihood of a pattern $\{n_i\}$ given a model $\{\nu_i\}$, to the likelihood of the "ideal" case where $n_i = \nu_i$, is defined as

$$\lambda_{\text{P}} = \frac{L(n|\nu)}{L(n|n)} = e^{n_{\text{tot}}-\nu_{\text{tot}}} \prod \left(\frac{\nu_i}{n_i}\right)^{n_i} \,. \tag{5.5}$$

The quantity $-2\log\lambda_{\text{P}}$, distributes like χ^2 with N degrees of freedom (Wilks [56]) in the limit where each bin is well populated:

$$\chi^2_{\text{P}} = -2\log\lambda_{\text{P}} = 2\sum\left(n_i \log\frac{n_i}{\nu_i} + \nu_i - n_i\right) \,. \tag{5.6}$$

Here N denotes the number of bins, i.e. 98 for top array. For a special case where the model predicts 0 signal ($\nu_i = 0$), $\log\frac{n_i}{\nu_i}$ is set to 0.

In the real detector, since we only care about the PMT pattern but not the total number of photo-electrons in *S1*, we set $\nu_i = \frac{n_{\text{tot}}}{\nu_{\text{tot}}} n_i$, normalizing the model to the event under examination. Since the model is taken from 662 keV gamma full energy peak, ν_{tot} is in the range of 600 p.e. to 1600 p.e.. n_{tot} in the dark matter relevant energy range is usually smaller than 200 p.e.. Therefore the down scaling wouldn't introduce much statistical uncertainty in the model into the formulation but the Poisson statistics of the event under examination should still dominate.

χ^2_{P} could be computed summing up all the data bins together, or be split into a few partial sums of sub groups of available data bins. For XENON100 events, four χ^2_{P} parameters are defined:

$$\chi^2_{\text{P,top}} = 2\sum_{i=1}^{98}() \qquad \text{Using top array only} \tag{5.7}$$

$$\chi^2_{\text{P,bot}} = 2\sum_{i=99}^{178}() \qquad \text{Using bottom array only} \tag{5.8}$$

$$\chi^2_{\text{P,all}} = 2\sum_{i=1}^{178}() \qquad \text{Using all the PMTs in the TPC} \tag{5.9}$$

$$\chi^2_{\text{P,ratio}} = -2\log\left(\lambda_{\text{P}}^{\text{top total}} \cdot \lambda_{\text{P}}^{\text{bottom total}}\right) \qquad \text{Using top total/bottom total} \tag{5.10}$$

The content inside of each pair of parentheses is that in equation (5.6). When the parameter is defined for the top array only ($\chi^2_{\text{P,top}}$), $\{\nu_i\}$ is scaled to have the sum equal to $\sum_{i=1}^{98} n_i$, the sum of top total. The same normalization rule applies to all other χ^2_{P} parameters.

The motivation to have three separate χ^2_{P} parameters, $\chi^2_{\mathrm{P,top}}$, $\chi^2_{\mathrm{P,bot}}$ and $\chi^2_{\mathrm{P,ratio}}$, instead of using $\chi^2_{\mathrm{P,all}}$ only, is from the observation that for the *S1* signal the (top total)/(bottom total) ratio is far from 1. As can be seen in Fig. 5.3 (bottom), the bottom PMT array could get a few times higher number of photo-electrons than the top PMT array. If all the PMTs contribute equally to χ^2_{P} as in $\chi^2_{\mathrm{P,all}}$, the contribution from the bottom array would be dominating thus making the top array information less pronounced. Instead, when top and bottom arrays are normalized separately and the likelihood ratios are computed individually as in $\chi^2_{\mathrm{P,top}}$ and $\chi^2_{\mathrm{P,bot}}$, the contribution from both arrays will be incorporated more effectively. Additionally, the likelihood ratio from (top total)/(bottom total) is put into a third parameter $\chi^2_{\mathrm{P,ratio}}$ to catch the events with abnormal light pattern in terms of top/bottom ratio. To incorporate all the above considerations, a combined χ^2_{P} parameter is defined as

$$\chi^2_{\mathrm{P,cmb}} = \chi^2_{\mathrm{P,top}} + \chi^2_{\mathrm{P,bot}} + \chi^2_{\mathrm{P,ratio}}\,. \tag{5.11}$$

Although the distribution of Likelihood parameter should asymptotically approach the χ^2 distribution of number of degrees of freedom (NDF$= N_{\mathrm{PMT}} - 1$) when every PMT is well illuminated, in reality, events of interest have low *S1* and only a small portion of PMTs have non-zero photon counts. Therefore, the distribution of the likelihood parameter is dependent on *S1* total and calibration is required to establish a selection criterion based on $\chi^2_{\mathrm{P,cmb}}$. Fig. 5.4 shows $\chi^2_{\mathrm{P,top}}$, $\chi^2_{\mathrm{P,bot}}$ and $\chi^2_{\mathrm{P,ratio}}$ as functions of their respective normalization factors and *S1* total on which $\chi^2_{\mathrm{P,cmb}}$ depends. It is clear that $\chi^2_{\mathrm{P,top}}$ and $\chi^2_{\mathrm{P,bot}}$ are highly dependent on their respective total number of photo-electrons collected. When *S1* total is low, only a small number of PMTs see signals therefore NDF is low. As *S1* total increases, photons spread to more PMTs resulting in higher NDF. As *S1* total increases to even higher values χ^2_{P} approaches the expected NDF when all the PMTs are well illuminated.

The combined parameter $\chi^2_{\mathrm{P,cmb}}$ should however depend on the total signal of all the PMTs. Therefore, its constituents $\chi^2_{\mathrm{P,top}}$, $\chi^2_{\mathrm{P,bot}}$ and $\chi^2_{\mathrm{P,ratio}}$ are plotted as functions of *S1* total in Fig. 5.4 bottom so that the three parameters can be added together in the same *S1* total space. The sum is shown in Fig. 5.6. In the dark matter search relevant region with $cS1 < 30\,\mathrm{p.e.}$, the dependence of $\chi^2_{\mathrm{P,cmb}}$ on *S1* total is strong. Since there is no theoretical description of this dependence, and Monte Carlo is not reliable due to unknowns in material light response, an empirical procedure is used to address the dependence and define anomalous event selection criteria.

5.3 Identification of Anomalous Events

Neutrons are used to probe the detector response to nuclear recoils, and hence to WIMP dark matter particles. Therefore, we use neutron calibration data with single scatter selection to define a cut on anomalous events. As shown in Fig. 5.5, $\chi^2_{\mathrm{P,cmb}}$ is plotted as a function of raw *S1* total. The band is divided into *S1* total bins. Below 25 p.e., *S1* total is binned by 1 p.e.; above 25 p.e. it is binned by 5 p.e.. A Gaussian fit is performed in each *S1* total slice to determine the mean and σ. An *S1* total dependent cut is established at the $\mu + 2\sigma$ level. A function of form $\log(a + bx + cx^2)$ is used to fit the $\mu + 2\sigma$ points in each bin. Gaussian fits were used to avoid the high-end outliers known as neutron-X events. Analogous to gamma-X events, neutron-X events are neutron multiple

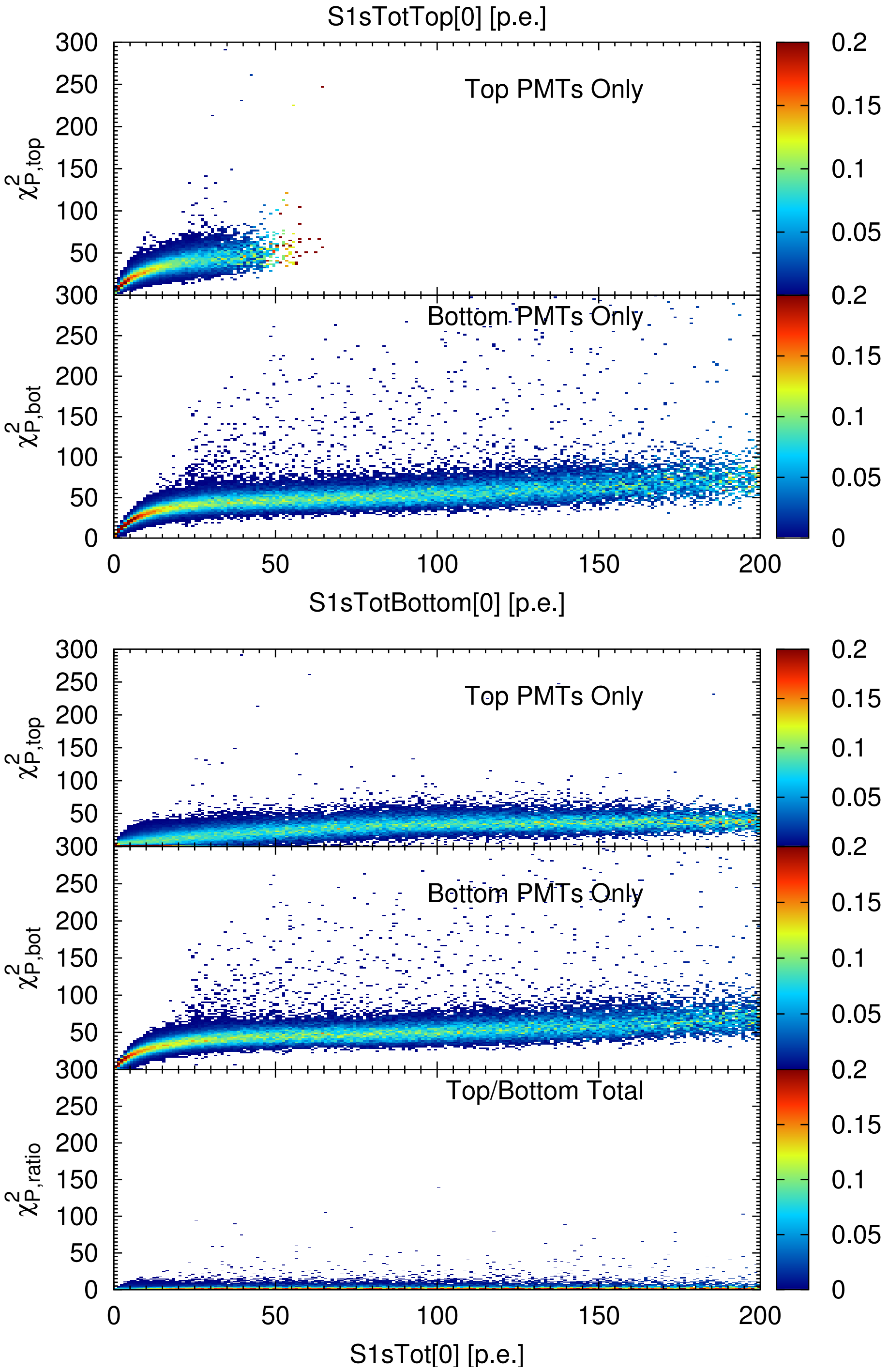

Figure 5.4: $\chi^2_{\mathrm{P,top}}$, $\chi^2_{\mathrm{P,bot}}$ and $\chi^2_{\mathrm{P,ratio}}$ as Functions of *S1* Total. Data from ^{60}Co electronic recoil calibration with *cS1* $< 200\,$p.e.. Color shows counts in the spectra. Top: $\chi^2_{\mathrm{P,top}}$ and $\chi^2_{\mathrm{P,bot}}$ vs. their respective normalization factors *S1* top total and *S1* bottom total. Bottom: $\chi^2_{\mathrm{P,top}}$, $\chi^2_{\mathrm{P,bot}}$ and $\chi^2_{\mathrm{P,ratio}}$ on the same *S1* total energy scale, so the three could be summed up meaningfully. Outliers are present at high χ^2_{P} values. They are anomalous events.

scatters with one interaction in the charge sensitive region and at least one interaction in the charge insensitive region.

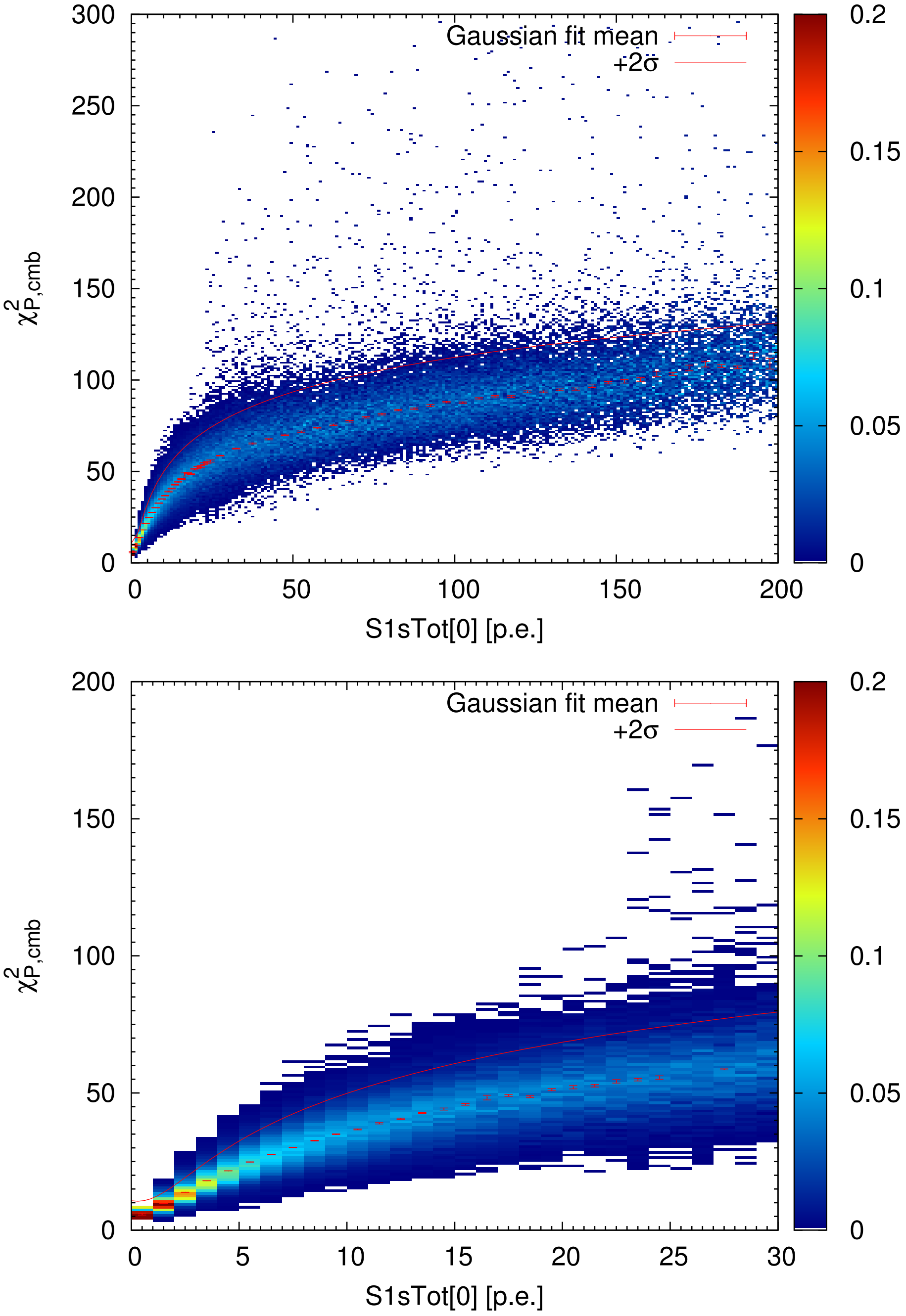

Figure 5.5: $\chi^2_{\mathrm{P,cmb}}$ vs. *S1* Total on Neutron Data. Color shows counts in the spectra. Red points with error bar show the Gaussian fit mean in each *S1* total slice. The red curve shows the cut defined at the $\mu + 2\sigma$ level. The bottom plot is the zoom of the top figure at low *S1* total.

After the cut is defined on the neutron calibration data, it is applied to the ^{60}Co electronic calibration data, as shown in Fig. 5.6. As a confirmation, the neutron data Gaussian fit results are overlaid as $\pm 1\sigma$ error bars, and they coincide well with the band shape of ^{60}Co. It confirms that $\chi^2_{\mathrm{P,cmb}}$ is a geometrical parameter, which depends only on the total number of photo-electrons but does not distinguish between nuclear and electronic recoils.

One major goal of the PMT pattern likelihood cut is to remove the anomalous leakage from the electronic recoil band into the dark matter search region that lies below the nuclear recoil median in the discrimination parameter space $\log(S2/S1)$. As shown in Fig. 5.7, a fraction of events (green dots) in ^{60}Co calibrated electronic recoil band is below the nuclear recoil band median (red curve). Some of those events are true single scatters and they appear to be below the nuclear recoil median purely due to statistical fluctuations. Some of them (red plus), however, are identified by the PMT pattern likelihood as anomalous events with additional *S1* coming from interactions in the charge insensitive region.

The anomalous events are identified as outliers above the $\mu + 2\sigma$ line in Fig. 5.6. In the energy range $0 < cS1 < 200$ p.e., anomalous events are concentrated close to the bottom of the detector, while true leakage (good) events are distributed evenly in the detector, as shown in Fig. 5.8. It is worth mentioning that the calibration source ^{60}Co is placed outside of the detector, therefore it is not surprising that there is a large event concentration at the outer border of the TPC.

For dark matter search, a fiducial volume is always selected to stay away from the border of the TPC. The performance of the PMT pattern likelihood cut is tested in the 40 kg fiducial volume and summarized in table 5.1. Since the cut is defined at $\mu+2\sigma$ on the nuclear recoil data, it loses 2.5 % of nuclear recoil or WIMP signal acceptance. At the mean time, the cut rejects 40 % to 70 % of leakage events. The cut reduces the leakage background in the dark matter search region significantly.

Energy range	Total leakage events	Cut away	Left over	Rejection
$cS1 < 20$ p.e.	88	36	52	41.0 %
20 p.e. $< cS1 <$ 200 p.e.	340	244	96	71.8 %

Table 5.1: PMT Pattern Likelihood cut performance on ^{60}Co leakage events in 40 kg fiducial volume. Rejection is defined as events failing the cut over the total number of leakage events.

Summary

With 3D positioning in the LXeTPC, an expected *S1* PMT pattern map for an interaction happening at (x, y, z) is established from calibration data. For an event under examination, its PMT pattern is compared to the expected pattern according to its reconstructed 3D position. The likelihood for the PMT pattern to be a legitimate single scatter event is computed. Events with anomalous PMT patterns are rejected with tested high efficiency.

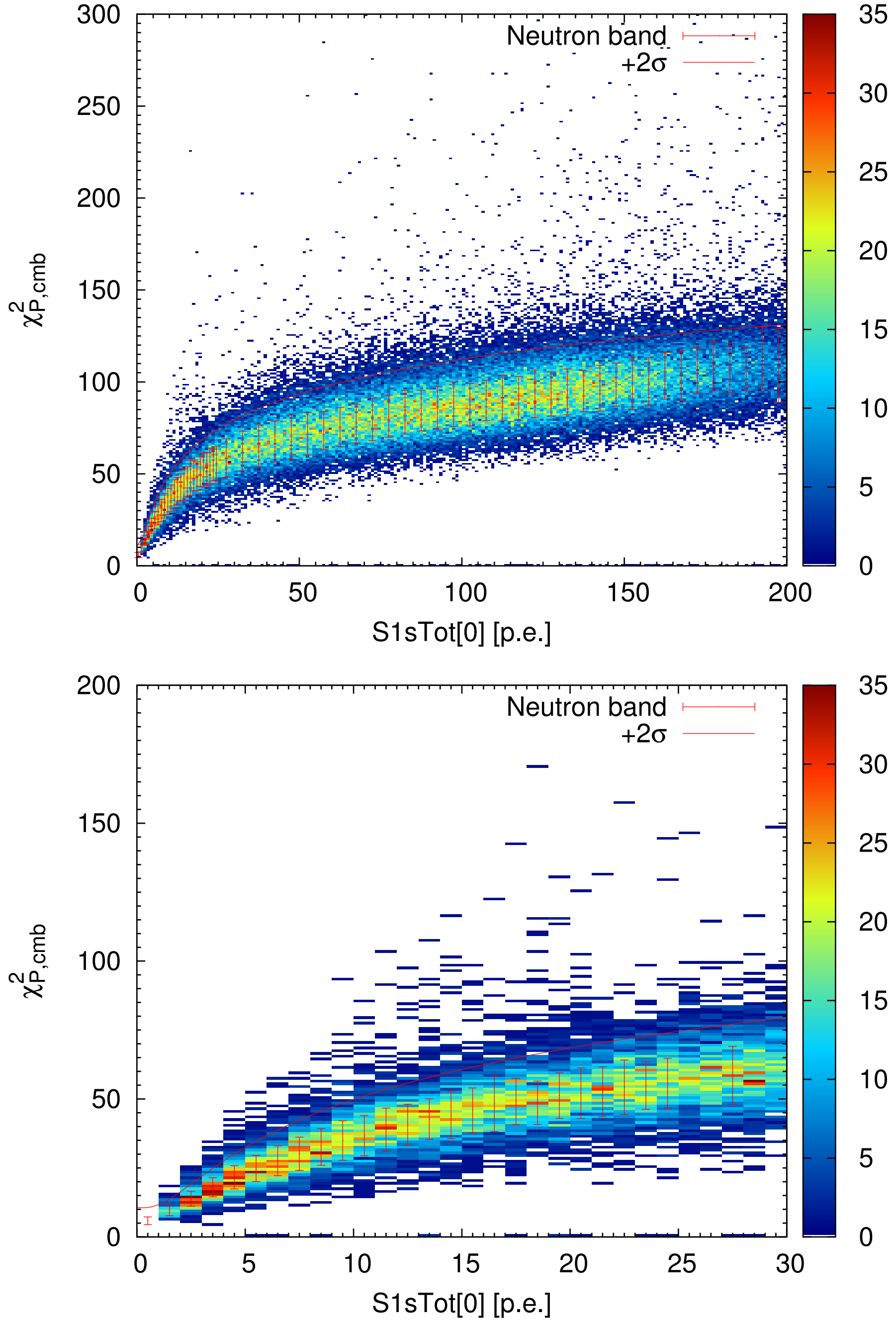

Figure 5.6: Removal of Anomalous Events in ^{60}Co Data. Color shows counts in the spectra. Red error bars show the Gaussian fit $\pm 1\sigma$ on neutron data. It is not an indication of any type of error but merely an overlay of neutron data on the ^{60}Co data. Red curve shows the $\mu + 2\sigma$ cut. Bottom plot is the zoom-in of the top one at low *S1* total.

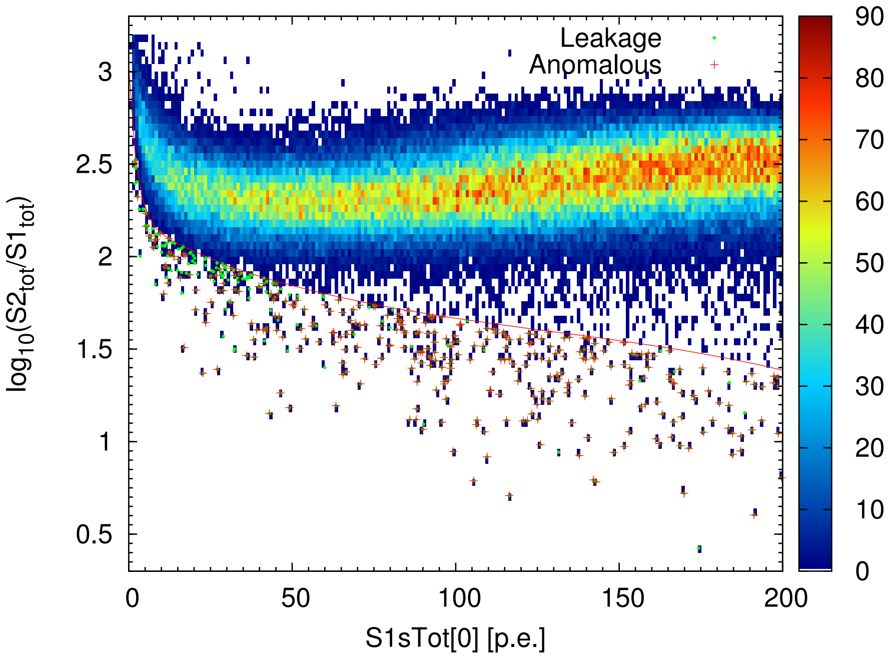

Figure 5.7: Removal of Anomalous Events in ^{60}Co Data Leaking Below Nuclear Recoil Median. Color shows electronic recoil band calibrated using ^{60}Co (with units in counts). Red curve shows the nuclear recoil median. Green dots are events in ^{60}Co leaking below the nuclear recoil median. When a green dot is overlaid with a red plus, the event is identified as an anomalous event and rejected.

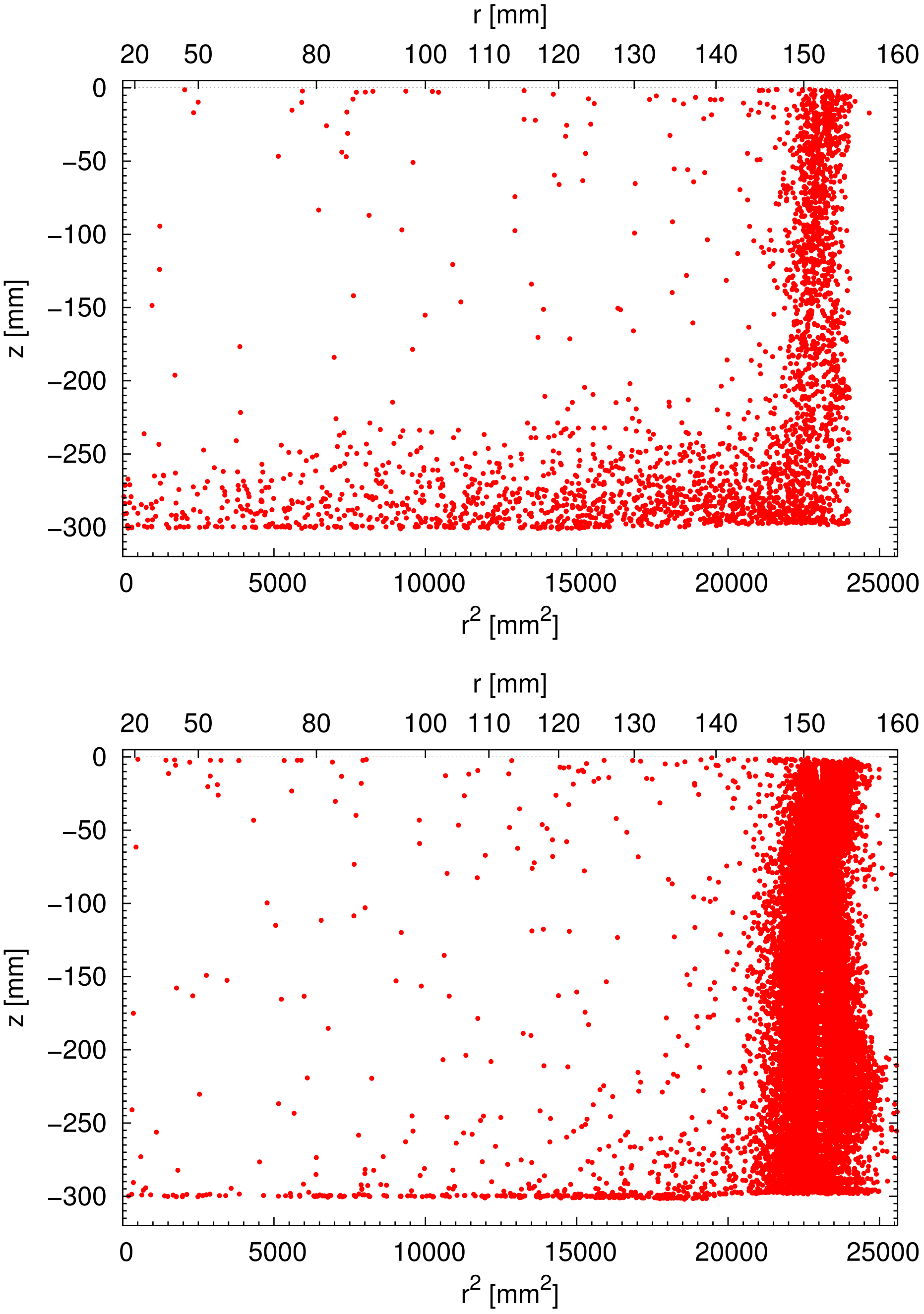

Figure 5.8: Spatial Distribution of Anomalous Events in ^{60}Co Data Leaking Below Nuclear Recoil Median. Events are selected in the energy range of $0 < cS1 < 200$ p.e.. Top: distribution of events identified as anomalous. Bottom: distribution of events passing the PMT pattern likelihood cut (good events).

Chapter 6

Results from 100.9 Days of Dark Matter Data in Run08

In winter 2009, from October 20th to November 12th, 11.17 live days of dark matter data was taken. This first dark matter result (Aprile et al. [7]) from XENON100 clearly demonstrated the excellent performance of the detector and its capability for dark matter search. Later on, between January 13th and June 8th, 2010, 100.9 live days of data was taken for dark matter search. Detector parameters were being continuously monitored. A small portion of exposure when questionable detector parameters were present is rejected and is not included in the 100.9 days of data. Dark matter data was blinded for the region of interest and was not accessible to analyzers. Analysis was built upon calibration data and an unblinded part of dark matter data outside of the dark matter region of interest. Data were unblinded after the WIMP search region was finalized and analysis tools were ready. This chapter describes the results from 100.9 days of dark matter search.

6.1 WIMP Search Region of Interest (ROI)

As described in Chapter 3, XENON100 uses scintillation light *S1* to determine the energy deposition, and log(*S2*/*S1*) as the discrimination parameter. To identify an event as a WIMP interaction, it is necessary to know its energy deposition as well as to identify it as nuclear recoil instead of electronic recoil background. Therefore, a WIMP search window (or "region of interest", ROI) is defined in the log(*S2*/*S1*)-*S1* space. The ROI has four sides, based on calibration data shown in Fig. 6.1. The left and right sides are set at 4 p.e. and 30 p.e. in *S1*, defining the energy window for WIMP search. The choice of 4 p.e. as the lower boundary is based on the ability for the software to pick *S1* pulses out of noise in raw waveforms. The upper bound is chosen at 30 p.e. due to the fact that the expected WIMP recoil spectrum drops rapidly as energy deposition increases. Expanding the energy range to even higher values would not benefit the WIMP search much but rather add more background. The upper bound of the ROI is set at 99.75 % rejection of electronic recoil events (2.807σ assuming the band is of Gaussian shape). Based on electronic recoil calibration, the meaning of this line is that below this line, 0.25 % of electronic recoil events are expected to be present and are no longer distinguishable from nuclear recoil events. The lower bound of the ROI is a composition of two lines: raw $S2 > 300$ p.e. and nuclear recoil band 3σ lower limit, whichever is higher. Raw $S2 > 300$ p.e. is the software $S2$ threshold, chosen to stay above the trigger threshold. The nuclear recoil band 3σ lower limit is chosen to eliminate events with very small $S2$s, which are likely noise. With all the four sides determined, the WIMP search ROI is setup. It is shown as the blue shaded area in Fig. 6.2.

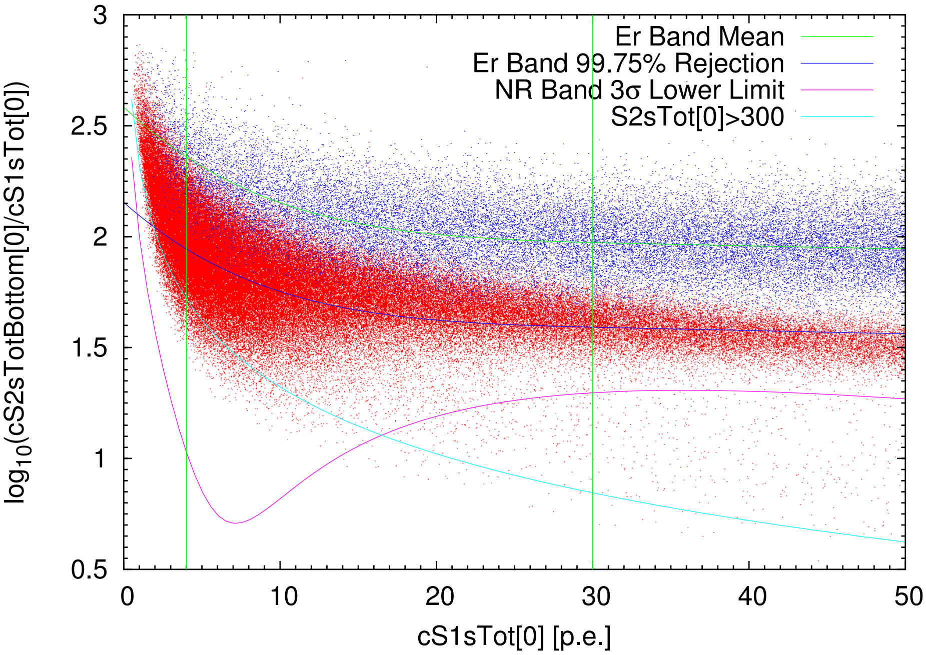

Figure 6.1: Electronic recoil and Nuclear Recoil Bands. Red dots represent nuclear recoil (from ^{241}AmBe source) while blue dots represent electronic recoil (from ^{60}Co source). Note that the light blue curve representing `S2sTot[0]>300` is only approximate, since one cannot draw a line corresponding to $S2$Tot in the c$S2$TotBottom space.

Also, a 48 kg fiducial volume is selected, shown as the green curve in Fig. 6.7. Since the external backgrounds are mostly stopped at the outer border of the sensitive volume, a fiducial volume selected to be away from the edge could reduce the background. At the same time, to increase the total exposure, fiducial volume is desired to be as large as possible. The choice of 48 kg is the balance between the two major counter-acting factors.

6.2 Background Prediction

In the WIMP search ROI, the observed events are a mixture of background and true WIMP events. Since the essence of WIMP search is to see if there is excess of events on top of the background events from known physics, it is very important to predict the number of background events in the ROI. The background constitutes two parts: the neutron background and the electronic recoil background that “leaks” from electronic recoil band into the WIMP ROI. The electronic recoil background is referred to as the "leakage" background.

The neutron background in the XENON100 detector comes from two sources: (α, n) reaction and spontaneous fission from detector and shield materials, and muon induced neutrons. We rely solely on Monte Carlo simulation to predict neutron background from both sources. The simulation (Kish [33]) shows that in 100.9 days, in the WIMP ROI, $0.11^{+0.08}_{-0.04}$ neutron events in total are expected.

The electronic recoil leakage background can be decomposed into two parts as well: the Gaussian leakage and the anomalous leakage. The electronic band is assumed to have Gaussian shape in $\log(S2/S1)$. Since the upper bound of WIMP ROI is set at 99.75 % rejection, there are still 0.25 % of events below the line. This is referred to as the Gaussian leakage. Another type of events, which are multiple scatter electronic recoil events, but show only one $S1$ and one $S2$ therefore pass all the event selection cuts, are also present in the WIMP ROI. As discussed in Chapter 5, a cut is developed to remove such events, however, the cut is not 100 % efficient so that a small number of such events still exist. This type of event is referred to as the anomalous leakage. ^{60}Co data is used to estimate the leakage into the WIMP ROI, as shown in Fig. 6.2.

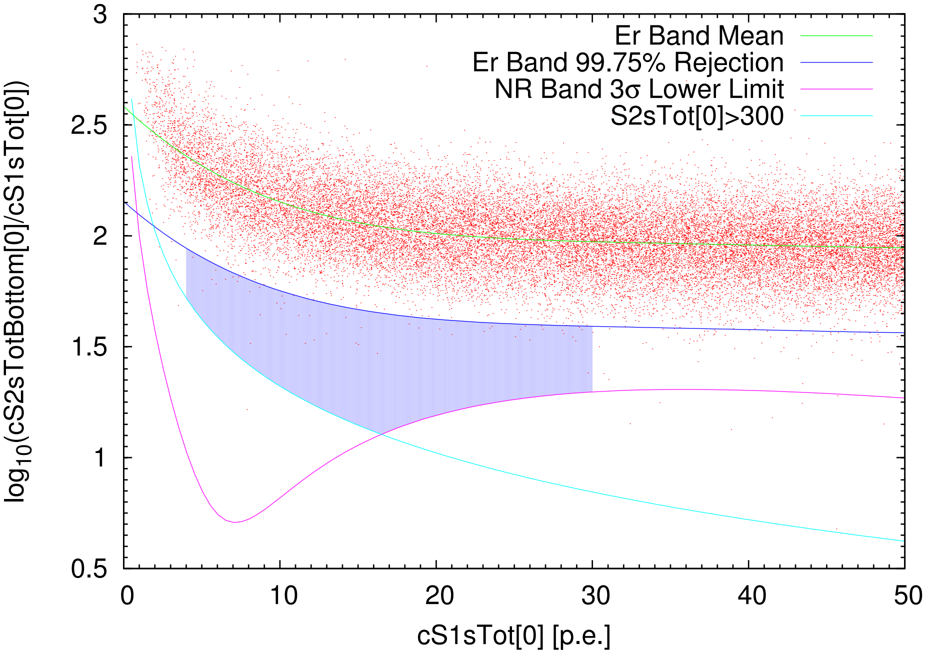

Figure 6.2: ^{60}Co Band for Background Prediction.

To estimate the Gaussian leakage, the electronic recoil band is flattened to have zero mean in $\log(S2/S1)$ regardless of $S1$. The procedure is to obtain mean values in each $S1$ slice (1 p.e. wide) of the band, and fit a polynomial through all the mean points (green curve in Fig. 6.2), then subtract this mean line from every point in the electronic recoil band. This procedure removes the energy ($S1$) dependence of the band and guarantees a zero mean value of the band. The flattened band is shown in Fig. 6.3 (Top). The shape of WIMP ROI is transformed accordingly. Since the energy dependence is removed, the band could be summed up in $S1$ throughout the ROI from 4 p.e. to 30 p.e.. The spectrum of $\Delta \log(S2/S1)$ is shown in Fig. 6.3 (Bottom). A Gaussian fit to the summed spectrum confirms that the bulk of the spectrum could be described by Gaussian very well, where some excess of events do exist in the tail at low $\Delta \log(S2/S1)$ value which is in the WIMP ROI. The excess in the tail is precisely the anomalous leakage. Since the bulk of the band is well described by a Gaussian, it is straightforward to estimate the Gaussian leakage using the fitted value and scaling the exposure using the number of events seen in the calibration data and in the bulk part of dark matter data. The Gaussian leakage is estimated to be 1.14 ± 0.48 in 100.9 days.

The excess of events on top of the expected Gaussian leakage is considered as anomalous leakage. Monte Carlo simulation shows that ^{60}Co data models anomalous events from the background well. Therefore it is justified to use ^{60}Co data to estimate the anomalous leakage in the background. The excess is computed by subtracting the expected Gaussian leakage. It is then scaled according to the exposure, yielding an anomalous leakage prediction of $0.56^{+0.21}_{-0.27}$.

Combining all the background contributions in the WIMP ROI, the total background prediction for 100.9 days exposure is 1.8 ± 0.6 events. Background contributions are summarized in Tab. 6.1.

Neutron Background	Gaussian Leakage	Anomalous Leakage	Total
$0.11^{+0.08}_{-0.04}$	1.14 ± 0.48	$0.56^{+0.21}_{-0.27}$	1.8 ± 0.6

Table 6.1: Background Estimation in WIMP ROI

6.3 Event Selection and Acceptance

Setting up a WIMP ROI according to the electronic recoil background rejection only establishes how well we can reject the background. To complete the analysis, the probability of accepting WIMP events has to be estimated as well. The WIMP acceptance is the product of two acceptances: the overall event selection acceptance and the nuclear recoil acceptance in the WIMP ROI.

So far not mentioned, but assumed by default, is that all the events in both calibration and background (dark matter) data, are events that pass through a series of selection criteria, or "cuts". The cuts are designed to serve two major purposes: to reject noise while accepting true physical events, and to pick up single scatter events. All the cuts used are listed in Tab. 6.2. Every cut is associated with an acceptance. The acceptance is not about how many events pass the cut out of the total number of events to start with, but the probability that real desired physical events are accepted by the cut. The distinction is that, for instance, if a cut removes only noise, its acceptance is 100 %. Various techniques and data samples were used to estimate the acceptance of each cut. The acceptances of some of the cuts, such as *S1* coincidence and *S1* PMT pattern cuts, have been discussed in previous chapters. Overall, with all the cuts combined, the acceptance is shown in Fig. 6.5 (blue curve) as a function of *S1*. The rising in acceptance from low *S1* to about 8 p.e. is mainly due to the *S1* coincidence requirement and *S2* threshold. Afterwards, at higher energies, the acceptance becomes more or less constant at about 80 %.

The cut acceptance characterizes the overall probability a desired physical event is selected. Applied to nuclear recoil events, it is the acceptance of the whole nuclear recoil band. However, due to the way that the WIMP ROI is setup, especially the fact that the upper bound—99.75 % electronic recoil rejection line, is cutting deep into the nuclear recoil band (Fig. 6.4 blue curve),

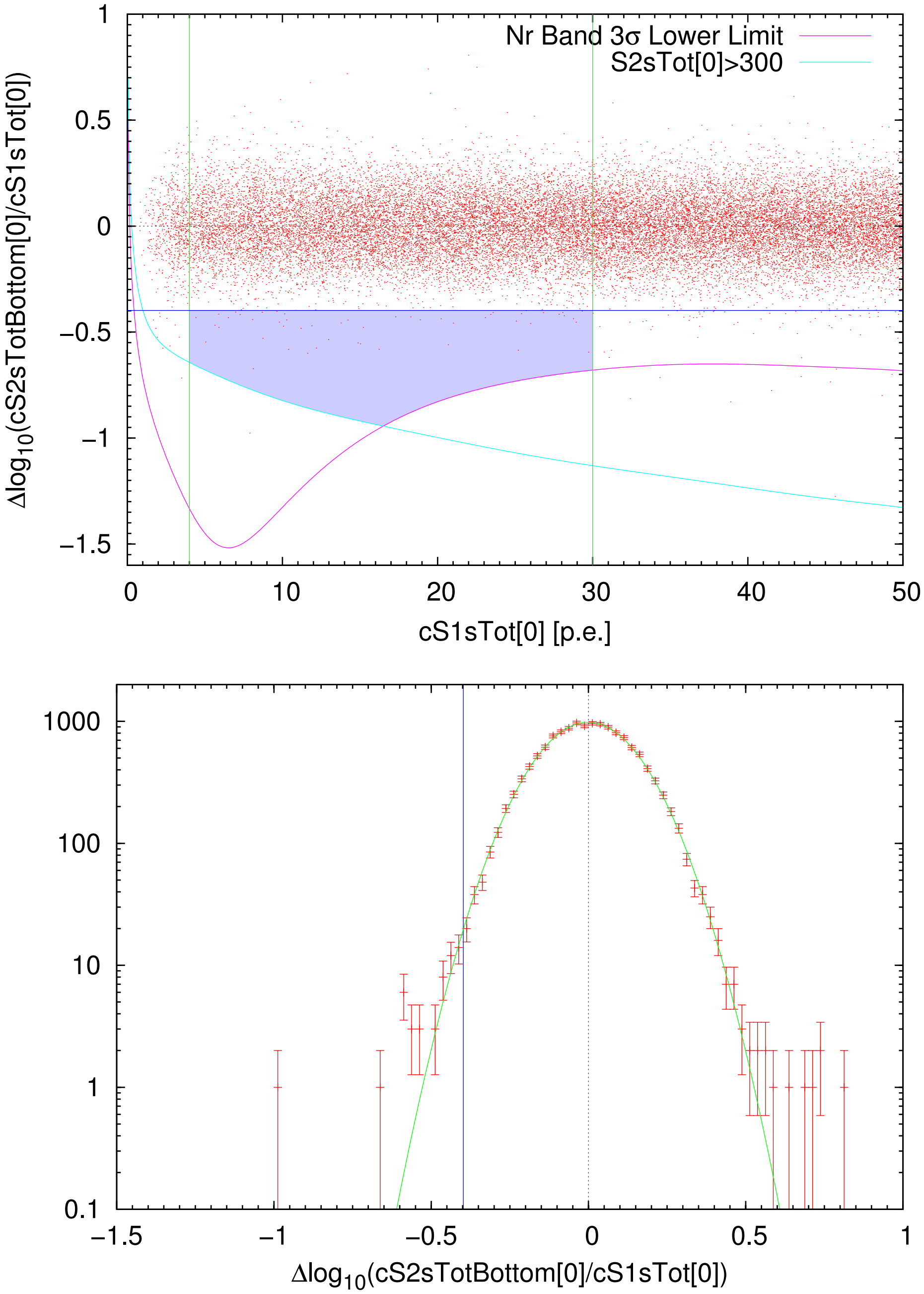

Figure 6.3: ^{60}Co Band in Flattened Space for Background Prediction. Top: flattened band and corresponding WIMP ROI. Bottom: spectrum of the flattened band summed from 4 p.e. to 30 p.e. and a Gaussian fit. The blue line marks the 99.75 % rejection.

Cut	Description
`Xsignalnoise2`	Selection on signal-to-noise ratio.
`Xs2asym0`	Selection on *S2* asymmetry.
`Xs2pmtorder0`	Remove hot spots where only one PMT sees unusually high *S2*.
`Xs1coin0`	Requiring at least 2 PMTs see signal.
`Xs2peaks0`	Requiring raw *S2* to be larger than software threshold 300 p.e..
`Xs2width5`	Removing *S2*s with unusual width according to their drift time.
`Xhighlog0`	Removing events with unusually high $\log(S2/S1)$ value.
`Xlownoise0`	Removing gas events according to *S2*.
`Xs1single4`	Selecting events with single *S1* pulse.
`Xs2single3`	Selecting events with single *S2* pulse.
`Xs1patternlnl1`	Removing events with anomalous *S1* PMT pattern.
`Xveto2`	Removing events with energy deposition in the active veto.
`Xposrec1`	Removing events with reconstructed positions not agreed among the three position reconstruction methods.
`Xs2chisquare0`	Removing events with unusually high χ^2 in position reconstruction.

Table 6.2: Event Selection Cuts. Leading 'X' represents a cut. Trailing number indicates the version of the cut.

WIMP acceptance must be much reduced. To estimate the WIMP acceptance in the ROI, we do simple number counting, to compute the fraction of nuclear recoil events in the WIMP ROI out of the total number of nuclear recoil events. The fraction, which is the nuclear recoil acceptance in the WIMP ROI, is shown as green points in Fig. 6.5.

Eventually, the total WIMP acceptance, which is the product of cut acceptance and nuclear recoil acceptance in the ROI, is shown as the red curve in Fig. 6.5 The WIMP acceptance is at 20 % to 30 % level.

6.4 WIMP Candidate Events

With WIMP ROI defined and event acceptance determined, it is now ready to investigate into the real dark matter data in run08.

6.4.1 Blind Analysis

The XENON100 collaboration followed the practice of blind analysis to investigate the dark matter data. The dark matter region, which is the later defined ROI plus some extra margin (*S1* up to 40 p.e. and discrimination parameter below 90 % electronic recoil rejection), was automatically masked by software and not visible to anybody. Analyzers were able to use all the calibration data and background data that is away from the dark matter region, to optimize the cuts, to refine the WIMP ROI, to determine the acceptance, to estimate the background events, and to improve the analysis tools. Only when all the parameters were settled and all tools were in place, we opened the dark matter region, or "unblinded" the data.

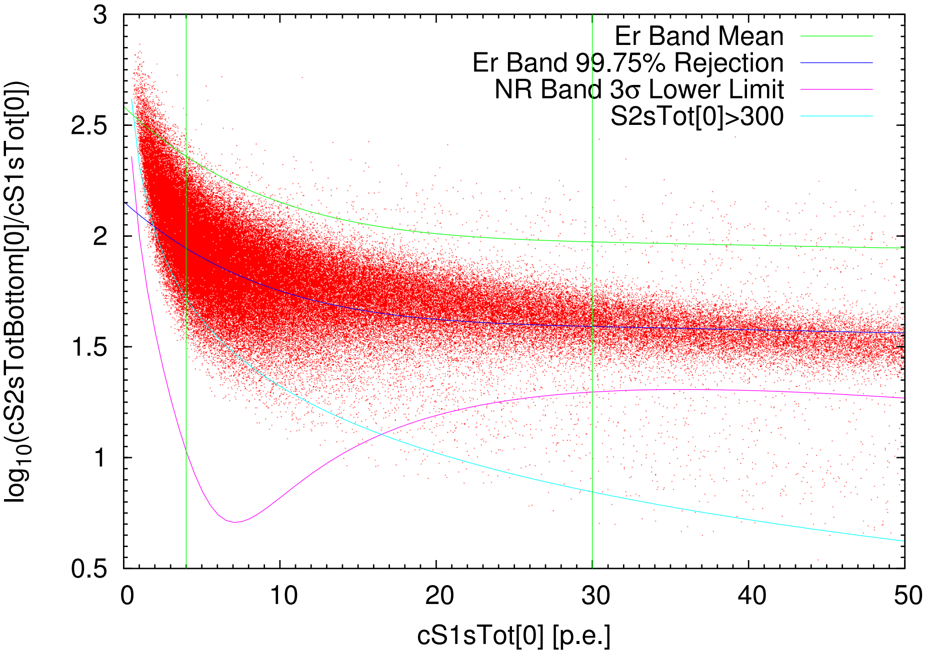

Figure 6.4: Nuclear Recoil Band.

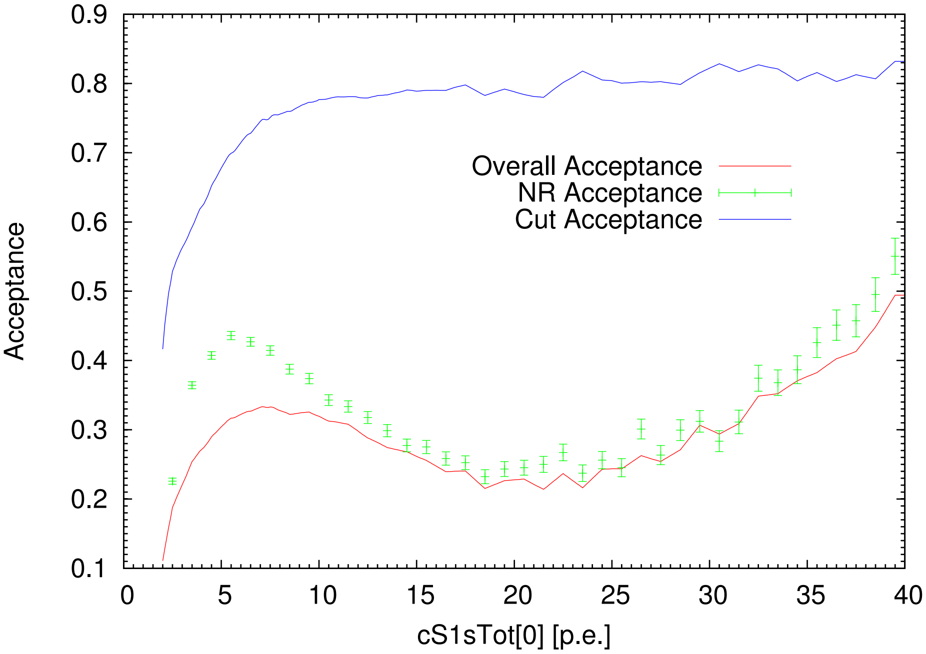

Figure 6.5: Acceptance. Cut acceptance is the acceptance of cuts applied on all the nuclear recoil events. Nuclear recoil acceptance is the acceptance of nuclear recoil events in the WIMP ROI. The overall acceptance is the product of the two.

The unblinded data is shown in Fig. 6.6. There are six events in the a priori defined WIMP ROI. They are labeled as WIMP candidate events and are listed in Tab. 6.3. Their spatial distribution is shown in Fig. 6.7

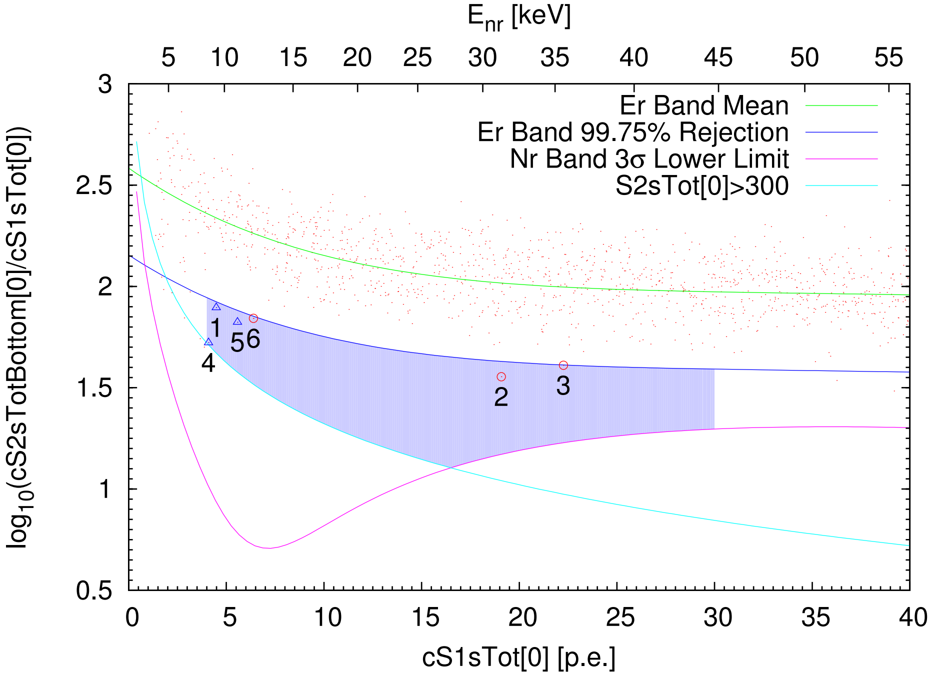

Figure 6.6: Dark Matter Candidate Events in the Region of Interest. Event No. 1,4,5 (blue triangle) are identified as noise and are later removed from WIMP exclusion limit computation. Event No. 2,3,6 (red circle) are valid WIMP candidates.

id	dataset	event id	c*S1* [p.e.]	c*S2*Bottom [p.e.]	noise?
1	`xe100_100122_1202_000022`	22575	4.48596	352.394	Yes
2	`xe100_100123_1948_000072`	72663	19.0802	684.069	No
3	`xe100_100212_1727_000070`	70062	22.2635	909.144	No
4	`xe100_100329_1619_000011`	11764	4.08904	215.575	Yes
5	`xe100_100518_1223_000010`	10207	5.57245	370.857	Yes
6	`xe100_100603_1620_000038`	38063	6.3934	444.902	No

Table 6.3: Dark Matter Candidate Events. Event No. 1,4,5 are identified as noise and are later removed from WIMP exclusion limit computation.

In the energy region of WIMP search, not considering the discrimination, there are many events in 100.9 days distributing almost uniformly in the detector except for the edges. Nearly all of them are electronic recoil events therefore are outside of WIMP ROI. While electronic recoil background events happen close to the edge of the sensitive volume are likely to be from external sources, events in the 48 kg fiducial volume are mostly from beta decay of ^{85}Kr that is well mixed with liquid xenon. Although ^{85}Kr is only at ppt level of concentration in liquid xenon, after distillation removal, it still dominates the electronic background in the fiducial volume. Thanks to the discrimination power using $\log(S2/S1)$, only 1.8 ± 0.6 of electronic recoil background events would leak into the WIMP

ROI. Therefore, the observed 6 events would be a clear excess over background, which indicates the observation of WIMPs. However, before drawing a clear conclusion, the six WIMP candidate events should be closely examined event by event.

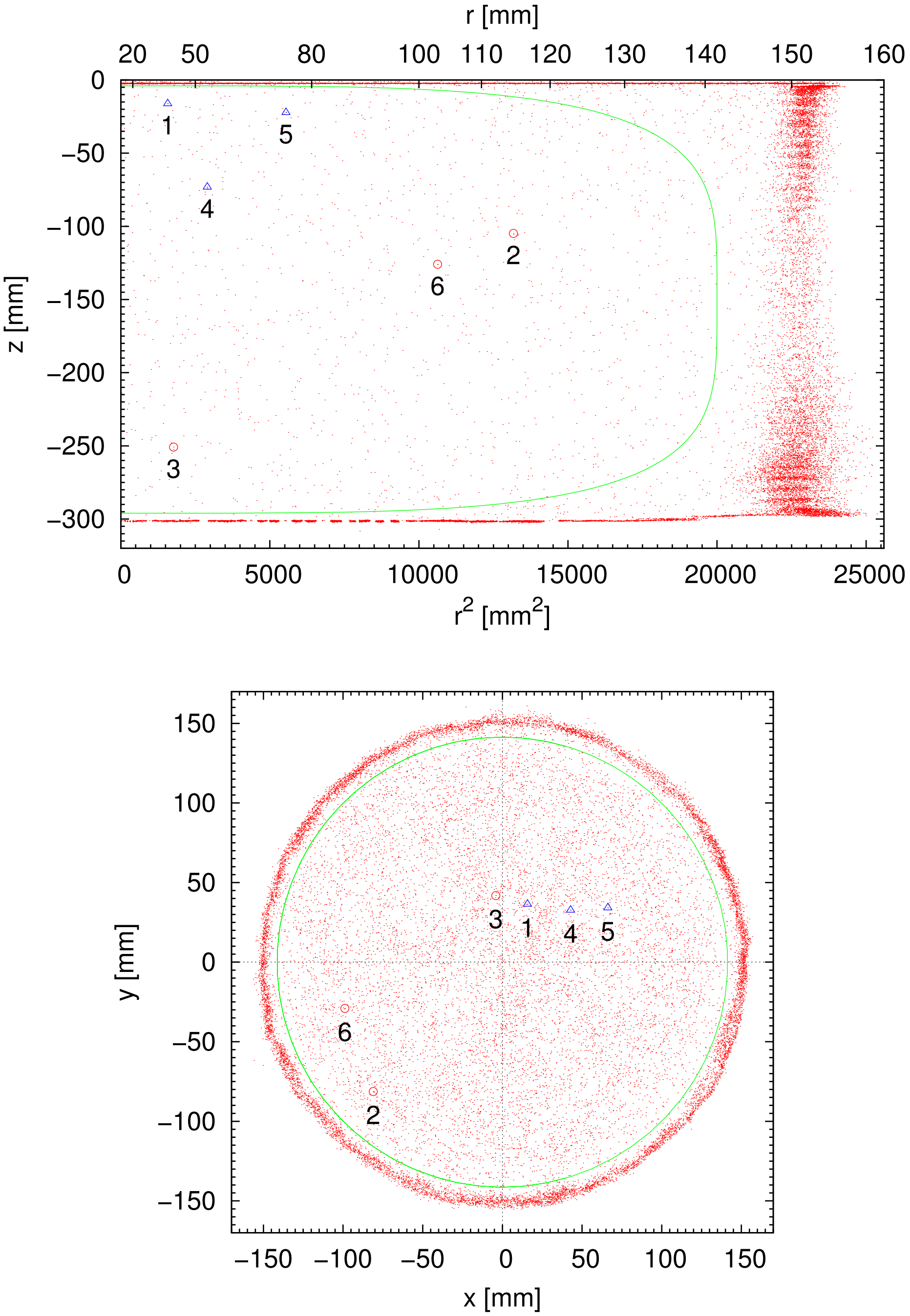

Figure 6.7: Spatial Distribution of Dark Matter Candidate Events. Red dots are all background events in the range $4 \leq cS1 \leq 30\,$p.e.. Red circles represent WIMP candidate events. Blue triangles mark noise events in the WIMP ROI. Green curve shows the boundary of 48 kg fiducial volume.

6.4.2 Post-Unblinding Discussion

In principle, following a blind analysis protocol, one should take the outcome as is after unblinding, and use it for final results. However, in reality, despite the tremendous effort put into refining the analysis, nonphysical events could still pass through all the selection criteria, and we cannot use such events as WIMP signals. Event inspection is necessary to identify nonphysical events. A clear sign of nonphysical event is noise being picked up as *S1* in waveform. Physical *S1* should be a highly asymmetric spike sticking out of the baseline, while noise is usually symmetric oscillation around the baseline.

Another good reason to reject events with wrongly picked up *S1*, is that such events would have wrong reconstructed position in (x, y, z) thus wrong corrected *S1* and *S2*. Since the wrong *S1* is picked up, such *S1* is not related to the *S2* at all so that the drift time, hence z, is wrong. Since *S1* light yield correction and *S2* electron lifetime corrections rely on z, their values after correction would be wrong. Since the energy scale and discrimination both rely on *S1* and *S2*, wrong values could just accidentally place them in the WIMP ROI.

Details about these six dark matter candidate events, their *S1* and *S2* PMT patterns, and waveforms, are shown from Fig. 6.8 to Fig. 6.13. Waveforms are the sum of all 178 PMT channels with individual PMT gain corrected. From visual inspection, all the 6 candidate events have good *S2*s, however, 3 of them have bad *S1*s. It is summarized in the following:

1. *S1* picked up at $t \approx 210\,\mu\text{s}$ is a good $2 \sim 3\,\text{p.e.}$ spike only seen by PMT125, together with a noise packet seen by PMT152. The noise on PMT152 exceeds *S1* threshold, hence is considered as a valid *S1*. Together with PMT125, the total *S1* passes the 2-fold coincidence requirement therefore is picked up. However, because PMT152 gives only noise, the coincidence condition is falsely satisfied. This event should be rejected.

2. *S1* picked up at $t \approx 157.8\,\mu\text{s}$ is a good *S1*. This is a valid WIMP candidate event.

3. *S1* picked up at $t \approx 73.4\,\mu\text{s}$ is a good *S1*. This is a valid WIMP candidate event.

4. *S1* picked up at $t \approx 176.5\,\mu\text{s}$ is a clear noise packet oscillating around the baseline. This event should be rejected.

5. *S1* picked up at $t \approx 206.5\,\mu\text{s}$ is a clear noise packet oscillating around the baseline. This event should be rejected.

6. *S1* picked up at $t \approx 145.6\,\mu\text{s}$ is a good *S1*. This is a valid WIMP candidate event.

Noise packets on the waveform baseline have 100 kHz repetition rate, and they are induction from PMT high voltage power supply. A new cut, putting more stringent requirement on *S1* pulse width, and require that when symmetric noise is seen on a PMT channel, the *S1* coincidence requirement is added by 1, could remove all the noise events in the WIMP ROI and in the electronic recoil background band.

The conclusion from the post-unblinding event inspection, is that 3 out of the 6 WIMP candidate events are noise. Only the left over 3 events should not be considered as true WIMP candidates.

Since 3 events is not far from estimated background of 1.8 ± 0.6 events, we cannot claim a WIMP discovery, but rather set an upper limit for WIMP exclusion.

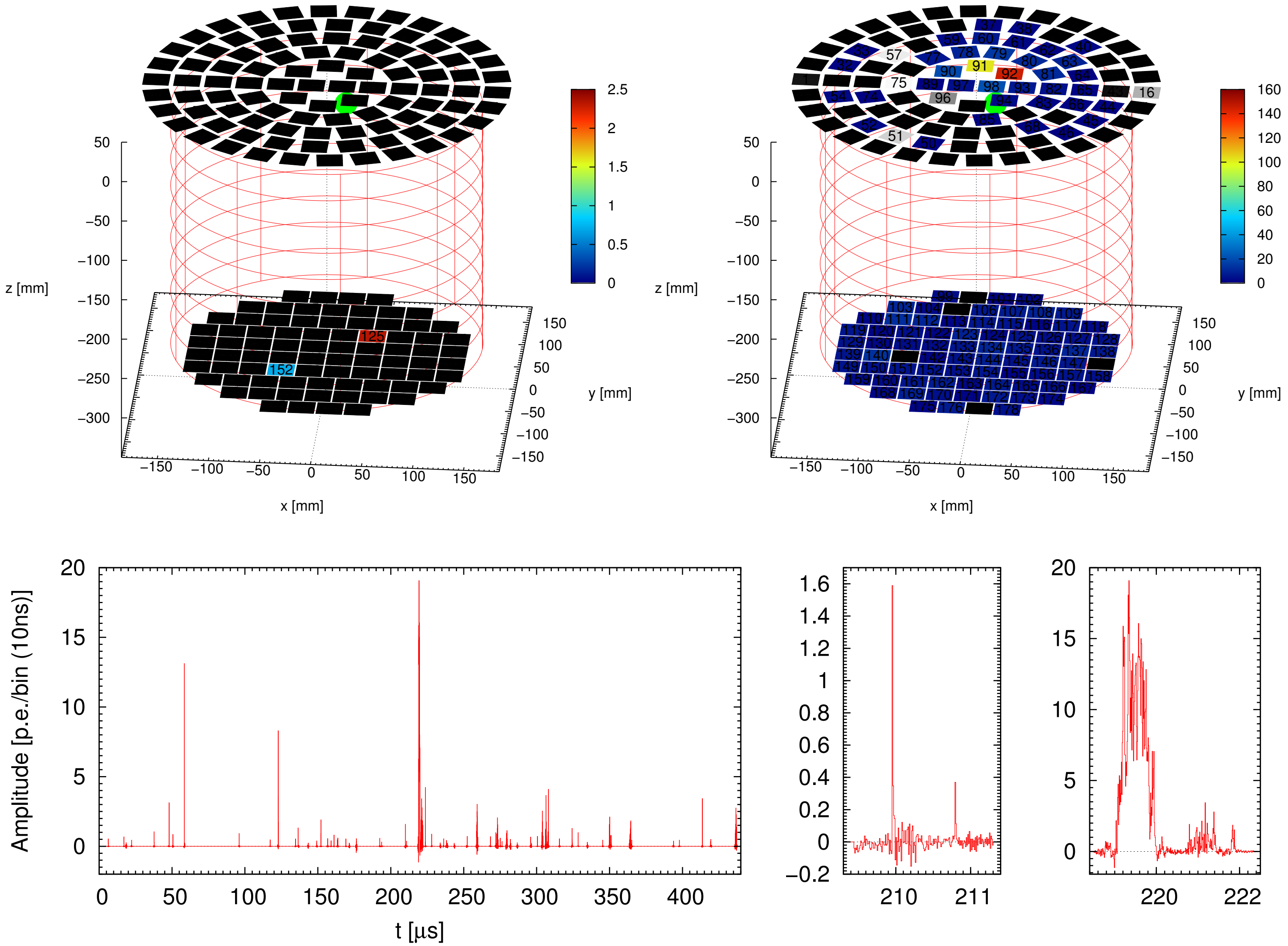

Figure 6.8: WIMP Candidate Event 1. *S1*, *S2* patterns and waveform. Color scale shows number of photo-electrons (p.e.)

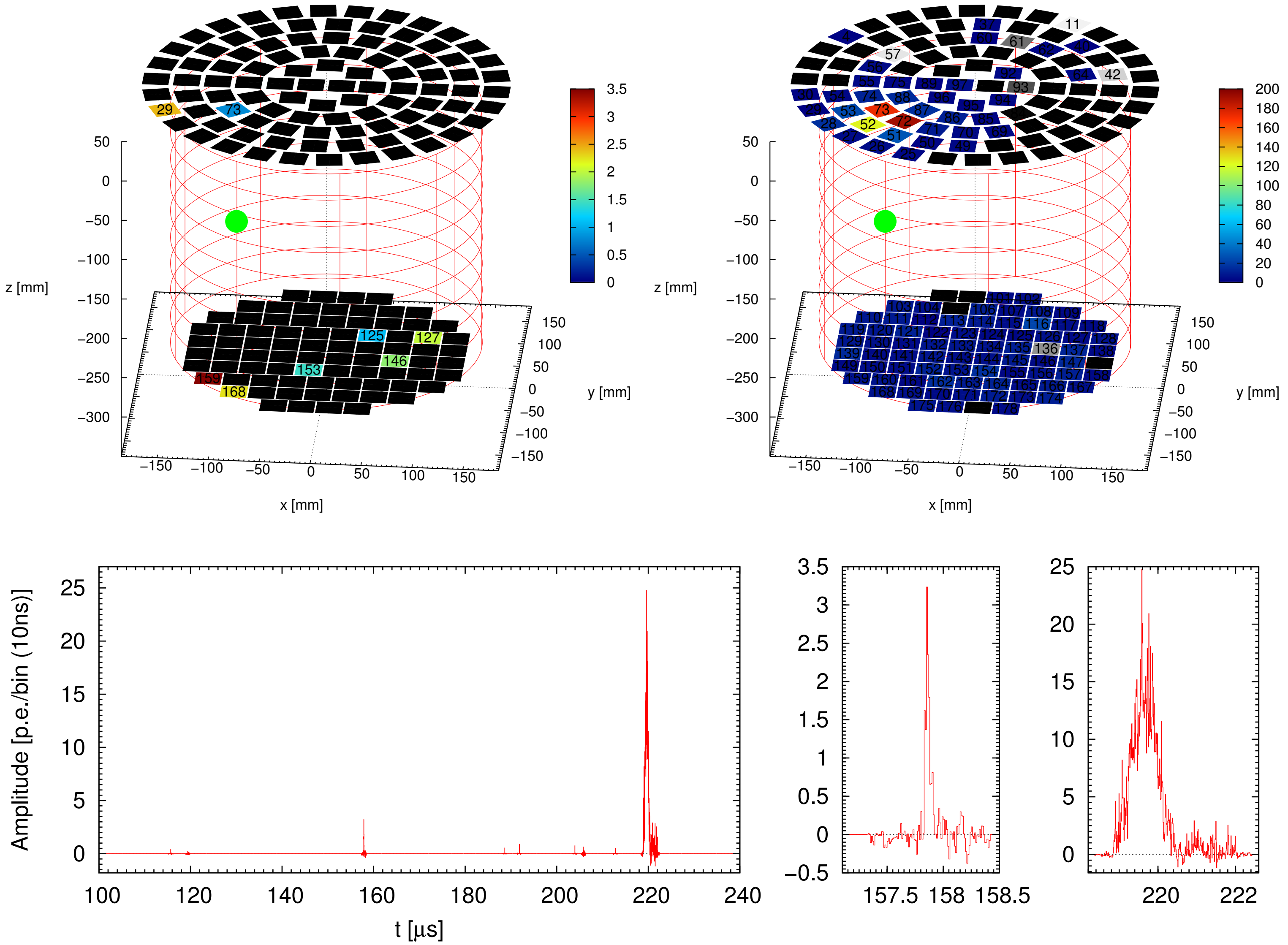

Figure 6.9: WIMP Candidate Event 2. *S1*, *S2* patterns and waveform.

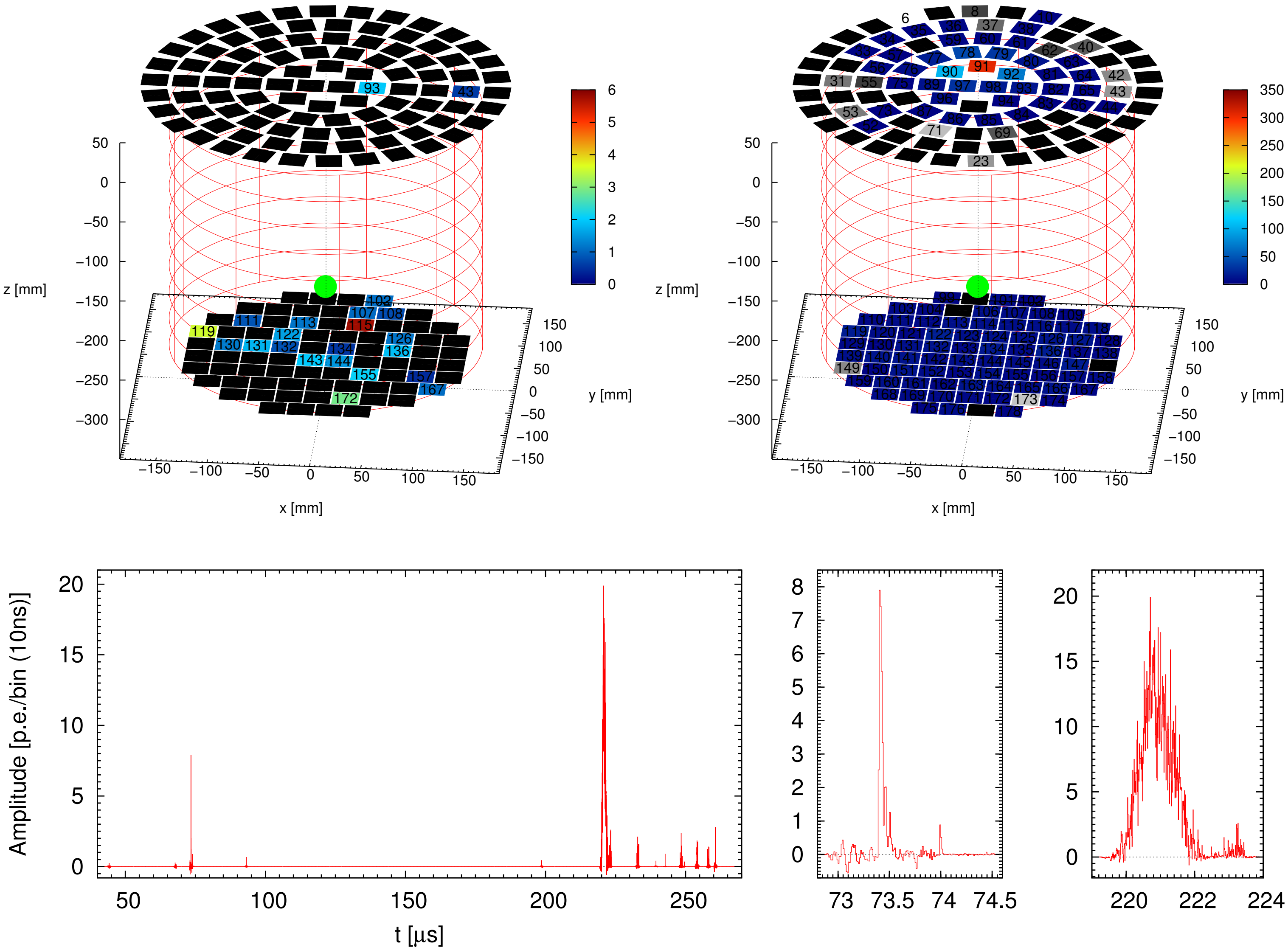

Figure 6.10: WIMP Candidate Event 3. *S1*, *S2* patterns and waveform.

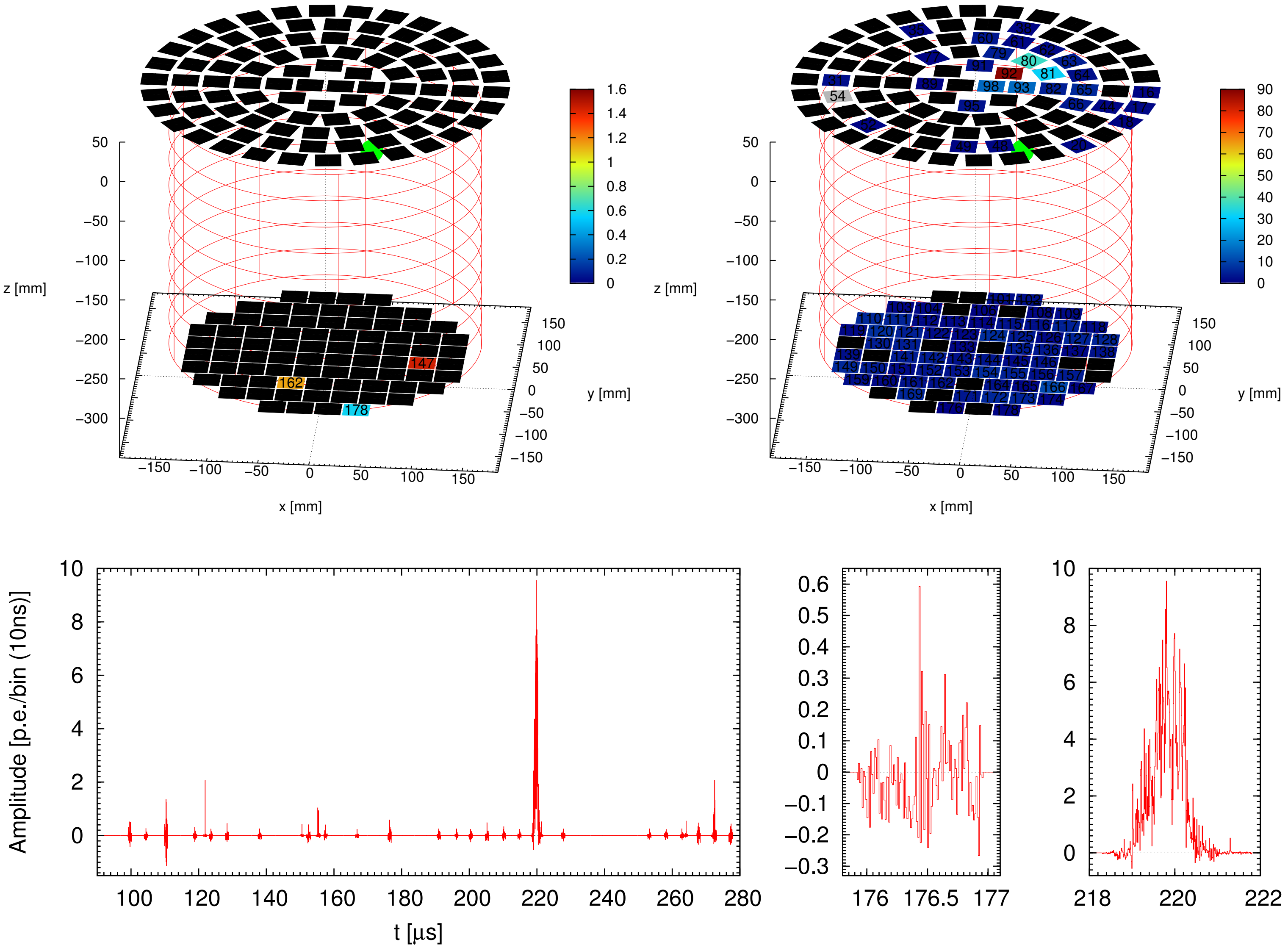

Figure 6.11: WIMP Candidate Event 4. *S1*, *S2* patterns and waveform.

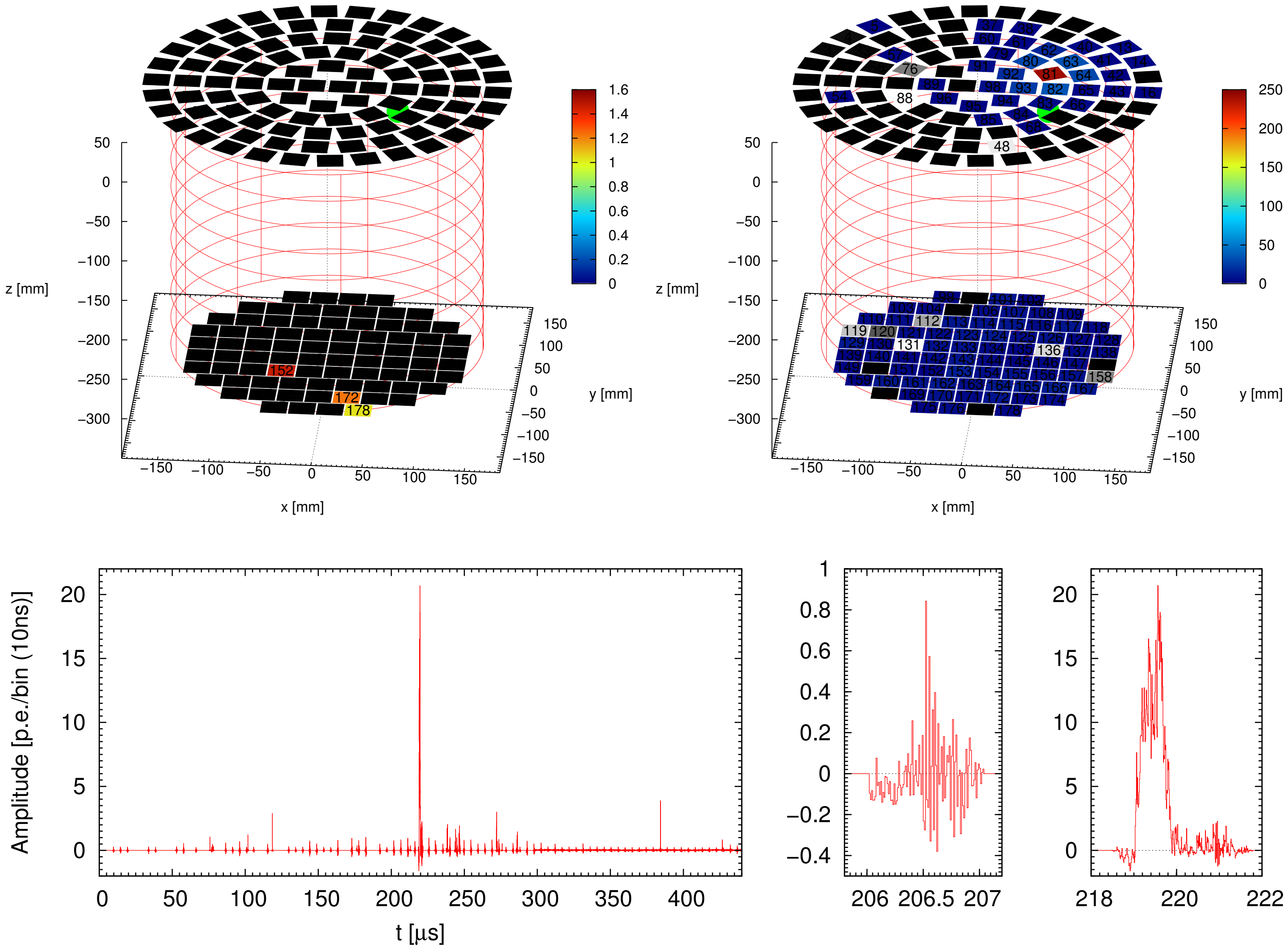

Figure 6.12: WIMP Candidate Event 5. *S1*, *S2* patterns and waveform.

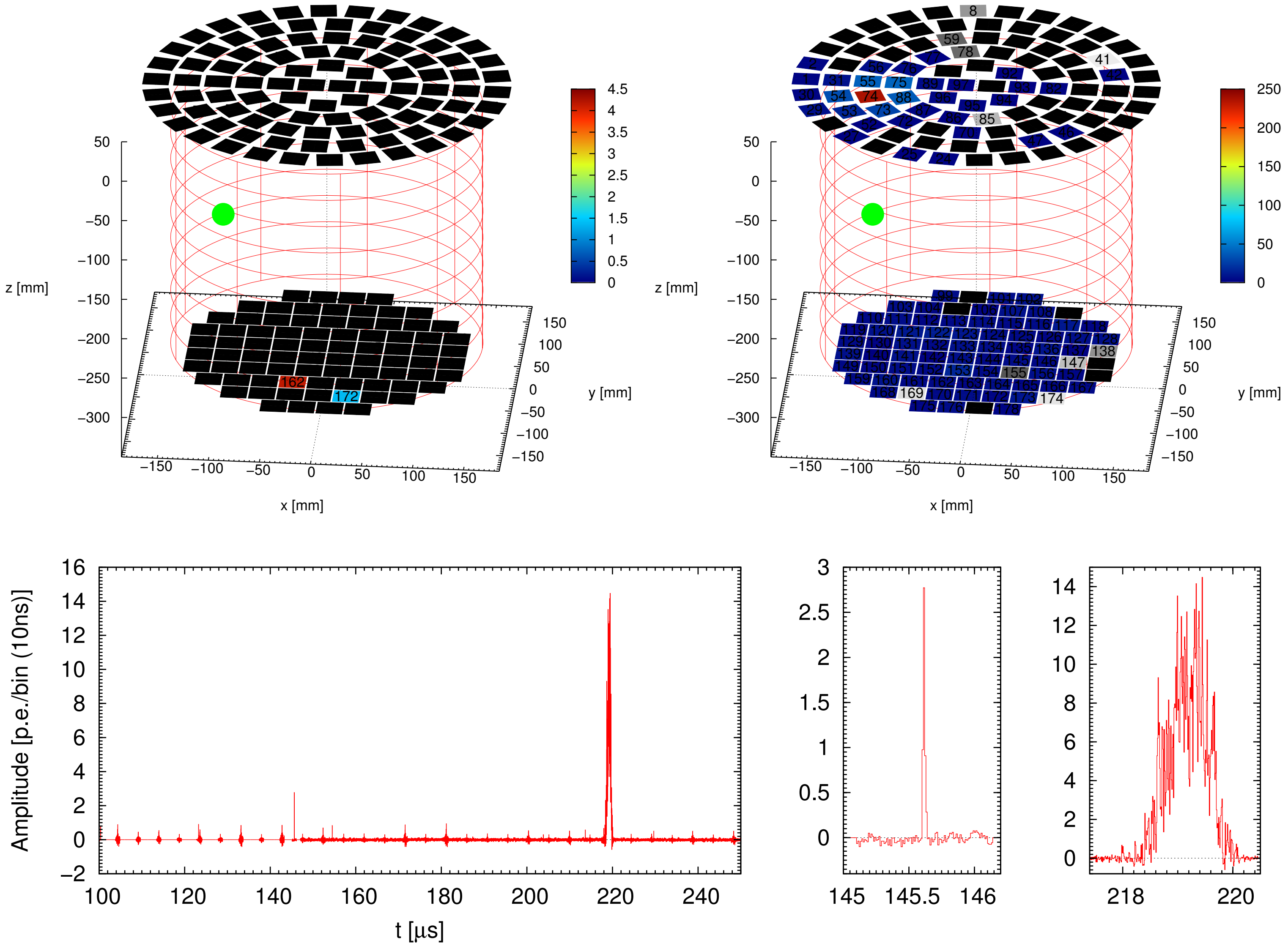

Figure 6.13: WIMP Candidate Event 6. *S1*, *S2* patterns and waveform.

6.5 Exclusion Limits

Traditionally a 90 % single sided upper limit is set for WIMP exclusion. A method described by Yellin [61] is used to compute the exclusion limit taking into account the 3 observed events on top of an estimated 1.8 ± 0.6 background. Astrophysical parameters and models used were discussed in Chapter 1. The exclusion limit of spin independent WIMP-nucleon cross section as a function of WIMP mass is shown as blue curve in Fig. 6.14. The curve here is the result from a cut based analysis. An alternative method, Profile Likelihood, which takes into account all the uncertainties (XENON100 Collaboration [60]), gives a completely compatible result (XENON100 Collaboration [59]).

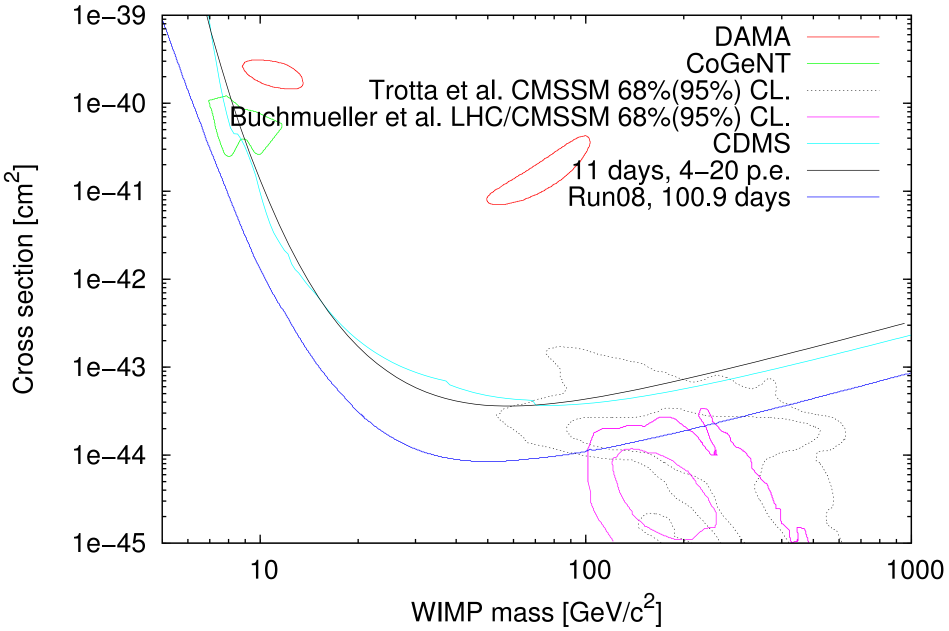

Figure 6.14: WIMP Exclusion Limits. Energy scale is determined using the global $\mathcal{L}_{\rm eff}$ fit extrapolated logarithmically to 0 at $E_{\rm nr} = 1\,$keV (light blue curve in Fig. 3.3). Previously claimed WIMP regions from DAMA (Savage et al. [49]) and CoGeNT (Aalseth et al. [1]) are shown as red and green islands, respectively. CMSSM (Trotta et al. [55]) and CMSSM+LHC (Buchmueller et al. [13]) allowed regions are plotted as black dotted and pink contours. Exclusion limits from CDMS Collaboration [15] and XENON100 11 days (Aprile et al. [7]) are plotted as black and light blue curves.

XENON100 100.9 days of data sets a limit that completely excludes DAMA and CoGeNT claimed WIMP region, and cuts into supersymmetric WIMP parameter space, as well as the region constrained by initial LHC results. It has a minimum cross section $7.0 \times 10^{-45}\,\mathrm{cm}^2$ at WIMP mass $50\,\mathrm{GeV/c}^2$.

Chapter 7

Summary and Outlook

XENON100 100.9 days data sets the most stringent limit on WIMP-nucleon cross section as of April 2011. It completely excludes previously claimed WIMP regions by experiments like DAMA and CoGeNT, therefore eliminates the low mass WIMP interpretation. The results also supersedes the sensitivity achieved by other experiments such as CDMS by a factor close to 10. XENON100 is the detector experimentally verified to have the lower electromagnetic background among all leading direct WIMP dark matter search detectors.

While XENON100 and other direct search experiments aim at detecting naturally existing cosmic WIMPs, collider experiments like LHC try to reveal the nature of WIMPs by creating them at high energy collisions. These two types of experiments are complementary in the sense that they connect cosmology with the extension of standard model of particle physics. The limit from XENON100 data already cuts into the CMSSM parameter space allowed by initial LHC data. It will be extremely interesting to see if results from both sides would agree, as improvements will be made in the near future.

As for the future of XENON detectors, there is no doubt that the detector is going to be made bigger to employ larger target mass to increase the exposure. On top of this, a few improvements could be made. First, *S2* should be incorporated into the determination of nuclear recoil energy scale. Currently only *S1* is used for nuclear recoil energy scale. Since *S1* is usually very low, and as the detector becomes bigger, it gets even lower, its fluctuation is large, hence the energy resolution is bad. On the other hand, *S2*, which is directly proportional to the number of ionization electrons, has a higher number thus lower fluctuation. And as long as the xenon cleanness is maintained, hence the electron lifetime is long enough, *S2* collection would suffer less than that of *S1* as the detector gets bigger. However, to utilizes the *S2* signal for energy scale, nuclear recoil charge yield at low energy has to be measured. There is no such measurements available in literature so far.

Although using *S2* could achieve a lower energy threshold, to retain the full 3D positioning capability, *S1* detection is required, and low *S1* detection efficiency would become a limiting factor for overall event acceptance in a larger detector. In designing a larger detector, it would be essential to optimize the optical arrange to maximize *S1* light collection. Part of the requirements could be achieved by further increasing the electric mesh transparency. However, doing so would at the same time allow more electric field leakage through the mesh. The designed and optimization of the two systems should be coordinated.

In data analysis, although supported by data, the assumption that the band in log($S2/S1$) discrimination parameter space is Gaussian, is not well justified and lacks physical explanation. Further investigation is needed in this issue. A clear model of the band shape would allow a better background event estimation.

After all, WIMP dark matter could well be a false hypothesis. However, the great experimental effort in XENON100 to achieve the lowest electronic recoil background ever is of very significant scientific value by itself.

Appendix A

Mesh Transparency

Mesh is an important element in XENON100 detector. It maintains electric potential while allowing photons and electrons to pass through. One design constrain is the light loss on meshes. Here we document the computation of mesh transparency, particularly the solid angle averaged overall transparency.

We idealize the mesh that all the wires are cylinders and they form square holes. And we denote the pitch between wires as p and the wire diameter as d. For view perpendicular to the mesh plane, the transparency is defined as the light passing ratio

$$T_{\mathrm{v}} = \frac{(p-d)^2}{p^2} = \left(1 - \frac{d}{p}\right)^2 . \tag{A.1}$$

Following the same principle in defining transparency, but looking at the mesh from a different angle at (θ, φ) (here we use spherical coordinate), T should change with the view angle. To calculate $T(\theta, \varphi)$, let's examine Fig. A.1. We fix angle φ (which determines segment OG and EF) but change angle θ, the view of a square mesh unit $ABCD$ transforms to a parallelogram $abcd$, which is essentially the projection of a tilted square onto XY plane. The tilting axis is along the line EF. By changing angle θ, the projection of vertices A, B, C and D, which are a, b, c and d, move along segments AA', BB', CC' and DD', respectively, while keeping $aA' = cC'$, $bB' = dD'$, E–a–d colinear and F–c–b colinear.

If we consider the total area of the square, the projection area should be $A_{\mathrm{proj}} = p^2 \cos\theta$. However, to calculate the transparent area, we have to subtract the area of the projection of border wires. Because the wires are cylinders, the width of the projection of wires does not change with θ, which results in the non-proportional edge length shrinking of the inner transparent area. Our task here is to calculate the transparent area by calculating the edge lengths of the inner parallelogram and the angle $\angle abc$.

It is straight forward to calculate

$$ab = p\sqrt{\cos^2(\varphi) + \sin^2(\varphi)\cos^2(\theta)} \tag{A.2}$$

$$bc = p\sqrt{\sin^2(\varphi) + \cos^2(\varphi)\cos^2(\theta)}\,, \tag{A.3}$$

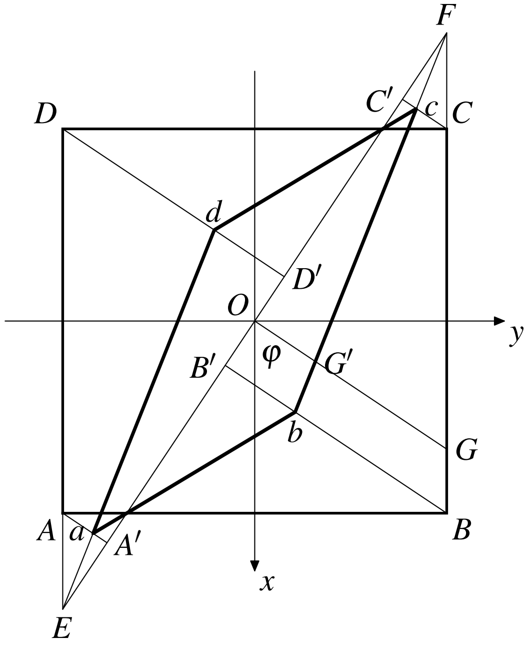

Figure A.1: Projection of a square

and the corresponding inner parallelogram edge lengths

$$l_1 = p\sqrt{\cos^2(\varphi) + \sin^2(\varphi)\cos^2(\theta)} - \frac{d}{\sin\angle abc} \tag{A.4}$$

$$l_2 = p\sqrt{\sin^2(\varphi) + \cos^2(\varphi)\cos^2(\theta)} - \frac{d}{\sin\angle abc}\,, \tag{A.5}$$

where

$$\sin\angle abc = \frac{1}{\sqrt{1 + \cos^4(\varphi)\tan^2(\varphi)\cos^2(\theta)\tan^4(\theta)}}\,. \tag{A.6}$$

Therefore the area of the inner parallelogram is

$$A_{\text{inner}} = l_1 l_2 \sin\angle abc, \tag{A.7}$$

and the transparency at certain angle (θ, φ) is

$$T(\theta,\varphi) = \frac{A_{\text{inner}}}{p^2\cos(\theta)}\,. \tag{A.8}$$

For solid angle averaged transparency, we compute

$$T_{\text{avg}}\left(\frac{p}{d}\right) = \frac{16}{4\pi}\int_{\frac{\pi}{4}}^{\frac{\pi}{2}} d\varphi \int_0^{\theta|_{\min(l_1,l_2)=0}} T(\theta,\varphi)\sin\theta d\theta\,. \tag{A.9}$$

This step is no longer analytical and is done in Mathematica® at a series of $\frac{p}{d}$ values. Noticeably we use function `Boole[`$l_1 > 0$ && $l_2 > 0$`]` to circumvent the equation solving of $\theta|_{\min(l_1,l_2)=0}$.

For hexagonal meshes, the transparency computation becomes complicated. A brute-force simulation was developed to simulate the transparency of hexagonal mesh as a function of θ. Interestingly, the θ dependent result for a hexagonal mesh is very close to a square of the same pitch and wire sizes, as shown in Fig. 2.5.

This page intentionally left blank

Bibliography

[1] C. E. Aalseth, P. S. Barbeau, N. S. Bowden, B. Cabrera-Palmer, J. Colaresi, J. I. Collar, S. Dazeley, P. de Lurgio, J. E. Fast, N. Fields, C. H. Greenberg, T. W. Hossbach, M. E. Keillor, J. D. Kephart, M. G. Marino, H. S. Miley, M. L. Miller, J. L. Orrell, D. C. Radford, D. Reyna, O. Tench, T. D. Van Wechel, J. F. Wilkerson, and K. M. Yocum. Results from a search for light-mass dark matter with a p-type point contact germanium detector. *Phys. Rev. Lett.*, 106 (13):131301, Mar 2011. doi: 10.1103/PhysRevLett.106.131301. 6.14

[2] D. Akimov et al. Measurements of scintillation efficiency and pulse shape for low energy recoils in liquid xenon. *Phys. Lett. B*, 524:245, 2002. 3.2

[3] C. Alcock et al. The MACHO project: Microlensing results from 5.7 years of LMC observations. *Astrophys. J.*, 542:281–307, 2000. 1.1.2

[4] E. Aprile and T. Doke. Liquid xenon detectors for particle physics and astrophysics. *Rev. Mod. Phys.*, 82(3):2053–2097, Jul 2010. doi: 10.1103/RevModPhys.82.2053. 3.2

[5] E. Aprile, C. E. Dahl, L. de Viveiros, R. J. Gaitskell, K. L. Giboni, J. Kwong, P. Majewski, K. Ni, T. Shutt, and M. Yamashita. Simultaneous measurement of ionization and scintillation from nuclear recoils in liquid xenon for a dark matter experiment. *Phys. Rev. Lett.*, 97(8): 081302, Aug 2006. doi: 10.1103/PhysRevLett.97.081302. 3.2, 3.2

[6] E. Aprile, L. Baudis, B. Choi, K. L. Giboni, K. Lim, A. Manalaysay, M. E. Monzani, G. Plante, R. Santorelli, and M. Yamashita. New measurement of the relative scintillation efficiency of xenon nuclear recoils below 10 kev. *Phys. Rev. C*, 79(4):045807, Apr 2009. doi: 10.1103/PhysRevC.79.045807. 3.2

[7] E. Aprile, K. Arisaka, F. Arneodo, A. Askin, L. Baudis, A. Behrens, K. Bokeloh, E. Brown, J. M. R. Cardoso, B. Choi, D. B. Cline, S. Fattori, A. D. Ferella, K.-L. Giboni, A. Kish, C. W. Lam, J. Lamblin, R. F. Lang, K. E. Lim, J. A. M. Lopes, T. Marrodán Undagoitia, Y. Mei, A. J. Melgarejo Fernandez, K. Ni, U. Oberlack, S. E. A. Orrigo, E. Pantic, G. Plante, A. C. C. Ribeiro, R. Santorelli, J. M. F. dos Santos, M. Schumann, P. Shagin, A. Teymourian, D. Thers, E. Tziaferi, H. Wang, and C. Weinheimer. First dark matter results from the xenon100 experiment. *Phys. Rev. Lett.*, 105(13):131302, Sep 2010. doi: 10.1103/PhysRevLett.105.131302. 6, 6.14

[8] E. Aprile et al. Scintillation response of liquid xenon to low energy nuclear recoils. *Phys. Rev. D.*, 72:072006, 2005. 3.2

[9] F. Arneodo et al. Scintillation efficiency of nuclear recoil in liquid xenon. *Nucl. Instr. and Meth. A*, 449:147, 2000. 3.2

[10] K. G. Begeman, A. H. Broeils, and R. H. Sanders. Extended rotation curves of spiral galaxies: dark haloes and modified dynamics. *Monthly Notices of the Royal Astronomical Society*, 249: 523–537, 1991. 1.1.1, 1.1

[11] R. Bernabei et al. *Eur. Phys. J. direct C*, 11:1, 2001. 3.2

[12] Tobias Bruch, Justin Read, Laura Baudis, and George Lake. Detecting the milky way's dark disk. *Astrophysical Journal*, 696:920–923, May 2009. 1.2.1

[13] O. Buchmueller et al. Implications of Initial LHC Searches for Supersymmetry. *arXiv:1102.4585*, 2011. 6.14

[14] E. M. Burbidge, G. R. Burbidge, D. J. Crampin, V. C. Rubin, and K. H. Prendergast. The rotation and mass of NGC 6503. *Astrophys. J.*, 139:539–544, 1964. 1.1

[15] CDMS Collaboration. Dark matter search results from the CDMS II experiment. *Science*, 327 (5973):1619–1621, 2010. 6.14

[16] Spencer Chang, Graham D. Kribs, David Tucker-Smith, and Neal Weiner. Inelastic dark matter in light of DAMA/LIBRA. *Phys. Rev. D.*, 79:043513, 2009. 1.2.2

[17] V. Chepel et al. Scintillation efficiency of liquid xenon for nuclear recoils with the energy down to 5 keV. *Astropart. Phys.*, 26:58, 2006. 3.2

[18] COBE/FIRAS. Far infrared absolute spectrophotometer. `http://lambda.gsfc.nasa.gov/product/cobe/firas_overview.cfm`. 1.1.1

[19] E. Conti, R. DeVoe, G. Gratta, T. Koffas, S. Waldman, J. Wodin, D. Akimov, G. Bower, M. Breidenbach, R. Conley, M. Danilov, Z. Djurcic, A. Dolgolenko, C. Hall, A. Odian, A. Piepke, C. Y. Prescott, P. C. Rowson, K. Skarpaas, J-L. Vuilleumier, K. Wamba, and O. Zeldovich. Correlated fluctuations between luminescence and ionization in liquid xenon. *Phys. Rev. B*, 68 (5):054201, Aug 2003. doi: 10.1103/PhysRevB.68.054201. 3.1

[20] Walter Dehnen and James J. Binney. Local stellar kinematics from hipparcos data. *Monthly Notices of the Royal Astronomical Society*, 298:387–394, 1998. 1.2.1

[21] Tadayoshi Doke and Kimiaki Masudab. Present status of liquid rare gas scintillation detectors and their new application to gamma-ray calorimeters. *Nucl. Instr. and Meth. A*, 420:62–80, 1999. 2.6, 2.6.1

[22] Todayoshi Doke. Recent developments of liquid xenon detectors. *Nucl. Instr. and Meth.*, 196: 87–96, 1982. 2.7.3

[23] Andrzej K. Drukier, Katherine Freese, and David N. Spergel. Detecting cold dark-matter candidates. *Phys. Rev. D.*, 33(12):3495–3508, 1986. 1.2.1

[24] Albert Einstein. Lens-like action of a star by the deviation of light in the gravitational field. *Science*, 84(2188):506–507, 1936. 1.1.1

[25] F. Favata, A. Smith, M. Bavdaz, and T. Kowalski. Light yield as a function of gas pressure and electric field in gas scintillation proportional counters. *Nucl. Instr. and Meth. A*, 294(3): 595–601, 1990. 2.7, 2.7

[26] Raphaël Gavazzi, Tommaso Treu, Jason D. Rhodes, Léon V. E. Koopmans, Adam S. Bolton, Scott Burles, Richard J. Massey, and Leonidas A. Moustakas. The sloan lens ACS survey. iv. the mass density profile of early-type galaxies out to 100 effective radii. *Astrophys. J.*, 667(1): 176–190, 2007. 1.1.1

[27] David Graff and Katherine Freese. Analysis of a hubble space telescope search for red dwarfs: limits on baryonic matter in the galactic halo. *Astrophys. J.*, 456:49, 1996. 1.1.2

[28] Hamamatsu. Photomultiplier tubes, 2006. `http://sales.hamamatsu.com/assets/applications/ETD/pmt_handbook_complete.pdf`. 4.1.2

[29] Richard H. Helm. Inelastic and elastic scattering of 187-MeV electrons from selected even-even nuclei. *Physical Review*, 104(5):1466–1475, 1956. 1.2.2, 1.2.2

[30] Akira Hitachi and Tan Takahashi. Effect of ionization density on the time dependence of luminescence from liquid argon and xenon. *Phys. Rev. B.*, 27:5279–5285, 1983. 2.6

[31] Joshua Jortner, Lothar Meyer, Stuart A. Rice, and E. G. Wilson. Localized excitations in condensed Ne, Ar, Kr, and Xe. *J. Chem. Phys.*, 42:4250, 1965. 2.1

[32] Gerard Jungman, Marc Kamionkowski, and Kim Griest. Supersymmetric dark matter. *Phys. Rept.*, 267:195–373, 1996. doi: 10.1016/0370-1573(95)00058-5. 1.1.3

[33] Alexander Kish. Nuclear recoil background prediction for run_08. `https://xecluster.lngs.infn.it/dokuwiki/doku.php?id=xenon:xenon100:analysis:run8ubp:nrbg`. 6.2

[34] S Kubota, M Hishida, and J Raun. Evidence for a triplet state of the self-trapped exciton states in liquid argon, krypton and xenon. *J. Phys. C.*, 11(12):2645, 1978. 2.6, 2.6.1

[35] J. D. Lewin and P. F. Smith. Review of mathematics, numerical factors, and corrections for dark matter experiments based on elastic nuclear recoil. *Astroparticle Physics*, 6:87–112, 1996. 1.2.2, 1.2.2, 1.2.2

[36] J. Lindhard and M. Scharff. Energy dissipation by ions in the kev region. *Phys. Rev.*, 124: 128–130, 1961. 3.2

[37] Marlo Martin. Exciton self-trapping in rare-gas crystals. *J. Chem. Phys.*, 54:3289, 1971. 2.1

[38] Kenneth J. Mighell. Parameter estimation in astronomy with poisson-distributed data. i. the χ^2_γ statistic. *Astrophysical Journal*, 518:380–393, 1999. 4.1.2

[39] M. Milgrom. A modification of the newtonian dynamics as a possible alternative to the hidden mass hypothesis. *Astrophysical Journal*, 270:365–370, 1983. 1.1.2

[40] J. Najita, G. Tiede, and S. Carr. From stars to superplanets: The low-mass initial mass function in the young cluster IC 348. *Astrophys. J.*, 541:977–1003, 2000. 1.1.2

[41] K. Ni, R. Hasty, T. M. Wongjirad, L. Kastens, A. Manzur, and D.N. McKinsey. Preparation of neutron-activated xenon for liquid xenon detector calibration. *Nucl. Instr. and Meth. A*, 582: 569–574, 2007. 3.3.2, 4.3.3

[42] James H. Parker Jr. and John J. Lowke. Theory of electron diffusion parallel to electric fields. *Phys. Rev.*, 181(1):290–311, 1969. 2.7.4

[43] G. Plante, E. Aprile, R. Budnik, B. Choi, K. L. Giboni, L. Goetzke, R. F. Lang, K. E. Lim, and A. J. Melgarejo Fernandez. New measurement of the scintillation efficiency of low energy nuclear recoils in liquid xenon. *submitted to PRD and at arXiv:1104.2587*, 2011. 3.2, 3.3

[44] William H. Press, Saul A. Teukolsky, William T. Vetterling, and Brian P. Flannery. *Numerical Recipes*, chapter 10. Cambridge University Press, third edition, 2007. 4.1.2

[45] William H. Press, Saul A. Teukolsky, William T. Vetterling, and Brian P. Flannery. *Numerical Recipes*, chapter 3. Cambridge University Press, third edition, 2007. 4.1.2

[46] V. C. Rubin, W. K. J. Ford, and N. Thonnard. Rotational properties of 21 sc galaxies with a large range of luminosities and radii, from NGC 4605 $r = 4\,\mathrm{kpc}$ to UGC 2885 $r = 122\,\mathrm{kpc}$. *Astrophys. J.*, 238:471–487, 1980. 1.1.1

[47] F. P. Santos, T. H. V. T. Dias, A D. Stauffer, and C. A. N. Conde. Three-dimensional monte carlo simulation of the vuv electroluminescence and other electron transport parameters in xenon. *J. Phys. D*, 27:42–48, 1994. 2.7.3

[48] Chris Savage, Katherine Freese, and Paolo Gondolo. Annual modulation of dark matter in the presence of streams. *Phys. Rev. D.*, 74:043531, 2006. 1.2.1, 1.2.1

[49] Christopher Savage, Graciela Gelmini, Paolo Gondolo, and Katherine Freese. Compatibility of DAMA/LIBRA dark matter detection with other searches. *arXiv:0808.3607*, 2009. 6.14

[50] H. R. Skullerud. Longitudinal diffusion of electrons in electrostatic fields in gases. *J. Phys. B*, 2:696–705, 1969. 2.7.4

[51] Martin C. Smith, Gregory R. Ruchti, Amina Helmi, Rosemary F. G. Wyse, J. P. Fulbright, K. C. Freeman, J. F. Navarro, G. M. Seabroke, M. Steinmetz, M. Williams, O. BienaymÃľ, J. Binney, J. Bland-Hawthorn, W. Dehnen, B. K. Gibson, G. Gilmore, E. K. Grebel, U. Munari, Q. A. Parker, R.-D. Scholz, A. Siebert, F. G. Watson, and T. Zwitter. The RAVE survey: constraining the local galactic escape speed. *Monthly Notices of the Royal Astronomical Society*,

379(2):755–772, 2007. ISSN 1365-2966. doi: 10.1111/j.1365-2966.2007.11964.x. URL `http://dx.doi.org/10.1111/j.1365-2966.2007.11964.x`. 1.2.1

[52] Peter Sorensen. Anisotropic diffusion of electrons in liquid xenon with application to improving the sensitivity of direct dark matter searches. *arXiv:1102.2865*, 2011. 2.7.4, 2.7.4

[53] Peter Sorensen and Carl Eric Dahl. Nuclear recoil energy scale in liquid xenon with application to the direct detection of dark matter. *Phys. Rev. D*, 83(6):063501, Mar 2011. doi: 10.1103/PhysRevD.83.063501. 3.2

[54] P. Tisserand et al. Limits on the MACHO content of the Galactic Halo from the EROS-2 survey of the Magellanic clouds. *Astron. Astrophys.*, 469:387–404, 2007. 1.1.2

[55] R. Trotta, F. Feroz, M. P. Hobson, L. Roszkowski, and R. Ruiz de Austri. The impact of priors and observables on parameter inferences in the Constrained MSSM. *arXiv:0809.3792*, 2008. 6.14

[56] S. S. Wilks. The large-sample distribution of the likelihood ratio for testing composite hypotheses. *Ann. Math. Statist.*, 9(1):60–62, 1938. 5.2

[57] WMAP Science Team. Seven-year wilkinson microwave anisotropy probe (WMAP) observations. `http://lambda.gsfc.nasa.gov/product/map/dr4/map_bibliography.cfm`. 1, 1.1.1, 1.3

[58] XENON100 Collaboration. A study of the electromagnetic background in the XENON100 experiment. *Phys. Rev. D.*, 83:082001, 2011. 2.1, 2.6

[59] XENON100 Collaboration. Dark matter results from 100 live days of XENON100 data. *arXiv:1104.2549*, 2011. 6.5

[60] XENON100 Collaboration. Likelihood approach to the first dark matter results from XENON100. *arXiv:1103.0303*, 2011. 6.5

[61] S. Yellin. Finding an upper limit in the presence of an unknown background. *Phys. Rev. D*, 66(3):032005, Aug 2002. doi: 10.1103/PhysRevD.66.032005. 6.5

[62] Fritz Zwicky. Die rotverschiebung von extragalaktischen nebeln. *Helv. Phys. Acta*, 6:110–127, 1933. 1

[63] Fritz Zwicky. On the masses of nebulae and of clusters of nebulae. *Astrophys. J.*, 86:217, 1937. 1